Insights on Metal Ions and Misfolded Proteins in Alzheimer's Disease Using Flavonoid Derivatives and X-ray Fluorescence Microscopy

by

Alaina Sara DeToma

A dissertation submitted in partial fulfillment
of the requirements for the degree of
Doctor of Philosophy
(Chemistry)
in the University of Michigan
2013

Doctoral Committee:

Assistant Professor Mi Hee Lim, Chair
Associate Professor Sylvie Garneau-Tsodikova, University of Kentucky
Professor Vincent L. Pecoraro
Professor Ayyalusamy Ramamoorthy

To my parents, Dominic and Deborah, with the utmost gratitude for their unconditional love and support.
With all my love, always.

Acknowledgments

I am indebted to my advisor, Professor Mi Hee Lim, for her guidance during my Ph.D. The primary reason I was able to conduct this research and prepare this dissertation is because I selected an advisor who truly cares about her students and who has gone to extraordinary lengths to help us succeed. I am deeply grateful for the time she spent to educate me as a scientist, for giving me a chance to try everything, and for her endless encouragement. I am proud to come from her lab knowing that I am ready to tackle any challenge, and I am eager to see what exciting science emerges from the Lim lab in the near future.

I would like to thank my committee members for their time and effort in helping me achieve my research program. Professor Vincent Pecoraro went out of his way to serve on my committee, even participating in my candidacy exam from France! I am grateful for the inorganic chemistry expertise he was able to share with me. I would like to thank Professor Ayyalusamy Ramamoorthy for his continued support as a collaborator and committee member. I have enjoyed the opportunity to learn more biophysical chemistry from him and from his lab, as well as the insight brought forward from our mutual interests in amyloids. I am grateful to Professor Sylvie Garneau-Tsodikova for joining my doctoral committee and bringing her medicinal chemistry perspective to my research, as well as for all of the informal conversations we have had in the halls of LSI. Finally, I would like to acknowledge Professor Jason Gestwicki, who formerly served on my committee during candidacy, for his continued support of my research.

If not for my undergraduate education at Elizabethtown College, I would not have had the proper foundation to pursue a post-graduate degree in chemistry. I would especially like to thank Dr. Charles D. Schaeffer, Jr., my undergraduate research mentor, for introducing me to research and for continuing to be a supportive advisor even after leaving Musser Hall. I am also grateful to the entire faculty and staff in the

Elizabethtown College chemistry department for always welcoming me back to visit and for their role in my education and career development, including Dr. Kristi Kneas, Dr. James MacKay, Dr. Gary Hoffman, Dr. Tom Hagan, Dr. Ray Reeder, Dr. Jeff Rood, Mrs. Linda Ebright, and Mrs. Kris Tussing. I must also thank my high school chemistry teacher, Mr. Richard Sweger, for sparking my interest in chemistry and encouraging me to stick with it even “over my dead body.”

I share the credit of my work with the many wonderful people I have had the pleasure of collaborating with on various projects. While individual research contributions are acknowledged at the beginning of each chapter, I would like to elaborate on a few here. First, I am grateful to Dr. Jung-Suk Choi for her patience and mentorship that began in my rotation. Her efforts made a significant impact on my entire graduate school career. I would also like to thank Dr. Xiaoming He and Dr. Sanghyun Lee for their mentorship and our collaborations, as well as Yihong Liu for being supportive of our group and for taking the time to teach me how to do cell culture. I have had the opportunity to work with some great undergraduates, especially Kevin O’Neill, who helped me to process some of the XRF data, Caitlin McCarthy from UM Flint, who did cell studies for some earlier flavonoid work, and Emma Garst, an NSF REU student from Mt. Holyoke College, as well as Isaac Kimsey, a rotation student. I extend my gratitude to the other past and current Lim lab members who have been invaluable in my development as a scientist: Nichole Schmidt, Chen Wang, Jingli Cheng, Nate Merrill, Hyun Min Park, Michael Beck, Yuzhong Liu, Jin Hoon Kim, Arkah Ghosh, Younwoo Nam, Dr. Masha Savelieff, Juhye Kang.

I am also grateful to the kind colleagues of LSI in neighboring labs and in the Chemistry department who were always willing to lend reagents or discuss science. I must also thank everyone in the administrative/IT/facilities suite at LSI, especially Erin, Sheila, Cathy, Betty, Chris, Michelle, AJ, and Leigh Ann, for everything they have done to support our research and for all of the conversations we’ve had.

I owe special thanks to my fellow lab members whose friendship went beyond the science on which we collaborated. First, I would like to thank Dr. Joseph Braymer for being a supportive friend and colleague for always encouraging me when I needed it. Thanks for the stories, ice cream, and science! I am also fortunate for the friendship

of Akiko Kochi, who understood me when I started acting weird, helped me when the TEM was wonky, and made sure there was enough chocolate around. “Good game, Coach!” I am also grateful to Amit Pithadia for many deep conversations about science and deep conversations not about science, and for being a great supporter as I finished up my Ph.D. I will definitely miss our trips to JC, TK Wu, the pie place (RIP), Starbucks, Timmy’s, etc.!

It would have been impossible for me to have made it this far without the most wonderful family and friends. I would like to thank my entire extended family for being such great cheerleaders. There are too many people to name, but they know who they are and they are the best. So many of my friends from home have lent their support to me. I especially want to thank Critch for the encouraging cards, Amanda for the entertaining and supportive messages over the years, and Laura for understanding what it is like to be in grad school. I also want to thank Tanya for being a great friend here at Michigan. It certainly helped being able to go grab coffee on a regular basis as we both finished up and needed a sympathetic ear.

Next, I have to thank my best friend and always “roomie,” Becky, for everything she has done to be there for me when she couldn’t physically be here. Her continued friendship through our (almost) daily chats made me feel like I wasn’t actually far away. I’m lucky to have such a dependable friend who knows that sometimes all you need is to meet your best friend for lunch and a cupcake, even if it means you both have to drive 4 hours to make that happen.

To my brother, Dan, thank you for being my closest confidant over the years. You are such an inspiration to me and I am very lucky and proud to call you my brother. I’m thankful for all you and Rebecca (and Wallie!) have done to support me. I love you guys.

To Justin, thank you for staying by my side unconditionally, for supporting me during difficult times, and for never giving up on us. You have made me so happy in ways I didn’t know were possible. As we are about to close this chapter (finally), I can’t wait to see what comes next. I love you.

Finally, I want to thank my parents. I am convinced that if you have people like these that love you, nothing could be impossible. Mom and Dad, words could never

ever express how lucky I am to have you as parents. Thank you for being the best role models for who I wanted to become, for always believing in me, for giving me perspective on things when I could only see right in front of me, and for allowing me to be “fearless.” Finally, thank you for coming to visit me as often as you did, whether it was to take care of the car, to just visit, or to go to Hell (Hell, Michigan, that is!). Those visits were always so much fun and made the next stretch of time more bearable. I love you both more than you know. And that’s the kind of hairpin I am!

Table of Contents

Dedication ii
Acknowledgments iii
List of Tables xii
List of Figures xiii
List of Abbreviations xvii
Abstract xxi
Chapter 1: Connecting Metal Homeostasis, Protein Aggregation, and Neurodegenerative Diseases 1
1.1. Bioinorganic chemistry in the brain 2
1.2. Protein misfolding and human neurodegenerative diseases 3
1.3. Bioinorganic chemistry and protein misfolding in Alzheimer's disease 6
1.3.1. Alzheimer's disease (AD) and amyloid-β (Aβ) 6
1.3.2 Amyloid precursor protein (APP) and Aβ generation 7
1.3.3. Aggregated Aβ species and their contribution to neurotoxicity 8
1.3.4. Metal ions in AD and their interactions with Aβ 10
1.3.5. Small molecule-based approaches to understanding metal–Aβ interaction and neurotoxicity 14
1.4. Conclusion 17
1.5. Scope of this thesis 18
1.6. References 19
Chapter 2: Myricetin and Luteolin: Naturally Occurring Regulators of Metal-Induced Aβ Aggregation and Neurotoxicity 23
2.1. Introduction 24
2.2. Results and discussion 26
2.2.1. Metal binding properties of myricetin and luteolin 26
2.2.2. Modulation of metal-associated Aβ aggregation by myricetin and luteolin 30

2.2.3. Regulation of H_2O_2 production from Cu(II)-associated Aβ species *in vitro* 34

2.2.4. Regulation of toxicity from metal-associated Aβ species in human neuroblastoma cells by myricetin and luteolin 36

2.3. Conclusion 37

2.4. Experimental 38

2.4.1. Materials and methods 38

2.4.2. Metal binding studies 39

2.4.3. Amyloid-β (Aβ) peptide experiments 39

2.4.4. Gel electrophoresis and Western blotting 40

2.4.5. Transmission electron microscopy (TEM) 40

2.4.6. H_2O_2 production measured by the horseradish peroxidase/Amplex Red assay 41

2.4.7. Cell viability measurements by the MTT assay 41

2.5. References 42

Chapter 3: Insights into the Anti-Amyloidogenic Properties of the Green Tea Extract EGCG: Metal-Free *versus* Metal-Associated Aβ Species 45

3.1. Introduction 46

3.2. Results and discussion 48

3.2.1. EGCG distinctly modulates Aβ aggregation induced by Cu(II) or Zn(II) 48

3.2.2. EGCG diminishes metal-free and metal–Aβ toxicity in living cells 51

3.2.3. EGCG directly binds to Aβ peptide and causes conformational changes 52

3.2.4. Molecular modeling studies present that EGCG could interact directly with Aβ monomer 57

3.2.5. Metal binding of EGCG occurs in both the absence and presence of Aβ 62

3.2.6. EGCG forms ternary complexes with metal-treated Aβ 64

3.3. Conclusion 66

3.4. Experimental 67

3.4.1. Materials and procedures 67

3.4.2. Metal binding experiments 68

3.4.3. Aβ aggregation experiments 68

3.4.4. Gel electrophoresis and Western blotting 69

3.4.6. Cell viability measurements 70
3.4.7. Ion mobility-mass spectrometry (IM-MS) 70
3.4.8. Docking studies 71
3.4.9. Molecular dynamics simulations 71
3.4.10. 2D NMR spectroscopy 72
3.5. References 73
Chapter 4: Reactivity of Synthetic Aminoisoflavone Derivatives with Metal–Aβ Species *In Vitro* and in Living Cells 76
4.1 Introduction 77
4.2. Results and discussion 80
4.2.1. Design and synthesis of aminoisoflavone derivatives 80
4.2.2. Solution speciation studies of aminoisoflavones 82
4.2.3. Metal binding studies 83
4.2.4. EPR investigations of Cu(II)–4 complexes 89
4.2.5. Interaction of aminoisoflavones with Aβ species 92
4.2.6. Aβ aggregation in the absence and presence of aminoisoflavones 102
4.2.7. Antioxidant properties 108
4.2.8. Cell viability studies 110
4.2.9. Blood-brain barrier (BBB) permeability 115
4.3. Conclusion 116
4.4. Experimental 118
4.4.1. Materials and methods 118
4.4.2. General procedure for the preparation of hydroxylated 2-amino-3-aryl-4*H*-chromen-4-ones (1-4) 119
4.4.3. Determination of solution speciation from acidity constants for aminoisoflavones and stability constants for Cu(II)–4 complexes 120
4.4.4. Metal binding studies 121
4.4.5. Electron paramagnetic resonance (EPR) investigations of Cu(II)–4 complexes 121
4.4.6. Electrochemistry of 4 122
4.4.7. Isothermal titration calorimetry (ITC) for measurement of thermodynamic parameters for the interaction of 1, 2, or 4 with Aβ 122

4.4.8. Docking studies of aminoisoflavones against Aβ40 monomer 123
4.4.9. NMR sample preparation 123
4.4.10. NMR measurements 124
4.4.11. Amyloid-β (Aβ) experiments 124
4.4.12. Gel electrophoresis and Western blotting 125
4.4.13. Transmission electron microscopy (TEM) 125
4.4.14. Trolox equivalence antioxidant capacity (TEAC) Assay 126
4.4.15. Horseradish peroxidase (HRP)/Amplex Red assay for detection of H_2O_2 126
4.4.16. Cell viability measurements 127
4.4.17. Parallel artificial membrane permeability assay adapted for BBB (PAMPA-BBB) 127
4.5. References 128
Chapter 5: Visualization of Transition Metals in Cortical and Hippocampal Brain Tissues from an Alzheimer's Disease Mouse Model 134
5.1. Introduction 135
5.2. Results and discussion 136
5.2.1. Metal contents and distributions in hippocampal and cortical tissues from the brains of AD and wild-type mice by μ-XRF imaging 136
5.2.2. Metal correlations 140
5.3. Conclusion 142
5.4. Experimental 143
5.4.1. Animal care and tissue preparation 143
5.4.2. Synchrotron μ-X-ray fluorescence (μ-XRF) microscopy 143
5.5. References 144
Chapter 6: Concluding Remarks and Perspectives 146
Appendix A: Quantifying Potential Changes in Metal Homeostasis in Glaucoma by Synchrotron μ-X-ray Fluorescence (μ-XRF) Imaging 150
A.1. Introduction 150
A.2. Results and discussion 153
A.2.1. Imaging of metals and quantification of Fe, Cu, and Zn in the retina and superior colliculus 153
A.3. Conclusion and Future Directions 157

A.4. Experimental 157
A.4.1. Animal care and tissue preparation 157
A.4.2. Synchrotron μ-X-ray fluorescence (μ-XRF) microscopy 158
A.5. References 159

List of Tables

Table 3.1. Collision cross-section (CCS) of 3^+ and 4^+ states of $A\beta_{40}$ monomer and related species. 56

Table 3.2. Dissociation constants of $A\beta_{40}$–EGCG complexes. 57

Table 4.1. Thermodynamic values for the interaction of **1**, **2**, and **4** with $A\beta_{40}$ determined by isothermal titration calorimetry (ITC). 93

Table 4.2. BBB permeability assessed by PAMPA-BBB, Lipinski's rules, and logBB calculation. 116

Table 5.1. Average metal contents in cortical and hippocampal regions of APPswe/PS1ΔE9 (APPswe) and wild type (WT) mice brain tissues. 139

List of Figures

Figure 1.1. Nucleation polymerization model of amyloid aggregation. 5
Figure 1.2. Cleavage of APP by α-, β-, and γ-secretases in the non-amyloidogenic and amyloidogenic pathways. 8
Figure 1.3. Reactive oxygen species (ROS) generated by redox cycling of Cu-bound Aβ under reducing conditions (Fenton chemistry). 11
Figure 1.4. Multifunctional small molecules that can be used to investigate Cu(II)/Zn(II)-associated Aβ species in AD. 16
Figure 2.1. Chemical structures of myricetin and luteolin. 25
Figure 2.2. Cu(II) and Zn(II) binding studies with myricetin and luteolin by UV-Vis spectroscopy. 27
Figure 2.3. Structures used to investigate metal chelation sites of flavonoids. 28
Figure 2.4. Job plots of Cu(II) with myricetin and luteolin. 29
Figure 2.5. UV-Vis studies showing the interaction of myricetin with metal ions in the presence of Aβ. 30
Figure 2.6. Inhibitory effect of luteolin and myricetin on the formation of metal-induced Aβ aggregates. 31
Figure 2.7. TEM images of the samples containing myricetin from Figure 2.6. 31
Figure 2.8. Transformation of metal-induced Aβ aggregates by luteolin or myricetin. 33
Figure 2.9. Modulation of Cu(II)–Aβ-induced H_2O_2 production by myricetin and luteolin. 35
Figure 2.10. Modulation of metal-free and metal-induced Aβ toxicity in human neuroblastoma SK-N-BE(2)-M17 cells. 36
Figure 3.1. Structure of (−)-epigallocatechin-3-gallate (EGCG). 47
Figure 3.2. Assessment of the ability of EGCG to modulate metal-free and metal-associated $A\beta_{40}$ aggregation *in vitro*. 49

Figure 3.3. Concentration dependence of EGCG on modulation of Cu(II)-induced Aβ aggregation. 50
Figure 3.4. Disaggregation of preformed metal-free and metal-associated Aβ aggregates by EGCG.. 51
Figure 3.5. Effect of EGCG on $A\beta_{40}$ or metal–$A\beta_{40}$ species in living cells. 52
Figure 3.6. Interaction of EGCG with $A\beta_{40}$. 54
Figure 3.7. Analysis of the Aβ species resulting from the inhibition experiment (Figure 3.2) in the same buffer used for IM-MS (Figures 3.6 and 3.13) by gel electrophoresis using immunoblotting (6E10). 55
Figure 3.8. Docking studies of EGCG with $A\beta_{40}$ monomer (PDB 2LFM) by AutoDock Vina. 60
Figure 3.9. Molecular modeling of EGCG-bound $A\beta_{40}$. 60
Figure 3.10. Molecular modeling of EGCG-bound $A\beta_{40}$ based on docking structures (Figure 3.8). 61
Figure 3.11. Histogram of the frequency of the structures with the corresponding CCS. 62
Figure 3.12. Cu(II) and Zn(II) binding of EGCG determined by UV-Vis. 63
Figure 3.13. Interactions of EGCG with metal–$A\beta_{40}$ species. 65
Figure 3.14. Interactions of $A\beta_{40}$ with Cu(II) and Zn(II) by MS. 66
Figure 4.1. Chemical structures of naturally occurring flavonoids and synthetic aminoisoflavones (**1**-**4**). 79
Figure 4.2. Solution speciation studies of aminoisoflavones (**1**-**4**). 83
Figure 4.3. Cu(II) binding studies of the aminoisoflavones. 84
Figure 4.4. Zn(II) binding properties of aminoisoflavones. 85
Figure 4.5. Interaction of **4** with Cu(II) in the presence of $A\beta_{40}$. 86
Figure 4.6. Solution speciation studies of Cu(II)–**4** complexes. 88
Figure 4.8. EPR spectra of partially oxidized **4** in absence and presence of $ZnCl_2$.. 90
Figure 4.9. Cyclic voltammetry of **4**. 91
Figure 4.10. Interaction of **1** and **4** with low MW $A\beta_{40}$ at near stoichiometric ratios. 95
Figure 4.11. Chemical shift changes in low MW $A\beta_{40}$ induced by **1** and **4**. 96

Figure 4.12. Docking studies of **1**, **2**, and **4** with metal-free Aβ40 (PDB ID 2LFM). 99
Figure 4.13. Interaction of low MW Aβ40 with a 5 equiv of **1**. 99
Figure 4.14. ^{1}H spectra of low MW Aβ40 titrated with **1** and **4**. 100
Figure 4.15. Interaction of **1** and **4** with Aβ40 fibrils by STD NMR. 101
Figure 4.16. Investigation of the ability of aminoisoflavones (**1**-**4**) to modulate the formation of metal-free and metal-induced Aβ40 and Aβ42 aggregates. 104
Figure 4.17. Disassembly of metal-free and metal-associated Aβ40 and Aβ42 aggregates by aminoisoflavones. 105
Figure 4.18. Inhibition and disaggregation experiments employing methoxylated aminoisoflavone precursors (**1a**, **2a**, and **4a**). 107
Figure 4.19. Radical scavenging ability of aminoisoflavones (**1**-**4**) determined by the Trolox equivalence antioxidant capacity (TEAC) assay. 109
Figure 4.20. H_2O_2 production in the presence of Aβ40, Cu(II), and ligands. 110
Figure 4.21. Cell viability for aminoisoflavones in the absence and presence of $CuCl_2$ or $ZnCl_2$ in human neuroblastoma SK-N-AS cells. 112
Figure 4.22. Cell viability for aminoisoflavones in the absence and presence of $CuCl_2$ or $ZnCl_2$ in human neuroblastoma SK-N-BE(2)-M17 cells. 114
Figure 4.23. Influence of aminoisoflavones on SK-N-BE(2)-M17 (M17) cell viability in the presence of metal-free and metal-associated Aβ40 and Aβ42 114
Figure 5.1. Visualization of Fe, Cu, and Zn in brain tissues of AD (APPswe/PS1ΔE9) and wild-type (WT) mice by microbeam X-ray fluorescence (μ-XRF) imaging. 137
Figure 5.2. Visualization of Fe, Cu, and Zn in brain tissues APPswe mice by microbeam X-ray fluorescence (μ-XRF) imaging. 138
Figure 5.3. Histograms of Fe, Cu, and Zn amounts in selected brain tissue regions of AD APPswe or WT mice. 140
Figure 5.4. Correlation of metal contents (μg/cm^2) in regions of APPswe and WT mice brain tissue according to co-incident metal concentrations. 141
Figure A.1. Images depicting the concentration of Fe, Cu, Zn, K, and Ca in retinal tissues from first sample set. 154

Figure A.2. Quantification of Fe, Cu, and Zn content in retinal and brain (SC) tissue from first sample set. 155
Figure A.3. Images depicting the concentration of Fe, Cu, and Zn in brain tissues from second sample set. 156
Figure A.4. Quantification of Fe, Cu, and Zn content in retinal and brain (SC) tissue from second sample set. 156

List of Abbreviations

2D	Two-dimensional
Aβ	Amyloid-β
AD	Alzheimer's disease
ADDL	Aβ-derived diffusible ligands
AFM	Atomic force microscopy
ALS	Amyotrophic lateral sclerosis
APP	Amyloid precursor protein
APPswe	Swedish mutation of APP
APH-1	Anterior pharynx-defective-1
APS	Advanced Photon Source
ATD	Arrival time distribution
ATP	Adenosine triphosphate
BBB	Blood-brain barrier
BioCAT	Biophysics Collaborative Access Team
BSA	Bovine serum albumin
CCS	Collision cross section
CD	Circular dichroism
CNS	Central nervous system
CO_2	Carbon dioxide
CQ	Clioquinol
Cu	Copper
$CuCl_2$	Copper(II) chloride
$Cu(OAc)_2$	Copper(II) acetate
$CuSO_4$	Copper(II) sulfate
ddH_2O	Double-distilled water
DMEM	Dulbecco's modified Eagle medium

DMSO	Dimethyl sulfoxide
EDTA	2-({2-[Bis(carboxymethyl)amino]ethyl}(carboxymeth-yl)amino)acetic acid
EGCG	(−)-Epigallocatechin-3-gallate
EPR	Electron paramagnetic resonance
ESI	Electrospray ionization
EtOAc	Ethyl acetate
EXAFS	Extended X-ray absorption fine structure
FBS	Fetal bovine serum
Fe	Iron
H_2O_2	Hydrogen peroxide
HBT	2-(2-hydroxyphenyl)benzothiazole
HD	Huntingdon's disease
HEPES	(2-[4-(2-hydroxyethyl)piperazin-1-yl]ethanesulfonic acid)
HMQC	Heteronuclear multiple quantum correlation
HRP	Horseradish peroxidase
Hx	Hexanes
IM-MS	Ion mobility-mass spectrometry
IOP	Intraocular pressure
K_d	Dissociation constant
Lut	Luteolin
m/z	Mass-to-charge ratio
M17	SK-N-BE(2)-M17
MD	Molecular dynamics
MEM	Minimal essential media
Metal–Aβ	Metal-associated Aβ
MT-3	Metallothionein-3
MTT	3-(4,5-dimethylthiazol-2-yl)-2,5-diphenyltetrazolium bromide
MW	Molecular weight
Myr	Myricetin
N2a	Neuro-2a
NaCl	Sodium chloride

nESI	Nanospray ESI
NH_4OH	Ammonium hydroxide
NMDA	*N*-Methyl-D-aspartate
NMR	Nuclear magnetic resonance
O_2	Dioxygen
PBS	Phosphate-buffered saline
PD	Parkinson's disease
PEN-2	Presenilin enhancer-2
PEX	Pseudoexfoliation syndrome
pI	Isoelectric point
PS	Presenilin
PS1ΔE9	Exon 9 deletion in PS1
RGC	Retinal ganglion cell
ROI	Region of interest
ROS	Reactive oxygen species
sAPPα/β	Soluble APP α/β fragment
SC	Superior colliculus
SEVI	Semen-derived enhancer of virus infection
SOD	Superoxide dismutase
SOFAST	Band-selective optimized flip-angle short transient
SDS	Sodium dodecyl sulfate
TBS	Tris-buffered saline
TBS-T	Tris-buffered saline containing Tween-20
ThT	Thioflavin-T
TEM	Transmission electron microscopy
UCUCA	University Committee on Use and Care of Animals
UV-Vis	UV-Visible spectroscopy
Vitamin E	α-Tocopherol
v/v	Volume/volume ratio
WT	Wild-type
w/v	Weight/volume ratio

XAS	X-ray absorption spectroscopy
XRF	X-ray fluorescence
μ-XRF	μ-X-ray fluorescence
Zn	Zinc
$ZnCl_2$	Zinc(II) chloride
ZnT	Zinc transporter

Abstract

The incidence of Alzheimer's disease (AD) worldwide has been accelerating at a staggering rate, demonstrating the need to understand its origins clearly. Misfolded proteins such as amyloid-β (Aβ) have been believed to contribute to the disease. Additionally, it has been suggested that the normal functions and localization of metal ions such as Fe(II/III), Cu(I/II), and Zn(II) could be disrupted in the AD brain. There has been evidence to support the possible interplay between Cu(II) and/or Zn(II) with Aβ-related pathology (*i.e.*, metal–amyloid hypothesis); however, this relationship has yet been to be fully elucidated. A growing interest this possible association with AD pathology has led to new strategies for interrogating the metal–Aβ relationship using small molecule metal chelators. Flavonoids are abundant plant-derived molecules that have been known to bind metal ions and interact with Aβ peptides; however, the synergism of these properties toward metal-associated Aβ has previously received little attention. In this thesis, selected flavonoid derivatives were investigated to formulate a structure-interaction-reactivity relationship among chemical structures, metal ions, and Aβ/metal–Aβ species. The molecules myricetin and luteolin, found in fruits and vegetables, were initially screened and found to influence the reactivity of metal–Aβ species. Building upon these initial observations, the interaction and reactivity of the well-known green tea polyphenol (−)-epigallocatechin-3-gallate (EGCG) were explored at the molecular level through biochemical and biophysical investigations. These findings suggest that metal–Aβ–flavonoid species can be generated and possibly lead to off-pathway aggregation *in vitro*. We further identified the specific contributions of structural features by synthetic manipulation of the flavonoid framework to aminoisoflavone derivatives. Appropriate tuning of hydrophilic and hydrophobic properties within the structural backbone can modify the balance of metal binding and Aβ interaction, which may account for their reactivity toward Aβ and/or metal–Aβ. Taken

together, the studies presented herein demonstrate the utility of flavonoids as a source of structures for direct use and/or synthetic modification from which a structure-interaction-reactivity relationship can be formulated for metal-free and metal-associated Aβ species, which will provide insight into development of chemical tools to uncover the involvement of metal–amyloid species in AD.

Chapter 1: Connecting Metal Homeostasis, Protein Aggregation, and Neurodegenerative Diseases

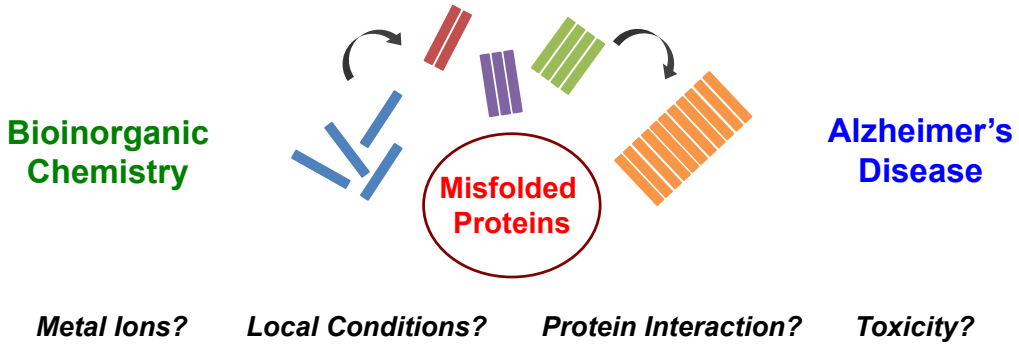

A portion of this chapter was previously published in DeToma, A. S.;‡ Salamekh, S.;‡ Ramamoorthy, A.; Lim, M. H. *Chem. Soc. Rev.* **2012**, *41*, 608-621. (‡ Equal contribution)

1.1. Bioinorganic chemistry in the brain

Bioinorganic chemistry is an interdisciplinary field that seeks to understand the role of metal ions in living systems.[1,2] Metals have unique chemical properties that render them useful in an array of scenarios. For example, metal ions can mediate catalysis in an enzyme, confer structural stability to a protein, participate in chemical signaling, or facilitate electron transfer.[1,3] As a result of their prevalence in biology, interest in metal involvement in human health has continued to develop in the last several decades. In particular, studies on the roles of metal ions in the brain and central nervous system (CNS) comprise a sub-field of bioinorganic chemistry called metalloneurochemistry.[4] Bioinorganic chemists are uniquely qualified to address questions in metalloneurochemistry by applying knowledge of the fundamental principles of inorganic chemistry and biochemistry to characterization of the structure, function, and reactivity of metals in the CNS.[4] Methods of traditional inorganic spectroscopy (*e.g.*, electron paramagnetic resonance (EPR), Mössbauer) have been developed and modified to investigate details of these complex systems at the molecular level, such as the coordination chemistry of metal ions in protein active sites. Moving forward, the field has also taken an interest in the mechanisms of storage, transport, and uptake of metal ions (*i.e.*, homeostasis), particularly for those that are abundant (*e.g.*, Ca(II), K(I)) and for trace elements (*e.g.*, transition metals).[5]

Metal ion homeostasis must be tightly controlled, especially in the brain, to maintain health. Fe, Cu, and Zn are important in brain function; the accessibility of multiple oxidation states for Fe (*i.e.*, +2, +3) and Cu (*i.e.*, +1, +2) makes these ions important for a variety of redox processes, while Zn, which exists only in the +2 state, often confers structural stability and participates in signal transduction.[1,4,6] Ensuring that the metals are available and directed to the appropriate sites involves a variety of transporters and chaperone proteins.[1,2,5-7] The proteins transferrin and ferritin are mainly responsible for transport and storage of Fe in the ferric form. Fe is also found within heme-proteins such as hemoglobin and myoglobin, where Fe(II) participates in storage of dioxygen (O_2).[6] There are several proteins involved in Cu homeostasis; among them, ceruloplasmin is a key player for Cu storage in the blood and facilitates the cycling of Fe(II)/Fe(III) *via* ferroxidase activity.[6] The Cu transporter ATP7A facilitates passage of

Cu across the blood-brain barrier (BBB) where it resides within metallothionein-3 (MT-3).[6,8] The MT proteins are important for maintaining Zn homeostasis as well, but Zn(II) is also found in the brain in vesicles and in a "free" pool.[8] Zn transporters, ZnT, sequester and export Zn(II), while uptake is mediated by various receptors (*e.g.*, *N*-methyl-D-aspartate (NMDA)-dependent voltage gated channels). Zn(II) has been shown to play an important role in signal transduction and memory, and deficits have been implicated in cognitive decline.[8] It is becoming more apparent that dysfunction of these regulatory mechanisms can be detrimental. Failure of the Cu transporter ATP7A, for example, is implicated in Cu overload associated with Wilson's disease.[6] Therefore, recent interest in metal ion homeostasis as an underlying cause of neurodegenerative disease (*e.g.*, Alzheimer's, Parkinson's) has gained attention. The involvement of metal ion homeostasis in Alzheimer's disease (AD) will be discussed further (*vide infra*).

1.2. Protein misfolding and human neurodegenerative diseases

Proteins have a multitude of responsibilities in biology owing to their great structural diversity. Since protein structure is closely linked to function, proper adaptation of secondary, tertiary, and quaternary structure is critical. Often, the protein folding process is mediated by other proteins, such as chaperones, which help newly synthesized peptides achieve their functional state.[9] When these processes are interrupted or misregulated, it is possible for a protein to adopt a stable, but non-native conformation.[10] As a result, misfolded proteins have been implicated in a wide variety of human diseases, many of which involve neurodegeneration.

Neurodegenerative diseases commonly associated with protein misfolding include AD, Parkinson's disease (PD), Huntington's disease (HD), and amyotrophic lateral sclerosis (ALS or Lou Gehrig's disease). Some other diseases have been recently reclassified as neurodegenerative diseases as new insights on their pathologies are discovered (*e.g.*, glaucoma; see Appendix A for more details). In general, each of these diseases is related to aging, affects different regions of the brain and CNS, and can occur sporadically or be inherited.[10] Insoluble protein deposits in affected tissues were found to be another connection among these diseases. Upon more detailed characterization, it was found that despite unique primary sequences, the

proteins within the aggregates from AD, PD, HD, and ALS had similar conformations. They were long and fibrillar, as observed by transmission electron microscopy (TEM) and atomic force microscopy (AFM), had cross-β structure, and reacted with dyes such as Congo red and thioflavin-T (ThT).[10-12] Currently, proteins with these characteristics are classified as amyloids.

Most amyloidogenic proteins are categorized as "misfolded," since they can aggregate into a variety of intermediate forms and may be related to toxicity.[13] Amyloid formation typically occurs through a nucleation-dependent model with a sigmoidal growth pattern, in which a slow lag phase precedes rapid fibril formation (Figure 1.1).[14,15] In the lag phase, self-association of monomers and oligomer formation are thermodynamically unfavorable; however, when the proper "seed" has been produced, fibril growth can occur. Fibril growth can be accelerated by incubating a solution of the peptide with preformed seeds. Aggregation is also impacted by modifying conditions, such as pH, temperature, salt concentration, and agitation.[16] For example, nearing the isoelectric point (pI) of the protein accelerates aggregation as solubility is minimal near the pI. Growth of amyloid aggregates typically occurs upon self-association *via* hydrophobic contacts in an effort to exclude water. Owing to their thermodynamic stability, biophysical characterization of fibril structures has been more easily achieved. There have also been methods developed to stabilize monomeric peptides (*e.g.*, lower temperatures, addition of detergents) allowing for their structure determination.[15] The intermediates between monomers and fibrils include oligomers and protofibrils.[10] In contrast to monomers or fibrils, oligomers have been difficult to characterize due to their transient nature. Protofibrils tend to be somewhat more stable than oligomers as they immediately precede fibril formation. Structurally, protofibrils begin to display some characteristics of fibrils, including cross-β structure. They are usually 4-11 nm in diameter and less than 200 nm long while mature fibrils are larger in size (*ca.* 10 nm diameter) and their length is on the μm scale.

The contribution of amyloid protein aggregates to toxicity remains controversial and several theories have been proposed.[10] First, it has been proposed that aggregates directly cause toxicity from a "gain of toxic activity." Several possible "toxic activities" have been discussed, including the ability of aggregates to induce signaling pathways

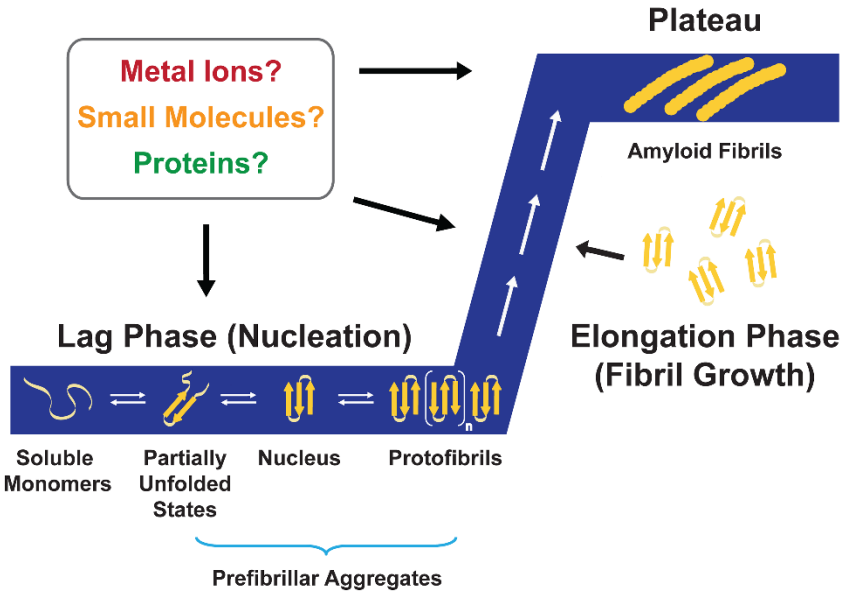

Figure 1.1. Nucleation polymerization model of amyloid aggregation. Soluble monomeric forms of the peptides, such as amyloid-β (Aβ), self-associate during the lag phase (nucleation). This forms a nucleus that can be rapidly extended during the fibril growth period called the elongation phase. Amyloid fibrils are the end product of this process, and their thermodynamic stability allows them to reach a stage called the plateau. The aggregation processes produce a sigmoidal kinetic trace that is depicted in the figure (blue).

(*e.g.*, that initiate apoptosis), to disrupt membranes leading to pore formation, or to cause oxidative damage to biomolecules.[10] An alternative view is that amyloid aggregates can also cause a "loss of function" that leads to disease. For example, aberrant metal chelation by metal-binding amyloidogenic peptides could disrupt metal homeostasis and compromise cell health (*vide infra*). Finally, inflammation caused by the presence of aggregates has been suggested.[10] Each of these possibilities is reasonable to consider, which likely accounts for the difficulties in clearly defining the relationship among amyloid protein deposits, neurodegeneration, and disease with certainty. Overall, it appears that these diseases share common traits that could be beneficial targets for therapeutics in the future. In addition, it is important to consider the impact of additional factors (*e.g.*, metal ions, proteins, reactive oxygen species (ROS)) and how key players from multiple hypotheses may govern disease progression. Recognizing the challenges that remain to characterize the complexity of protein

misfolding diseases, the remainder of this chapter will emphasize a specific example, AD, including how its misfolding may be perpetuated by metal ions and current efforts to address the interrelationship between these factors using small molecules.

1.3. Bioinorganic chemistry and protein misfolding in Alzheimer's disease

1.3.1. Alzheimer's disease (AD) and amyloid-β (Aβ)

AD is the most prevalent form of dementia primarily among elderly adults, which is associated with severe cognitive impairment and memory loss.[15,17] Currently, over 5 million Americans are afflicted by AD, placing a severe burden on socioeconomic resources.[17] Although the symptomatic and pathological signs of AD have been identified, a complete understanding of their origins remains elusive. This uncertainty has impeded progress toward developing effective preventive and disease modifying therapeutics; the presently available drugs only alleviate the symptoms temporarily and are unable to deter or cure the disease.[15,17-19] While some cases of AD are attributed to genetic inheritance, the majority of cases are sporadic.[18] Confirmation of the AD diagnosis is contingent upon the identification of misfolded protein aggregates, including neurofibrillary tangles composed of hyperphosphorylated tau protein and senile plaques mainly composed of Aβ peptides, as well as extensive oxidative damage and neuronal loss in the brain *post mortem*.[18,19] Within the mature plaques from diseased brains, high concentrations of metals, such as Fe, Cu, and Zn, have been also found, possibly representing their dyshomeostasis and miscompartmentalization in the diseased state.[15,19,20] This finding implies that along with protein aggregate accumulation, metals may contribute to AD onset and progression.[19-27] Taken together, misfolded Aβ species, metal ion dyshomeostasis/miscompartmentalization, and oxidative stress partially represent AD etiology.[18-27] Herein, the generation and aggregation of Aβ and the role of metal ions in AD and Aβ-related events, along with development of multifunctional small molecules to illustrate some current approaches to understand the nature of the metal–Aβ interaction and its potential contributions to AD, will be discussed.

1.3.2 Amyloid precursor protein (APP) and Aβ generation

The Aβ peptide is the predominant component of the senile plaques that accumulate in various brain regions and pathologically represent the AD condition.[10,18-22,24-26,28-30] Its involvement in AD neuropathogenesis has been extensively studied following the establishment of the amyloid cascade hypothesis, which implicated Aβ as a causative agent in AD.[28] The Aβ peptide is composed of 38-43 amino acid residues and is generated through sequential proteolytic cleavage of the amyloid precursor protein (APP).[18,19,31] APP is a transmembrane protein with three common isoforms, APP_{695}, APP_{751}, and APP_{770}, which among them, APP_{695} is most common in the neuronal cells.[18,31] The function of APP is still incompletely defined, but with two metal binding domains E1 (residues 124-189; APP_{770} numbering) and E2 (residues 376-554), it has been suggested that APP could be involved in regulating metal ion (*e.g.*, Cu) transport and homeostasis.[6,27,31-34] A recent report suggested that APP exhibits ferroxidase activity in a similar manner to that of ceruloplasmin (a Cu transport protein) whereby APP facilitates Fe export from neuronal cells; inhibition of this activity by reserves of Zn(II) could be connected to elevated levels of Fe measured in AD (*vide infra*).[35]

The proteases responsible for APP cleavage and Aβ generation distinguish the resulting forms of Aβ as either non-amyloidogenic (normal) or amyloidogenic (disease-related) (Figure 1.2).[18,19,27,31] Processing of APP by α-secretase initiates the non-amyloidogenic cleavage pathway, with initial scission between K687 and L688 (APP_{770} numbering) affording a large soluble fragment (sAPPα) and leaving a portion of the APP molecule membrane-bound (Figure 1.2). The amyloidogenic pathway begins with APP cleavage by β-secretase (β-site APP cleaving enzyme, BACE1) nearer to the *N*-terminus of APP between residues M671 and D672. The remaining membrane-bound fragments from both paths are finally processed by γ-secretase, which requires four protein components for its activity: presenilin (PS1 or PS2), nicastrin, anterior pharynx-defective-1 (APH-1), and presenilin enhancer-2 (PEN-2).[18,31,36] The γ-secretase complex cleaves the *C*-terminal fragments within the membrane to produce monomeric Aβ peptides of varying lengths and amyloidogenic preferences. The full-length peptides,

Aβ40 and Aβ42, are produced through the amyloidogenic pathway (the amino acid sequence of Aβ42 is DAEFRHDSGYEVHHQKLVFFAEDVGSNKGAIIGLMVGGVVIA) (Figure 1.2). Monomeric Aβ tends to aggregate, forming low molecular weight (MW) Aβ species, oligomers, protofibrils, and fibrils (*vide supra*; Figure 1.1).

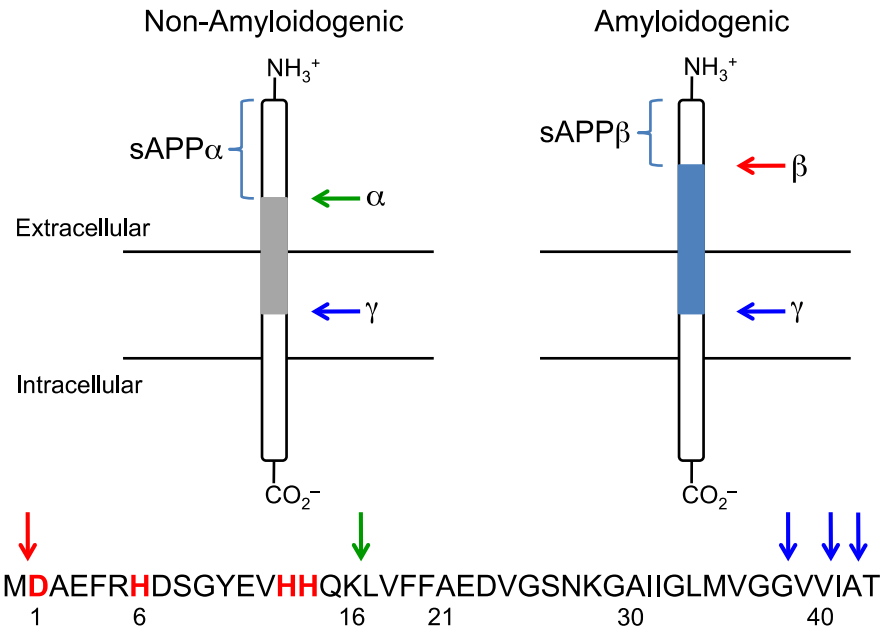

Figure 1.2. Cleavage of APP by α-, β-, and γ-secretases in the non-amyloidogenic and amyloidogenic pathways, respectively. The common full-length peptides, Aβ40 and Aβ42, in AD are formed through the amyloidogenic pathway.

1.3.3. Aggregated Aβ species and their contribution to neurotoxicity

Aβ is a relatively small peptide for which the innate function has not been fully established. The structure of Aβ monomer features hydrophilic *N*-terminus and hydrophobic *C*-terminus, which play a role in driving its aggregation in an effort to minimize unfavorable interactions with the aqueous environment.[19] Residues contained in the region from L17-A21 are identified as key contributors to self-recognition, due to their primarily hydrophobic nature, which might be influential in producing the higher-order structures.[19,37] Fibrils of Aβ40 adopt β-strand characteristics in two regions, from residues 12-24 and 30-40 and their side chain interactions stabilize the cross-β sheet

within the fibrillar structure.[38] Within the peptide, a turn occurs in the region from G25-G29 that is stabilized by a combination of electrostatic interactions such as a salt bridge between D23 and K28.[19,37,38]

$A\beta_{42}$ is the primary constituent of the senile plaques; the two additional hydrophobic residues at the *C*-terminus enhance its tendency to aggregate over $A\beta_{40}$, although the shorter peptide ($A\beta_{40}$) accounts for the major product of γ-secretase cleavage yielding $A\beta$ peptides.[18,19] $A\beta$ undergoes conformational changes during aggregation where the native random coil structure can be modified to either α-helical or β-strand-like forms.[37,39] The conformational changes, however, are highly conditional and slight changes in parameters such as pH, peptide concentration, and metal ion concentration may lead to diverse amyloid aggregates that may be ordered or may be amorphous.[20,40] The array of known polymorphic forms of $A\beta$ aggregates aside from the monomers and fibrils, which includes oligomers, protofibrils, annular structures, $A\beta$-derived diffusible ligands (ADDLs), and globulomers, has been reviewed.[40]

It is still not clear which $A\beta$ conformation is directly linked to neuropathogenesis. Some recent evidence implicates soluble low molecular weight (MW) $A\beta$ species, such as dimers, instead of the plaques as the relevant neurotoxic species.[19,30,36,41] In the early stages of AD, reduction of synaptic function and impairment of learning and memory formation processes (*e.g.*, long-term potentiation) may be caused by the smaller $A\beta$ assemblies, such as oligomers; these species possibly interfere with neurotransmission and/or other signaling pathways in the cells.[36] The occurrence of physiological responses in the brain such as inflammation and neuronal death as the disease progresses, however, could be attributable to these soluble aggregated species, the plaques, or a combination of various species in association with each other. Additional mechanisms proposed for the toxicity of $A\beta$ aggregates are related to interactions with other biomacromolecules (*e.g.*, pore formation within lipid membranes) and oxidative stress (*e.g.*, lipid peroxidation).[19,36]

1.3.4. Metal ions in AD and their interactions with Aβ

As described in Section 1.1, essential transition metal ions, such as Cu(I/II) and Zn(II), have important functions in the brain, such neurotransmission.[20,42] Due to the association of high levels of Fe, Cu, and Zn with Aβ aggregates from diseased brain tissue, these metals have been suspected to be linked to the pathological events of AD; however, this area remains contested.[18-21,43-46] Cu(I/II) and Zn(II) have recently garnered the most attention for being able to directly bind to the Aβ peptides.[18-21,43-46] Both metals are usually found in association with biological ligands, but a pool of "free" or loosely bound (*i.e.*, chelatable) ions can exist in the synaptic cleft, making them accessible to Aβ peptides that are released into the synapse.[22,24,43] The concentrations of Cu(II) and Zn(II) can reach up to 15 μM and 300 μM, respectively, in the glutamergic synapses during neurotransmission, from which only a fraction may be sufficient to be related to the disease pathology.[20,22,42,43] An early study estimated the levels of metals in the Aβ plaques to be in the high micromolar to low millimolar range, with total plaque content being reported at *ca.* 0.9 mM for Fe, 0.4 mM for Cu, and 1 mM for Zn.[20,22,23,44] While the original paper[47] likely sparked interest in the connection of metal ions in AD, it has been argued that its excessive citation may have biased the field toward believing the metal contents in the brain increase.[7,48] Currently, it is believed that concentrations of Fe and Cu are relatively unchanged between AD and control brains; Zn is known to be depleted with aging, so a slightly greater loss of Zn may be associated with AD.[7] Instead, an alternative view worthy of more attention is that the miscompartmentalization/relocation of metal ions in AD, which may be the result of its association with Aβ in discrete areas, is a factor that contributes to the disease.[6,7,15]

Despite the uncertain nature of the metal–Aβ interaction *in vivo*, it has been established that metal ions are able to bind to Aβ *in vitro* (Figure 1.1).[19,20,27,45,46] Both Cu(II) and Zn(II) have been shown to bind to Aβ in a 1:1 fashion, although it has been also reported that Aβ can bind up to approximately two equivalents of Cu(II). The coordination environment of the Cu(II) and Zn(II) has been investigated using an array of spectroscopic methods including nuclear magnetic resonance (NMR), EPR, UV-Visible (UV-Vis) spectroscopy, circular dichroism (CD), and extended X-ray absorption

fine structure (EXAFS).[27,43,45,46,49] Several probable coordination modes have been proposed, but the exact identity of the ligands for these ions has not been fully elucidated. The current evidence suggests a binding environment containing a mixture of nitrogen and oxygen donor atoms for both Cu(II) and Zn(II), for which three histidine residues (H6, H13, and H14) are likely to be included (*vide infra*).

The previous studies of Cu-bound Aβ monomers suggest several metal binding features, given the complexity of the solution speciation measured under various experimental conditions.[20,27,43,45,46] Depending on the oxidation state of Cu (*e.g.*, Cu(I) or Cu(II)), different binding modes and coordination environments on the metal center have been observed. The reducing conditions of the brain validate the determination of Cu(I) binding properties, but there have been fewer studies on Cu(I)–Aβ compared to Cu(II)–Aβ. Cu(I) binding to the monomer was found to occur in a linear environment *via* the imidazole rings of two His ligands.[50,51] More recently, the interaction of Cu(I) to $A\beta_{42}$ oligomers was reported.[52] These results indicated that the coordination environment of Cu(I) in oligomers was different from that in monomers; a tetrahedral environment was identified. Unlike Cu(I)–Aβ monomer species, the Cu(I)–Aβ oligomers were found to be highly reactive to O_2.[52] These findings may be valuable to understanding Cu–Aβ redox chemistry since the cycling of Cu(I/II) could facilitate production of ROS (Figure 1.3), which can lead to oxidative stress.[45,53,54]

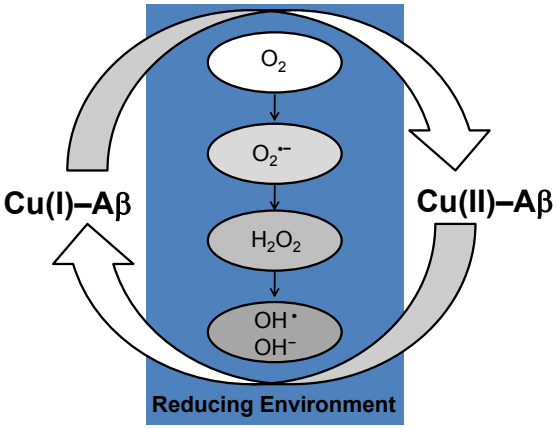

Figure 1.3. Reactive oxygen species (ROS) generated by redox cycling of Cu-bound Aβ under reducing conditions (Fenton chemistry).

The coordination environment of Cu(II)-bound Aβ has been widely studied, with the general agreement that the binding mode is dynamic and conditional (*e.g.*, pH-dependent).[27,45,46] The current consensus is that in the physiologically relevant range (*ca.* pH 7.4), Aβ tends to involve three nitrogen and one oxygen (3N1O) donor atoms coordinated to Cu(II). Commonly referred to as "species I," two binding modes for Cu(II)–Aβ have been suggested. The first involves the three histidine residues (H6, H13, and H14) along with the carboxylate of D1 and the second involves two histidine residues, the *N*-terminal amine, and the D1–A2 or A2–E3 backbone carbonyl.[27,34,45,46,55] Above pH 8 the coordination mode for Cu(II), there is evidence that the coordination mode is altered giving rise to "species II." Likely maintaining a 3N1O coordination environment, the deprotonated D1–A2 backbone amide, A2–E3 backbone carbonyl oxygen, N-terminal amine, and a His side chain or the three histidine residues and the carbonyl oxygen from the backbone of A2 have been suggested.[27,34,46] While Cu(II)–Aβ complexes likely form a four-coordinate species, Zn(II)–Aβ may coordinate four to six ligands. There is a consensus that the three histidine residues are responsible for binding; however, the fourth, fifth, and/or sixth ligands have been more difficult to identify.[15] Thus, Cu and Zn in Aβ plaques could be directly bound to the peptides.

Previously, it has been suggested that Fe accumulation could be due to its association with other proteins or biological ligands (*e.g.*, heme) that are found within the aggregates and not directly to the peptide. Recently, the binding mode of Fe(II) to Aβ has been proposed.[55] An octahedral geometry was suggested with similar residues used as for Cu(II). The current model suggests that three histidine imidazole rings could participate, along with the *N*-terminal amine, the carboxylate of D1 or E3, and the carbonyl of D1 or H6. Continued efforts to characterize Fe(II) binding to Aβ peptides will be critical toward formulating the relationship of metals to AD.

Metal binding to Aβ has been suggested to initiate peptide aggregation and neurotoxicity.[18-27,43,45,46] When considering the Aβ aggregation according to the nucleation polymerization model (*vide supra*, Figure 1.1), the formation of the initial nucleus and subsequent elongation into the familiar cross-β-sheet nature of the fibrils tends to be a rather slow process in quiescent, metal-free conditions *in vitro*; however,

in the presence of metal ions like Cu(II) and Zn(II), the aggregation kinetics can be accelerated.[43,56] Substoichiometric amounts of Cu(II) have been shown to reduce fibril generation time by half pH 7.4 as a result of the peptide nearing its isoelectric point.[56] Cu(II) also facilitates Aβ aggregation under slightly acidic conditions.[57] Treatment of Aβ with micromolar concentrations of Zn(II) leads to insoluble amorphous peptide species in a rapid process occurring within milliseconds.[58]

Dissociation constants (K_d) indicative of the binding affinity of metal ions to Aβ have been measured though calorimetric and spectroscopic methods.[20,43,45,46] For Cu(II), the reported K_d values range from attomolar to nanomolar. The affinity of Aβ for Zn(II) is on the order of micromolar concentrations. The length of Aβ does not significantly impact these binding affinities in $A\beta_{40}$ *versus* $A\beta_{42}$, and similar binding affinities are observed for the monomer and preformed Aβ aggregates; however, the experimental conditions used to attain these data can dramatically influence the outcomes.[46] Nevertheless, it is valuable to be aware of the approximate range of the dissociation constants for metal ions with Aβ. Such information may be helpful for selecting chemical tools that are directed toward the metal ions associated with various Aβ species. In general if the small molecules have similar affinity for metal ions as Aβ (approximately within the same order of magnitude), then there exists a possibility for competition between the ligand and peptide for metal binding (*vide infra*).[46,59-61]

Another effect of metal binding to Aβ in AD includes the exacerbation of neurotoxicity and oxidative damage.[18-27,43,45,46] Toxicity has been demonstrated to be higher for Cu–Aβ species *in vitro*, particularly because the Fenton-type redox cycling between Cu(II) and Cu(I) could be sustainable under the reducing environments of the brain (Figure 1.3). ROS produced from this chemistry, such as hydrogen peroxide (H_2O_2) and hydroxyl radical, can cause oxidative damage to biological molecules, membranes (*e.g.*, lipid peroxidation), and organelles (*e.g.*, mitochondria).[7] Usually, oxidative stress is avoided by a variety of endogenous antioxidant defense systems (*e.g.*, catalases, Cu,Zn-superoxide dismutase (SOD)). MT-3 has also been suggested to offer some antioxidant protection by exchanging its bound Zn for the Cu associated with Aβ to silence its redox cycling.[7] When these neuroprotective mechanisms are

overwhelmed, however, extensive oxidative stress may prevail and cause neuronal death.[7,62]

1.3.5. Small molecule-based approaches to understanding metal–Aβ interaction and neurotoxicity

Several studies have identified the deleterious effects caused by metal binding, the relationship between Cu/Zn–Aβ interaction and AD remains to be clarified. The pursuit of small molecules as chemical tools to interrogate the metal–Aβ interaction and associated events such as aggregation and neurotoxicity may provide a handle for further dissecting the etiology of this disease. Not only could effective compounds lead to new molecular-level insights but they may also be promising chemical candidates for developing potential AD therapeutics. Initially, metal chelation therapy was explored by employing general metal chelating compounds to remove or potentially block these metal ions from interacting with Aβ to alleviate aggregate deposition and ROS production (Figure 1.4; *e.g.*, clioquinol (CQ), EDTA).[18-22,63-65] From this approach, the involvement of metal ions in AD has been acknowledged and new methods to design compounds for potentially elucidating how metal-associated Aβ species (metal–Aβ species) are connected to the neuropathology of AD have been explored.

Investigations with 8-hydroxyquinoline derivatives, CQ (Figure 1.4) and PBT2, *in vitro* and *in vivo* have suggested their ability to interrupt the associations between metal ions and Aβ, to sequester redox active metal ions, and to transport metal ions across the membrane leading to their redistribution (*i.e.,* ionophore activity).[20-22,63] Due to limited utility and adverse effects of CQ,[20,22,63] its analogue PBT2 has been of recent interest as it leads to better ionophore behavior, greater depletion of amyloid deposits, and improved performance on neuropsychological tests in AD patients.[66] These observations have provided evidence that metal ion homeostasis is misregulated in AD and that mitigating this dyshomeostasis may be of therapeutic value. Although showing progress and lending credibility to metal chelation therapy in AD, these 8-hydroxyquinoline compounds have disadvantages for probing the direct correlation between metal ions and Aβ due to the lack of Aβ interaction functionality, such as alteration of biological metal ion homeostasis rather than metal ions within Aβ

species.[21,22,59,63,67] Therefore, rational structure-based design approaches have been attempted for the construction of more versatile metal chelators containing additional modes of action for specifically targeting and elucidating the role of metal ions associated with Aβ.

Expanding upon the concept of metal chelation, multifunctional compounds that incorporate various functionalities for direct Aβ interaction, ROS mediation, or improved BBB permeability in tandem with capturing metals ions have evolved. Combining more than one function into a single molecule may assist in localizing compounds near metal-Aβ species in the brain (Figure 1.4).[20,59,67,68] For one of these classes, the strategy has been to promote metal complexation by increasing the number of donor atoms to generate multidentate ligand frameworks.[69] Along with sequestration of the redox active metal ions (*e.g.*, Cu(I/II)) from Aβ species, multidentate ligands could orient the metal center to disfavor geometric reorganization with changing oxidation states.[69] Another approach is to prepare prochelators with concealed metal binding sites that, in principle, prevent systemic metal coordination by activating only upon reaching a biological target or stimulus (*e.g.*, enzymes, ROS).[20,68,70-72] In one prochelator framework, a boronic acid masks the hydroxyl group of 8-hydroxyquinoline (QBP; Figure 1.4) until activation by H_2O_2 resulting in the cleavage of the boron protecting group. In the presence of redox active Cu–Aβ and O_2, the production of H_2O_2 will stimulate the delivery of 8-hydroxyquinoline, which can chelate metal ions, mitigate ROS production, and reduce metal-induced Aβ aggregation *in vitro*.[70] Orvig and co-workers have developed a family of glycosylated 3-hydroxy-4-pyridinones capable of metal binding and antioxidant activity upon cleavage of the sugar group (Figure 1.4).[71] Inclusion of the sugar moiety would exploit GLUT-1 transporters at the BBB allowing for more facile penetration into the brain whereby it could be readily hydrolyzed by β-glucosidase enzymes to reveal the active chelators. These compounds have demonstrated comparable antioxidant activity to α-tocopherol (vitamin E) and were able to solubilize metal-induced Aβ aggregates. Taking this approach one step further, pyridinone glycoside derivatives that also include Aβ interaction moieties have been recently reported (Figure 1.4).[72] Combining prochelation, BBB permeability, antioxidant activity, and Aβ recognition functionalities

successfully within one molecule is attractive for not only understanding the relationship of metal–Aβ species and neurotoxicity in AD but also for a future therapeutic direction.

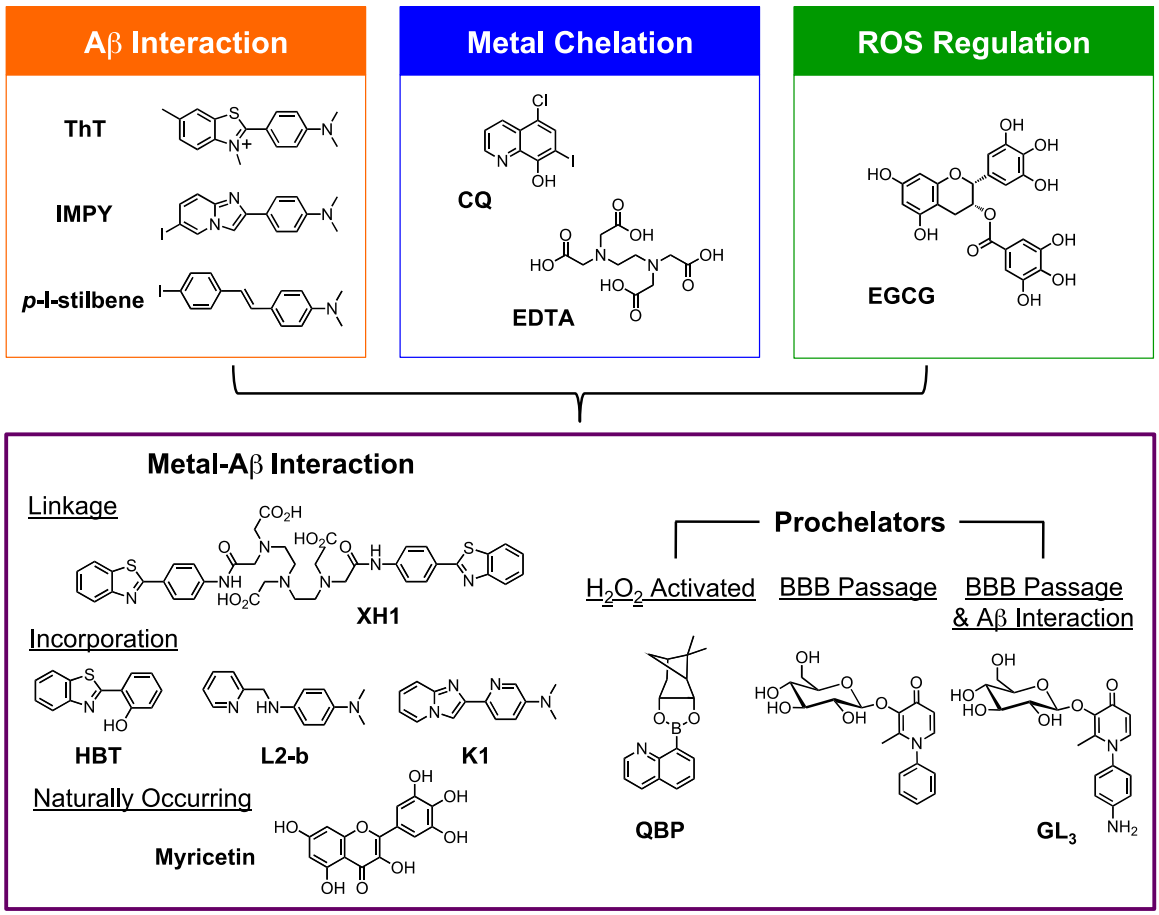

Figure 1.4. Multifunctional small molecules that can be used to investigate Cu(II)/Zn(II)-associated Aβ species in AD by combining properties of Aβ interaction (orange), metal chelation (blue), and/or ROS regulation (green). Other structural moieties can be implemented in the design to introduce different reactivity (*e.g.*, ROS-activated metal chelation ability (prochelators), enhanced BBB permeability). Multifunctional molecules are shown in the purple box. Flavonoids such as EGCG have demonstrated antioxidative properties. Abbreviations for compounds: ThT = thioflavin-T, 2-[4-(dimethylamino)phenyl]-3,6-dimethylbenzothiazolium; IMPY = 6-iodo-2-(4′-dimethylamino)phenylimidazo[1,2-*a*]pyridine; *p*-I-stilbene = *N*,*N*-dimethyl-4-[(1*E*)-2-(4-iodophenyl)ethenyl]benzenamine; CQ = 5-chloro-7-iodo-8-hydroxyquinoline; EDTA = *N*,*N*′-1,2-ethanediylbis[*N*-(carboxymethyl)]glycine; EGCG = epigallocatechin-3-gallate, XH1 = *N*,*N*-bis[2-[[2-[[4-(2-benzothiazolyl)phenyl]amino]-2-oxoethyl](carboxymethyl) amino]ethyl]glycine; HBT = 2-(2-hydroxyphenyl)benzothiazole; L2-b = N^1,N^1-dimethyl-N^4-(pyridin-2-ylmethyl)benzene-1,4-diamine; K1 = 6-(imidazo-[1,2-*a*]pyridin-2-yl)-*N*,*N*-dimethylpyridin-3-amine; QBP = quinoline boronic acid, pinanediol ester; the prochelator for BBB passage = 3-(D-glucopyranosyloxy)-2-methyl-1-phenyl-4(1*H*)-pyridinone; GL_3 = 1-(4-aminophenyl)-3-(β-D-glucopyranosyloxy)-2-methyl-4(1*H*)-pyridinone.

The third synthetic approach to this problem has been to design compounds that could specifically target metal ions associated with Aβ species is the installation of metal chelation properties into molecules previously determined to interact with Aβ. This strategy has branched into two similar approaches through synthetic manipulation: linkage and incorporation.[20,59,67,68] In the former case, either a small molecule Aβ imaging agent or a complementary peptide recognition sequence (*e.g.*, KLVFF) is tethered to a metal chelating framework (*e.g.*, ThT-based compound XH1, Figure 1.4).[73,74] In the latter approach, a metal chelation site is directly placed into the known Aβ recognition framework. Molecules from the second strategy include modified neutral ThT derivatives (*e.g.*, HBT; Figure 1.4) and two generations of compounds based on the stilbene and IMPY frameworks that present different degrees of biocompatibility and reactivity toward metal–Aβ species (*e.g.*, L2-b, K1; Figure 1.4).[20,59-61,67,68,75,76] Limited *in vivo* studies have been conducted with the designed compounds so far (*i.e.*, XH1 reduced amyloid burden in a double-transgenic mouse model), and one study showed the ability of L2-b to disassemble biologically derived high molecular weight Aβ species from human AD brain tissue homogenates.[61,67,73] Following these studies, further designs have emerged, including incorporation of heteroatoms into the diphenylpropynone imaging agent framework and linkage of a ThT derivative/*o*-vanillin hybrid to an *N*-(2-pyridylmethyl)amine for metal chelation.[77,78] Ongoing investigations with these and other molecules will surely provide clarity on the relationship between metal ions, Aβ, and AD in the future.

1.4. Conclusion

The unique properties of amyloid proteins pose a challenge for traditional drug design; however, the significance of AD and other amyloidogenic diseases, and their shared pathological hallmarks, drives development of novel therapeutic strategies. Efforts to clarify the current understanding of these diseases and the factors impacting them are progressing at an encouraging pace. Innovative ideas to apply small molecule-based approaches to define the roles of metal ions in AD could be used as a stepping-stone into similar approaches for other aspects of protein misfolding conditions. Fundamental information gleaned from these types of studies could also be beneficial to

accelerate drug and diagnostic discovery for AD. To successfully accomplish this in the future, however, a full understanding of the pathophysiological relationship between the formation of misfolded proteins, their interactions with other biological components, and the onset and progression of the diseases is compulsory.

1.5. Scope of this thesis

In addition to the synthetic design approach described above, selective rational screening of known molecules was pursued as part of this dissertation to identify beneficial frameworks that target and modulate metal-associated Aβ species. Reports connecting diet to incidence of AD hinted that certain molecules could play a role in maintaining brain health.[79,80] For example, the occurrence of AD is as much as four times lower in India compared to the United States.[81] Many have cited this trend to the high consumption of curcumin, which is found in the turmeric of curry-based dishes of the Indian diet.[81,82] Curcumin has been known to inhibit amyloid aggregation and attenuate neurotoxicity, which could account for this dramatic trend.[82,83]

Additionally, naturally occurring flavonoids have been shown to mitigate Aβ aggregation and offer neuroprotection.[84,85] Although these molecules have been well-studied and have attractive structural moieties for this purpose, their application to metal-associated Aβ in AD had not been investigated previously. Thus, the studies presented in this thesis illustrate the first example where flavonoids have been used to target and modulate metal-induced Aβ aggregation and neurotoxicity *in vitro*. Chapter 2 details the studies using myricetin and luteolin for this purpose. Following this, Chapter 3 describes use of (−)-epigallocatechin-3-gallate (EGCG) as a mechanistic probe to understand small molecule interactions with metal–Aβ species and how they influence reactivity. Ultimately, the successful application of these initial studies to a design strategy was achieved with the aminoisoflavone derivatives in Chapter 4. Chapter 5 and Appendix A describe experiments to quantify metals in AD and glaucoma, respectively, using μ-X-ray fluorescence (μ-XRF), which could be used to further elucidate the role of metals in these neurodegenerative diseases.

Therefore, the multifunctionality of designed and naturally occurring compounds has been demonstrated *in vitro* and in living cells based on their ability to block metal-

induced Aβ aggregation, to reverse the degree of amyloid aggregation, and to prevent toxicity from metal-Aβ species. Toward applications to understand the role of metal ions associated with Aβ in AD, these strategies motivated by metal chelation are in promising initial stages. The attempts thus far to rationally design multifunctional molecules have provided a foundation on which the details of metal–Aβ interaction may be revealed more completely and applied to the comprehensive picture of the nature of AD.

1.6. References

1. Lippard, S. J.; Berg, J. M., *Principles of Bioinorganic Chemistry*. University Science Books: California, 1994.
2. Gray, H. B.; Stiefel, E. I.; Valentine, J. S.; Bertini, I., *Biological Inorganic Chemistry: Structure and Reactivity*. University Science Books: California, 2007.
3. Gray, H. B. *Proc. Natl. Acad.Sci. U. S. A.* **2003**, *100*, 3563-3568.
4. Burdette, S. C.; Lippard, S. J. *Proc. Natl. Acad. Sci. U. S. A.* **2003**, *100*, 3605-3610.
5. Mbatia, H. W.; Burdette, S. C. *Biochemistry* **2012**, *51*, 7212-7224.
6. Kepp, K. P. *Chem. Rev.* **2012**, *112*, 5193-5239.
7. Greenough, M. A.; Camakaris, J.; Bush, A. I. *Neurochem. Int.* **2013**, *62*, 540-555.
8. Ayton, S.; Lei, P.; Bush, A. I. *Free Radical Biol. Med.* **2012**.
9. *Harper's Illustrated Biochemistry*. 27th ed.; McGraw-Hill Medical: New York, 2006.
10. Soto, C. *Nat. Rev. Neurosci.* **2003**, *4*, 49-60.
11. Fändrich, M. *Cell. Mol. Life Sci.* **2007**, *64*, 2066-2078.
12. Reinke, A. A.; Gestwicki, J. E. *Chem. Biol. Drug Des.* **2011**, *77*, 399-411.
13. Chiti, F.; Dobson, C. M. *Annu. Rev. Biochem.* **2006**, *75*, 333-366.
14. Moreno-Gonzalez, I.; Soto, C. *Semin. Cell Dev. Biol.* **2011**, *22*, 482-487.
15. DeToma, A. S.; Salamekh, S.; Ramamoorthy, A.; Lim, M. H. *Chem. Soc. Rev.* **2012**, *41*, 608-621.
16. Harrison, R. S.; Sharpe, P. C.; Singh, Y.; Fairlie, D. P. *Rev. Physiol., Biochem., Pharmacol.* **2007**, *159*, 1-77.
17. Alzheimer's Association. *Alzheimers Dement.* **2012**, *8*, 131-168.
18. Jakob-Roetne, R.; Jacobsen, H. *Angew. Chem. Int. Ed.* **2009**, *48*, 3030-3059.
19. Rauk, A. *Chem. Soc. Rev.* **2009**, *38*, 2698-2715.
20. Scott, L. E.; Orvig, C. *Chem. Rev.* **2009**, *109*, 4885-4910.
21. Bonda, D. J.; Lee, H. G.; Blair, J. A.; Zhu, X.; Perry, G.; Smith, M. A. *Metallomics* **2011**, *3*, 267-270.
22. Bush, A. I.; Tanzi, R. E. *Neurotherapeutics* **2008**, *5*, 421-432.
23. Zatta, P.; Drago, D.; Bolognin, S.; Sensi, S. L. *Trends Pharmacol. Sci.* **2009**, *30*, 346-355.
24. Bolognin, S.; Drago, D.; Messori, L.; Zatta, P. *Med. Res. Rev.* **2009**, *29*, 547-570.
25. Hureau, C.; Faller, P. *Biochimie* **2009**, *91*, 1212-1217.

26. Barnham, K. J.; Masters, C. L.; Bush, A. I. *Nat. Rev. Drug Discov.* **2004**, *3*, 205-214.
27. Gaggelli, E.; Kozlowski, H.; Valensin, D.; Valensin, G. *Chem. Rev.* **2006**, *106*, 1995-2044.
28. Hardy, J. A.; Higgins, G. A. *Science* **1992**, *256*, 184-185.
29. Soto, C. *FEBS Lett.* **2001**, *498*, 204-207.
30. Ross, C. A.; Poirier, M. A. *Nat. Med.* **2004**, *10*, S10-S17.
31. Lichtenthaler, S. F.; Haass, C.; Steiner, H. *J. Neurochem.* **2011**.
32. Ciuculescu, E. D.; Mekmouche, Y.; Faller, P. *Chemistry* **2005**, *11*, 903-909.
33. Eskici, G.; Axelsen, P. H. *Biochemistry* **2012**, *51*, 6289-6311.
34. Savelieff, M. G.; Lee, S.; Liu, Y.; Lim, M. H. *ACS Chem. Biol.* **2013**.
35. Duce, J. A.; Tsatsanis, A.; Cater, M. A.; James, S. A.; Robb, E.; Wikhe, K.; Leong, S. L.; Perez, K.; Johanssen, T.; Greenough, M. A.; Cho, H. H.; Galatis, D.; Moir, R. D.; Masters, C. L.; McLean, C.; Tanzi, R. E.; Cappai, R.; Barnham, K. J.; Ciccotosto, G. D.; Rogers, J. T.; Bush, A. I. *Cell* **2010**, *142*, 857-867.
36. Haass, C.; Selkoe, D. J. *Nat. Rev. Mol. Cell Biol.* **2007**, *8*, 101-112.
37. Lazo, N. D.; Grant, M. A.; Condron, M. C.; Rigby, A. C.; Teplow, D. B. *Protein Sci.* **2005**, *14*, 1581-1596.
38. Petkova, A. T.; Ishii, Y.; Balbach, J. J.; Antzutkin, O. N.; Leapman, R. D.; Delaglio, F.; Tycko, R. *Proc. Natl. Acad. Sci. U. S. A.* **2002**, *99*, 16742-16747.
39. Butterfield, S. M.; Lashuel, H. A. *Angew. Chem. Int. Ed.* **2010**, *49*, 5628-5654.
40. Miller, Y.; Ma, B.; Nussinov, R. *Chem. Rev.* **2010**, *110*, 4820-4838.
41. Chimon, S.; Shaibat, M. A.; Jones, C. R.; Calero, D. C.; Aizezi, B.; Ishii, Y. *Nat. Struct. Mol. Biol.* **2007**, *14*, 1157-1164.
42. Tamano, H.; Takeda, A. *Metallomics* **2011**.
43. Tougu, V.; Tiiman, A.; Palumaa, P. *Metallomics* **2011**, *3*, 250-261.
44. Frederickson, C. J.; Koh, J. Y.; Bush, A. I. *Nat. Rev. Neurosci.* **2005**, *6*, 449-462.
45. Faller, P. *ChemBioChem* **2009**, *10*, 2837-2845.
46. Faller, P.; Hureau, C. *Dalton Trans.* **2009**, 1080-1094.
47. Lovell, M. A.; Robertson, J. D.; Teesdale, W. J.; Campbell, J. L.; Markesbery, W. R. *J. Neurol. Sci.* **1998**, *158*, 47-52.
48. Schrag, M.; Mueller, C.; Oyoyo, U.; Smith, M. A.; Kirsch, W. M. *Prog. Neurobiol.* **2011**, *94*, 296-306.
49. Hou, L.; Zagorski, M. G. *J. Am. Chem. Soc.* **2006**, *128*, 9260-9261.
50. Shearer, J.; Szalai, V. A. *J. Am. Chem. Soc.* **2008**, *130*, 17826-17835.
51. Hureau, C.; Balland, V.; Coppel, Y.; Solari, P. L.; Fonda, E.; Faller, P. *J. Biol. Inorg. Chem.* **2009**, *14*, 995-1000.
52. Shearer, J.; Callan, P. E.; Tran, T.; Szalai, V. A. *Chem. Commun.* **2010**, *46*, 9137-9139.
53. Himes, R. A.; Park, G. Y.; Siluvai, G. S.; Blackburn, N. J.; Karlin, K. D. *Angew. Chem. Int. Ed.* **2008**, *47*, 9084-9087.
54. Feaga, H. A.; Maduka, R. C.; Foster, M. N.; Szalai, V. A. *Inorg. Chem.* **2011**, *50*, 1614-1618.
55. Bousejra-ElGarah, F.; Bijani, C.; Coppel, Y.; Faller, P.; Hureau, C. *Inorg. Chem.* **2011**, *50*, 9024-9030.

56. Sarell, C. J.; Wilkinson, S. R.; Viles, J. H. *J. Biol. Chem.* **2010**, *285*, 41533-41540.
57. Atwood, C. S.; Moir, R. D.; Huang, X.; Scarpa, R. C.; Bacarra, N. M.; Romano, D. M.; Hartshorn, M. A.; Tanzi, R. E.; Bush, A. I. *J. Biol. Chem.* **1998**, *273*, 12817-12826.
58. Noy, D.; Solomonov, I.; Sinkevich, O.; Arad, T.; Kjaer, K.; Sagi, I. *J. Am. Chem. Soc.* **2008**, *130*, 1376-1383.
59. Hureau, C.; Sasaki, I.; Gras, E.; Faller, P. *ChemBioChem* **2010**, *11*, 950-953.
60. Rodríguez-Rodríguez, C.; Sánchez de Groot, N.; Rimola, A.; Álvarez-Larena, Á.; Lloveras, V.; Vidal-Gancedo, J.; Ventura, S.; Vendrell, J.; Sodupe, M.; González-Duarte, P. *J. Am. Chem. Soc.* **2009**, *131*, 1436-1451.
61. Choi, J.-S.; Braymer, J. J.; Nanga, R. P. R.; Ramamoorthy, A.; Lim, M. H. *Proc. Natl. Acad. Sci. U. S. A.* **2010**.
62. Cuajungco, M. P.; Faget, K. Y.; Huang, X.; Tanzi, R. E.; Bush, A. I. *Ann. N. Y. Acad. Sci.* **2000**, *920*, 292-304.
63. Bandyopadhyay, S.; Huang, X.; Lahiri, D. K.; Rogers, J. T. *Exp. Opin.Ther. Targets* **2010**, *14*, 1177-1197.
64. Chen, T.; Wang, X.; He, Y.; Zhang, C.; Wu, Z.; Liao, K.; Wang, J.; Guo, Z. *Inorg. Chem.* **2009**, *48*, 5801-5809.
65. Rodríguez-Rodríguez, C.; Telpoukhovskaia, M.; Orvig, C. *Coord. Chem. Rev.* **2012**, *256* 2308-2332.
66. Faux, N.; Ritchie, C.; Gunn, A.; Rembach, A.; Tsatsanis, A.; Bedo, J.; Harrison, J.; Lannfelt, L.; Blennow, K.; Zetterberg, H.; Ingelsson, M.; Masters, C.; Tanzi, R.; Cummings, J.; Herd, C.; Bush, A. *J. Alzheimers Dis.* **2010**, *20*, 509-516.
67. Braymer, J. J.; DeToma, A. S.; Choi, J.-S.; Ko, K. S.; Lim, M. H. *Int. J. Alzheimers Dis.* **2011**.
68. Perez, L. R.; Franz, K. J. *Dalton Trans* **2010**, *39*, 2177-2187.
69. Deraeve, C.; Boldron, C.; Maraval, A.; Mazarguil, H.; Gornitzka, H.; Vendier, L.; Pitie, M.; Meunier, B. *Chem. Eur. J.* **2008**, *14*, 682-696.
70. Dickens, M. G.; Franz, K. J. *ChemBioChem* **2010**, *11*, 59-62.
71. Green, D. E.; Bowen, M. L.; Scott, L. E.; Storr, T.; Merkel, M.; Bohmerle, K.; Thompson, K. H.; Patrick, B. O.; Schugar, H. J.; Orvig, C. *Dalton Trans.* **2010**, *39*, 1604-1615.
72. Scott, L. E.; Telpoukhovskaia, M.; Rodriguez-Rodriguez, C.; Merkel, M.; Bowen, M. L.; Page, B. D. G.; Green, D. E.; Storr, T.; Thomas, F.; Allen, D. D.; Lockman, P. R.; Patrick, B. O.; Adam, M. J.; Orvig, C. *Chem. Sci.* **2011**, *2*, 642-648.
73. Dedeoglu, A.; Cormier, K.; Payton, S.; Tseitlin, K. A.; Kremsky, J. N.; Lai, L.; Li, X.; Moir, R. D.; Tanzi, R. E.; Bush, A. I.; Kowall, N. W.; Rogers, J. T.; Huang, X. *Exp. Gerontol.* **2004**, *39*, 1641-1649.
74. Wu, W.-h.; Lei, P.; Liu, Q.; Hu, J.; Gunn, A. P.; Chen, M.-s.; Rui, W.-f.; Su, X.-y.; Xie, Z.-p.; Zhao, Y.-F.; Bush, A. I.; Li, Y.-m. *J. Biol. Chem.* **2008**, *283*, 31657-31664.
75. Hindo, S. S.; Mancino, A. M.; Braymer, J. J.; Liu, Y.; Vivekanandan, S.; Ramamoorthy, A.; Lim, M. H. *J. Am. Chem. Soc.* **2009**, *131*, 16663-16665.
76. Choi, J.-S.; Braymer, J. J.; Park, S. K.; Mustafa, S.; Chae, J.; Lim, M. H. *Metallomics* **2011**.

77. Pithadia, A. S.; Kochi, A.; Soper, M. T.; Beck, M. W.; Liu, Y.; Lee, S.; DeToma, A. S.; Ruotolo, B. T.; Lim, M. H. *Inorg. Chem.* **2012**, *51*, 12959-12967.
78. Sharma, A. K.; Pavlova, S. T.; Kim, J.; Finkelstein, D.; Hawco, N. J.; Rath, N. P.; Mirica, L. M. *J. Am. Chem. Soc.* **2012**, *134*, 6625-6636.
79. Knekt, P.; Kumpulainen, J.; Jarvinen, R.; Rissanen, H.; Heliovaara, M.; Reunanen, A.; Hakulinen, T.; Aromaa, A. *Am. J. Clin. Nutr.* **2002**, *76*, 560-568.
80. Grant, W. B. *Alzheimers Dis. Rev.* **1997**, *2*, 42-55.
81. Palanivelu, K.; Mishra, S. *Ann. Indian Acad. Neurol.* **2008**, *11*, 13-19.
82. Esatbeyoglu, T.; Huebbe, P.; Ernst, I. M.; Chin, D.; Wagner, A. E.; Rimbach, G. *Angew. Chem. Int. Ed.* **2012**, *51*, 5308-5332.
83. Reinke, A. A.; Gestwicki, J. E. *Chem. Biol. Drug Des.* **2007**, *70*, 206-215.
84. Mandel, S.; Amit, T.; Bar-Am, O.; Youdim, M. B. *Prog. Neurobiol.* **2007**, *82*, 348-360.
85. Ishige, K.; Schubert, D.; Sagara, Y. *Free Radical Biol. Med.* **2001**, *30*, 433-446.

Chapter 2: Myricetin and Luteolin: Naturally Occurring Regulators of Metal-Induced Aβ Aggregation and Neurotoxicity

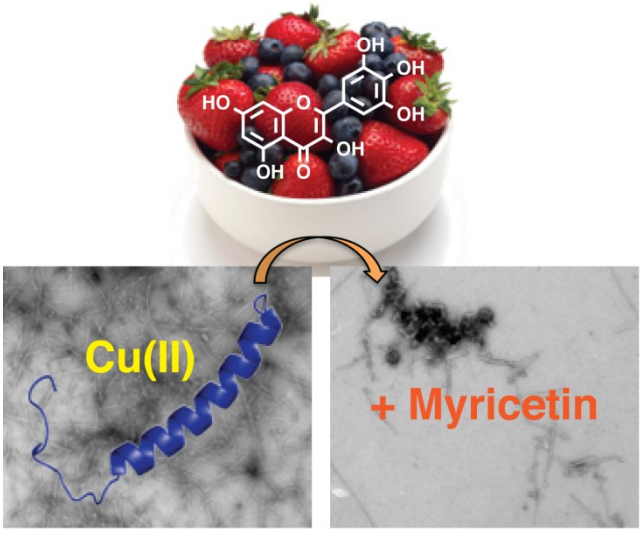

The results presented in this chapter for myricetin were previously published (DeToma, A. S.;‡ Choi, J.-S.;‡ Braymer, J. J.; Lim, M. H. *ChemBioChem* **2011**, *12*, 1198-1201. ‡ Equal contribution.). *In vitro* aggregation studies were obtained in collaboration with Dr. Jung-Suk Choi. Dr. Choi also conducted the cell experiments. Joseph J. Braymer contributed to writing of the manuscript.

2.1. Introduction

One of the most severe and incurable forms of neurodegeneration, Alzheimer's disease (AD), is identified by the accumulation of aggregated amyloid-β (Aβ) peptides in the brain.[1-7] It has been proposed that disruption of metal ions in the brain, such as Cu(II) and Zn(II), along with the misfolded Aβ peptides, could influence the disease progression as well.[1-12] Namely, it has been found that Cu(II) and Zn(II) can bind to Aβ, which can enhance peptide aggregation and in the case of redox active metal ions (*e.g.*, Cu(I/II))), facilitate the generation of reactive oxygen species (ROS) leading to oxidative stress.[1-12] While peptide aggregation and oxidative stress have been implicated in AD, the connection between metal ions and Aβ species in the development of this disease remains unclear.

To clarify the function of metal ions in Aβ-related pathological events, small molecule-based tools that have structural characteristics to simultaneously interact with both metal ions and Aβ have been sought.[3,5,6,12-23] Several small molecules have been designed to target metal-associated Aβ (metal–Aβ) species and to interrogate metal-induced Aβ aggregation and toxicity according to a rational structure-based design strategy.[3,5,6,12-15] Many of these structures have been derived from known Aβ plaque imaging agents;[16-20] however, due to the multiple factors that may be involved in AD neuropathogenesis, discovery of novel structural frameworks is an ongoing effort and will be a valuable component toward advancement of this design strategy. In order to identify new classes of basic scaffolds and to formulate a structure-interaction-reactivity relationship, structural modifications developed *via* a rational structure-based design approach or through systematic screening and/or selection of naturally occurring compounds can be envisioned.

Flavonoids are a class of polyphenolic compounds that are abundant in natural products, such as berries, fruits, and vegetables, and they have been investigated as potential therapeutic agents in human diseases such as cancer, cardiovascular diseases, and neurodegenerative diseases.[24-32] Over 60 clinical trials focusing on flavonoids have been initiated; however, none has succeeded in bringing forth approval for the treatment of any disease.[33] The proposed and completed clinical trials utilize only

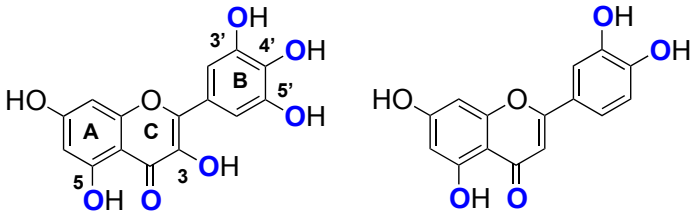

Figure 2.1. Chemical structures of myricetin (Myr, left) and luteolin (Lut, right). The rings are labeled A, B, and C to identify the rings in the core flavonoid framework. Numbered positions indicate sites with OH groups (blue) for potential metal binding.

a few different flavonoid structures to target numerous conditions, presumably due to multitude of possible modes of action for these compounds *in vivo*.[30]

A number of flavonoid molecules representing the various structural classes have been independently shown to chelate metal ions and interact with Aβ.[28,32,34-37] Chelation properties for various flavonoids have been characterized, providing some useful insights into its binding properties (*e.g.*, stoichiometry of complex formation, donor atoms, stability constants) (*vide infra*). The previous studies have demonstrated that flavonoids can have multiple potential sites for metal chelation, including positions between the 4-oxo and the 3- or 5-OH groups in the A and C ring or in catechol or pyrogallol groups in the B ring (Figure 2.1). In addition, flavone-based imaging agents developed for *in vivo* detection of Aβ plaques were found to have 5-321 nM binding affinity, supporting that the flavonoid framework could interact with aggregated Aβ species.[38] The influence of flavonoids on Aβ aggregation has also been investigated, and some of these structures can block Aβ assembly.[25,28,31,32] Akaishi *et al.* defined a structure-interaction relationship among several flavonoid structures and Aβ in an effort to account for the inhibitory activity of a specific example, fisetin; they reported that the presence of OH groups in the 3' and 4' position on the B ring were more capable of inhibiting Aβ aggregation due to OH groups in the 3 or 7 position of the A ring did not significantly impact the reactivity.[32] Taken together, one of the well-studied flavonols, myricetin, was found to produce metal complexes with binding stoichiometries of 1:1 or 1:2[34,35] and its anti-amyloidogenic activity toward metal-free Aβ species has been attributed to its reversible binding to fibrillar forms of Aβ over monomers.[28]

Despite the known interactions of myricetin and other members of the flavonoid family with metal ions and/or Aβ, their effect on metal-induced Aβ aggregation pathways and toxicity was not previously reported. To investigate whether naturally occurring flavonoids could exhibit bifunctionality (*i.e.*, metal chelation and Aβ interaction) to target metal–Aβ species and modulate their aggregation and toxicity, myricetin and luteolin were initially selected.[22] These investigations were also pursued in order to identify chemical structures with utility for development of novel molecules to target metal ions, Aβ species, and other factors that might be involved in AD neuropathogenesis. Herein, we present that myricetin and luteolin were capable of modulating Cu(II)- and Zn(II)-induced Aβ aggregation *in vitro* and toxicity in human neuroblastoma cells. To the best of our knowledge, these were the first studies to establish the reactivity of naturally occurring flavonoids toward metal–Aβ-related events and could lead to further investigations of a wide range of flavonoids as useful chemical reagents or templates for applications in AD research.[22]

2.2. Results and discussion

2.2.1. Metal binding properties of myricetin and luteolin

In order to describe the potential bifunctionality of these molecules (*i.e.*, metal chelation, Aβ interaction), the metal binding properties of myricetin and luteolin were confirmed by UV-Visible (UV-Vis) spectroscopy (Figure 2.2). In agreement with the previous UV-Vis studies,[34] a bathochromic shift of the optical band (*ca.* 377 to 450 nm) was observed upon addition of $CuCl_2$ (1 equiv) to myricetin (40 μM) in 20 mM HEPES, pH 7.4, 150 mM NaCl (Figure 2.2). Under the same conditions, an optical change was also observed for luteolin (40 μM) with $CuCl_2$ (1 equiv). The addition of 5 equiv of $ZnCl_2$ to a solution of either myricetin or luteolin in similar conditions was required to produce a noticeable shift in the spectrum. Overall, these studies suggest that both molecules were capable of binding to both Cu(II) and Zn(II).

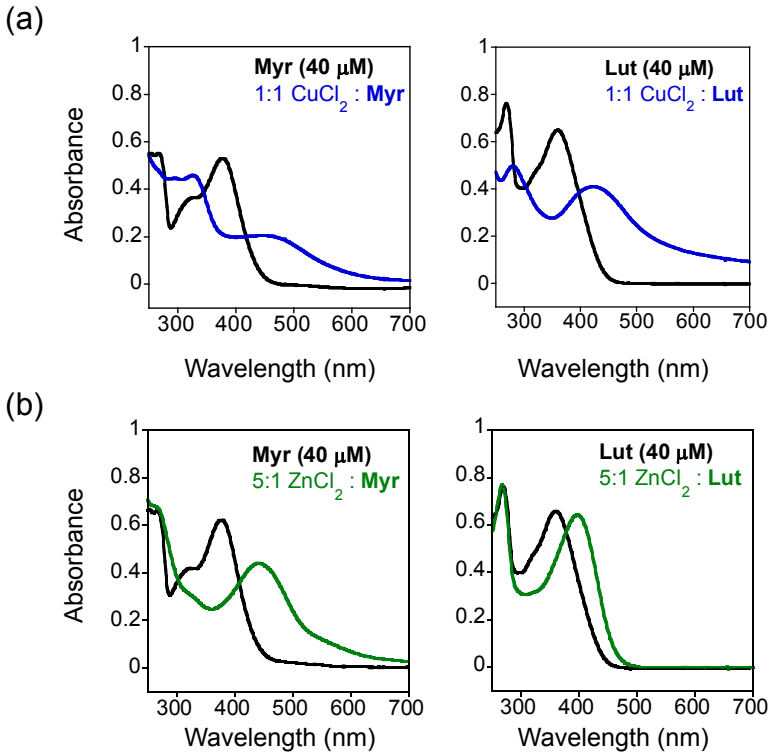

Figure 2.2. Cu(II) and Zn(II) binding studies with myricetin (Myr, left) and luteolin (Lut, right) by UV-Vis spectroscopy. A 40 μM solution of Myr or Lut was prepared in a buffered solution containing 20 mM HEPES, pH 7.4, 150 mM NaCl and treated with (a) 1 equiv of $CuCl_2$ or (b) 5 equiv of $ZnCl_2$ for 5 min.

Although the observed spectral changes provided evidence that Cu(II) and Zn(II) are able to bind to these structures, the exact donor atoms involved in metal binding cannot be clearly identified by this method. Recently, Cheng and coworkers have systematically investigated stability constants for Fe(III) complexes with three flavonoids (Figure 2.3), each possessing only one of the commonly proposed chelation sites (*i.e.*, 3-OH/4-keto, 5-OH/4-keto, 3',4'-dihydroxy (catechol)).[39] Their goal was to differentiate the influence of various binding moieties in other flavonoids by treating the individual components separately. Their results indicated that the catechol moiety on the B ring of the flavonoid to be most influential for binding Fe(III) at physiological pH.[39]

The catechol structure has reported stability constants of 7.95 and 13.5 with Fe(II), 13.9 and 24.9 with Cu(II), and 9.9 and 17.4 with Zn(II) for 1:1 and 1:2 complexes, respectively.[40] Myricetin and luteolin contain a combination of the chelation sites investigated by Cheng and coworkers, commonly sharing the 5-OH/4-keto and catechol

moieties; thus, it could be suggested that elements of the catechol moiety may also be involved in Cu(II) and Zn(II) chelation for these molecules. Myricetin, however, has an additional OH group in the 5' position and in the 3 position that may complicate the mixture of metal–myricetin complexes in solution. Thus, delineating the exact coordination environment and stoichiometry of metal-bound complexes could be complicated due to the multiple binding sites.

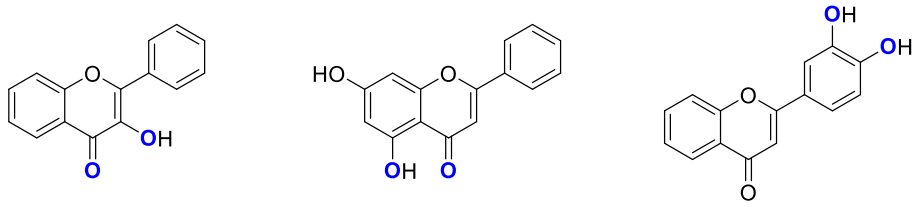

Figure 2.3. Structures used to investigate metal chelation sites of flavonoids in the study by Cheng and co-workers.[39]

Several spectrophotometric procedures have been described in the literature to measure the stoichiometry of metal–ligand complexes and were developed according to the work of Job, Bent and French, and Nach.[41] Job's method, which is more widely applied, employs various ratios of equimolar ligand and metal solutions to find a ratio of maximum absorbance.[41,42] For several of the flavonoids (*e.g.*, rutin, quercetin, morin, 3-hydroxyflavone), these methods indicated 1:1 or 1:2 stoichiometry (metal/ligand) with the divalent cations of Cu, Zn, Co, Ni, and others.[41] Applying Job's method of continuous variation, the binding stoichiometry between Cu(II) and myricetin or luteolin was investigated (Figure 2.4).[16,42] Equimolar solutions of the ligand and $CuCl_2$ (40 μM for myricetin, 50 μM for luteolin) were mixed in various molar ratios from 0–1 in 20 mM HEPES buffer (pH 7.4, 150 mM NaCl). The change in absorbance of the metal–ligand absorption band was monitored and plotted against the molar ratio of Cu(II) in solution. For both molecules, the maximum absorption occurred near a molar ratio of 0.5, indicating a binding stoichiometry of 1:1 Cu(II)/ligand.

While these results indicate the metal binding properties of myricetin and luteolin in an Aβ-free solution, the ability of these compounds to compete for metal binding with Aβ would support their utility in further investigations using metal-induced Aβ aggregation and neurotoxicity (*vide infra*). Therefore, UV-Vis studies were performed to

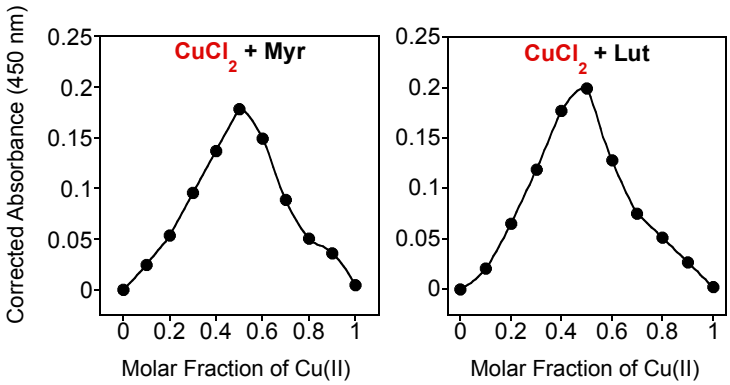

Figure 2.4. Job plots of Cu(II) with myricetin (Myr, left, 40 μM initial) and luteolin (Lut, right, 50 μM initial) in 20 mM HEPES, pH 7.4, 150 mM NaCl.[42]

determine if myricetin could interact with Cu(II) or Zn(II) that may already be associated with Aβ (Figure 2.5). After myricetin (25 μM) was added to the preincubated solution of Aβ (25 μM) and $CuCl_2$ or $ZnCl_2$ (25 μM), new absorption bands that resembled the metal–myricetin complexes in an Aβ-free solution appeared after 5 min. These results suggest that the possible interaction of myricetin with metal ions surrounded by Aβ could lend this molecule to be classified as bifunctional molecules, which may be used to rationalize their effects on metal-induced Aβ reactivity *in vitro*.

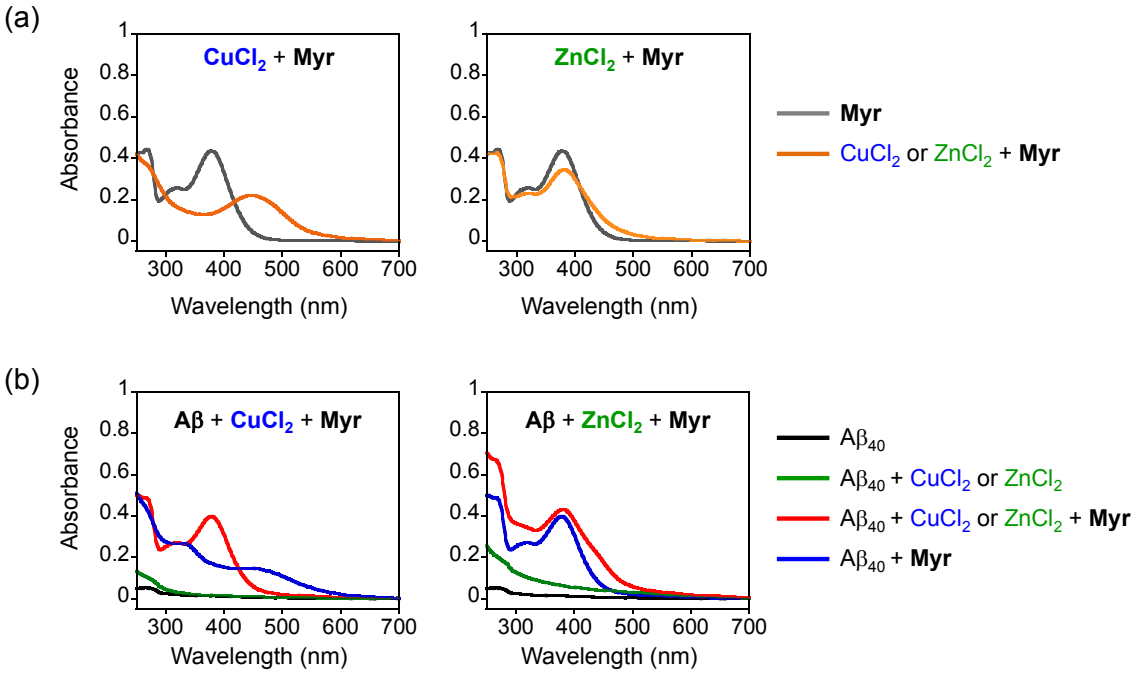

Figure 2.5. UV-Vis studies showing the interaction of myricetin (Myr) with metal ions in the presence of Aβ. (a) The spectra of Myr in the absence (blue) and presence (red) of $CuCl_2$ or $ZnCl_2$ following 5 min incubation. (b) The spectra of the samples containing Aβ, metal ions, and/or myricetin. To Aβ (black), $CuCl_2$ or $ZnCl_2$ was added immediately and incubated for 2 min (green). The solution containing Aβ and $CuCl_2$ or $ZnCl_2$ was treated with Myr for 5 min (red). The spectrum of metal-free Aβ and Myr is shown in blue. Experimental conditions: [Aβ] = 25 μM, [$CuCl_2$ or $ZnCl_2$] = 25 μM, [Myr] = 25 μM, 20 mM HEPES, pH 7.4, 150 mM NaCl, room temperature.

2.2.2. Modulation of metal-associated Aβ aggregation by myricetin and luteolin

The reactivity of myricetin toward metal–Aβ species was probed using *in vitro* Aβ aggregation studies conducted in the presence and absence of metal ions (Figures 2.6, 2.7, and 2.8) according to reported procedures.[16-23,43] To understand the degree to which myricetin and luteolin were able to prevent the formation of metal-associated Aβ aggregates (inhibition experiment, Figure 2.6 and 2.7), fresh Aβ (25 μM) was treated with $CuCl_2$ or $ZnCl_2$ (25 μM) for 2 min followed by 24 h incubation with myricetin or luteolin (50 μM). The alteration of metal-associated Aβ aggregate formation was visualized using gel electrophoresis with Western blotting (6E10 anti-Aβ antibody) and by transmission electron microscopy (TEM). First, the Western blots from the inhibition experiment showed that for Aβ incubated with $CuCl_2$ or $ZnCl_2$, the inclusion of myricetin or luteolin in the sample solution increased the amount of soluble peptides that were small enough to to enter the gel compared with the untreated metal–Aβ control samples (Figures 2.6 and 2.7). In particular, those Aβ species having molecular weight (MW) ≤ 32 kDa were more prominent. It has been reported that upon Aβ fibrillogenesis, mature Aβ fibrils, such as those observed by TEM, cannot enter the gel, causing them to either be retained at the gel entrance or to be insufficiently delivered to the gel.[44,45] Since these compounds may interfere with Aβ fibrillogenesis, the amount of Aβ species that are therefore small enough to permeate the gel matrix is increased and more of these species are able to be separated in the gel. Second, TEM images were collected for samples containing Aβ, metal ions, and myricetin and those without myricetin (Figure 2.7). The Aβ aggregates formed in the presence of Cu(II) or Zn(II) were large and contained fibrillar morphological features. When those solutions also contained myricetin, mainly smaller-sized Aβ species were visualized, consistent with the Western

blot results (Figure 2.6). These aggregates were also morphologically different from the control samples as they appeared to be amorphous instead of fibrillar. Therefore, these results and observations might suggest that myricetin and luteolin are capable of inhibiting or altering metal-induced Aβ aggregation.

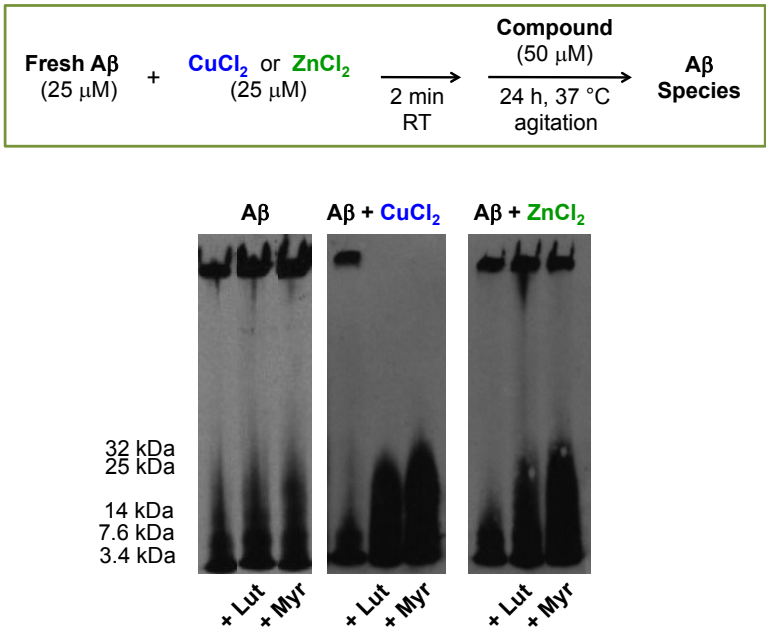

Figure 2.6. Inhibitory effect of luteolin (Lut) and myricetin (Myr) on the formation of metal-induced Aβ aggregates. Top: Scheme of the inhibition experiment. Bottom: Aβ species visualized by gel electrophoresis using Western blot with an anti-Aβ antibody 6E10. Experimental conditions: [Aβ] = 25 μM, [$CuCl_2$ or $ZnCl_2$] = 25 μM, [Lut or Myr] = 50 μM, pH 7.4, 37 °C, 24 h, constant agitation.

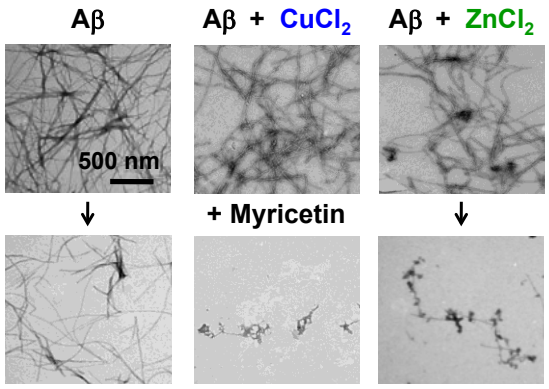

Figure 2.7. TEM images of the samples containing myricetin from Figure 2.6.

As a comparison, the effect of both flavonoids on metal-free Aβ aggregation in the inhibition experiment was investigated (Figures 2.6 and 2.7). By Western blot, the difference in the distribution of Aβ species for myricetin- or luteolin-treated Aβ species was not as noticeable among lower MW Aβ species. In the absence of metal ions at the same condition, long fibrillar Aβ aggregates were observed by TEM. With myricetin, the morphology closely resembled the untreated control sample of only Aβ. Upon comparison of the metal-free Aβ species in the presence of myricetin with the Cu(II)- and Zn(II)-treated Aβ samples (Figure 2.6 and 2.7), myricetin had a stronger ability to modulate metal-induced Aβ aggregation compared to metal-free Aβ aggregation.

In addition to the inhibition experiments, the ability of myricetin and luteolin (50 μM) to disaggregate metal-free and metal-associated Aβ aggregates generated after 24 h incubation of fresh Aβ (25 μM) without or with metal chloride salts (25 μM) was also evaluated (disaggregation experiment, Figure 2.8).[16-23,43] Similar to the inhibition experiment, neither myricetin nor luteolin had a noticeable influence on the metal-free Aβ aggregate size distribution according to the Western blot. Unlike the inhibition experiment, however, where both compounds could modulate metal-mediated Aβ aggregation, myricetin and luteolin demonstrated different reactivity toward the preformed metal–Aβ aggregates. Following 4 h treatment, luteolin had only a moderate impact on metal-associated Aβ aggregates. A slightly larger amount of gel permeable Cu(II)–Aβ species were observed in the presence of luteolin compared to the control, but almost no difference was detected between the Zn(II)–Aβ control and the sample containing luteolin. Myricetin was able to disrupt the Aβ aggregates preformed in the presence both Cu(II) and Zn(II) to produce a variety of smaller Aβ species capable of entering the gel matrix relative to those from control samples containing no ligand (Figure 2.8). The effect of myricetin on these aggregates appeared to be dependent on whether the Aβ samples were treated with Cu(II) or Zn(II). For the Cu(II)-treated samples, a wider distribution of low MW Aβ species are observed as visualized by the smearing throughout the lane. The Zn(II)-treated Aβ samples presented a less dispersed distribution of sizes, however. Instead, more of the gel permeable Zn(II)–Aβ species had higher MW. The Aβ species from these experiments were visualized by

TEM, where a mixture of species was observed. In contrast to the conformation of metal–Aβ species that were seen by TEM for the control samples (Cu(II)- or Zn(II)-treated Aβ), there were amorphous aggregates along with fragmented fibrillar Aβ species in the samples containing myricetin. Therefore, it is plausible to attribute the increased amounts of Aβ species that are small enough to enter the gel and have altered morphology to the myricetin-induced disassembly of metal–Aβ aggregates.

Overall, these results suggest that flavonoids may be effective to preferentially target and modulate a variety Aβ species generated in metal-triggered over metal-free Aβ aggregation pathways. Comparison of the reactivity for myricetin and luteolin suggests that certain structural differences, such as the additional OH groups of myricetin, may improve the versatility of one ligand framework over another for this purpose. Both molecules, however, could control metal-mediated Aβ aggregation to a greater extent than metal-free Aβ aggregation from early stages of aggregation. The

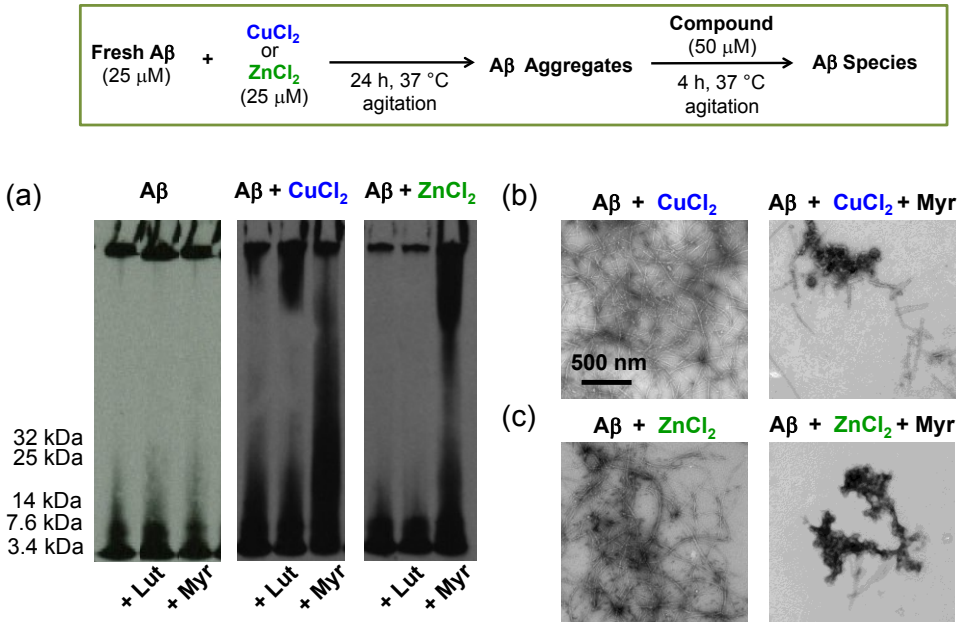

Figure 2.8. Transformation of metal-induced Aβ aggregates by luteolin (Lut) or myricetin (Myr). Top: Scheme of the disaggregation experiment. Bottom: (a) Aβ species visualized by gel electrophoresis using Western blot with an anti-Aβ antibody 6E10. (b) TEM images of the samples from (a) with myricetin. Experimental conditions: [Aβ] = 25 μM, [$CuCl_2$ or $ZnCl_2$] = 25 μM, [Lut or Myr] = 50 μM, pH 7.4, 37 °C, 4 h, constant agitation.

flexibility of monomeric and other low MW species might facilitate both compounds' accessibility for metal binding. According to the disaggregation results, the more structured metal–Aβ aggregates appeared to be more sensitive to myricetin, which could be related to the minor structural differences of myricetin and luteolin. Thus, naturally occurring flavonoids offer an accessible library of known molecules with potential to target and modulate metal-associated Aβ aggregation to varying extents.

2.2.3. Regulation of H_2O_2 production from Cu(II)-associated Aβ species *in vitro*

There has been great interest in the anti- and pro-oxidant capabilities of flavonoid compounds since oxidative damage is a hallmark of many diseases including AD.[46-48] In AD, the production of ROS by redox active metals (*e.g.*, Cu(I/II), Fe(II/III)) bound to Aβ peptides may occur *via* processes such as Fenton chemistry.[49,50] Along with the breakdown of endogenous antioxidant systems, ROS production has been suggested to cause oxidative stress leading to the pervasive neuronal damage in AD.[51-53] There have been some efforts to use antioxidants to potentially combat this aspect of AD, but they have been met with limited success.[54]

To investigate this aspect of reactivity, a horseradish peroxidase/Amplex Red assay was conducted to measure the ability of myricetin and/or luteolin to mitigate the production of H_2O_2 *in vitro* (Figure 2.9).[16,17,19,21,55,56] To mimic the conditions that may facilitate H_2O_2 production in the brain, $A\beta_{40}$ was incubated with $CuCl_2$ before introducing the compounds, along with ascorbate as a reducing agent to sustain Fenton cycling. Oxidation of Amplex Red by H_2O_2 to fluorescent resorufin was used to quantify H_2O_2 production in the system. As expected, Cu–Aβ species produced H_2O_2, indicated by the fluorescence increase. The fluorescence values for the samples treated with compounds were normalized to that of the Cu–Aβ control. When Cu–Aβ species were treated with either myricetin or luteolin, there was a reduced amount of H_2O_2 produced (*ca.* 30% less for myricetin and 70% less for luteolin).[21] As a positive control, the known chelator EDTA (EDTA = ethylenediaminetetraacetic acid; 2-((2-[bis(carboxymethyl)amino]ethyl)(carboxymethyl)amino)acetic acid) resulted in *ca.* 15% production of H_2O_2 compared to the control samples.

Although the antioxidant properties of myricetin and luteolin have been reported,[57] another plausible mechanism for this activity could be connected to their ability to chelate free transition metal ions (*e.g.*, Fe(II/III)) that are redox active and participate in Fenton chemistry.[47,48] In one sense, sequestration of the metal ion may prevent its redox cycling and, subsequently, production of ROS; alternatively, the polyphenolic ligands could be responsible for reducing the metal ion to produce a species that could perpetuate the Fenton cycle (pro-oxidant).[48] Some mass spectrometric (MS) studies have also directly detected the oxidation of flavonoid ligands

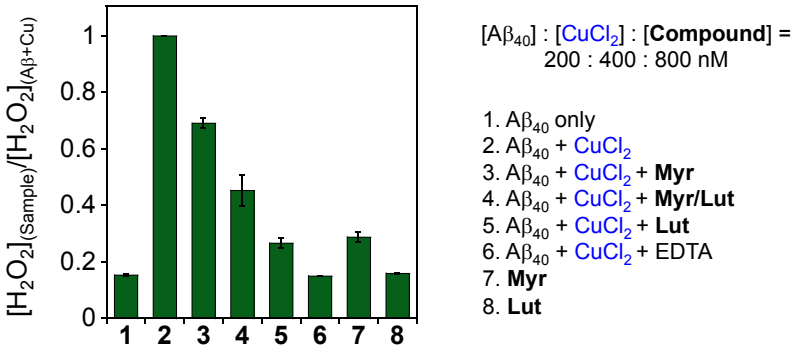

Figure 2.9. Modulation of Cu(II)–Aβ-induced H_2O_2 production by myricetin (Myr) and luteolin (Lut). The amount of H_2O_2 was measured by the horseradish peroxidase (HRP)/Amplex Red assay. Experimental conditions: [Aβ] = 200 nM, [$CuCl_2$] = 400 nM, [compound] = 800 nM, [ascorbate] = 10 μM, [Amplex Red] = 50 μM, [HRP] = 1 U/mL, phosphate buffered saline (PBS), pH 7.4; $\lambda_{ex/em}$ = 530/590. Catalase attenuates the fluorescence signal.

in the presence of metal ions by loss of hydrogen atoms (*e.g.*, in the 2 and 3 position of the saturated molecule naringenin)[58] and connected this to other studies indicated the necessity of hydrogen-donating properties for antioxidant behavior.[58] Some recent observations have supported the conclusion that the antioxidant activity is derived primarily from the 3-OH/4-keto site unless a catechol or gallol moiety is present.[46] It has also been proposed that structures having fewer OH groups might favor oxidation of the flavonoid over deprotonation as a mechanism for counteracting the reduction of the metal ion. These possibilities validate the consideration of stability constant and reduction potential measurements for fully understanding the reactivity of flavonoids in the presence and absence of metal ions for future studies. Thus, myricetin and luteolin

could partially attenuate Cu–Aβ mediated H_2O_2 production, but their inability to completely quench ROS production, perhaps due to their potential pro-oxidant properties, may limit their use for this aspect.

2.2.4. Regulation of toxicity from metal-associated Aβ species in human neuroblastoma cells by myricetin and luteolin

Whether these molecules might also display beneficial properties in biological systems, the toxicity of myricetin and luteolin to living cells in the absence and presence of metal ions and/or Aβ was investigated. The cytotoxicity of the metal ions, myricetin, and the corresponding metal–myricetin complexes were measured by the MTT (MTT = 3-(4,5-dimethylthiazol-2-yl)-2,5-diphenyltetrazolium bromide) assay following incubation of human neuroblastoma SK-N-BE(2)-M17 cells (M17) for 24 h. The cells, which were maintained in media containing 10% fetal bovine serum (FBS), presented suitable cell survival with metal ion alone (10 μM), flavonoid alone (20 μM), or flavonoid and $CuCl_2$ or $ZnCl_2$ for 24 h.

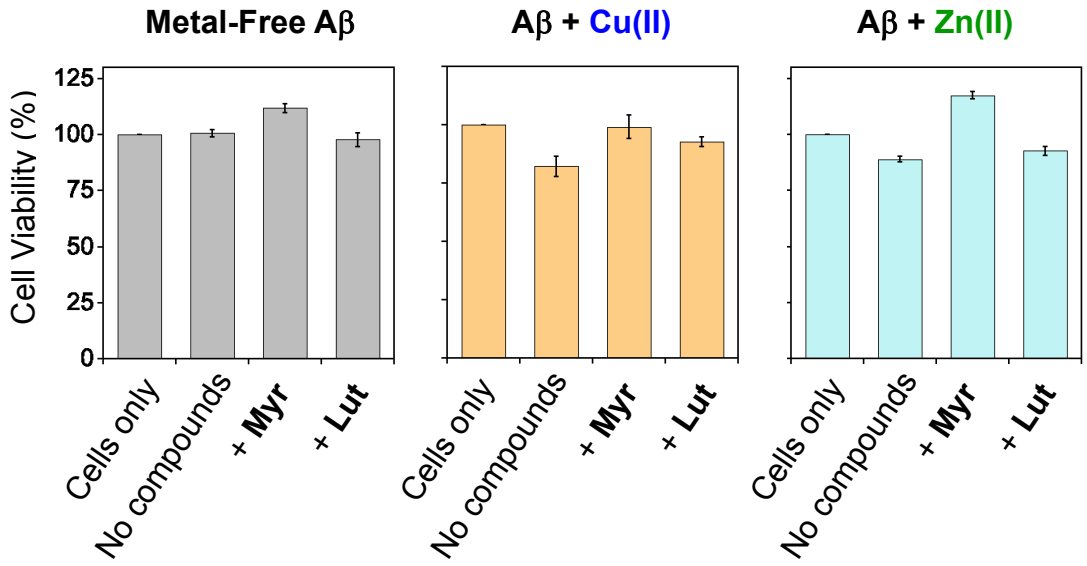

Figure 2.10. Modulation of metal-free and metal-induced Aβ toxicity in human neuroblastoma SK-N-BE(2)-M17 cells. Cells were treated with Aβ (10 μM), $CuCl_2$ or $ZnCl_2$, and/or myricetin (Myr) or luteolin (Lut) (20 μM, 1% v/v DMSO) for 24 h. Cell viability was measured by the MTT assay and was calculated relative to cells containing 1% v/v DMSO (Control). Error bars represent the standard error of three independent experiments.

The neuroprotective properties of myricetin against toxicity generated in the M17 cells by externally introduced metal ions and Aβ was pursued. With only Aβ (10 μM), no toxicity was detected, while the treatment of cells with Aβ (10 μM) and $CuCl_2$ or $ZnCl_2$ (10 μM) for 24 h resulted in 81(±3.2)% and 89(±1.4)% cell survival, respectively (Figure 2.10). The moderate toxicity of Aβ incubated with metal chloride salts in this setting occurred even in the presence of bovine serum albumin (BSA), a well-known metal chelator that is a major component of FBS, demonstrating that Aβ can compete for metal ions under these relevant conditions, which may be a factor in neurotoxicity.[59,60] In the cells containing Aβ (20 μM), $CuCl_2$ or $ZnCl_2$ (10 μM), and myricetin or luteolin (20 μM) with 24 h incubation, cell survival was improved. Luteolin was able to block toxicity of Cu(II)-treated Aβ, but had a lesser impact on Zn(II)–Aβ-induced toxicity, consistent with the observation that luteolin could influence disaggregation of Cu(II)–Aβ but not Zn(II)–Aβ. In the case of myricetin, cell viability for the Cu(II)- and Zn(II)-treated Aβ was recovered to over 100%. Potentially contributing to the improved cell viability was the interaction of myricetin with the metal–Aβ species to generate metal–myricetin complexes. It has been previously reported that transition metal complexes of flavonoids (*e.g.*, epigallocatechin-3-gallate, rutin) were beneficial to cell survival potentially through stabilization of the flavonoid structure and/or generation of additional sites for dismutation of the ROS, superoxide ($O_2^{\bullet -}$).[61,62] Thus, despite having some pro-oxidant properties, it could be possible for myricetin or luteolin to mitigate neurotoxicity in living systems by other mechanisms. Details of this neuroprotective function are deserving of further attention. Overall, enhanced cell survival in these samples can be attributed to interaction of myricetin with metal ions associated with Aβ, thereby implying the efficiency of myricetin to overcome the cytotoxicity of metal–Aβ species in living cells.

2.3. Conclusion

In summary, myricetin and luteolin are naturally occurring flavonoids that can chelate metal ions and have anti-amyloidogenic activity toward Aβ; however, the influence of any naturally occurring flavonoids on metal-involved Aβ aggregation and

neurotoxicity had not been studied prior to this work. The investigations herein demonstrated that both molecules may be able to modulate metal-induced Aβ aggregation more effectively than metal-free Aβ aggregation. Both compounds were able to inhibit metal-induced Aβ aggregation, but myricetin displayed greater control on preformed Aβ aggregates containing Cu(II) or Zn(II) than luteolin. Furthermore, both compounds could attenuate the cytotoxicity of Aβ treated with metal ions, but myricetin could accomplish this more effectively than luteolin. Interestingly, the ability to quench ROS production may not be an accurate indicator of the ability of a molecule to modulate metal-induced Aβ toxicity in living cells, as luteolin more effectively quenched H_2O_2 production than myricetin. Overall, our studies demonstrate the high potential of the flavonoid family as a class of chemical tools and/or therapeutic agents for AD. Moreover, this work may also provide insight into current efforts for developing a new class of small molecules with bifunctionality that can target metal-associated Aβ species and regulate metal-induced Aβ events in the AD brain.[3,5,6,12,14-22,43]

2.4. Experimental

2.4.1. Materials and methods

All reagents were purchased from commercial suppliers and used as received unless stated otherwise. $A\beta_{40}$ was purchased from AnaSpec (Fremont, CA, USA). The amino acid sequence for the $A\beta_{40}$ peptide is DAEFRHDSGYEVHHQKLVFF-AEDVGSNKGAIIGLMVGGVV. Myricetin was purchased from AvaChem Scientific (San Antonio, TX, USA) and luteolin was purchased from Alfa Aesar (Ward Hill, MA, USA); both compounds were used without further purification. Optical spectra were collected on an Agilent 8453 UV-Vis spectrophotometer. TEM images were taken at the Microscopy and Image Analysis Laboratory at the University of Michigan using a Philips CM-100 transmission electron microscope (Andover, MA, USA). A SpectraMax M5 microplate reader (Molecular Devices, Sunnyvale, CA, USA) was used for measurements of fluorescence for the horseradish peroxidase/Amplex Red assay and absorbance for the cell viability assay.

2.4.2. Metal binding studies

To understand metal binding properties, optical spectra were obtained for the solutions of either myricetin or luteolin (40 μM in 20 mM HEPES (2-[4-(2-hydroxyethyl)piperazin-1-yl]ethanesulfonic acid), pH 7.4, 150 mM NaCl) as well as myricetin or luteolin incubated with $CuCl_2$ (40 μM) or $ZnCl_2$ (200 μM) for 5 min. To verify if metal chelation occurs by myricetin in the presence of Aβ, optical studies were carried out on the samples of Aβ (25 μM) and $CuCl_2$ or $ZnCl_2$ (25 μM, 2 min incubation, room temperature) in the absence and presence of myricetin (25 μM, incubation for 5 min, room temperature).

Job's method of continuous variation was employed to measure the stoichiometry for $CuCl_2$ with myricetin and luteolin in solution.[16,42] The molar fraction of $CuCl_2$ in the solution was varied from 0–1 with the initial myricetin concentration of 40 μM and initial luteolin concentration of 50 μM. The samples were prepared in a buffered solution of 20 mM HEPES, pH 7.4, 150 mM NaCl. The UV-Vis spectra of each sample were recorded and the change in absorbance at λ_{max} corresponding to the metal–ligand absorption band (450 nm for both compounds) was plotted against the molar fraction of Cu(II) in solution.

2.4.3. Amyloid-β (Aβ) peptide experiments

Aβ samples were prepared according to the previously reported procedures.[16-23,43] The Aβ peptide was dissolved in NH_4OH (1% v/v aq), aliquoted, lyophilized, and stored at −80 °C. Stock solutions of Aβ were prepared prior to the experiments by redissolving the lyophilized Aβ with NH_4OH (1% v/v aq, 10 μL) and diluting with ddH_2O. All solutions for inhibition and disaggregation studies were prepared in a buffered solution (20 μM HEPES, pH 7.4, 150 μM NaCl). For the inhibition studies, fresh Aβ (25 μM) was incubated with either $CuCl_2$ or $ZnCl_2$ (25 μM) for 2 min at room temperature followed by addition of myricetin or luteolin (50 μM, 1% v/v DMSO). The solutions were incubated for 24 h at 37 °C with constant agitation. For the disaggregation studies, Aβ aggregates were prepared by treating fresh Aβ (25 μM) with $CuCl_2$ or $ZnCl_2$ (25 μM) for 24 h at 37 °C with agitation. Afterwards, either myricetin or luteolin (50 μM) was added

and the resulting solutions were incubated for 4 h at 37 °C with agitation. Metal-free Aβ samples for the inhibition and disaggregation experiments were prepared at the same condition in the absence of metal chloride salts. The degree of Aβ aggregation and the morphology of Aβ species samples from the inhibition and disaggregation studies were analyzed using gel electrophoresis using Western blotting with an anti-Aβ antibody 6E10 and by TEM, respectively.[16-23,43]

2.4.4. Gel electrophoresis and Western blotting

The reactions described in Section 2.4.3. were visualized by gel electrophoresis followed by Western blotting using an anti-Aβ antibody (6E10).[16-23,43] Each sample (25 μM Aβ, 10 μL) was separated on a 10-20% gradient Tris-tricine gel (Invitrogen, Grand Island, NY, USA). The gel was transferred onto a nitrocellulose membrane, blocked with bovine serum albumin (BSA, 3% w/v, Sigma, St. Louis, MO, USA) in Tris-buffered saline (TBS, Fisher, Pittsburgh, PA, USA) containing 0.1% Tween-20 (Sigma,TBS-T) for 3 h at room temperature, and incubated with an anti-Aβ antibody 6E10 (1:2,000, Covance, Princeton, NJ, USA) in 2% BSA (v/v, TBS-T) for 3 h at room temperature. The membrane was probed with the horseradish peroxidase-conjugated goat anti-mouse secondary antibody diluted (Cayman Chemical, Ann Arbor, MI, USA) in 2% BSA (v/v, TBS-T) for 1 h at room temperature. The Thermo Scientific Supersignal West Pico Chemiluminescent Substrate was used to visualize protein bands.

2.4.5. Transmission electron microscopy (TEM)

Samples for TEM were prepared by following the previously reported method.[16-20,22,43] Glow-discharged grids (Formar/Carbon 300-mesh, Electron Microscopy Sciences, Hatfield, PA, USA) were treated with samples from the inhibition or disaggregation experiments (5 μL) for 2 min at room temperature. Excess sample solution was removed using filter paper followed by washing three times with ddH_2O. Each grid was incubated with uranyl acetate (1% v/v ddH_2O, 5 μL) for 1 min. Extra uranyl acetate was removed and the grids were dried for 15 min at room temperature. Images from each sample were taken by a Philips CM-100 transmission electron microscope (80 kV, 25,000x magnification).

2.4.6. H_2O_2 production measured by the horseradish peroxidase/Amplex Red assay

The production of H_2O_2 by Cu(II)–Aβ species in the presence of dioxygen (O_2) and a reducing agent (ascorbate) was monitored by the horseradish peroxidase (HRP)/Amplex Red assay.[16,17,19,21,55,56] To a black polystyrene 96-well assay plate (Corning, Corning, NY, USA), $A\beta_{40}$ (200 nM) was diluted in phosphate buffered saline (PBS, pH 7.4, Invitrogen, Grand Island, NY, USA) and incubated with $CuCl_2$ (400 nM) for 1 h with agitation at room temperature. Afterward, the Cu–Aβ mixture was treated with each compound (800 nM, 1% v/v DMSO) for 1 h with agitation at room temperature. The solutions were treated with ascorbate (10 μM) and after 5 min, with a solution containing HRP (1 U/mL, Invitrogen) and Amplex Red (100 μM, Anaspec, Fremont, CA, USA) mixture. The plate was incubated for 15 min with agitation at room temperature before measuring the fluorescence emission intensity ($\lambda_{ex}/\lambda_{em}$ = 530/590 nm). Catalase (10 μL of 100 U/mL) was added to verify H_2O_2 production in the samples. The total volume was 100 μL in each well at the end of the experiment.

2.4.7. Cell viability measurements by the MTT assay

Human neuroblastoma SK-N-BE(2)-M17 (M17) cells were purchased from the American Type Culture Collection. The M17 cells were maintained in media containing [Minimum Essential Media (MEM, GIBCO)] (50%) and [Ham's F12K Kaighn's Modification Media (F12K, Cellgro)] (50%), supplemented with 10% (v/v) fetal bovine serum (FBS, Atlanta Biologicals, Atlanta, GA, USA), 100 U/mL penicillin and 100 μg/mL streptomycin (Invitrogen). The cells were grown at 37 °C in a humidified atmosphere of 5% CO_2. Cell viability was measured using the MTT (MTT = 3-(4,5-dimethylthiazol-2-yl)-2,5-diphenyltetrazolium bromide, Sigma) assay.[16,17,19,20,22] Cells were seeded in a 96 well plate (16,000 cells in 100 μL per well) and treated with Aβ (10 μM) and $CuCl_2$ or $ZnCl_2$ (10 μM) immediately followed by myricetin or luteolin (20 μM). After 24 h incubation of the cells at 37 °C, the cells were treated with 25 μL MTT (5 mg/mL in PBS) for 4 h at 37 °C. The cells were lysed in an acidified solution containing *N*,*N*-dimethylformamide (pH 4.5, 50% v/v aq, Sigma) and sodium dodecyl sulfate (SDS, 20%

w/v, Sigma) overnight at room temperature in the dark. The absorbance (A_{600}) was measured using a microplate reader and cell viability (%) was calculated relative to that of cells containing 1% DMSO (v/v).

2.5. References

1. Jakob-Roetne, R.; Jacobsen, H. *Angew. Chem. Int. Ed.* **2009**, *48*, 3030-3059.
2. Rauk, A. *Chem. Soc. Rev.* **2009**, *38*, 2698-2715.
3. Scott, L. E.; Orvig, C. *Chem. Rev.* **2009**, *109*, 4885-4910.
4. Gaggelli, E.; Kozlowski, H.; Valensin, D.; Valensin, G. *Chem. Rev.* **2006**, *106*, 1995-2044.
5. DeToma, A. S.; Salamekh, S.; Ramamoorthy, A.; Lim, M. H. *Chem. Soc. Rev.* **2012**, *41*, 608-621.
6. Pithadia, A. S.; Lim, M. H. *Curr. Opin. Chem. Biol.* **2012**, *16*, 67-73.
7. Savelieff, M. G.; Lee, S.; Liu, Y.; Lim, M. H. *ACS Chem. Biol.* **2013**, *8*, 856-865.
8. Huang, X.; Moir, R. D.; Tanzi, R. E.; Bush, A. I.; Rogers, J. T. *Ann. N. Y. Acad. Sci.* **2004**, *1012*, 153-163.
9. Zhu, X.; Su, B.; Wang, X.; Smith, M. A.; Perry, G. *Cell. Mol. Life Sci.* **2007**, *64*, 2202-2210.
10. Faller, P. *ChemBioChem* **2009**, *10*, 2837-2845.
11. Faller, P.; Hureau, C. *Dalton Trans.* **2009**, 1080-1094.
12. Perez, L. R.; Franz, K. J. *Dalton Trans.* **2010**, *39*, 2177-2187.
13. Rodríguez-Rodríguez, C.; Telpoukhovskaia, M.; Orvig, C. *Coord. Chem. Rev.* **2012**, *256* 2308-2332.
14. Braymer, J. J.; DeToma, A. S.; Choi, J.-S.; Ko, K. S.; Lim, M. H. *Int. J. Alzheimers Dis.* **2011**, *2011*, 623051.
15. Hureau, C.; Sasaki, I.; Gras, E.; Faller, P. *ChemBioChem* **2010**, *11*, 950-953.
16. Hindo, S. S.; Mancino, A. M.; Braymer, J. J.; Liu, Y.; Vivekanandan, S.; Ramamoorthy, A.; Lim, M. H. *J. Am. Chem. Soc.* **2009**, *131*, 16663-16665.
17. Choi, J.-S.; Braymer, J. J.; Nanga, R. P. R.; Ramamoorthy, A.; Lim, M. H. *Proc. Natl. Acad. Sci. U. S. A.* **2010**, *107*, 21990-21995.
18. Choi, J.-S.; Braymer, J. J.; Park, S. K.; Mustafa, S.; Chae, J.; Lim, M. H. *Metallomics* **2011**, *3*, 284-291.
19. Braymer, J. J.; Choi, J.-S.; DeToma, A. S.; Wang, C.; Nam, K.; Kampf, J. W.; Ramamoorthy, A.; Lim, M. H. *Inorg. Chem.* **2011**, *50*, 10724-10734.
20. Pithadia, A. S.; Kochi, A.; Soper, M. T.; Beck, M. W.; Liu, Y.; Lee, S.; Detoma, A. S.; Ruotolo, B. T.; Lim, M. H. *Inorg. Chem.* **2012**, *51*, 12959-12967.
21. He, X.; Park, H. M.; Hyung, S. J.; DeToma, A. S.; Kim, C.; Ruotolo, B. T.; Lim, M. H. *Dalton Trans.* **2012**, *41*, 6558-6566.
22. DeToma, A. S.; Choi, J.-S.; Braymer, J. J.; Lim, M. H. *ChemBioChem* **2011**, *12*, 1198-1201.
23. Hyung, S.-J.; DeToma, A. S.; Brender, J. R.; Lee, S.; Vivekanandan, S.; Kochi, A.; Choi, J.-S.; Ramamoorthy, A.; Ruotolo, B. T.; Lim, M. H. *Proc. Natl. Acad. Sci. U. S. A.* **2013**, *110*, 3743-3748.
24. Wang, H. K. *Expert Opin. Invest. Drugs* **2000**, *9*, 2103-2119.

25. Porat, Y.; Abramowitz, A.; Gazit, E. *Chem. Biol. Drug Des.* **2006**, *67*, 27-37.
26. Ono, K.; Yoshiike, Y.; Takashima, A.; Hasegawa, K.; Naiki, H.; Yamada, M. *J. Neurochem.* **2003**, *87*, 172-181.
27. Ong, K. C.; Khoo, H. E. *Gen. Pharmacol.* **1997**, *29*, 121-126.
28. Hirohata, M.; Hasegawa, K.; Tsutsumi-Yasuhara, S.; Ohhashi, Y.; Ookoshi, T.; Ono, K.; Yamada, M.; Naiki, H. *Biochemistry* **2007**, *46*, 1888-1899.
29. Hamaguchi, T.; Ono, K.; Murase, A.; Yamada, M. *Am. J. Pathol.* **2009**, *175*, 2557-2565.
30. Di Carlo, G.; Mascolo, N.; Izzo, A. A.; Capasso, F. *Life Sci.* **1999**, *65*, 337-353.
31. Carver, J. A.; Duggan, P. J.; Ecroyd, H.; Liu, Y.; Meyer, A. G.; Tranberg, C. E. *Bioorg. Med. Chem.* **2010**, *18*, 222-228.
32. Akaishi, T.; Morimoto, T.; Shibao, M.; Watanabe, S.; Sakai-Kato, K.; Utsunomiya-Tate, N.; Abe, K. *Neurosci. Lett.* **2008**, *444*, 280-285.
33. clinicaltrials.gov.
34. Mira, L.; Fernandez, M. T.; Santos, M.; Rocha, R.; Florencio, M. H.; Jennings, K. R. *Free Radical Res.* **2002**, *36*, 1199-1208.
35. Cao, S.; Jiang, X.; Chen, J. *J. Inorg. Biochem.* **2010**, *104*, 146-152.
36. Ehrnhoefer, D. E.; Bieschke, J.; Boeddrich, A.; Herbst, M.; Masino, L.; Lurz, R.; Engemann, S.; Pastore, A.; Wanker, E. E. *Nat. Struct. Mol. Biol.* **2008**, *15*, 558-566.
37. Bieschke, J.; Russ, J.; Friedrich, R. P.; Ehrnhoefer, D. E.; Wobst, H.; Neugebauer, K.; Wanker, E. E. *Proc. Natl. Acad. Sci. U. S. A.* **2010**, *107*, 7710-7715.
38. Ono, M.; Watanabe, R.; Kawashima, H.; Kawai, T.; Watanabe, H.; Haratake, M.; Saji, H.; Nakayama, M. *Bioorg. Med. Chem.* **2009**, *17*, 2069-2076.
39. Engelmann, M. D.; Hutcheson, R.; Cheng, I. F. *J. Agric. Food Chem.* **2005**, *53*, 2953-2960.
40. Martell, A. E.; Smith, R. M., *Critical Stability Constants*. Plenum Press: New York City, 1974; Vol. 3.
41. Malešev, D.; Kuntić, V. *J. Serb. Chem. Soc.* **2007**, *72*, 921-939.
42. Huang, C. Y. *Methods Enzymol.* **1982**, *87*, 509-525.
43. Mancino, A. M.; Hindo, S. S.; Kochi, A.; Lim, M. H. *Inorg. Chem.* **2009**, *48*, 9596-9598.
44. Hartley, D. M.; Walsh, D. M.; Ye, C. P.; Diehl, T.; Vasquez, S.; Vassilev, P. M.; Teplow, D. B.; Selkoe, D. J. *J. Neurosci.* **1999**, *19*, 8876-8884.
45. Klug, G. M. J. A.; Losic, D.; Subasinghe, S. S.; Aguilar, M. I.; Martin, L. L.; Small, D. H. *Eur. J. Biochem.* **2003**, *270*, 4282-4293.
46. Verdan, A. M.; Wang, H. C.; Garcia, C. R.; Henry, W. P.; Brumaghim, J. L. *J. Inorg. Biochem.* **2011**, *105*, 1314-1322.
47. Perron, N. R.; Wang, H. C.; Deguire, S. N.; Jenkins, M.; Lawson, M.; Brumaghim, J. L. *Dalton Trans.* **2010**, *39*, 9982-9987.
48. Perron, N. R.; Brumaghim, J. L. *Cell Biochem. Biophys.* **2009**, *53*, 75-100.
49. Smith, D. G.; Cappai, R.; Barnham, K. J. *Biochim. Biophys. Acta* **2007**, *1768*, 1976-1990.
50. Allsop, D.; Mayes, J.; Moore, S.; Masad, A.; Tabner, B. J. *Biochem. Soc. Trans.* **2008**, *36*, 1293-1298.

51. Wang, X.; Michaelis, E. K. *Front. Aging Neurosci.* **2010**, *2*, 12.
52. Palacios, H. H.; Yendluri, B. B.; Parvathaneni, K.; Shadlinski, V. B.; Obrenovich, M. E.; Leszek, J.; Gokhman, D.; Gasiorowski, K.; Bragin, V.; Aliev, G. *CNS Neurol. Disord.: Drug Targets* **2011**, *10*, 149-162.
53. Nakamura, T.; Cho, D. H.; Lipton, S. A. *Exp. Neurol.* **2012**, *238*, 12-21.
54. Faller, P.; Hureau, C. *Chem. Eur. J.* **2012**, *18*, 15910-15920.
55. Deraeve, C.; Boldron, C.; Maraval, A.; Mazarguil, H.; Gornitzka, H.; Vendier, L.; Pitie, M.; Meunier, B. *Chem. Eur. J.* **2008**, *14*, 682-696.
56. Himes, R. A.; Park, G. Y.; Siluvai, G. S.; Blackburn, N. J.; Karlin, K. D. *Angew. Chem. Int. Ed.* **2008**, *47*, 9084-9087.
57. Rice-Evans, C. A.; Miller, N. J.; Paganga, G. *Free Radical Biol. Med.* **1996**, *20*, 933-956.
58. Fernandez, M. T.; Mira, M. L.; Florêncio, M. H.; Jennings, K. R. *J. Inorg. Biochem.* **2002**, *92*, 105-111.
59. Masuoka, J.; Saltman, P. *J. Biol. Chem.* **1994**, *269*, 25557-25561.
60. Zhang, Y.; Akilesh, S.; Wilcox, D. E. *Inorg. Chem.* **2000**, *39*, 3057-3064.
61. Kagaya, N.; Kawase, M.; Maeda, H.; Tagawa, Y.; Nagashima, H.; Ohmori, H.; Yagi, K. *Biol. Pharm. Bull.* **2002**, *25*, 1156-1160.
62. Afanas'eva, I. B.; Ostrakhovitch, E. A.; Mikhal'chik, E. V.; Ibragimova, G. A.; Korkina, L. G. *Biochem. Pharmacol.* **2001**, *61*, 677-684.

Chapter 3: Insights into the Anti-Amyloidogenic Properties of the Green Tea Extract EGCG: Metal-Free *versus* Metal-Associated Aβ Species

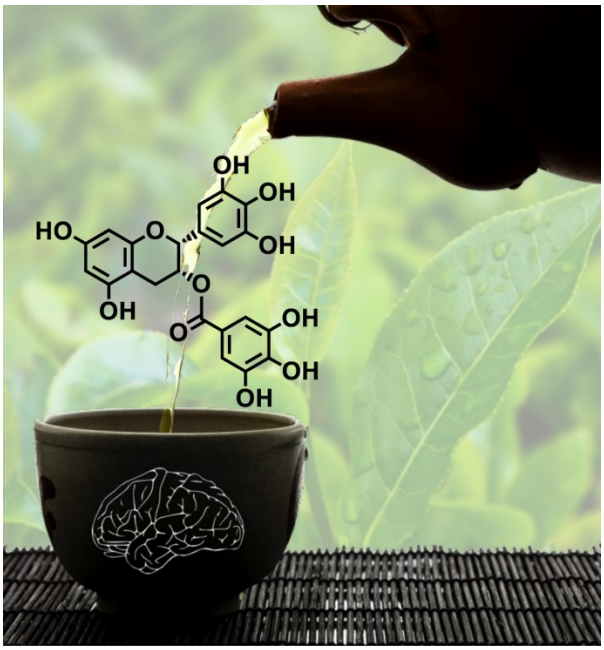

Image by Younwoo Nam and Alaina DeToma, courtesy of Thinkstock.

This chapter is based on previously published work (Hyung, S.-J.; DeToma, A. S.; Brender, J. R.; Lee, S.; Vivekanandan, S.; Kochi, A.; Choi, J.-S.; Ramamoorthy, A.; Ruotolo, B. T.; Lim, M. H. *Proc. Natl. Acad. Sci. U. S. A.* **2013**, *110*, 3743-3748.). We thank Professor Brandon Ruotolo and Dr. Suk-Joon Hyung for IM-MS experiments and simulations. We thank Professor Ayyalusamy Ramamoorthy, Dr. Jeffrey Brender, and Dr. Subramanian Vivekanandan for 2D NMR experiments with Aβ and Zn(II)–Aβ with EGCG. *In vitro* biochemical investigations and cell studies in this chapter were obtained in collaboration with Dr. Sanghyun Lee, Akiko Kochi, and Dr. Jung-Suk Choi.

3.1. Introduction

The brain of individuals suffering from Alzheimer's disease (AD) has protein aggregates composed of misfolded amyloid-β (Aβ) peptide. The Aβ peptides are produced endogenously through enzymatic cleavage of amyloid precursor protein. Aβ monomers can misfold and oligomerize into various intermediates prior to the formation and elongation of fibrils that exhibit a characteristic cross-β sheet structure.[1-5] The accumulation of aggregated Aβ species has been a key feature of the amyloid cascade hypothesis, which cites that these aggregates are possible causative agents in AD. In addition, transition metals, such as Cu and Zn, whose misregulation leads to aberrant neuronal function, have a suggested link to AD pathology.[1,3-9] Both *in vitro* and *in vivo* studies have provided evidence for the direct interactions of metal ions with Aβ and their presence within Aβ plaques, indicating the formation of metal-associated Aβ (metal–Aβ) species. These metal–Aβ species have been implicated in processes that could lead to neurotoxicity (*e.g.*, metal-induced Aβ aggregation and metal–Aβ-mediated reactive oxygen species (ROS) generation).[1,3-9] The involvement of metal–Aβ species in AD pathogenesis, however, has not been clearly elucidated. In order to advance our understanding of the potential neurotoxicity of metal-Aβ species, efforts to develop chemical tools capable of interacting directly with metal–Aβ species and modulating their reactivity *in vitro* and in biological systems are underway.[1,9-21] In particular, novel bifunctional compounds that contain elements for metal chelation and Aβ interaction have recently been prepared or identified *via* rational structure-based design strategies or systematic selection of natural products.

Naturally occurring flavonoids have been shown to interact with amyloidogenic peptides and arrest or redirect aggregation pathways.[22-29] These studies have mainly been conducted under metal-free conditions. For example, the green tea extract, (–)-epigallocatechin-3-gallate (EGCG; Figure 3.1) is known as an anti-oxidative and anti-inflammatory agent for numerous human diseases[30] and has exhibited anti-amyloidogenic reactivity with various disease-related peptides (*e.g.*, Aβ, α-synuclein, islet amyloid polypeptide, semen-derived enhancer of viral infection (SEVI)).[22-24,27,28,31-34] Nontoxic amorphous peptide species were observed upon incubation of α- synuclein

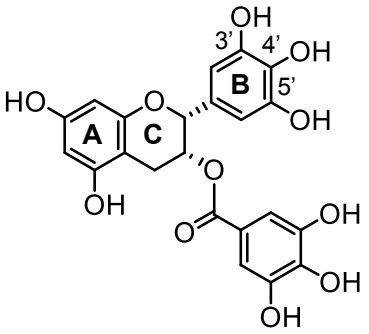

Figure 3.1. Structure of (−)-epigallocatechin-3-gallate [(2*R*,3*R*)-5,7-dihydroxy-2-(3,4,5-trihydroxyphenyl)-3,4-dihydro-2*H*-1-benzopyran-3-yl 3,4,5-trihydroxybenzoate] (EGCG). The letters A, B, and C identify the rings of the flavonoid core structure and numbers indicate positions of OH groups.

and metal-free Aβ with EGCG, presumably through the direct peptide–EGCG interactions that were proposed to alter the peptide assembly from the expected fibrillar structures in favor of an off-pathway intermediate.[23,24] EGCG has also been shown to restructure preformed metal-free Aβ aggregates into unstructured, stable, and nontoxic conformations.[24] These observations suggest a broad ability for EGCG to disrupt both early-stage and late-stage aggregation processes. Although EGCG is also able to chelate metal ions,[35,36] its influence on metal-bound Aβ structure and reactivity has not fully elucidated.[37]

Here, we present the ability of EGCG to modulate metal (Cu(II) or Zn(II))-induced Aβ aggregation to produce small, unstructured peptide aggregates to a different extent than metal-free Aβ aggregation, which may translate to reduced metal–Aβ toxicity in living cells. In order to rationalize the anti-amyloidogenic reactivity of EGCG at the molecular level, Aβ interaction properties in the absence and presence of metal ions were investigated using ion mobility-mass spectrometry (IM-MS)[38,39] and two-dimensional (2D) NMR spectroscopy. Our IM-MS and 2D NMR results were also supported by molecular dynamics simulations to create a comprehensive molecular-level mechanism of EGCG action and reactivity. The interaction of EGCG with metal-free Aβ monomers and dimers induced structurally compact peptide conformations that likely led to the generation of amorphous Aβ aggregates. In addition, our biophysical investigations for EGCG-treated metal–Aβ species imply the formation of ternary

complexes, which may explain the remarkable ability of this molecule to influence metal-induced Aβ aggregation over the metal-free case. Overall, these studies provide a clear structure-based mechanism for EGCG action toward both metal-free and metal-associated Aβ species and build a foundation for development and application of small molecules as chemical tools for elucidating AD pathogenesis.

3.2. Results and discussion

3.2.1. EGCG distinctly modulates Aβ aggregation induced by Cu(II) or Zn(II)

We investigated the ability of EGCG to inhibit the formation of metal-free or metal-associated $A\beta_{40}$ aggregates (inhibition experiment, Figures 3.2 and 3.3) or to disassemble preformed aggregated species with or without metal ions (disaggregation experiment, Figure 3.4) by gel electrophoresis with Western blotting using an anti-Aβ antibody (6E10), as well as by transmission electron microscopy (TEM). These methods were employed to visualize the changes in size distribution and morphology that are not accurately represented using other biological assays (*e.g.*, thioflavin-T (ThT) assay).[40,41]

As shown in Figures 3.2 and 3.3 (inhibition experiment), EGCG displayed an enhanced ability to generate and stabilize low molecular weight (MW) Aβ aggregates when metal ions such as Cu(II) and Zn(II) were present. In comparison, only a modest amount of low MW aggregates was detected at long incubation times in metal-free Aβ samples treated with EGCG (lane 2, Figure 3.2(a)). Aggregates with a distribution of sizes (MW ≤ 25 kDa or ≤ 32 kDa for EGCG-treated Cu(II)–Aβ or Zn(II)–Aβ species (lane 4 or 6)) were observed even after only a 2 or 4 h incubation of Cu(II)- or Zn(II)-containing Aβ solutions with EGCG and were mostly maintained following a 24 h incubation. There was a slight dependence on the EGCG concentration for Cu(II)-treated Aβ species at the 4 h time point, where smaller sizes of Aβ species (MW ≤ 25 kDa) could be produced even using substoichiometric equivalents of EGCG (*e.g.*, 1:4:4 EGCG:Cu(II):Aβ, Figure 3.3). TEM images showed that Aβ samples incubated with either Cu(II) or Zn(II) and EGCG resulted in dramatic inhibition of the fibril formation

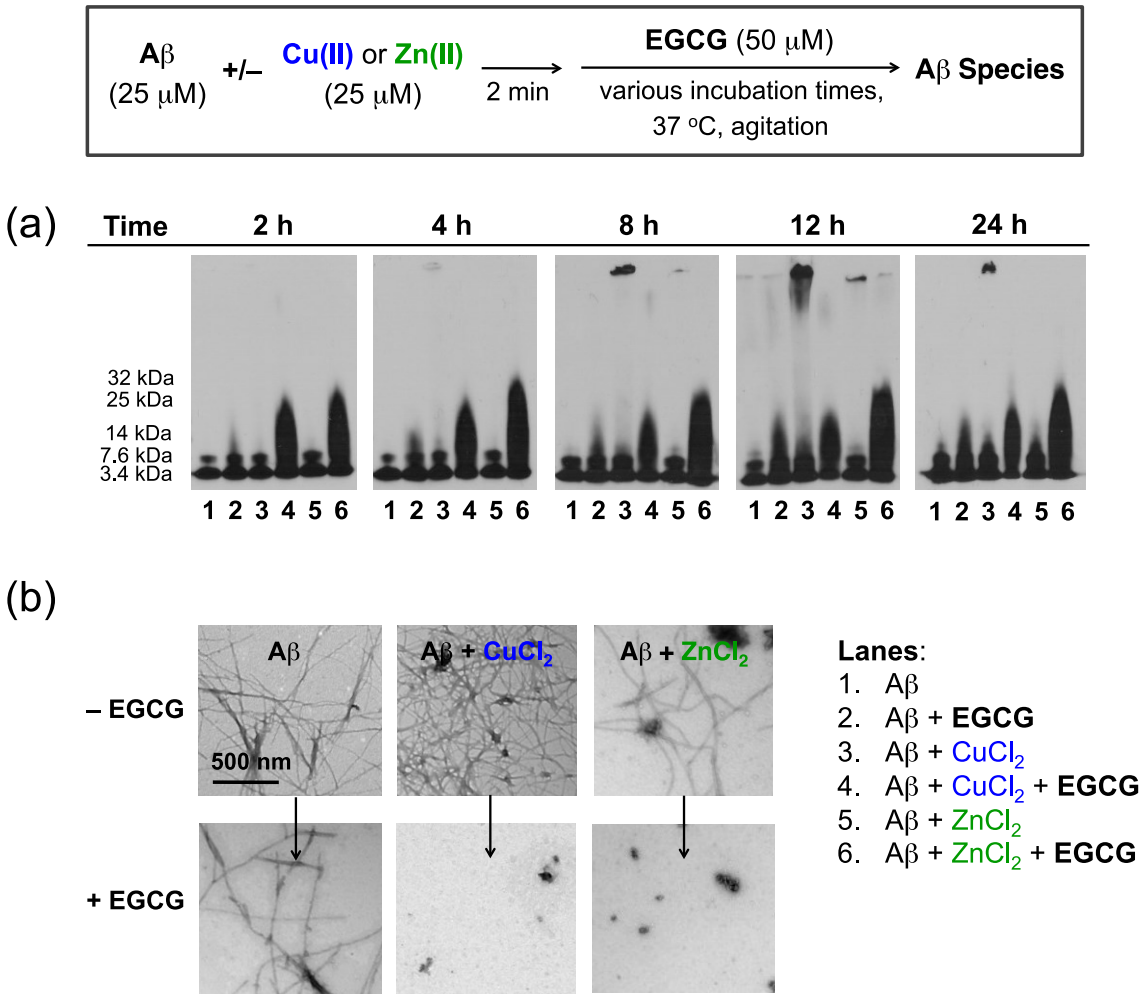

Figure 3.2. Assessment of the ability of EGCG to modulate metal-free and metal-associated $A\beta_{40}$ aggregation *in vitro*. (a) Aβ species (from the inhibition experiment) visualized by gel electrophoresis using immunoblotting with an anti-Aβ antibody (6E10). Inhibition experiment (Scheme, top): Aβ (25 μM) with or without $CuCl_2$ or $ZnCl_2$ (25 μM) were incubated with EGCG (50 μM) for 2, 4, 8, 12, or 24 h (20 μM HEPES, pH 6.6 or 7.4, 150 μM NaCl; 37 °C; constant agitation). (b) TEM images of the samples from (a) after 24 h incubation.

process compared to those treated only with metal ions (Figure 3.2(b)). In those systems, fibril growth was arrested and the aggregates were observed to be smaller in size. Furthermore, the unstructured shapes of the aggregates were distinct from the fibrillar forms found in the metal–Aβ samples without EGCG;[37] EGCG alone did not significantly change the morphology of metal-free Aβ species, which remained mostly long and fibrillar.

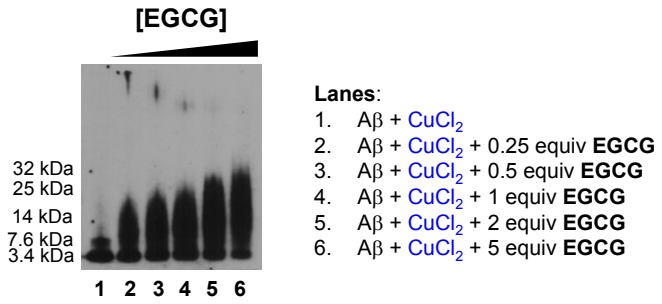

Figure 3.3. Concentration dependence of EGCG on modulation of Cu(II)-induced Aβ aggregation. Aβ samples were incubated with $CuCl_2$ and varying amounts of EGCG (0–125 μM) for 4 h and were visualized by gel electrophoresis and Western blotting (6E10). Experimental conditions: [Aβ] = 25 μM; [$CuCl_2$] = 25 μM; 20 μM HEPES, pH 6.6, 150 μM NaCl; 37 °C; constant agitation; final concentration of DMSO (1% v/v).

To investigate the effect of EGCG on transformation of aggregated Aβ forms (disaggregation experiment, Figure 3.4), the compound was incubated with preformed, metal-free or metal-treated $A\beta_{40}$ aggregates for various time periods and analyzed by Western blotting and TEM. From these results, differences in aggregate distribution were detected for metal–Aβ samples compared to metal-free Aβ samples (Figure 3.4(a)). The results for Cu(II)– or Zn(II)–Aβ indicated that even for short time periods (*i.e.*, 2 or 4 h), a varied amount of low MW (≤ 32 kDa) Aβ species was present. Cu(II)–Aβ aggregates treated with EGCG showed progressively weakening intensities in the Western blot upon longer incubation, while Zn(II)–Aβ aggregates treated with EGCG maintained a fairly constant intensity as time progressed. TEM analysis revealed some shorter fibrillar segments for EGCG-treated Cu(II)–Aβ, while the EGCG-treated Zn(II)–Aβ samples mainly produced amorphous species (Figure 3.4(b)). Metal-free Aβ species incubated with EGCG partially retained fibrillar morphology, but some species were smaller in size than those observed in EGCG-untreated samples. Taken together, our results indicate that EGCG could discriminate between metal-free and metal-associated Aβ species driving the formation of low MW aggregates at the expense of larger ones, demonstrating that the anti-amyloidogenic behavior of EGCG is distinctive toward metal–Aβ species.

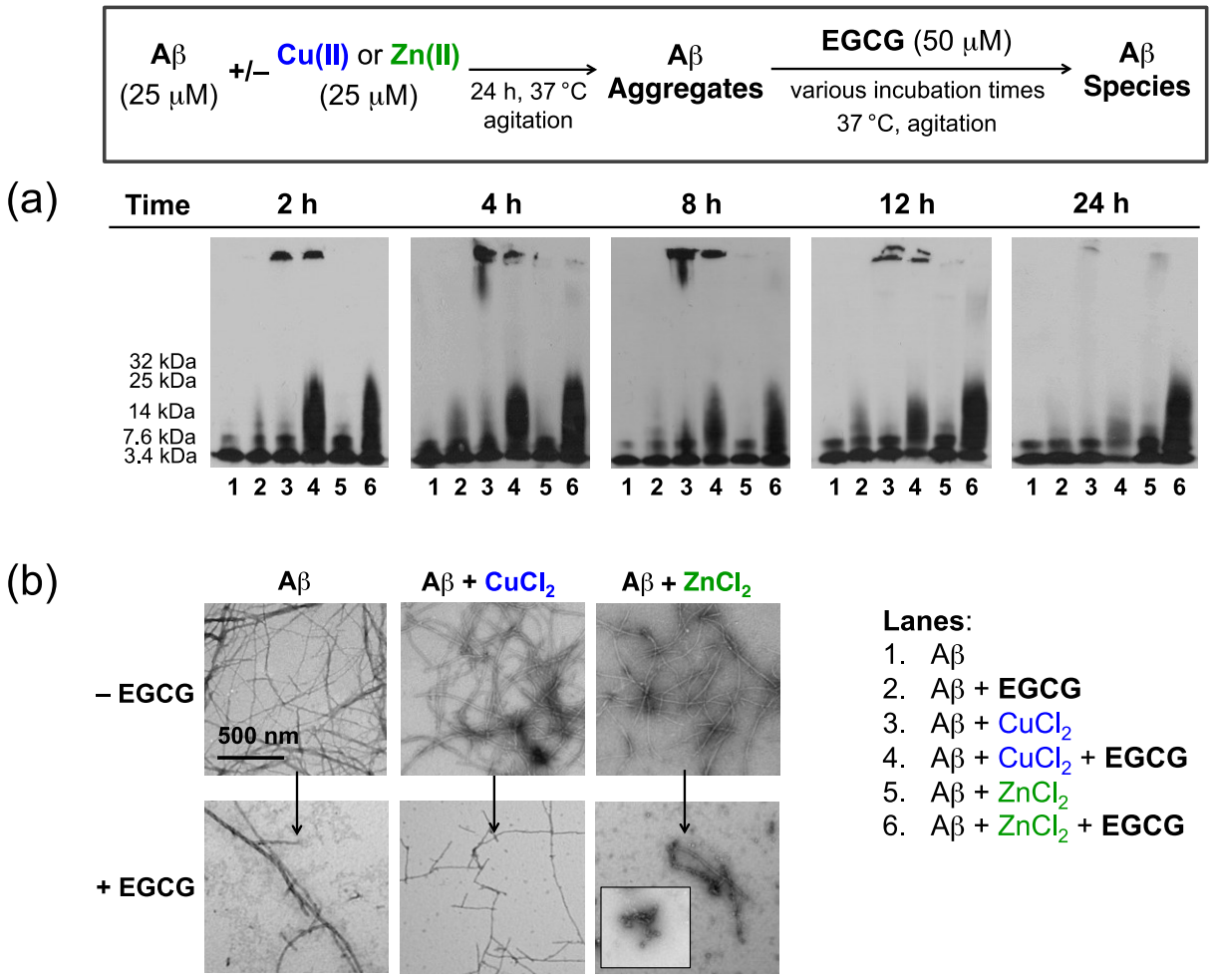

Figure 3.4. Disaggregation of preformed metal-free and metal-associated Aβ aggregates by EGCG. (a) Samples from the disaggregation experiment were analyzed by gel electrophoresis followed by immunoblotting with an anti-Aβ antibody (6E10) (Scheme, top). Aβ (25 μM) and/or $CuCl_2$ or $ZnCl_2$ (25 μM) were incubated for 24 h to produce Aβ aggregates. Afterward, EGCG (50 μM) was added to the preformed metal-free and metal-associated Aβ aggregates followed by incubation for 2, 4, 8, 12, or 24 h (20 μM HEPES, pH 6.6 or 7.4, 150 μM NaCl; 37 °C; constant agitation) and analysis by gel electrophoresis. (b) TEM images of the 24 h incubated samples from (a).

3.2.2. EGCG diminishes metal-free and metal–Aβ toxicity in living cells

Previous studies have suggested that EGCG is able to alleviate toxicity of metal-free Aβ species in living cells;[23,24] however, a comparison of its influence on the toxicity of both metal-free and metal-Aβ species has not been reported. Murine Neuro-2a (N2a) neuroblastoma cells were used to probe the toxicity of EGCG, metal chloride salts (*i.e.*, $CuCl_2$ and $ZnCl_2$), and/or $A\beta_{40}$ for 24 h (Figure 3.5). It was determined that EGCG (10 or

20 μM) with and without metal ions (10 μM) was relatively nontoxic to the living cells. In addition, the toxicity presented with both metal-free and metal-treated Aβ was negligible upon incubation with EGCG. Overall, these cell studies suggest that EGCG may mitigate the effect of metal-free or metal-Aβ-induced processes in complex, heterogeneous environments, which may be related to EGCG-mediated alteration of metal-free or metal–Aβ conformations. [23,24,27,28,37]

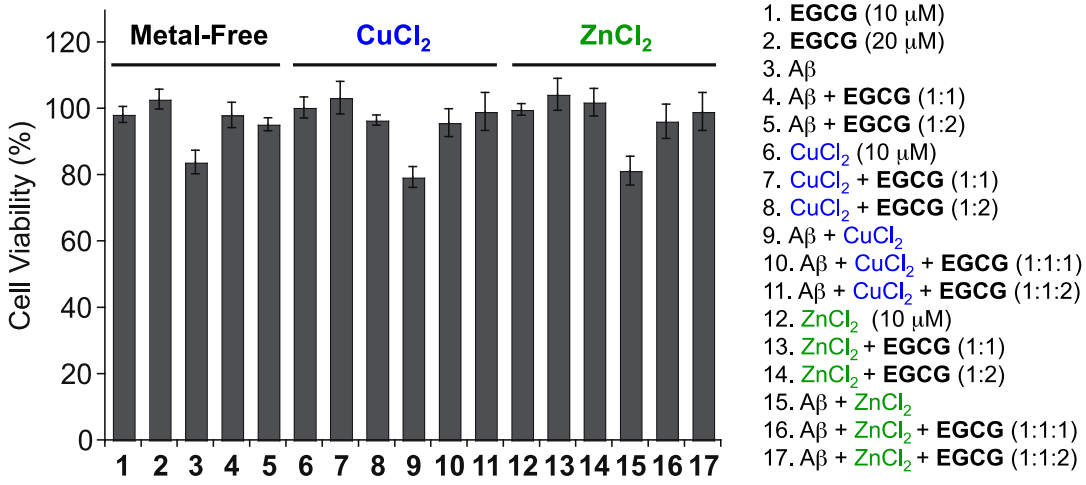

Figure 3.5. Effect of EGCG on $A\beta_{40}$ or metal–$A\beta_{40}$ species in living cells. Cell viability measurements in the presence of metal-free and metal-treated Aβ species with or without EGCG in murine Neuro-2a (N2a) neuroblastoma cells. Cells treated with Aβ, metal ions, and/or EGCG were incubated for 24 h at 37 °C. Cell viability was measured using the MTT assay and viability was calculated relative to cells containing equivalent amounts of DMSO (0-1%, v/v). Error bars represent the standard error from three independent experiments.

3.2.3. EGCG directly binds to Aβ peptide and causes conformational changes

To characterize the interactions between EGCG and $A\beta_{40}$, we first recorded 2D $^{1}H/^{15}N$ SOFAST-HMQC NMR spectra on samples with different molar ratios of EGCG in 25 mM HEPES, pH 7.3, with 25 mM NaCl at 4 °C (Figure 3.6(a); 2D band-selective optimized flip-angle short transient (SOFAST)-heteronuclear multiple quantum correlation (HMQC)). Under these conditions, the addition of EGCG to freshly dissolved $A\beta_{40}$ (76 μM) caused partial precipitation in the sample even with substoichiometric concentrations of EGCG, suggesting EGCG could result in the production of aggregates from Aβ monomers. This precipitation was reflected in the SOFAST-HMQC spectra by a

near-uniform decrease in intensity of all resonances of monomeric Aβ, most likely due to the depletion of Aβ monomers and enrichment of both soluble and insoluble higher-order oligomers of Aβ (Figure 3.6(a)).

To gain more insight into soluble oligomeric species invisible to NMR, IM-MS experiments were performed on samples with varying molar ratios of EGCG under conditions designed to probe their solution stoichiometry and structure.[38,39,42] IM-MS has been emerging as a useful technique to uncover protein structure of soluble species in the gas phase generated from heterogeneous solutions.[38,39,43] The coupling of IM and MS techniques allows samples to be separated not only by the mass/charge (*m/z*) ratio, but also according to their size/conformation.[38,43] This is useful especially for uncovering unique peptide conformations and overall topology even when *m/z* is identical. IM-MS uses soft ionization methods like electrospray ionization (ESI) to generate protein complex ions in the gas phase that are separated by IM. The mobility of the ions is quantified by their drift time, which depends on several physical features (*e.g.*, mass, charge, and collision cross section (CCS or Ω) area).[43] More compact peptide ions, having a smaller CCS, will have higher mobility and therefore lower drift times; conversely, less compact ions will require a longer time to travel through the IM. Mass separation and ion detection are the final steps before generating a multi-dimensional contour plot representing the drift time/CCS, mass/charge (*m/z*), and intensity.[38,43] IM-MS is often nicely complemented by additional biophysical methods, including molecular dynamics simulations and NMR, to validate the gas phase structural information that was obtained. The use of this technique to investigate the Aβ aggregation equilibrium has been well established,[39,43] and current investigations on amyloid aggregation mediated by small molecules will be aided by this method.

In the absence of EGCG, Aβ (10 μM) existed primarily as a mixture of monomers and dimers as found by IM-MS (Figure 3.6(b)). The mass spectrum of Aβ contained peaks for the 4^+ and 3^+ states at 1083 and 1444 *m/z*, respectively. The formation of complexes between Aβ and EGCG was apparent from a solution containing Aβ (10 μM) and EGCG (20 μM) (Figure 3.6(c)). At this molar ratio, the signal corresponding to a complex composed of 1:1 stoichiometry was dominant in this dataset, as shown by the Aβ–EGCG complex in the 4^+ and 3^+ states at *m/z* = 1198 and 1597, respectively.

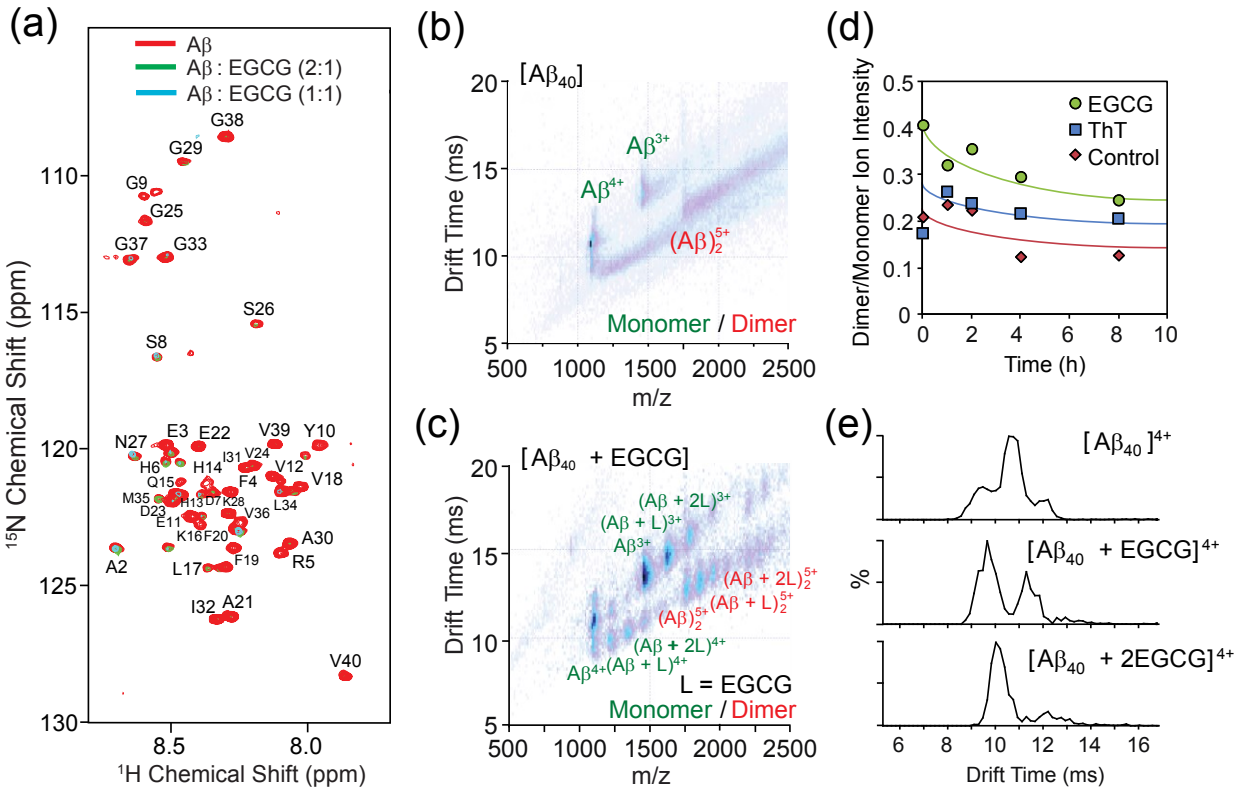

Figure 3.6. Interaction of EGCG with Aβ40. (a) Titration of Aβ with EGCG monitored by 2D $^{1}H/^{15}N$ SOFAST-HMQC NMR spectroscopy. Substoichiometric amounts of EGCG caused a large uniform drop in intensity. (b) A plot of ion mobility (IM) drift time *versus* *m/z* for metal-free Aβ40 (10 μM) showed monomeric and dimeric forms of the peptide under conditions used for our experiments (100 mM ammonium acetate buffer, pH 7.4). (c) Similar IM-MS data as in (b) for samples containing EGCG added in solution (20 μM) revealed multiple binding modes for EGCG with the monomeric and dimeric form of Aβ. (d) MS-based time course experiments revealed that EGCG (green circles) could solubilize larger amounts of the dimeric forms of the peptide in solution when compared to ThT (blue squares) and only peptide (red diamonds) control data. (e) Close inspection of the IM drift time profiles for the 4^{+} state of the peptide indicated at least three resolved conformational families and that EGCG binding could produce a larger population of compact Aβ40 peptides (CCS: 796, 716, and 633 $Å^2$, top to bottom, Table 3.1).

Additional binding modes were also observed with ratios of 1:2, 2:1, and 2:2 Aβ/EGCG. Aβ dimers and their EGCG complexes were resolved in the 5^{+} state at *m/z* 1733, 1824, and 1916, respectively. The relative abundance of Aβ dimers was significantly increased in samples incubated with EGCG compared to Aβ samples without any additional molecules or with ThT (a fluorescent probe that binds to Aβ fibrils,

but not monomers or small oligomers)[44] (Figure 3.6(d)). This finding suggests that EGCG could facilitate the generation of soluble higher-order Aβ structures in solution, which was also supported through gel analysis of the samples prepared under conditions similar to the IM-MS experiment (Figure 3.7). As shown in Figure 3.6(d), the gradual decrease of soluble dimeric Aβ species over monomeric Aβ species in the absence of EGCG or ThT was observed by IM-MS across time likely as a result of aggregation.[45] Analysis of samples over 8 h, which was within the typical lag phase for Aβ of 8 to 18 h,[46] was found to be complicated due to the formation of aggregates similar to those seen in the higher concentration NMR sample that were likely unstable under our electrospray ionization conditions. Throughout this time interval, however, Aβ samples containing EGCG showed consistently higher levels of dimeric species confirming that EGCG may promote and stabilize the formation of Aβ dimers.

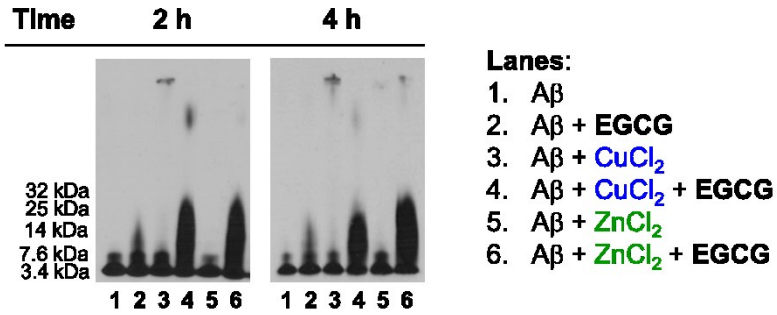

Figure 3.7. Analysis of the Aβ species resulting from the inhibition experiment (Figure 3.2) in the same buffer used for IM-MS (Figures 3.6 and 3.13) by gel electrophoresis using immunoblotting (6E10). Aβ (25 μM) with or without $CuCl_2$ or $ZnCl_2$ (25 μM) was incubated with EGCG (50 μM) for 2 or 4 h (100 mM ammonium acetate, pH 6.6 or 7.4, 37 °C, constant agitation).

IM-MS data also revealed the basis for a molecular level explanation for the observed preference of EGCG for Aβ dimers over monomers (Figure 3.6(c)). For $A\beta_{40}$ incubated with excess EGCG, IM arrival time distributions (ATDs) showed at least three resolved structural features, similar to previous data recorded for $A\beta_{42}^{3-}$,[47] allowing us to conformationally resolve distinct binding states. Binding of EGCG to Aβ shifted this distribution dramatically toward the most compact state (CCS, centered at *ca*. 654 $Å^2$; Figure 3.6(e) and Table 3.1); additional binding of EGCG shifted this distribution even further toward more compact monomer conformations. Similarly, the soluble dimer

bound to EGCG existed exclusively in a compact configuration (Figure 3.6(c)). The ion intensity values from mass spectra can be converted to EGCG dissociation constants (K_d) given certain assumptions and careful experimental protocols (Table 3.2).[48] These measurements revealed that the affinity of EGCG for the dimeric forms of Aβ was higher than that for monomers [K_d values of 139 μM for 2:1 and 43.5 μM for 2:2 (Aβ dimer/EGCG) compared to of 331 μM for the 1:1 and 47.1 μM for 1:2 (Aβ monomer/EGCG)]. These dissociation constants are in the range of previously reported K_d values, which varied based on temperature, concentration, and pH.[49] The results imply that the collapse of Aβ monomer and dimer into more compact conformations following initial EGCG binding could facilitate additional EGCG binding. In addition, Aβ dimers may have greater affinity for EGCG compared to monomers due to their preformed compact configuration, further suggesting that EGCG may bind to a region of the peptide that does not participate in dimer formation. Thus, IM-MS and NMR results indicate that EGCG interacts directly with Aβ species, leading to a structural transformation to more compact form.

Table 3.1. Collision cross-section (CCS) of 3^+ and 4^+ states of $A\beta_{40}$ monomer and related species.

	Conformation		
	1	**2**	**3**
$A\beta_{40(m)}^{4+}$	633.3 ± 1.2	715.6 ± 2.5	795.8 ± 8.3
$[A\beta_{40(m)} + Cu]^{4+}$	621.3 ± 2.6	745.6 ± 2.7	826.7 ± 9.5
$[A\beta_{40(m)} + 2Cu]^{4+}$	602.8 ± 1.8	744.5 ± 5.1	843.1 ± 13.2
$[A\beta_{40(m)} + EGCG]^{4+}$	653.7 ± 7.0	785.5 ± 11.7	
$[A\beta_{40(m)} + EGCG + Cu]^{4+}$	645.1 ± 8.9	795.3 ± 7.1	
$[A\beta_{40(m)} + EGCG + 2Cu]^{4+}$	641.0 ± 12.4	807.5 ± 6.0	
$[A\beta_{40(m)} + 2EGCG]^{4+}$	689.5 ± 6.5	833.7 ± 1.3	
$A\beta_{40(m)}^{3+}$	695.8 ± 8.0		
$[A\beta_{40(m)} + Cu]^{3+}$	695.9 ± 6.2		
$[A\beta_{40(m)} + 2Cu]^{3+}$	698.3 ± 10.4		
$[A\beta_{40(m)} + EGCG]^{3+}$	757.0 ± 8.0		
$[A\beta_{40(m)} + EGCG + Cu]^{3+}$	757.3 ± 5.9		
$[A\beta_{40(m)} + EGCG + 2Cu]^{3+}$	761.4 ± 3.1		
$[A\beta_{40(m)} + 2EGCG]^{3+}$	827.8 ± 12.1		

All values are reported in $Å^2$ and the errors are reported to one standard deviation.

Table 3.2. Dissociation constants of Aβ40–EGCG complexes.

		Dissociation Constant (μM)
Monomer	K_{d1}	330.5 ± 327.0
	K_{d2}	47.1 ± 27.9
Dimer	K_{d1}	138.6 ± 102.6
	K_{d2}	43.5 ± 20.7

In order to calculate the dissociation constants of EGCG (L) with Aβ40 monomer or dimer (P), we assumed that the relative intensity of the ions corresponds to the equilibrium concentration of the monomer/dimer complexes formed in solution. The binding and dissociation event is also assumed occur in a sequential manner where the dissociation constant corresponds to the equations below:

$$K_{d1} = \frac{[P]_{eq}[L]_{eq}}{[P{\cdot}L]_{eq}} \qquad [P \cdot L]_{eq} = \frac{R_1([P]_o - [P_D]_{eq})}{1+R_1} \qquad R_1 = \frac{I(P{\cdot}L^{n+})}{I(P^{n+})}$$

$$K_{d2} = \frac{[P{\cdot}L]_{eq}[L]_{eq}}{[P{\cdot}L_2]_{eq}} \qquad [P \cdot L_2]_{eq} = \frac{R_2([P]_o - [P_D]_{eq} - [P{\cdot}L]_{eq})}{1+R_2} \qquad R_2 = \frac{I(P{\cdot}L_2{}^{n+})}{I(P^{n+})}$$

3.2.4. Molecular modeling studies present that EGCG could interact directly with Aβ monomer

To aid the interpretation of the IM-MS and NMR data, peptide-ligand docking studies were conducted against ten structures of Aβ selected from a previously determined NMR structure of Aβ40 (PDB 2LFM)[50] (Figure 3.8). According to the docking results, EGCG had a tendency to associate with Aβ primarily near the hydrophilic *N*-terminus and the α-helical region spanning residues H13–D23.[50] This binding pocket is situated near the H6, H13, and H14 residues that may be involved in metal binding to Aβ, as well as to residues near the hydrophobic self-recognition sequence, suggested to be linked to Aβ aggregation pathways.[1,3,5,9,51-53] A combination of both polar (*e.g.*, hydrogen bonding, electrostatic interaction) and hydrophobic interactions was likely responsible for the close proximity of EGCG to both hydrophilic and hydrophobic portions of Aβ in solution. Furthermore, it appeared that the flexibility of EGCG was important in allowing the molecule to optimize several binding configurations with peptide and may be a contributing factor in its anti-amyloidogenic properties.[49]

Molecular dynamics (MD) simulations based on the ten docked structures of Aβ40–EGCG complex determined above (Figure 3.8) were carried out to identify the

conformers observed in the experimental IM-MS data and explore structural elements involved in the Aβ–EGCG interaction (Figures 3.9, 3.10, and 3.11). Specifically, the docked structures were allowed to anneal by exposing the positively charged, desolvated Aβ–EGCG complex to a series of rapid heating and cooling cycles. For each starting structure, 100 structures were sampled at 300 K and their force field energy was recorded. In addition, the orientationally averaged CCS values were determined for these model structures using the trajectory method.[54,55] The plot of CCS against force field energy showed the structures determined for Aβ–EGCG in the gas-phase possess a diverse range of sizes, with CCS values ranging from 600 to 900 $Å^2$ (Figures 3.9(a) and 3.10). While the structures did not cluster either to a narrow range of CCS or energy, we note that the docked conformation with the lowest binding energy led to structures with relatively smaller CCS values when compared to those starting structures having less favorable binding energies (Figure 3.11). Interestingly, Aβ simulated without EGCG occupied an even wider range of conformations than the Aβ–EGCG complexes as revealed by the broader distribution of CCS values (Figure 3.9(b)). In all cases, the experimentally determined values and trends were in good agreement with the MD results shown.

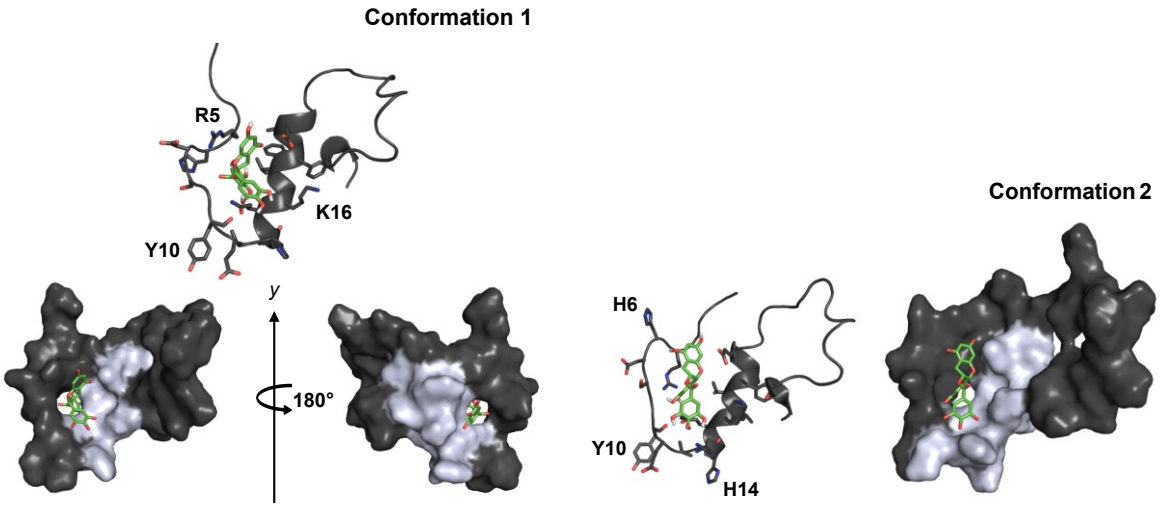

Conformation 3-a

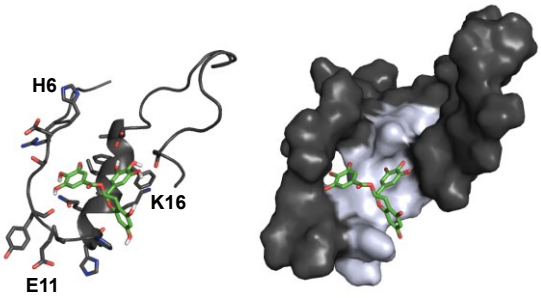

Conformation 3-b

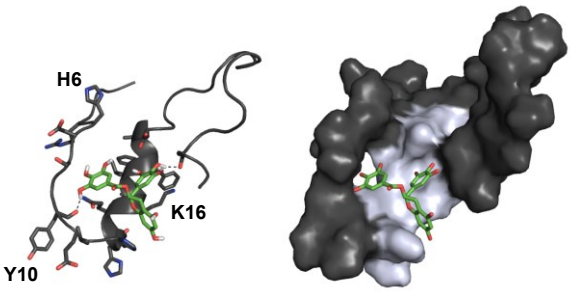

Conformation 4

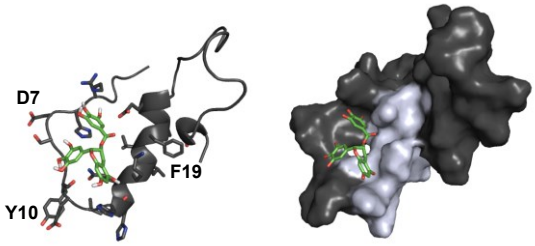

Conformation 5

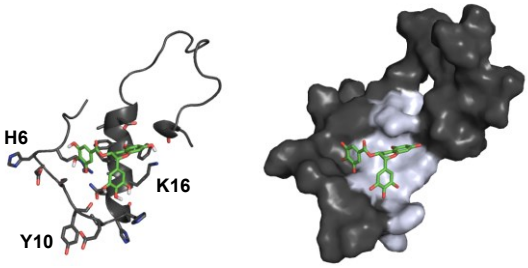

Conformation 6

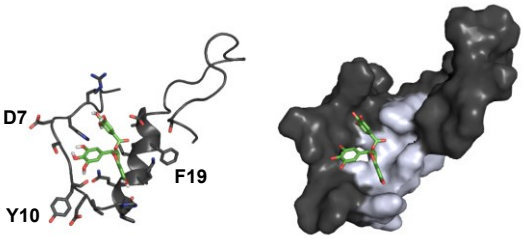

Conformation 7

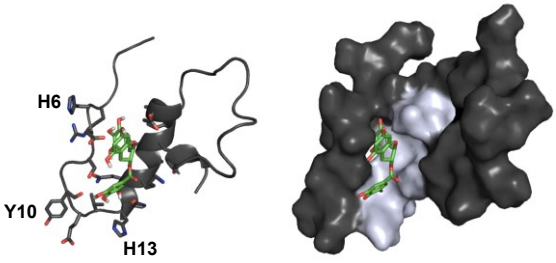

Conformation 8

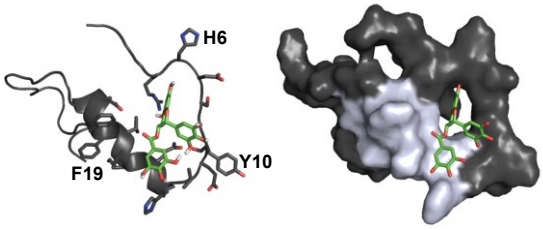

Conformation 9

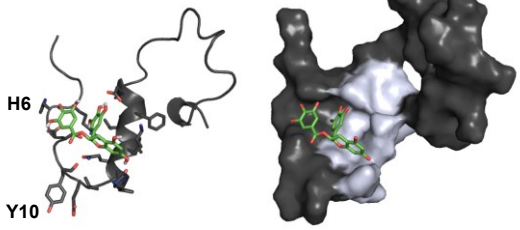

Conformation 10

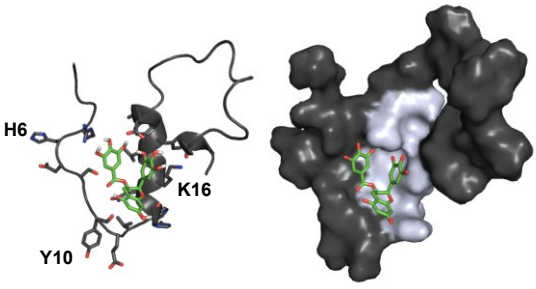

Conformation	Energy (kcal/mol)
1	−7.8
2	−7.5
3-a	−7.4
3-b	−7.3
4	−7.3
5	−7.0
6	−7.0
7	−6.8
8	−6.7
9	−6.3
10	−6.3

Figure 3.8. Docking studies of EGCG with Aβ40 monomer (PDB 2LFM) by AutoDock Vina. Cartoon (left) and surface (right) representations of top poses of EGCG with conformations (1-10) of Aβ are shown. Possible hydrogen bonding contacts are indicated with a dashed line (1.9-2.5 Å) and the α-helical region of the peptide is highlighted in gray for the surface images of Aβ. Binding energies predicted for EGCG with Aβ40 monomer are summarized in the table. Hydrogen atoms in the peptide are omitted for clarity.

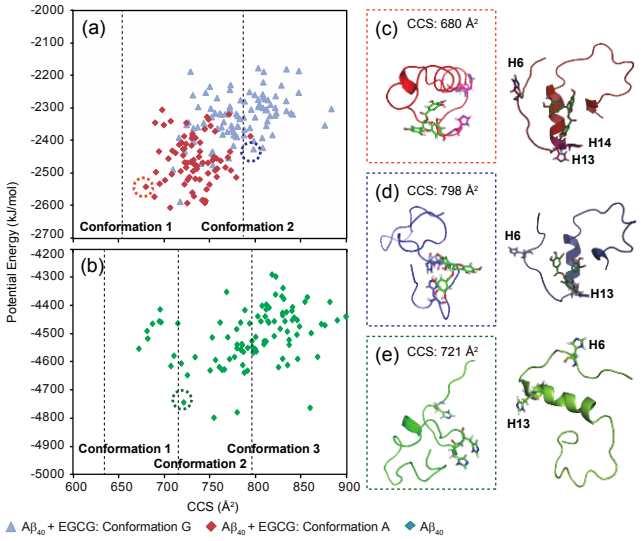

Figure 3.9. Molecular modeling of EGCG-bound Aβ40. (a) A plot of collision cross-section (CCS) against the potential energy of Aβ40–EGCG complexes generated by molecular dynamics simulation. Two binding states of the Aβ40–EGCG complex (conformations 1 and 10) visualized by docking studies (Figure 3.8) were subjected to a simulated annealing run, and 100 snapshots were sampled from the trajectory. (b) The corresponding run using the Aβ40 monomer structure is shown (green diamonds). The values of CCS of the discrete conformations observed by IM-MS are marked as dotted lines. A representative gas-phase structure from the molecular dynamics simulation (left) with the corresponding starting structure (right) are shown for the Aβ40–EGCG complex with relatively (c) low and (d) high potential energy, and (e) the Aβ40 monomer (PDB 2LFM).

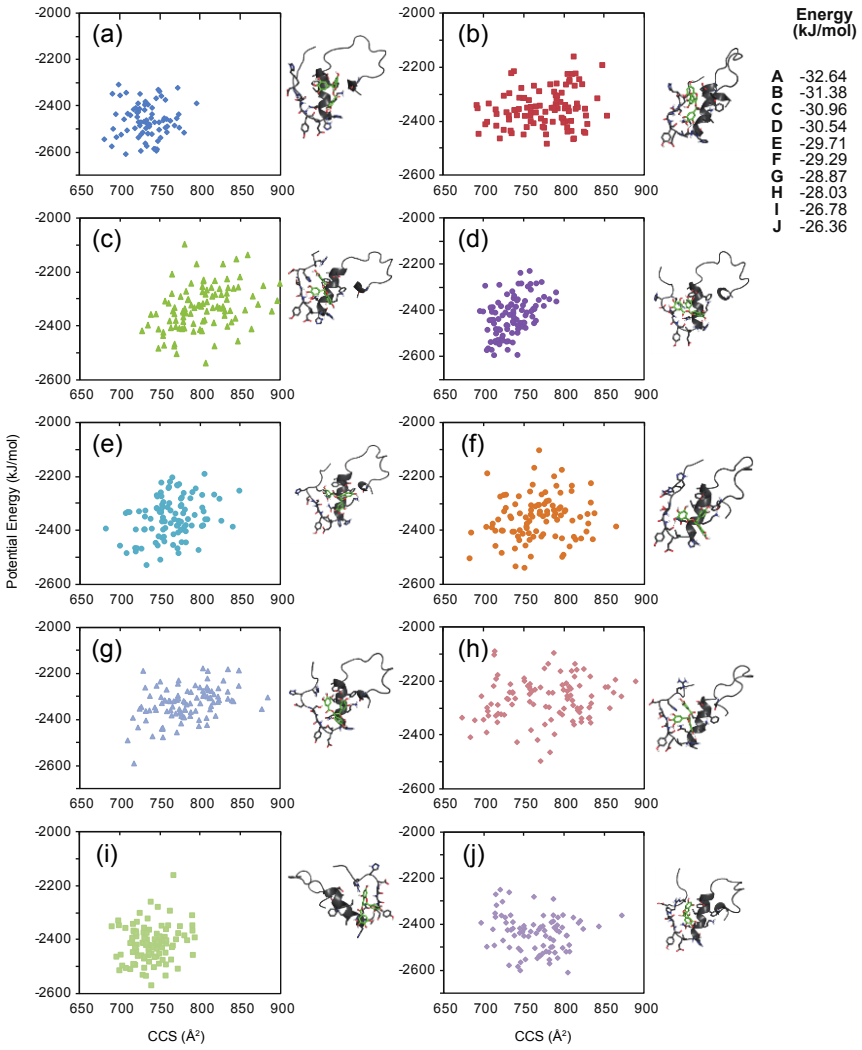

Figure 3.10. Molecular modeling of EGCG-bound Aβ_{40} based on docking structures (Figure 3.8). Ten conformation snapshots taken from molecular modeling of EGCG with the Aβ_{40} monomer (PDB 2LFM) from Figure 3.8 were chosen for molecular dynamics simulation. The 4^+ states of EGCG docked with Aβ_{40} monomer were subjected to simulated annealing cycle *in vacuo* for 20 ns and 100 structures were sampled at 300 K. (a-j) A plot of CCS against the potential energy. The corresponding energies (kJ/mol) are summarized in the list (top, right).

For those low-energy conformations whose CCS was close to the experimentally determined value of the compact structural feature of Aβ–EGCG complex, EGCG was slightly displaced from the residues considered to be associated with metal binding (H6, H13, and H14; Figure 3.9(c)).[1,3,5,9,51-53] By contrast, a select structure corresponding to a

more extended conformation showed that EGCG was in proximity to those residues in similarly to the docked pose (Figure 3.9(d)). Gas-phase MD simulations led to significant perturbations in peptide secondary structure, but retained a helical motif region both in the absence and presence of EGCG (Figure 3.9(c-e)). In all cases, the most favorable docked structures depicted in Figure 3.9 provided the starting structures that generated the best-fit gas-phase structures for the IM-MS data. Moreover, the magnitude of the compaction observed in our IM-MS experiments was reproduced computationally in our MD simulations, supporting the experimentally determined interaction of EGCG with Aβ.

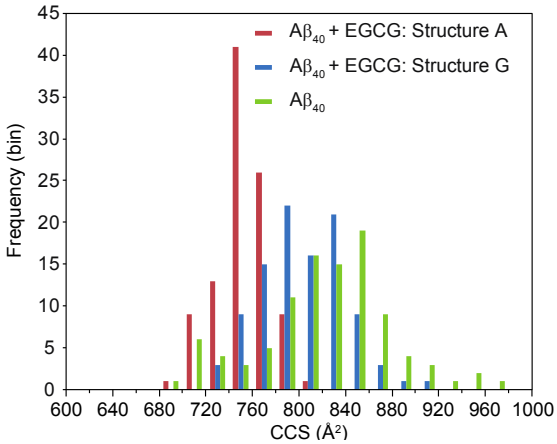

Figure 3.11. Histogram of the frequency of the structures with the corresponding CCS. The distribution of CCS across the trajectory run of 100 structures obtained from MD simulation is represented by this histogram. Color code: Red, low binding energy Aβ40–EGCG; blue, high binding energy Aβ40–EGCG; green, Aβ40. The histogram shows that structures generated from both complexes are relatively compact compared to that of EGCG-untreated Aβ40.

3.2.5. Metal binding of EGCG occurs in both the absence and presence of Aβ

In the framework of EGCG, OH groups found on the B ring and within the gallic acid moiety (Figure 3.1) could potentially be involved in Cu(II) and Zn(II) chelation.[35,36] In a buffered aqueous solution (pH 7.4), the UV-Vis absorption spectrum of EGCG (Figure 3.12(a)) showed features *ca.* 275 nm and 320 nm, consistent with previous reports.[36] The addition of 0.5 or 1 equiv of $CuCl_2$ enhanced the absorption around 320. Based on previous spectroscopic studies of Cu(II) with EGCG, it is possible that the UV-Vis spectra reflect an assortment of complexes.[35]

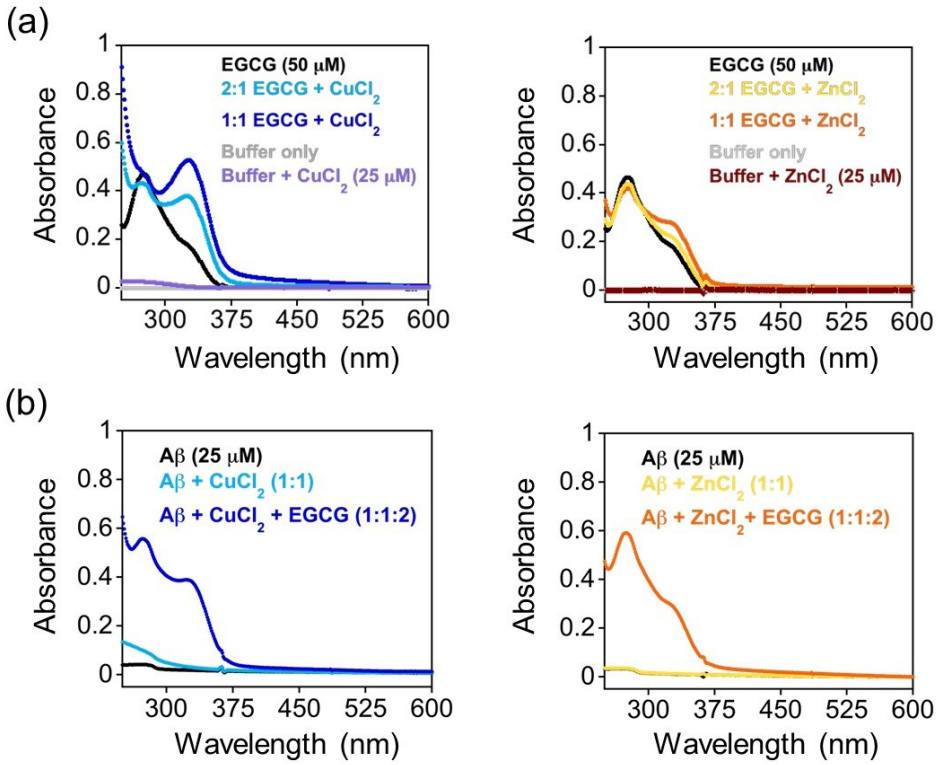

Figure 3.12. Cu(II) and Zn(II) binding of EGCG determined by UV-Vis. (a) The spectra were obtained upon 30 min incubation of 0.5 or 1 equiv of $CuCl_2$ (left) or $ZnCl_2$ (right) to EGCG (50 μM, black). The spectra of the buffered solutions were also acquired in the absence (gray) and presence of $CuCl_2$ (25 μM, left, purple) or $ZnCl_2$ (25 μM, right, brown) without EGCG. (b) The spectra were recorded from the samples containing $A\beta_{40}$ (25 μM), one equivalent of $CuCl_2$ (left) or $ZnCl_2$ (right) (2 min incubation), and/or EGCG (50 μM, 30 min incubation) at room temperature. All spectra were acquired in a buffered solution containing 20 mM HEPES, pH 7.4, 150 mM NaCl at room temperature.

Treatment of EGCG with 0.5 or 1 equiv of $ZnCl_2$ also caused an optical change, which confirmed Zn(II) binding to EGCG as well. Metal binding of EGCG in the presence of Aβ species was also investigated by UV-Vis (Figure 3.12(b)). Optical bands from the samples containing Aβ, Cu(II) or Zn(II), and EGCG modestly resembled those from the samples at the peptide-free conditions, indicating the possibility that EGCG has an appropriate binding affinity for Cu(II) and/or Zn(II) to sufficiently compete with Aβ for the metal ions. This observation could indicate a possibility for ternary complex formation among Aβ, metal ions, and EGCG (*vide infra*), which could be related to the previously discussed ability of EGCG to modulate *in vitro* metal–Aβ aggregation.

3.2.6. EGCG forms ternary complexes with metal-treated Aβ

To elucidate interactions of $A\beta_{40}$, EGCG, and Cu(II) or Zn(II), IM-MS and 2D NMR investigations were performed (Figure 3.13). Mass spectra showed peaks corresponding to Cu(II)–Aβ species in 1:1 and 1:2 stoichiometries, and both types of Cu(II)–Aβ complexes bound to either 1 or 2 equiv of EGCG (Figure 3.13(a); [Aβ] = 10 μM; [Cu(II)] = 20 μM).[56] IM data recorded for the monomeric Aβ complexes showed that Cu(II) binding had a similar influence on $A\beta_{40}^{4+}$ as that observed for Aβ–EGCG complexes (Figure 3.6). As presented in Figure 3.13(c), Cu(II) binding could cause the peptide to favor the most compact of the three conformational families observed in apo-Aβ datasets, and such structural features became more pronounced in IM arrival time distribution (ATD) profiles upon additional Cu(II) binding. Likewise, IM ATDs acquired for ternary complexes, involving EGCG, Cu(II), and Aβ, exhibited that the relative abundance of compact structural conformations was augmented for higher stoichiometry Cu(II) to Aβ–EGCG complexes (Figure 3.13(d)). The structural compaction of Cu(II)–Aβ even with EGCG suggests that Cu(II) could interact with Aβ in a non-cooperative manner.

Under the same conditions as the experiments of Cu(II)–Aβ above, IM-MS analysis of Zn(II) with $A\beta_{40}$ showed weaker association, even in the presence of excess Zn(II) (Figure 3.14). Thus, to understand the interaction of EGCG with Zn(II)-treated $A\beta_{40}$ species, 2D SOFAST-HMQC NMR was employed. The addition of $ZnCl_2$ to $A\beta_{40}$ at a 1:1 molar ratio broadened and shifted resonances for the region around H6, H13, and H14, previously identified as the primary Zn(II) binding site in the peptide (Figure 3.13(e-g)).[1,3,5,9,51-53] The *C*-terminal region of the peptide (L17-V40) was mostly unaffected, except for the K28 and G29 resonances which were significantly broadened or shifted, respectively, upon treatment with Zn(II). The reasons for changes in this region of the peptide are not immediately clear; however, the *C*-terminus is involved in contacts with central hydrophobic core[50] and there is evidence that Zn(II) affects this interaction.[52] Addition of 1 equiv of EGCG to this sample of Aβ and Zn(II) largely reversed both the broadening and chemical shift changes for most of the peptide residues affected by introduction of Zn(II) (Figure 3.13(e-g)). Among the residues that were not completely

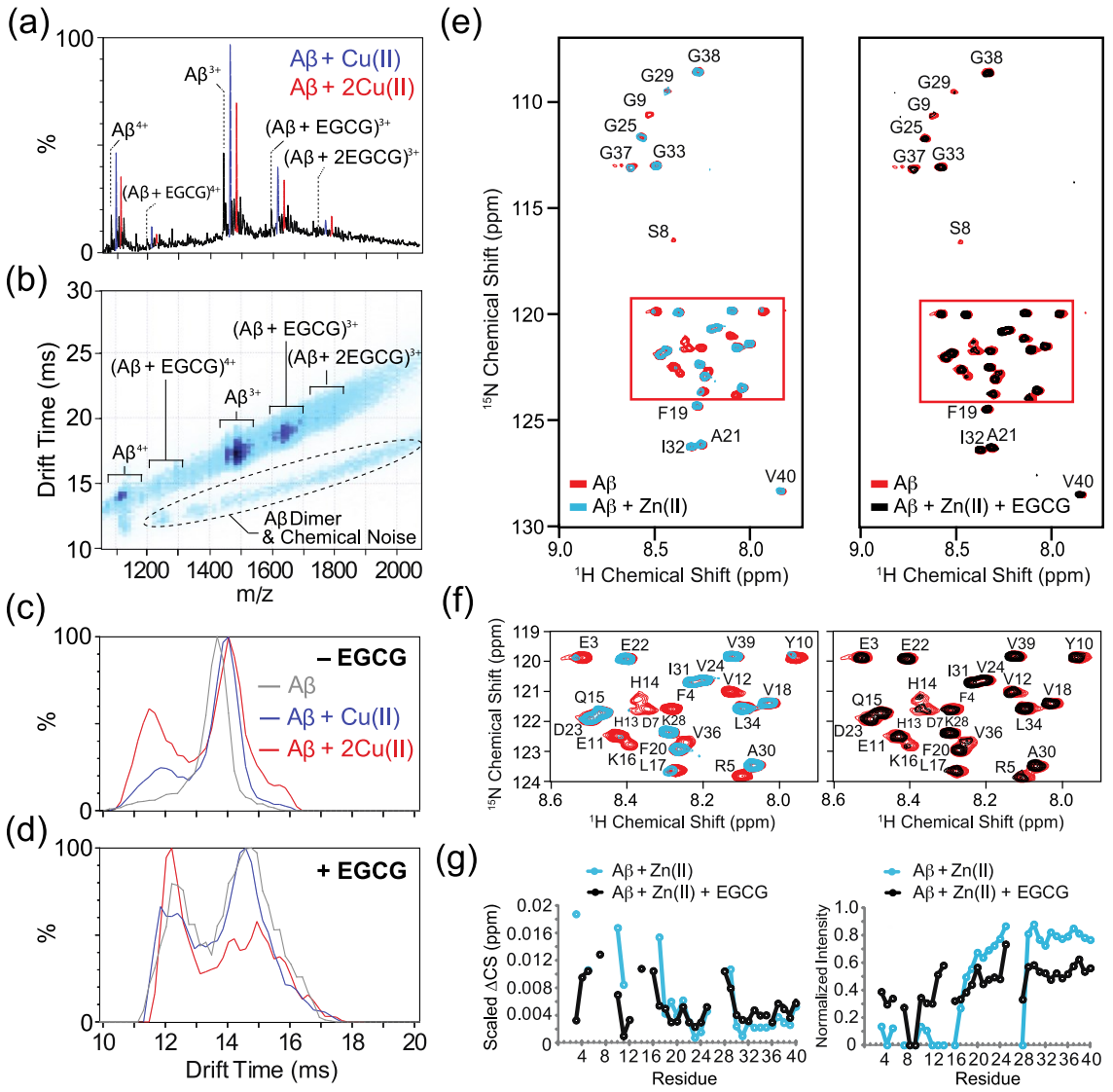

Figure 3.13. Interactions of EGCG with metal–Aβ_{40} species. (a) MS data for samples containing Aβ (10 μM), $Cu(OAc)_2$ (20 μM), and EGCG (20 μM) revealed the presence of ternary complexes. (b) A plot of IM drift time *versus m/z* indicated that monomeric Aβ species generated in (a) followed one IM-MS trend, whereas higher-order Aβ complexes and chemical noise components were clearly distinguished from these signals using IM-MS. (c) IM drift time spectra for control data where EGCG was not bound to the peptide revealed that Cu(II) binding acted to compact the peptide substantially. (d) Similar IM data as in (c) above showed that EGCG–Cu(II)–Aβ_{40} complexes further preferred compact configurations. (e) Analysis of EGCG and Zn(II) binding to Aβ_{40} by 2D SOFAST-HMQC NMR spectroscopy at 4 °C. On the left, addition of $ZnCl_2$ (38 μM) to Aβ (38 μM) caused the broadening and disappearance of specific peaks, primarily in the *N*-terminus. On the right, subsequent addition of EGCG (38 μM) to the Zn(II)–Aβ complex partially restored the signal intensity. (f) Expanded view of the highlighted regions of the 2D NMR spectra (e). (g) Changes in the chemical shift (left) and NMR signal intensity (right) upon binding.

restored were H13 and H14, which have been identified as ligands in Zn(II) binding to Aβ.[1,3,5,9,51-53] This may imply that some amount of Zn(II) remains associated with Aβ while the remainder is displaced by EGCG. Alternatively, the partial restoration of the resonance could represent the formation of a ternary complex of EGCG–Zn(II)–Aβ, as seen for the EGCG–Cu(II)–Aβ complexes studied by IM-MS. Finally, a combination of metal chelation/displacement by EGCG and ternary complex generation could occur simultaneously. Overall, our studies suggest that EGCG is able to interact with Cu(II)– or Zn(II)–Aβ species directly, likely leading to generation of ternary complexes with metal-associated Aβ, which may account for its anti-amyloidogenic reactivity with metal–Aβ species (Figures 3.2, 3.3, 3.4, and 3.7).

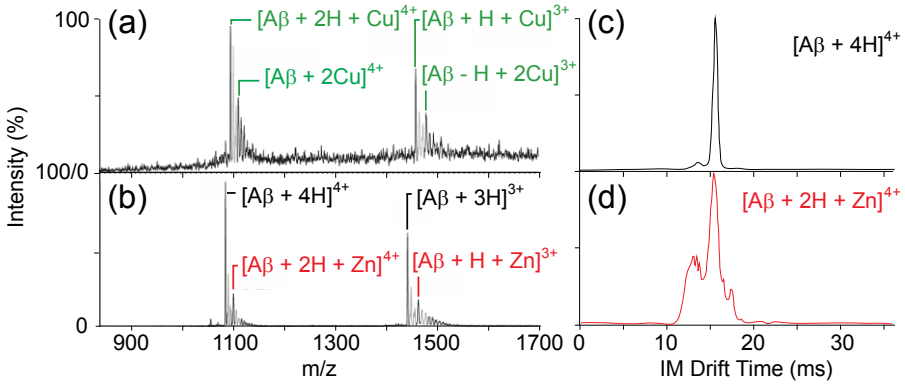

Figure 3.14. Interactions of $A\beta_{40}$ with Cu(II) and Zn(II) by MS. (a) MS data for $A\beta_{40}$ with $Cu(OAc)_2$ added in a ratio of 1:3. Both singly and doubly Cu(II)-bound peptides dominated the spectrum with little evidence of metal-free Aβ. (b) MS data for $A\beta_{40}$ with $Zn(OAc)_2$ added in the same molar ratio as in (a). As observed in previous studies, very little evidence of Zn(II) binding was observed, and most of the peptide was shown to be in its apo form. (c) IM arrival time distribution for Aβ in the 4^+ state. Three conformational families were observed, with the middle population dominant. (d) IM arrival time distribution for the Zn(II)–Aβ complex in the 4^+ state. A greater population of the compact form and the elongated state were observed, when compared to the IM arrival time distribution for Aβ only.

3.3. Conclusion

The green tea extract EGCG, having a structure capable of both metal chelation and Aβ interaction, was selected to further explore the reactivity of a well-known natural flavonoid with metal-free and metal-associated Aβ species and to provide structure-based insights into its mode of action at the molecular level. It was observed that

addition of EGCG to samples containing Cu(II)– or Zn(II)–Aβ species produced small amorphous Aβ aggregates, while EGCG-untreated samples generated mainly structured Aβ aggregates. This reactivity with Aβ was more noticeable in conditions containing metal ions, suggesting that EGCG was more capable of disrupting metal-mediated Aβ aggregation as compared to metal-free conditions. Furthermore, in living cells, incubation of EGCG with metal-free or metal-Aβ enhanced cell survival, which may represent its inhibitory effect on aggregation in complex settings. Our IM-MS and NMR results suggest that the overall mechanism of reactivity of EGCG with metal-free and metal-associated Aβ species could be driven by its ability to influence the structure of Aβ monomers and dimers (*i.e.*, formation of more compact conformations of Aβ and/or ternary complexes containing Aβ, Cu(II) or Zn(II), and EGCG in multiple stoichiometries). Taken together, the natural product, EGCG, could modulate the reactivity (*i.e.*, aggregation, toxicity) of metal–Aβ species through direct interactions with the peptide and its metal complexes. In addition, the molecular-level insights that underlie this altered reactivity suggest that EGCG might generate off-pathway Aβ intermediates preferentially in the presence of metal ions. Thus, the fundamental information on the structure-interaction-reactivity relationship presented here will undoubtedly aid in rational design and structure-based screening strategies for identifying chemical tools to elucidate the contributions of multiple and/or inter-connected factors in AD pathogenesis.

3.4. Experimental

3.4.1. Materials and procedures

All reagents were purchased from commercial suppliers and used as received unless otherwise noted. $A\beta_{40}$ was purchased from Anaspec (Fremont, CA, USA). EGCG was purchased from Sigma-Aldrich (St. Louis, MO, USA) and used without further purification. Trace metal contamination was removed from buffers and solutions used for metal binding and Aβ aggregation experiments (*vide infra*) by treating with Chelex (Sigma-Aldrich, St. Louis, MO, USA). Optical spectra were recorded using an Agilent

8453 UV-Visible (UV-Vis) spectrophotometer. Transmission electron microscopic images were taken using Philips CM-100 transmission electron microscope (Microscopy and Image Analysis Laboratory, University of Michigan, Ann Arbor, MI, USA). Measurements of absorbance for cell viability assays were measured by a SpectraMax M5 microplate reader (Molecular Devices, Sunnyvale, CA, USA). Mass spectra for studying the interaction of Aβ with EGCG in the absence and presence of Cu(II) were acquired on a quadrupole ion mobility time-of-flight mass spectrometer (Synapt G2 HDMS, Waters, Milford, MA, USA) and LCT Premier mass spectrometer (Waters, Milford, MA, USA) fitted with a nano-electrospray ionization (nESI) source. The NMR investigation of the Aβ interaction of EGCG with Zn(II) was conducted on a 600 MHz Bruker spectrometer equipped with a cryogenic probe at 4 °C.

3.4.2. Metal binding experiments

Unless otherwise stated, metal binding properties of EGCG (50 μM, 1% v/v DMSO) were studied in a Chelex-treated buffered solution containing 20 mM 2-[4-(2-hydroxyethyl)piperazin-1-yl]ethanesulfonic acid (HEPES), pH 7.4, 150 mM NaCl. To the solution containing EGCG, 0.5 or 1 equiv of $CuCl_2$ or $ZnCl_2$ was added and incubated for 30 min at room temperature. Additionally, UV-Vis spectra of Aβ (25 μM), Aβ incubated with $CuCl_2$ or $ZnCl_2$ (25 μM) for 2 min, and Aβ pretreated with $CuCl_2$ or $ZnCl_2$ followed by 30 min incubation with EGCG (50 μM) were acquired.

3.4.3. Aβ aggregation experiments

Aβ experiments were performed according to previously published methods.[13,16-20,29,40,57] Prior to experiments, $Aβ_{40}$ was dissolved in ammonium hydroxide (NH_4OH, 1% v/v aq), aliquoted, lyophilized overnight, and stored at −80 °C. For experiments described herein, a stock solution of the Aβ was prepared by dissolving the peptide in 1% NH_4OH (10 μL) and diluting with ddH_2O. The concentration of the solution was determined by measuring the absorbance of the solution at 280 nm (ε = 1450 $M^{-1}\,cm^{-1}$). The peptide stock solution was diluted to a final concentration of 25 μM in a Chelex-treated buffered solution containing HEPES (20 μM, pH 6.6 for Cu(II) samples or 7.4 for

metal-free and Zn(II) samples) and NaCl (150 μM). For the inhibition studies,[13,16-20,29,40,57] EGCG (50 μM, 1% v/v DMSO) was added to the sample of Aβ (25 μM) in the absence and presence of metal ions ($CuCl_2$ or $ZnCl_2$, 25 μM) followed by incubation at 37 °C with constant agitation for 2, 4, 8, 12, and 24 h. For the disaggregation studies,[13,16-20,29,40,57] Aβ with and without metal ions was incubated for 24 h at 37 °C with constant agitation prior to the addition of EGCG (50 μM) to the sample. The resulting samples were incubated at 37 °C with constant agitation for 2, 4, 8, 12, and 24 h.

3.4.4. Gel electrophoresis and Western blotting

Samples from the inhibition and disaggregation experiments were analyzed by gel electrophoresis (10-20% Tris-tricine gel, Invitrogen, Grand Island, NY, USA) and visualized by Western blot using an anti-Aβ antibody (6E10).[13,16-20,29,40,57] Following separation, the proteins were transferred onto nitrocellulose that was blocked with bovine serum albumin (BSA, 3% w/v, Sigma-Aldrich, St. Louis, MO, USA) in Tris-buffered saline (TBS) containing 0.1% Tween-20 (TBS-T) overnight. The membranes were incubated with the antibody (6E10, 1:2000, Covance, Princeton, NJ, USA) in a solution of 2% BSA (w/v in TBS-T) for 4 h at room temperature. After washing, the horseradish peroxidase-conjugated goat anti-mouse secondary antibody (1:5000; Cayman Chemical, Ann Arbor, MI, USA) in 2% BSA was added for 1 h at room temperature. The ThermoScientific SuperSignal West Pico Chemiluminescent Substrate (Rockford, IL, USA) was used to visualize the protein bands.

3.4.5. Transmission electron microscopy (TEM)

Samples for TEM were prepared according to a previously reported method.[13,17-20,29,40,57] Glow-discharged grids (Formar/Carbon 300-mesh, Electron Microscopy Sciences, Hatfield, PA, USA) were treated with Aβ samples from the inhibition and disaggregation experiments (5 μL) for 2 min at room temperature. Excess sample was removed using filter paper followed by washing with ddH_2O twice. Each grid was incubated with uranyl acetate (1% w/v ddH_2O, 5 μL, 1 min) and upon removal of excess was dried for 15 min at room temperature. Images from each sample were taken by a Philips CM-100 transmission electron microscope (80 kV, 25,000x magnification).

3.4.6. Cell viability measurements

The murine neuroblastoma Neuro-2a (N2a) cell line was purchased from the American Type Cell Collection (ATCC, Manassas, VA, USA). The cell line was maintained in media containing 45% DMEM, 50% OPTI-MEM, 5% fetal bovine serum (FBS, Atlanta Biologicals, Lawrenceville, GA, USA), 100 U/mL penicillin, and 100 μg/mL streptomycin (Gibco, Grand Island, NY, USA). The cells were grown in a humidified atmosphere with 5% CO_2 at 37 °C. For the MTT assay (MTT = 3-(4,5-dimethyl-2-thiazolyl)-2,5-diphenyl-2H-tetrazolium bromide), N2a cells were seeded in a 96 well plate (15,000 cells/100 μL).[13,17,19,20,29,57] The cells were treated with Aβ (10 μM) with or without $CuCl_2$ or $ZnCl_2$ (10 μM), followed by the addition of EGCG (10 or 20 μM, 1% v/v final DMSO concentration) and incubated for 24 h in the cells. The N2a cells were treated in parallel with only metal salts ($CuCl_2$ or $ZnCl_2$, 10 μM), EGCG (10 or 20 μM), or metal/EGCG (1:1 or 1:2 metal/EGCG ratio). After incubation, 25 μL MTT (5 mg/mL in phosphate buffered saline (PBS, pH 7.4, Gibco, Grand Island, NY, USA) was added to each well and the plate was incubated for 4 h at 37 °C. Formazan produced by the cells was solubilized using an acidic solution of *N*,*N*-dimethylformamide (50%, v/v aq) and sodium dodecyl sulfate (SDS, 20%, w/v) overnight at room temperature in the dark. The absorbance was measured at 600 nm using a microplate reader. Cell viability was calculated relative to cells containing an equivalent amount of DMSO. Error bars were calculated as standard error from three independent experiments.

3.4.7. Ion mobility-mass spectrometry (IM-MS)

Protein ions were generated using a nESI source and optimized to allow transmission of noncovalent protein complexes unless stated otherwise. Nanoflow electrospray capillaries were prepared in-house as previously described.[58] To generate protein complex ions, an aliquot of the sample (*ca*. 5 μL) was sprayed from the nESI emitter using capillary voltages ranging from 1.4–1.6 kV, with the source operating in positive ion mode and the sample cone operated at 20 V. The mass spectra were acquired with the following settings and tuned to avoid ion activation and preserve non-covalent protein–ligand complexes. The bias voltage was 40 V, with backing pressure at 5.39 mbar and ToF pressure at 9.74×10^{-7} mbar. The traveling-wave IM separator was

operated at a pressure of approximately 3.5 mbar of nitrogen and helium. Mass spectra were calibrated externally using a solution of cesium iodide (100 mg/mL) and analyzed using Masslynx 4.1 and Driftscope 2.0 software (Waters, Milford, MA, USA). Collision cross-section (CCS, Ω) measurements were externally calibrated using a database of known Ω in helium, including peptides, proteins, and protein complexes.[38,59] Samples were prepared by mixing stock solutions of $Cu(OAc)_2$, EGCG or ThT (1% v/v DMSO), and $A\beta_{40}$, dissolved in the aqueous solvent containing 100 mM NH_4OAc at pH 7.0, to generate a final peptide concentration of 10 μM. In order to study the relative abundance of dimeric to monomeric $A\beta_{40}$ the solution in the presence of EGCG or ThT, an aliquot of sample was analyzed at different time points by mass spectrometry and the intensity of the 3^+ and 4^+ ion of $A\beta_{40}$ monomer was compared with that of 5^+ ion of $A\beta_{40}$ dimer.

3.4.8. Docking studies

Flexible ligand docking studies using AutoDock Vina[60] for EGCG were conducted against the $A\beta_{40}$ monomer from the previously determined aqueous solution NMR structure (PDB 2LFM)[50]. Ten conformations were selected from among 20 within the PDB file (conformations 1, 3, 5, 8, 10, 12, 13, 16, 17, and 20). The MMFF94 energy minimization in ChemBio3D Ultra 11.0 was used to optimize the structure of EGCG for the docking studies. The structures of Aβ and EGCG were prepared in AutoDock Tools[61] and imported into PyRx[62], which was used to run AutoDock Vina. The entire peptide was contained within the search space having dimensions (*x*, *y*, *z*) (Å) of (25.76, 39.52, 38.63) and centered at (3.3428, −3.3088, −17.7921). The exhaustiveness for the docking runs was set at 1024. Docked models of EGCG were visualized with $A\beta_{40}$ using Pymol.

3.4.9. Molecular dynamics simulations

All simulations were started from the minimized solution NMR structure (PDB 2LFM)[50] of the $A\beta_{40}$ peptide. The simulations were performed using periodic boundary conditions in a cube with the minimum distance between the simulated molecules and the box wall being 1.0 nm. The MD simulations were performed using the GROMACS

software package[63] and GROMOS96 force field.[64] The LINCS algorithm was used to constrain all bond lengths in the peptides and EGCG, allowing an integration time step of 2 fs. The nonbonding pair list cutoff was set to 1.0 nm with the pair list updated every five time steps. The long-range electrostatic interactions were treated with the particle mesh Ewald method. The temperature and the pressure were maintained by coupling temperature and pressure baths using the method of Berendsen *et al.*[65] The peptide and ligand were separately coupled to external temperature and pressure baths. The temperature-coupling constant was 0.1 ps. The pressure was kept at 1 bar using weak pressure coupling with τ_p = 2.0 ps.[65]

The system was energy-minimized by steepest descent for 500 steps. After equilibration, simulated annealing was performed for Aβ_{40} and Aβ_{40}–EGCG complex ions in the gas-phase, having charged the three most-basic Aβ side chains (R5, K16, and K28) and the *N*-terminus (D1). The system was heated from 300 K to 500 K over 100 ps, then cooled to 300 K over the next 100 ps. The cycle was repeated over 20 ns. This leads to escape from low-lying energy traps and enhanced equilibration. For the Aβ_{40}–EGCG complex, ten 20 ns independent simulated annealing runs were performed from the Aβ_{40}–EGCG complexes generated by AutoDock Vina (*vide supra*). From the MD trajectory, 100 structures were sampled at 300 K and the CCS was calculated using Mobcal using a trajectory method algorithm.[54,55]

3.4.10. 2D NMR spectroscopy

The interactions of Aβ_{40} with EGCG in the absence and presence of Zn(II) were followed by 2D band-selective optimized flip-angle short transient (SOFAST)-heteronuclear multiple quantum correlation (HMQC) experiments at 4 °C.[66] ^{15}N-labeled Aβ_{40} (rPeptide, Bogart, GA, USA) was first dissolved in 1% NH_4OH and lyophilized. NMR samples were prepared from resuspending the solid in 1 mM NaOH (pH 10) and diluting with 10x HEPES–NaCl for a final buffer concentration of 25 mM HEPES, pH 7.3, with 25 mM NaCl and a final peptide concentration of either 38 μM (for samples containing [Aβ and Zn(II)] or [Aβ, Zn(II), and EGCG]) or 76 μM (for the sample of Aβ with EGCG). The pH was verified before the start of each titration and large aggregates were cleared by centrifugation through a 0.2 μm filter. Each spectrum was obtained from 256

t_1 experiments using either 32 or 64 transients (for the 76 and 38 μM samples, respectively) and a 100 ms recycle delay. 2D data were processed using TOPSPIN 2.1 (from Bruker). Resonance assignment and volume fit calculations were performed by SPARKY 3.113 with published assignments for Aβ as a guide.[49,67]

3.5. References

1. DeToma, A. S.; Salamekh, S.; Ramamoorthy, A.; Lim, M. H. *Chem. Soc. Rev.* **2012**, *41*, 608-621.
2. Ross, C. A.; Poirier, M. A. *Nat. Med.* **2004**, *10 Suppl*, S10-17.
3. Kepp, K. P. *Chem. Rev.* **2012**, *112*, 5193-5239.
4. Jakob-Roetne, R.; Jacobsen, H. *Angew. Chem. Int. Ed.* **2009**, *48*, 3030-3059.
5. Savelieff, M. G.; Lee, S.; Liu, Y.; Lim, M. H. *ACS Chem. Biol.* **2013**.
6. Crouch, P. J.; Barnham, K. J. *Acc. Chem. Res.* **2012**, *45*, 1604-1611.
7. Que, E. L.; Domaille, D. W.; Chang, C. J. *Chem. Rev.* **2008**, *108*, 1517-1549.
8. Eskici, G.; Axelsen, P. H. *Biochemistry* **2012**, *51*, 6289-6311.
9. Pithadia, A. S.; Lim, M. H. *Curr. Opin. Chem. Biol.* **2012**, *16*, 67-73.
10. Rodríguez-Rodríguez, C.; Telpoukhovskaia, M.; Orvig, C. *Coord. Chem. Rev.* **2012**, *256*, 2308-2332.
11. Braymer, J. J.; DeToma, A. S.; Choi, J.-S.; Ko, K. S.; Lim, M. H. *Int. J. Alzheimers Dis.* **2011**, *2011*, 623051.
12. Perez, L. R.; Franz, K. J. *Dalton Trans.* **2010**, *39*, 2177-2187.
13. Pithadia, A. S.; Kochi, A.; Soper, M. T.; Beck, M. W.; Liu, Y.; Lee, S.; DeToma, A. S.; Ruotolo, B. T.; Lim, M. H. *Inorg. Chem.* **2012**, *51*, 12959-12967.
14. Sharma, A. K.; Pavlova, S. T.; Kim, J.; Finkelstein, D.; Hawco, N. J.; Rath, N. P.; Kim, J.; Mirica, L. M. *J. Am. Chem. Soc.* **2012**, *134*, 6625-6636.
15. Jones, M. R.; Service, E. L.; Thompson, J. R.; Wang, M. C.; Kimsey, I. J.; DeToma, A. S.; Ramamoorthy, A.; Lim, M. H.; Storr, T. *Metallomics* **2012**, *4*, 910-920.
16. He, X.; Park, H. M.; Hyung, S.-J.; DeToma, A. S.; Kim, C.; Ruotolo, B. T.; Lim, M. H. *Dalton Trans.* **2012**, *41*, 6558-6566.
17. Braymer, J. J.; Choi, J.-S.; DeToma, A. S.; Wang, C.; Nam, K.; Kampf, J. W.; Ramamoorthy, A.; Lim, M. H. *Inorg. Chem.* **2011**, *50*, 10724-10734.
18. Choi, J.-S.; Braymer, J. J.; Park, S. K.; Mustafa, S.; Chae, J.; Lim, M. H. *Metallomics* **2011**, *3*, 284-291.
19. Choi, J.-S.; Braymer, J. J.; Nanga, R. P. R.; Ramamoorthy, A.; Lim, M. H. *Proc. Natl. Acad. Sci. U. S. A.* **2010**, *107*, 21990-21995.
20. Hindo, S. S.; Mancino, A. M.; Braymer, J. J.; Liu, Y.; Vivekanandan, S.; Ramamoorthy, A.; Lim, M. H. *J. Am. Chem. Soc.* **2009**, *131*, 16663-16665.
21. Wu, W.-h.; Lei, P.; Liu, Q.; Hu, J.; Gunn, A. P.; Chen, M.-s.; Rui, W.-f.; Su, X.-y.; Xie, Z.-p.; Zhao, Y.-F.; Bush, A. I.; Li, Y.-m. *J. Biol. Chem.* **2008**, *283*, 31657-31664.
22. Porat, Y.; Abramowitz, A.; Gazit, E. *Chem. Biol. Drug Des.* **2006**, *67*, 27-37.

23. Ehrnhoefer, D. E.; Bieschke, J.; Boeddrich, A.; Herbst, M.; Masino, L.; Lurz, R.; Engemann, S.; Pastore, A.; Wanker, E. E. *Nat. Struct. Mol. Biol.* **2008**, *15*, 558-566.
24. Bieschke, J.; Russ, J.; Friedrich, R. P.; Ehrnhoefer, D. E.; Wobst, H.; Neugebauer, K.; Wanker, E. E. *Proc. Natl. Acad. Sci. U. S. A.* **2010**, *107*, 7710-7715.
25. Ladiwala, A. R.; Dordick, J. S.; Tessier, P. M. *J. Biol. Chem.* **2011**, *286*, 3209-3218.
26. Lemkul, J. A.; Bevan, D. R. *Biochemistry* **2012**, *51*, 5990-6009.
27. Sinha, S.; Du, Z.; Maiti, P.; Klarner, F. G.; Schrader, T.; Wang, C.; Bitan, G. *ACS Chem. Neurosci.* **2012**, *3*, 451-458.
28. Lopez del Amo, J. M.; Fink, U.; Dasari, M.; Grelle, G.; Wanker, E. E.; Bieschke, J.; Reif, B. *J. Mol. Biol.* **2012**, *421*, 517-524.
29. DeToma, A. S.; Choi, J.-S.; Braymer, J. J.; Lim, M. H. *ChemBioChem* **2011**, *12*, 1198-1201.
30. Kim, J.; Lee, H. J.; Lee, K. W. *J. Neurochem.* **2010**, *112*, 1415-1430.
31. Meng, F.; Abedini, A.; Plesner, A.; Verchere, C. B.; Raleigh, D. P. *Biochemistry* **2010**, *49*, 8127-8133.
32. Chandrashekaran, I. R.; Adda, C. G.; MacRaild, C. A.; Anders, R. F.; Norton, R. S. *Biochemistry* **2010**, *49*, 5899-5908.
33. Chandrashekaran, I. R.; Adda, C. G.; Macraild, C. A.; Anders, R. F.; Norton, R. S. *Arch. Biochem. Biophys.* **2011**, *513*, 153-157.
34. Popovych, N.; Brender, J. R.; Soong, R.; Vivekanandan, S.; Hartman, K.; Basrur, V.; Macdonald, P. M.; Ramamoorthy, A. *J. Phys. Chem. B* **2012**, *116*, 3650-3658.
35. Pirker, K. F.; Baratto, M. C.; Basosi, R.; Goodman, B. A. *J. Inorg. Biochem.* **2012**, *112*, 10-16.
36. Sun, S.-l.; He, G.-q.; Yu, H.-n.; Yang, J.-g.; Borthakur, D.; Zhang, L.-c.; Shen, S.-r.; Das, U. N. *Mol. Nutr. Food Res.* **2008**, *52*, 465-471.
37. Cheng, X. R.; Hau, B. Y.; Veloso, A. J.; Martic, S.; Kraatz, H. B.; Kerman, K. *Anal. Chem.* **2013**, *85*, 2049-2055.
38. Ruotolo, B. T.; Benesch, J. L.; Sandercock, A. M.; Hyung, S. J.; Robinson, C. V. *Nat. Protoc.* **2008**, *3*, 1139-1152.
39. Bernstein, S. L.; Dupuis, N. F.; Lazo, N. D.; Wyttenbach, T.; Condron, M. M.; Bitan, G.; Teplow, D. B.; Shea, J. E.; Ruotolo, B. T.; Robinson, C. V.; Bowers, M. T. *Nat. Chem.* **2009**, *1*, 326-331.
40. Mancino, A. M.; Hindo, S. S.; Kochi, A.; Lim, M. H. *Inorg. Chem.* **2009**, *48*, 9596-9598.
41. Suzuki, Y.; Brender, J. R.; Hartman, K.; Ramamoorthy, A.; Marsh, E. N. G. *Biochemistry* **2012**, *51*, 8154-8162.
42. Ashcroft, A. E. *J. Am. Soc. Mass Spectrom.* **2010**, *21*, 1087-1096.
43. Williams, D. M.; Pukala, T. L. *Mass Spectrom. Rev.* **2013**.
44. Reinke, A. A.; Gestwicki, J. E. *Chem. Biol. Drug Des.* **2011**, *77*, 399-411.
45. Larson, J. L.; Ko, E.; Miranker, A. D. *Protein Sci.* **2000**, *9*, 427-431.
46. Hortschansky, P.; Schroeckh, V.; Christopeit, T.; Zandomeneghi, G.; Fändrich, M. *Protein Sci.* **2005**, *14*, 1753-1759.

47. Baumketner, A.; Bernstein, S. L.; Wyttenbach, T.; Bitan, G.; Teplow, D. B.; Bowers, M. T.; Shea, J. E. *Protein Sci.* **2006**, *15*, 420-428.
48. El-Hawiet, A.; Kitova, E. N.; Liu, L.; Klassen, J. S. *J. Am. Soc. Mass Spectrom.* **2010**, *21*, 1893-1899.
49. Wang, S. H.; Liu, F. F.; Dong, X. Y.; Sun, Y. *J. Phys. Chem. B* **2010**, *114*, 11576-11583.
50. Vivekanandan, S.; Brender, J. R.; Lee, S. Y.; Ramamoorthy, A. *Biochem. Biophys. Res. Commun.* **2011**, *411*, 312-316.
51. Rauk, A. *Chem. Soc. Rev.* **2009**, *38*, 2698-2715.
52. Rezaei-Ghaleh, N.; Giller, K.; Becker, S.; Zweckstetter, M. *Biophys. J.* **2011**, *101*, 1202-1211.
53. Faller, P. *ChemBioChem* **2009**, *10*, 2837-2845.
54. Mesleh, M. F.; Hunter, J. M.; Shvartsburg, A. A.; Schatz, G. C.; Jarrold, M. F. *J. Phys. Chem.* **1996**, *100*, 16082-16086.
55. Shvartsburg, A. A.; Jarrold, M. F. *Chem. Phys. Lett.* **1996**, *261*, 86-91.
56. It is worthwhile to note that the conditions in these experiments were not optimized for the formation of Aβ oligomers, and therefore the signal recorded for Aβ dimers and other oligomers at low abundance was insufficient to reveal the binding modes associated with higher-order Aβ or to determine the ligand binding constants associated with the tertiary complex (Figure 3.9(a) and (b)). .
57. Hyung, S.-J.; DeToma, A. S.; Brender, J. R.; Lee, S.; Vivekanandan, S.; Kochi, A.; Choi, J.-S.; Ramamoorthy, A.; Ruotolo, B. T.; Lim, M. H. *Proc. Natl. Acad. Sci. U. S. A.* **2013**, *110*, 3743-3748.
58. Hernández, H.; Robinson, C. V. *Nat. Protoc.* **2007**, *2*, 715-726.
59. Bush, M. F.; Hall, Z.; Giles, K.; Hoyes, J.; Robinson, C. V.; Ruotolo, B. T. *Anal. Chem.* **2010**, *82*, 9557-9565.
60. Trott, O.; Olson, A. J. *J. Comput. Chem.* **2010**, *31*, 455-461.
61. Morris, G. M.; Huey, R.; Lindstrom, W.; Sanner, M. F.; Belew, R. K.; Goodsell, D. S.; Olson, A. J. *J. Comput. Chem.* **2009**, *30*, 2785-2791.
62. Wolf, L. K. *Chem. Eng. News* **2009**, *87*, 31.
63. Lindahl, E.; Hess, B.; van der Spoel, D *J. Mol. Mod.* **2001**, *7*, 306-317.
64. van Gunsteren, W. F.; Billeter, S. R.; Eising, A. A.; Hunenberger, P. H.; Kruger, P.; Mark, A. E.; Scott, W. R. P.; Tironi, I. G., *Biomolecular Simulation: The GROMOS96 Manual and User Guide*. Vdf Hochschulverland ETH: Zürich, Switzerland, 1996.
65. Berendsen, H. J. C.; Postma, J. P. M.; van Gunsteren, W. F.; Nola, A. D.; Haak, J. R. *J. Chem. Phys.* **1984**, *81*, 3684-3690.
66. Schanda, P.; Brutscher, B. *J. Am. Chem. Soc.* **2005**, *127*, 8014-8015.
67. Yoo, S. I.; Yang, M.; Brender, J. R.; Subramanian, V.; Sun, K.; Joo, N. E.; Jeong, S. H.; Ramamoorthy, A.; Kotov, N. A. *Angew. Chem. Int. Ed.* **2011**, *50*, 5110-5115.

Chapter 4: Reactivity of Synthetic Aminoisoflavone Derivatives with Metal–Aβ Species *In Vitro* and in Living Cells

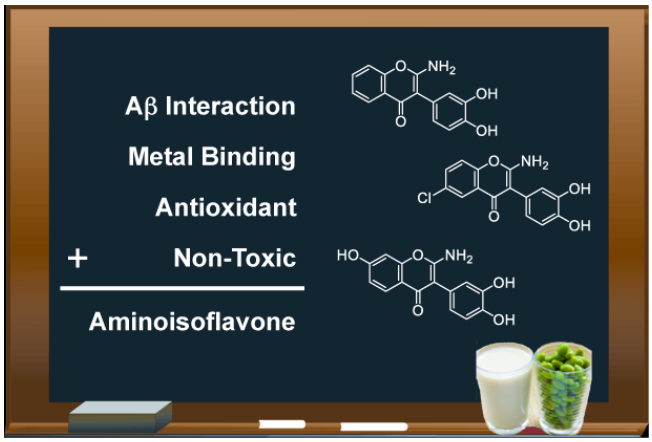

This chapter is based on work that will be submitted for publication. We thank Professor Gianfranco Balboni for providing the aminoisoflavone compounds and Professor Ayyalusamy Ramamoorthy, Dr. Jeffrey Brender, and Dr. Janarthanan Krishnamoorthy for 2D NMR experiments with Aβ. We also thank Younwoo Nam, Akiko Kochi, and Hyuck Jin Lee for assistance with ITC, TEM, and methoxylated aminoisoflavone gels, respectively. We are grateful to Professor Nicolai Lehnert and Professor Veronika Szalai for helpful discussions on the EPR data and to Dr. Lauren Goodrich and Amy Speelman for assistance with EPR experiments and simulations. We also thank Emily Nelson, Benjamin Klepser, and Tanya Breault for assistance with the electrochemistry experiments.

4.1 Introduction

Alzheimer's disease (AD) is rapidly becoming one of the prominent public health concerns worldwide, especially due to the present lack of a curative treatment.[1-5] AD is commonly classified as a protein misfolding disease due to the observation of proteinaceous aggregates in diseased brain tissue, including senile plaques and neurofibrillary tangles.[2-8] The primary components of the senile plaques are aggregated forms of amyloid-β (Aβ) peptides, which provided early evidence to propose the amyloid cascade hypothesis of AD.[3,9-12] According to this principle, self-association of monomeric Aβ into various amyloid assemblies produces neurotoxic species, leading to pathogenesis;[13,14] however, plaques can have heterogeneous composition, with other components in addition to aggregated forms of Aβ having been identified in the deposits. For example, metal ions have been found in association with the plaques and could be linked to neurotoxicity in AD. Furthermore, oxidative stress in the brain is indicated in AD and could also originate from several causes, including metal ions and their association with Aβ species, suggesting the complicated etiology of this disease.[4,5,8,15-20]

In particular, elucidating the role of metal ions (*i.e.*, Fe, Cu, Zn) found in senile plaques has been challenging.[2-5,8,11,21] Cu(I/II), Zn(II), and more recently Fe(II) have been shown to bind to Aβ peptides *in vitro*.[2-5,8,19,20,22-25] Consequently, Cu(II)- and Zn(II)-bound Aβ peptides have been found to aggregate more rapidly than their metal-free counterparts.[26,27] It has also been proposed that redox active metal ions, such as Cu(I/II), bound to Aβ could participate in redox cycling, leading to an overproduction of reactive oxygen species (ROS) and, subsequently, elevated oxidative stress.[17,18,28] As metal binding to Aβ may have multiple potential consequences, consideration of the direct interaction between these metal ions and Aβ peptides as a pathological factor is warranted; however, little evidence has been accumulated to clarify the involvement of metal-associated Aβ (metal–Aβ) species *in vivo* and their contribution to AD.

In an attempt to explore the connection between metal–Aβ species and AD, employing small molecules as chemical tools may be useful. For this purpose, there have been increasing efforts to probe Cu(II)–Aβ and Zn(II)–Aβ *in vitro* using compounds

with specific structural moieties for simultaneous interaction with metal ions and Aβ (*i.e.*, bifunctionality).[2,3,29-44] The majority of molecules for this purpose have been designed by direct modification of known Aβ plaque imaging agents.[29-31,45-53] In the incorporation design approach, heteroatoms for metal chelation are directly installed into the imaging agent framework.[30,31,34-40,43,44] This design strategy affords several advantages for future applications, including careful selection of moieties that could facilitate brain uptake.[2,29,30] Although several compounds with bifunctionality have provided useful insights into the reactivity of metal–Aβ, there remains much to be understood about these molecules' functions at the molecular level and the impact of their structural features on interaction and reactivity with metal-free and metal–Aβ species (*i.e.*, structure-interaction-reactivity relationship).

To expand on this idea, rational screening or selection of natural products has identified flavonoids as a source of chemical structures suitable for investigation and modification.[12,54,55] Flavonoids are plant-derived compounds that have been studied in models of inflammation, cancer, oxidative stress, and dementia.[56-58] Initially, myricetin (Figure 4.1a) was found to modulate of metal-mediated Aβ aggregation and neurotoxicity *in vitro* due to its metal chelation and Aβ interaction properties.[12] More recently, the influence of (−)-epigallocatechin-3-gallate (EGCG, Figure 4.1a) on both metal-free and metal-induced Aβ aggregation was characterized in detail at the molecular level through biochemical and biophysical studies.[54] This investigation indicated that EGCG binding to Aβ could generate metal–Aβ complexes with a compact conformation; in both cases, off-pathway Aβ aggregation occurred leading to amorphous Aβ aggregates.[54,59] In order to reconcile the previously reported findings using myricetin and EGCG with the rational design approach, it would be worthwhile to identify the essential structural moieties within a flavonoid framework required to target metal-free and metal–Aβ species and modulate their reactivity, which will offer small molecule candidates for chemical tools.

Herein, we report the design and preparation of simple flavonoid derivatives, aminoisoflavones (**1**-**4**, Figure 4.1b), as well as a detailed evaluation of their Cu(II), Zn(II), and Aβ interaction properties and their ability to regulate metal-free and metal-

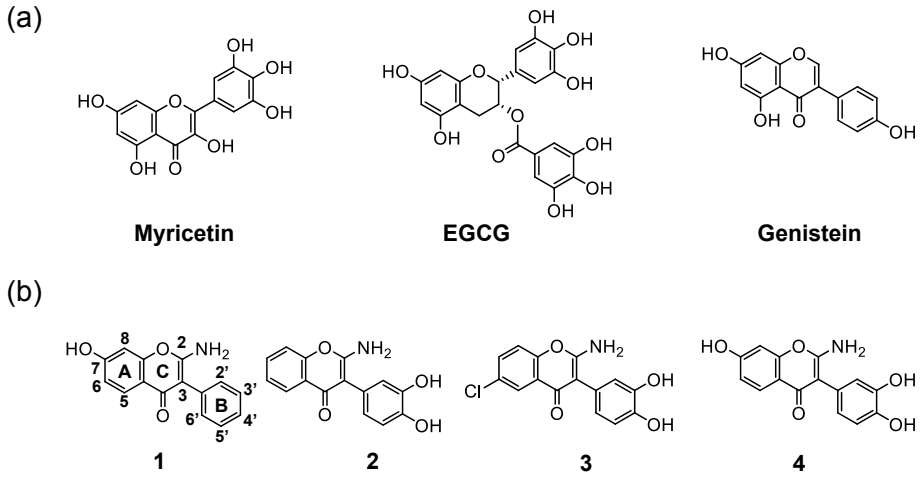

Figure 4.1. Chemical structures of (a) naturally occurring flavonoids (myricetin, EGCG, and genistein) and (b) synthetic aminoisoflavones (**1**-**4**). (a) Left to right: Myricetin, 3,5,7-trihydroxy-2-(3,4,5-trihydroxyphenyl)-4*H*-chromen-4-one; EGCG, (−)-epigallocatechin-3-gallate/(2*R*,3*R*)-5,7-dihydroxy-2-(3,4,5-trihydroxyphenyl)chroman-3-yl 3,4,5-trihydroxybenzoate; genistein, 5,7-dihydroxy-3-(4-hydroxyphenyl)-4*H*-chromen-4-one. (b) Left to right: **1**, 2-amino-7-hydroxy-3-phenyl-4*H*-chromen-4-one; **2**, 2-amino-3-(3,4-dihydroxyphenyl)-4*H*-chromen-4-one; **3**, 2-amino-6-chloro-3-(3,4-dihydroxyphenyl)-4*H*-chromen-4-one; **4**, 2-amino-3-(3,4-dihydroxyphenyl)-7-hydroxy-4*H*-chromen-4-one.

induced Aβ aggregation and cytotoxicity. These compounds were designed on the basis of naturally occurring isoflavones that are found in soy (*e.g.*, genistein, Figure 4.1a) and have been shown to block metal-free Aβ aggregation.[56,60] Previously, aminoisoflavones have been reported to have some biological applications, including aryl hydrocarbon receptor agonist/antagonist activity and carbonic anhydrase inhibition, suggesting the versatility of this class of molecules.[61,62] In the present study, several modifications were made to produce a small flavonoid library. A chemical moiety common to natural flavonoids, catechol, was incorporated in the isoflavone framework to provide a chelation site for Cu(II) and Zn(II). Although the coordination chemistry of catechol and its corresponding metal complexes is well known, knowledge of its role in flavonoid derivatives for targeting and modulating metal-free and metal-induced Aβ aggregation has received little attention. Additionally, incorporation of an amine functionality (*e.g.*, NH_2) could be used to gauge the tolerance of the framework to unnatural substituents, which might be useful for tuning the metal binding and/or Aβ interaction properties by

rational structure-based modifications in later stages. The studies presented herein demonstrate that deconstruction of naturally occurring flavonoids for redesign with selective inclusion of only a few functional groups is sufficient to effectively target metal ions, Aβ, and metal–Aβ and to subsequently influence their reactivity *in vitro*. Using our aminoisoflavone derivatives, the foundation of a structure-interaction-reactivity relationship for flavonoids toward metal-free and metal-associated Aβ is strengthened by detailed characterization of their properties at the molecular level.

4.2. Results and discussion

4.2.1. Design and synthesis of aminoisoflavone derivatives

In search of small molecules to interrogate the relationship between metal ions and Aβ species, selection of naturally occurring flavonoids has offered a new avenue for chemical tool development due to their multiple targeting capabilities, which may include various enzymes and ROS.[12,54,63,64] According to the initial results of myricetin (Figure 4.1a for structure),[12] an attempt to modify the flavonoid structure in order to influence metal-induced Aβ aggregation was made previously.[40] In that report, simplified flavonoid structures were selected; however, they were unable to alter the reactivity of metal–Aβ species, possibly due to the imbalance between metal binding and Aβ binding affinities.[40] Recognizing that certain structural moieties are common to natural flavonoids (*e.g.*, catechol group), we designed and prepared a new family of synthetic flavonoids, aminoisoflavones (**1**-**4**, 4.1b) with tractable structural modifications.

The aminoisoflavones are derived from the structures of soy isoflavones, such as genistein (Figure 4.1), which are known to have multiple biological effects, and they have been employed as Aβ aggregation inhibitors and as neuroprotective molecules.[60] Synthetic aminoisoflavone derivatives have been demonstrated previously to have inhibitory activity against various isoforms of human carbonic anhydrase (hCAI and hCAII),[62] a metalloenzyme that has been occasionally linked to AD.[65] Thus, we were curious to know whether the family of compounds could target and modulate another aspect of AD-related reactivity. The design of the new aminoisoflavones **1**-**4** (Figure 4.1) involves the *o*-dihydroxy moiety (*i.e.*, catechol) for metal chelation in **2**, **3**, and **4** and

substituents such as OH or Cl in the A ring to modify the electronics or sterics of the molecules to influence their reactivity with Aβ or metal–Aβ (*vide infra*). Compound **1** was prepared as an analogue of **4** that lacks the catechol group for comparison of interaction and reactivity with metal ions, Aβ, and metal–Aβ. The design further employs an unnatural substituent, a primary amine, in the 2 position of the C ring within the core framework of the isoflavone, which may be beneficial for improving solubility compared to naturally occurring flavonoids[66] (Figure 4.1). The inclusion of the amine group is also related to the design of Aβ plaque imaging agents and multifunctional small molecules, which have used amine derivatives to interact with the peptide.[45-48,53,67] Among them, the dimethylamino functionality has been commonly used;[45-48] however, the reported derivatives containing the primary amine can also enable interaction with Aβ.[48] The aminoisoflavones (**1**-**4**) presented here are synthesized by acidic cleavage of the methoxylated aminoisoflavone precursors,[62] and they were obtained in relatively high yield (76-86%) (Scheme 4.1). Thus, the multiple structural aspects of these aminoisoflavones, including the isoflavone framework, the catechol motif, and the primary amine, make them attractive candidates for detailed characterization of their chemical properties and subsequently their influence on metal-free and metal-induced Aβ aggregation *in vitro*, and toxicity induced by Aβ and metal–Aβ in living cells.

Scheme 4.1. Synthetic route for aminoisoflavones (**1**-**4**).

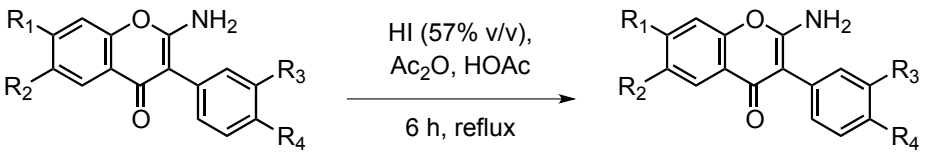

	R_1	R_2	R_3	R_4
1a	OCH_3	H	H	H
2a	H	H	OCH_3	OCH_3
3a	H	Cl	OCH_3	OCH_3
4a	OCH_3	H	OCH_3	OCH_3

	R_1	R_2	R_3	R_4
1	OH	H	H	H
2	H	H	OH	OH
3	H	Cl	OH	OH
4	OH	H	OH	OH

4.2.2. Solution speciation studies of aminoisoflavones

The acidity constants (pK_a) for the aminoisoflavones were determined by variable-pH spectrophotometric titrations (I = 0.1 M, room temperature) following previously reported procedures (Figure 4.2).[34,36-40,43,44,68,69] The primary amine common to all four aminoisoflavones was assigned to the most acidic pK_a values, consistent with the predicted values for these structures.[70] Deprotonation of the ammonium (RNH_3^+) to the primary amine (RNH_2) was represented by pK_a values of 1.3 ± 0.1 for **1**, 1.8 ± 0.5 for **2**, 2.2 ± 0.9 for **3**, and 1.5 ± 0.4 for **4**. With the exception of **1**, each of the structures contains the catechol moiety that has expected pK_a values for the hydroxyl groups of *ca.* 9 and 13.[71-73] The pK_a values for the catechol/catecholate equilibrium were 8.9 ± 0.2 and 12.3 ± 0.4 for **2**, 8.9 ± 0.3 and 11.7 ± 0.2 for **3**, and 9.1 ± 0.2 and 12.0 ± 0.2 for **4**, with the more basic pK_a value corresponding to deprotonation of the hydroxyl group in the *para* position.[71-73] An additional pK_a value corresponding to deprotonation of the hydroxyl substituent on the A ring in **1** and **4** was 7.9 ± 0.1 and 5.8 ± 0.3, respectively. Based on these pK_a values, speciation diagrams were drawn to illustrate the fraction of ligand protonation states at each pH in solution. Each ligand would exist mainly in its fully deprotonated form above pH 12 (*i.e.*, L), and would have an overall negative charge. At pH 7.4, the dominant species is expected to be neutral for **1** (LH), **2** (LH_2), and **3** (LH_2), or monodeprotonated for **4** (LH_2). For future applications of these molecules, neutral species would be favored for facilitating brain uptake via passive diffusion across the blood-brain barrier (BBB).[74] Furthermore, characterization of the species distribution could be valuable for rationalizing the metal/Aβ binding properties for these molecules as described below.

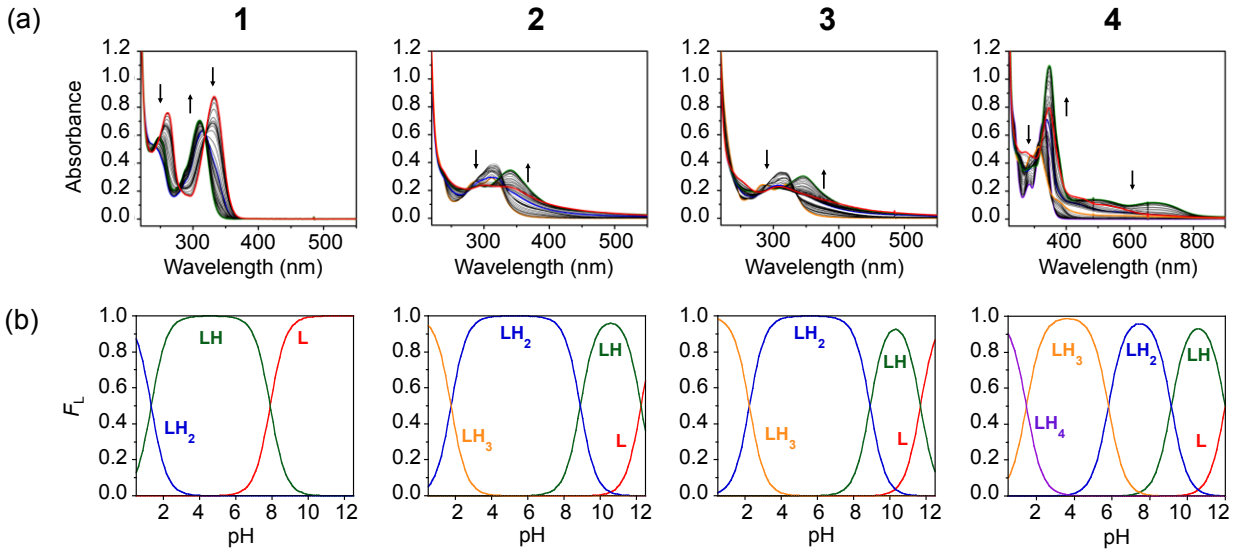

(c)

						pK_a[a]			
						1	**2**	**3**	**4**
LH_4	⇌	LH_3	+	H	(pK_{a1})	–	–	–	1.5(4)
LH_3	⇌	LH_2	+	H	(pK_{a2})	–	1.8(5)	2.2(9)	5.8(3)
LH_2	⇌	LH	+	H	(pK_{a3})	1.3(1)	8.9(2)	8.9(3)	9.1(2)
LH	⇌	L	+	H	(pK_{a4})	7.9(1)	12.3(4)	11.7(2)	12.0(2)

Figure 4.2. Solution speciation studies of aminoisoflavones (**1**-**4**). (a) Variable-pH UV-Vis titration spectra and (b) solution speciation diagrams for **1**-**4** (F_L = fraction of species in solution). (c) Summary of solution equilibria and acidity constants. Experimental conditions: [**1** or **4**] = 30 μM, [**2**] = 20 μM, [**3**] = 15 μM; I = 0.1 M NaCl; room temperature. Charges are omitted for clarity. [a] The error in the last digit is shown in parentheses.

4.2.3. Metal binding studies

The aminoisoflavones **2**, **3**, and **4** were designed to be capable of metal binding via a catechol group, similar to other polyphenols.[12,54,75,76] The catechol moiety is a prevalent ligand in biology, appearing in naturally occurring molecules such as flavonoids and in neurotransmitters (*e.g.*, dopamine, epinephrine).[72,77] Known to be a strong metal chelator, the inclusion of this functionality in the aminoisoflavone framework was anticipated to interact with metal ions surrounded by Aβ species.[72,73,78] Thus, the Cu(II) and Zn(II) binding properties of the aminoisoflavones were investigated initially by UV-Vis in the absence and presence of $A\beta_{40}$ (Figures 4.3, 4.4, and 4.5). More

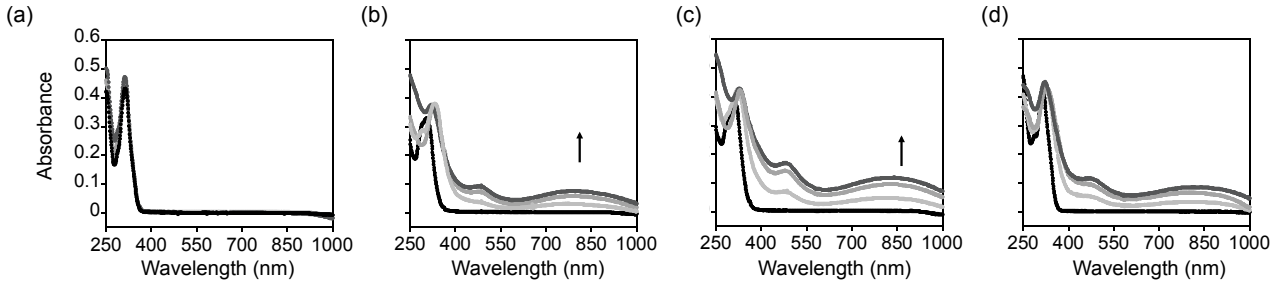

Figure 4.3. Cu(II) binding studies of the aminoisoflavones. Treatment of (a) **1**, (b) **2**, (c) **3**, or (d) **4** (black) with 0.5 equiv of $CuCl_2$ (light gray, incubated for 1-2 h), 1 equiv of $CuCl_2$ (medium gray, incubated for 10-30 min), or 5 equiv of $CuCl_2$ (dark gray, incubated for 5-30 min). Experimental conditions: [aminoisoflavone] = 20 μM; 1% v/v DMSO; 20 mM HEPES, pH 7.4, 150 mM NaCl; room temperature.

detailed Cu(II) binding properties were also characterized by variable-pH UV-Vis titrations and electron paramagnetic resonance (EPR) spectroscopy (*vide infra*).

Upon incubation of the aminoisoflavones **2**, **3**, and **4** (20 μM, 1% v/v DMSO) with $CuCl_2$ in an aqueous buffered solution (20 mM HEPES, pH 7.4, 150 mM NaCl), differences in the optical spectrum of the free ligand were observed (Figure 4.3). With 0.5 equiv of $CuCl_2$, new absorption features at *ca.* 480 nm were detected; additionally, prolonged incubation of the solution resulted in the appearance of a broad feature centered at *ca.* 800 nm.[79] Subsequent addition of $CuCl_2$ (1 or 5 equiv) enhanced the intensity of these peaks. When the experiment was conducted with **1**, which lacks the catechol group, there were no noticeable changes in the optical spectra (Figure 4.3).

Zn(II) binding to the aminoisoflavones was also investigated by UV-Vis. It should be noted that the ligand concentration was increased to a ten-fold excess (*i.e.*, 100 μM) relative to $ZnCl_2$ (10 μM) to detect an optical change upon metal binding (Figure 4.4). Similar to the Cu(II) binding data, addition of Zn(II) had no effect on the spectrum of **1** (Figure 4.4a). There were also no significant changes for **3** with Zn(II); however, **2** and **4** showed new features in the UV-Vis spectra after *ca.* 12-24 h incubation. For **2**, an increase in the peak at *ca.* 285 nm and a shift to *ca.* 390 nm were observed (Figure 4.4b). Similarly, **4** displayed a progressive bathochromic shift from *ca.* 320 nm to 350 nm over 24 h (Figure 4.4d). These spectral variations could be indicative of partial deprotonation of the hydroxyl groups upon Zn(II) binding.[77] Deprotonation of the ligand

might also cause a weak, broad feature around 800 nm that is similar to, but less intense than, that of the Cu(II) binding spectra.[79] This observation correlates to the Cu(II) speciation results at pH 7.4 detailed below, which suggests partial deprotonation of the catechol upon metal binding.[72,77] Thus, deprotonation of **4** from LH_2 to its LH form at pH 7.4 could possibly occur upon Zn(II) binding to some extent.

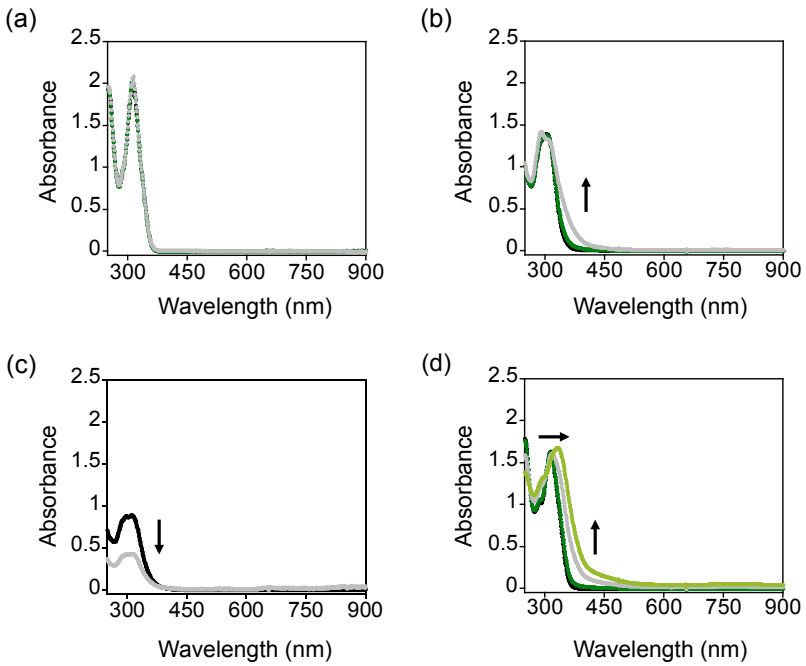

Figure 4.4. Zn(II) binding properties of aminoisoflavones [(a) **1**, (b) **2**, (c) **3**, or (d) **4** (black) with $ZnCl_2$ (dark green, 2 h incubation; gray, 12 h incubation; light green, 24 h incubation)]. Experimental conditions: [aminoisoflavone] = 100 μM; [$ZnCl_2$] = 10 μM; 1% v/v DMSO; 20 mM HEPES, pH 7.4, 150 mM NaCl; room temperature.

To anticipate whether the aminoisoflavones might bind to metal ions in the presence of Aβ, UV-Vis studies were conducted with $A\beta_{40}$, $CuCl_2$ and **4** (Figure 4.5). A solution of $A\beta_{40}$ (10 μM) was treated with $CuCl_2$ for 2 min followed by **4** for up to 3 h, resulting in final [Aβ]:[$CuCl_2$]:[**4**] ratios of 1:1:2, 2:1:2, 2:1:1, or 2:2:1. The first condition using a 1:1:2 ratio was representative of the concentrations used in the *in vitro* aggregation studies (*vide infra*), and the resulting Cu(II) binding spectra in the presence of Aβ were observed to have similar features as those acquired without peptide present (Figures 4.3 and 4.5). In the conditions using substoichiometric Cu(II) relative to Aβ, it

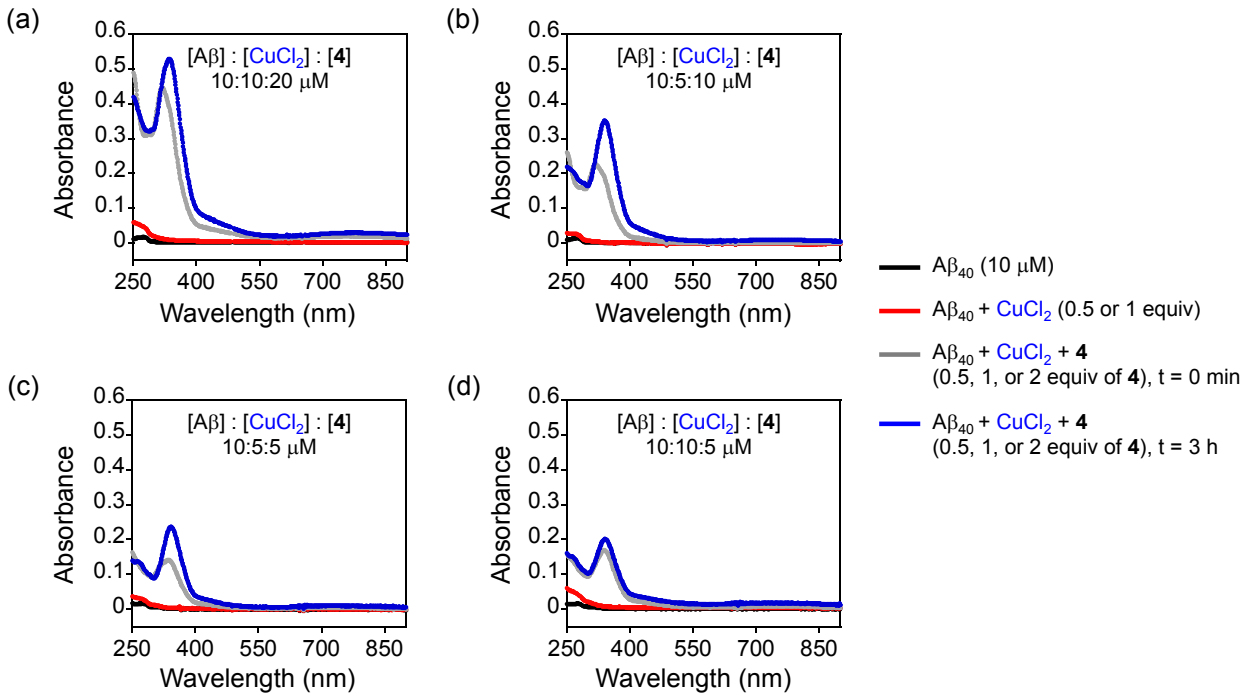

Figure 4.5. Interaction of **4** with Cu(II) in the presence of Aβ40. A solution containing Aβ40 (black) was treated with $CuCl_2$ (red) for 2 min followed by **4** (gray) for 3 h (blue). The ratios of Aβ40/$CuCl_2$/**4** were (a) 1:1:2, (b) 2:1:2, (c) 2:1:1, and (d) 2:2:1. Experimental conditions: [Aβ40] = 10 μM; [$CuCl_2$] = 5 or 10 μM; [**4**] = 5, 10, or 20 μM; 1% v/v DMSO; 20 mM HEPES, pH 7.4, 150 mM NaCl; room temperature.

was presumed that free Cu(II) in solution was minimal.[2-5,20] Incubation of **4** with the solution of Aβ and Cu(II) produced slight changes in the spectra indicating Cu(II)–**4** complex formation, supporting that this compound can possibly compete with Aβ as a ligand for Cu(II).

Overall, these investigations demonstrate binding of the catechol-containing aminoisoflavone derivatives to Cu(II) and Zn(II). The samples of solutions containing Cu(II) and the aminoisoflavones generated a unique optical feature, dominated by a low intensity transition bordering on the near-infrared region of the spectrum. This feature could correspond to changes in the electronic structure leading to a charge transfer process that populates a lower energy transition, as has been observed for different ligand frameworks.[80] Another possibility is that this feature represents a radical intermediate that was generated upon metal binding.[79,81,82] It has been well established that deprotonated catechol participates in an equilibrium that involves the partially

oxidized semiquinone and fully oxidized quinone.[81] In the presence of divalent cations such as Cu(II), this process might involve concomitant reduction of Cu(II) to Cu(I), while forming an oxidized ligand intermediate.[72,81,83] In a few cases, however, Cu(II)-semiquinone complexes have been reported; most of these complexes display are relatively colorless ($\varepsilon_{800} \approx 500$ $M^{-1}cm^{-1}$) and are paramagnetic,[79,84] which is consistent with our result. To advance the understanding of the Cu(II) binding properties of the aminoisoflavones, **4** was used as a model ligand for more detailed spectroscopic investigations.

First, stability constants ($\log\beta$) and the dissociation constants (K_d) of Cu(II)–**4** complexes in solution (1:2 [Cu(II)]/[**4**], I = 0.1 M, room temperature) were determined (Figure 4.6).[34,36,38-40,43,44,68,69] Based on the calculated $\log\beta$ values, a solution speciation diagram was generated and indicated a mixture of Cu(II)–**4** complexes in 1:1 and 1:2 Cu(II)/ligand ratios. At pH 7.4, Cu(LH) existed relatively predominantly (*ca.* 60%; $\log\beta$ = 30.0 ± 0.1; LH represents the monoprotonated form of **4** where the hydroxyl group in the *para* position of the B ring is protonated). There were additional species present at pH 7.4 such as Cu(L)(LH) (*ca.* 13%, $\log\beta$ = 40.7 ± 0.1) and $Cu(LH)_2$ (*ca.* 26%, $\log\beta$ = 48.4 ± 0.1). Upon titration, the solution was mainly 1:1 complexes below pH 7 (*i.e.*, $Cu(LH_2)$, $\log\beta$ = 35.8 ± 0.1; $Cu(LH_3)$, $\log\beta$ = 39.8 ± 0.1; $Cu(LH_4)$, $\log\beta$ = 42.2 ± 0.7). In addition to these species, Cu(L) ($\log\beta$ = 19.9 ± 0.3) and $Cu(L)_2$ ($\log\beta$ = 31.2 ± 0.3) were used to obtain a reasonable fit to the data; however, they accounted for a minor fraction of the solution speciation at pH 8. Above pH 9, $Cu(L)_2$ complexes were observed to be the main species. From this model, **4** was found to have high binding affinity for Cu(II) estimated based on the free Cu(II) concentration measured at a given pH (*i.e.*, pCu = $-\log[Cu(II)_{\text{unchelated}}]$).[34,36,39,40,43,44,68,69] At pH 7.4, which was used for the *in vitro* experiments and is physiologically relevant, the pCu value for **4** was 16.2, suggesting an estimated K_d for Cu(II)–**4** in the femtomolar range.

In order to minimize the number of ligand components in solution available to bind to Cu(II) and to optimize Cu(II) binding, the initial pH of the solution was adjusted to 8. Although the expected ligand form at this pH is the doubly protonated LH_2, upon Cu(II) binding the pK_a values for the catechol site could be lowered such that both the fully deprotonated (L) and monoprotonated (LH) ligand may exist in solution.[85,86] Under

this condition, a mixture of Cu(L)(LH) and Cu(LH) existed; however, there was also a minor contribution from $Cu(LH)_2$ and $Cu(L)_2$. These studies demonstrate that the aminoisoflavone ligands possessing a catechol moiety are capable of chelating Cu(II) showing 1:1 and 1:2 metal/ligand stoichiometry with different protonated ligand forms. The K_d value for **4** to Cu(II) was found to be *ca.* 0.1 fM, which is slightly stronger than most reported K_d values for Cu(II)–Aβ peptides (*i.e.*, nanomolar to picomolar) and could be used to rationalize the partial chelation of Cu(II) by **4** in the presence of Aβ observed by UV-Vis (*vide supra*).[2-5,19,20] Along with the Cu(II) binding studies in the presence of

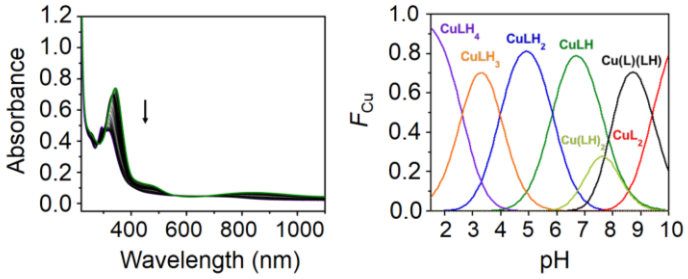

			$\log\beta^a$
Cu + L	⟷	Cu(L)	19.9(3)[b]
Cu + 2L	⟷	$Cu(L)_2$	31.2(3)
Cu + L + LH	⟷	Cu(L)(LH)	40.7(1)
Cu + 2LH	⟷	$Cu(LH)_2$	48.4(1)
Cu + LH	⟷	Cu(LH)	30.0(1)
Cu + LH_2	⟷	$Cu(LH_2)$	35.8(1)
Cu + LH_3	⟷	$Cu(LH_3)$	39.8(1)
Cu + LH_4	⟷	$Cu(LH_4)$	42.2(7)

Figure 4.6. Solution speciation studies of Cu(II)–**4** complexes. Top: Variable-pH UV-Vis titration spectra (left) and solution speciation diagram (right) for Cu(II)–**4** (F_{Cu} = fraction of species in solution relative to Cu(II)). Bottom: Summary of solution equilibria and stability constants (logβ). Experimental conditions: [$CuCl_2$] = 15 μM, [**4**] = 30 μM; pH 8; *I* = 0.1 M NaCl; room temperature. Charges are omitted for clarity. [a] The error in the last digit is shown in parentheses. [b] Cu(L) was introduced in the calculation to provide the best fit to the data, but was shown to constitute a negligible amount to the overall solution speciation.

Aβ (Figure 4.5), these data represent that it is possible for **4** and other catechol-containing aminoisoflavone compounds (*e.g.*, **2**, **3**) to be competitive ligands for Cu(II) with Aβ. Taken together, it might be possible for these ligands to partially sequester some of the Cu(II) or Zn(II) from Aβ in solution or to form a complex species similar to

that generated for the flavonoid EGCG with metal–Aβ species,[36,43,54] which may be correlated to their ability to modulate metal-induced Aβ aggregation *in vitro*.

4.2.4. EPR investigations of Cu(II)–4 complexes

As a result of its redox properties, catechol can be oxidized to a semiquinone (one electron oxidized form) or quinone (two electron oxidized form), each with distinguishable spectral properties.[81] In the presence of Cu(II), the deprotonated catechol (catecholate) could bind **4** and displayed metal-based EPR spectra. Electron transfer from catecholate to Cu(II), however, can yield a Cu(I)–semiquinone species that would appear as a ligand-based radical by EPR. As described above, Cu(II) binding to the aminoisoflavones produced a distinct optical feature at *ca.* 800 nm, which has been observed with other ligand frameworks and could correspond to a Cu(II)-semiquinone complex.[79,80] Given that several possible species have been reported as outcomes in similar reactions, it would be beneficial to characterize the Cu(II)–aminoisoflavone complexes generated in solution in more detail to better understand their contribution to reactivity with metal–Aβ species. Thus, the Cu(II) complexes with **4** formed in solution were characterized by EPR spectroscopy (Figures 4.7 and 4.8).

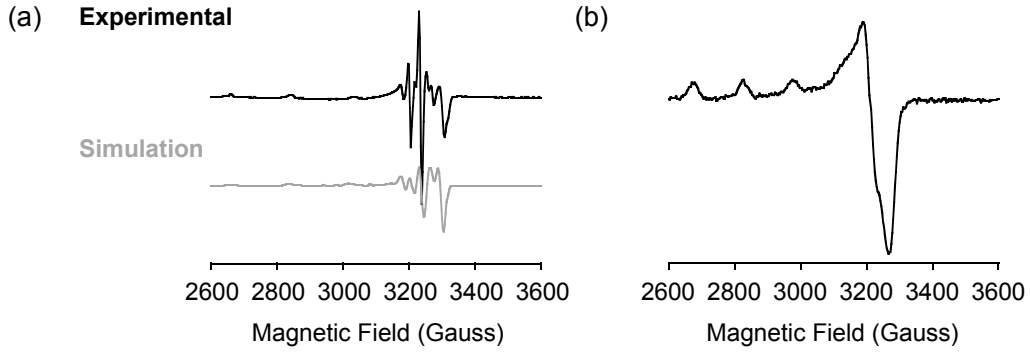

Figure 4.7. EPR spectra of (a) Cu(II)–**4** and (b) $CuSO_4$. (a) The EPR spectrum from the sample of **4** (500 μM) treated with $CuSO_4$ (250 μM) (top, black); EPR spectrum simulated by SpinCount (bottom, gray). (b) The EPR spectrum of the sample of $CuSO_4$ (250 μM) with EDTA (2.5 mM). Experimental conditions: 20 mM HEPES, pH 7.4, 150 mM NaCl. The spectra were recorded at 77 K with the instrument operating at 9.23 GHz, microwave power of 20 mW, a modulation frequency of 100 kHz, and a modulation amplitude of 5 G.

All solutions were prepared aerobically in HEPES buffer (20 mM, pH 7.4, 150 mM NaCl), similar to the UV-Vis metal binding studies (*vide supra*) and frozen for spectral acquisition. A sample of $CuSO_4$ (250 μM) with EDTA (2.5 mM) showed a typical axial Cu(II) EPR signal ($g_\perp$ = 2.053, $g_{//}$ = 2.288, $A_{//}$ = 560 MHz)[87,88] (Figure 4.7). Upon addition of $CuSO_4$ (250 μM) to a solution of **4** (500 μM), a spectrum with a well-resolved metal-based hyperfine splitting pattern was measured.[89] The spectrum was simulated in SpinCount with the following parameters: $g_\perp$ = 2.046, $g_{//}$ = 2.257, $A_\perp$ = 75 MHz, $A_{//}$ = 560 MHz, $sg_\perp$ = 0.005, $sg_{//}$ = 0.01 (Figure 4.7). Solutions frozen at different incubation time points over the course of 1 h displayed decreasing EPR intensity, with continued increase in the optical feature at 800 nm (data not shown). Due to possible formation of EPR detectable ligand-based intermediates with a catechol moiety, a solution of **4** that was partially oxidized via bulk electrolysis was investigated. To the solution, $ZnCl_2$ was added because Zn(II) has been known to stabilize semiquinone radicals.[90,91] When measured by EPR, an isotropic peak was observed at g = 1.995, indicating an organic radical form. No signal was observed, however, for the oxidized **4** in the absence of Zn(II), however, suggesting the generated radicals present in solution might couple to produce polymeric species that are EPR silent (Figure 4.8).[90]

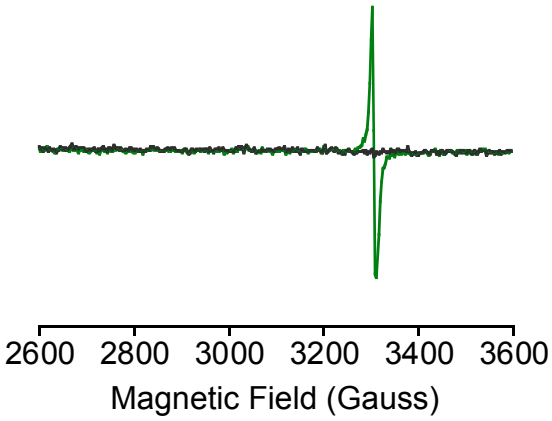

Figure 4.8. EPR spectra of partially oxidized **4** in absence (black) and presence (green) of $ZnCl_2$. The isotropic peak in (b) of oxidized **4** with Zn(II) was simulated with g = 2.00. All samples ([**4**] = 250 μM; [$ZnCl_2$] = 125 μM) were prepared in a buffered solution of 20 mM HEPES, pH 7.4, 150 mM NaCl. The EPR spectra were recorded with the instrument operating at 9.23 GHz, microwave power of 20 mW, a modulation frequency of 100 kHz, and a modulation amplitude of 5 G at 77 K.

The features of the EPR spectra from the sample of Cu(II)–**4** could represent a multitude of possible origins, especially owing to the redox properties of the catechol metal chelation group, which has an $E_{1/2}$ of *ca.* 75 mV versus SCE in **4** (Figure 4.9). In the literature, the valence tautomerization of Cu(II)–catechol interactions has been extensively investigated by Kaim and co-workers.[89,92] The spectrum shown in Figure 4.6is well matched to the reported spectrum for the catecholate form of the 3,5-di-*tert*-butoxy-*o*-benzoquinone complexed with Cu(II).[89,93] Reduction of Cu(II) to Cu(I) by the ligand to produce a Cu(I)–semiquinone that is not detectable by EPR, is plausible as well, which might be responsible for an overall decrease in EPR intensity. A Cu(I)-semiquinone would be expected to resemble an organic radical by EPR more than Cu(II), perhaps producing a spectrum similar to that in the presence of Zn(II) (Figure 4.8). The EPR spectra, however, do not suggest strong evidence for formation of the organic radical. Instead, the hyperfine splitting pattern appears to be mainly Cu(II)-centered throughout the course of the reaction.[89,94]

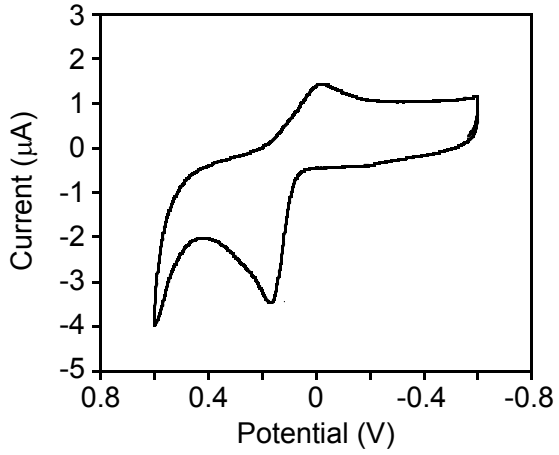

Figure 4.9. Cyclic voltammetry of **4**. Experimental conditions: [**4**] = 250 μM, 10% v/v DMSO; 20 mM HEPES, pH 7.4, 150 mM NaCl; room temperature, 10 mV/s scan rate.

There are several additional scenarios to account for the observed spectra. First, it has been suggested that coupling between Cu(II) in solution or the ratio of Cu(II) to ligand could reduce the EPR signal intensity in other polyphenolic ligand systems containing Cu(II).[90] Also, the addition of Cu(II) could stabilize the ligand (*i.e.*, as the

Cu(II)–catecholate) and prevent it from undergoing oxidation.[90] Coupled with the UV-Vis spectra of the Cu(II)–**4** complexes, however, formation of a Cu(II)–semiquinone complex is supported by the experimental evidence. The Cu(II)–semiquinone complex would be EPR silent due to antiferromagnetic coupling between the Cu(II) center and semiquinone radical,[84,93,95] and this complex typically displays low intensity transitions in the near-IR region of the spectrum. Therefore, this proposed intermediate is consistent with our results and would afford an overall decrease in EPR intensity with progressive generation of the intermediate.[79,95] Since the solution speciation studies indicate a mixture of 1:1 and 1:2 binding stoichiometries at pH 7.4 (Figure 4.6), it is not surprising that the EPR results also reveal the complexity of the solution. As described above, it is likely that our solution initially includes a Cu(II)–catecholate complex (1:1 or 1:2 Cu(II)/**4**) and over time could become partially oxidized to represent a heterogeneous species that containing either Cu(II)–semiquinone (1:1 or 1:2 Cu(II)/ligand) or Cu(II)(catecholate)(semiquinone) that is not detectable by EPR but has a spectral change by UV-Vis.[93] Overall, these investigations provide information on Cu(II) binding properties of **4** in detail.

4.2.5. Interaction of aminoisoflavones with Aβ species

The interaction between aminoisoflavones and Aβ species in solution was investigated by isothermal titration calorimetry (ITC), NMR, and docking studies. ITC was first used to measure thermodynamic parameters for the interaction of Aβ with **1**, **2**, and **4** (Table 4.1). Using a sequential binding model with one identical site to fit the data, these ligands were found to bind to $A\beta_{40}$ with *ca.* low mM affinity (K_A = (6.8 ± 3.0) x 10^4, (7.9 ± 2.9) x 10^3, and (3.2 ± 0.7) x 10^3 M^{-1} for **1**, **2**, and **4**, respectively) and with favorable values of Gibbs free energy (ΔG = −27.3 ± 1.1, −22.2 ± 0.9, and −19.9 ± 0.6 kJ/mol for **1**, **2**, and **4**, respectively) (Table 4.1). Different peptide–ligand interactions, however, likely accounted for favorable binding. For **1**, which lacks the catechol moiety, entropic contributions ($-T\Delta S$ = −38.7 ± 1.6 kJ/mol) were greater than enthalpic contributions (ΔH = +11.3 ± 1.2 kJ/mol). Conversely, the enthalpic term for **4** is large and negative in magnitude (ΔH = −116.3 ± 19.6 kJ/mol), while the contribution from

entropy is unfavorable ($-T\Delta S$ = +96.4 ± 19.6 kJ/mol). Similar to **4**, compound **2** showed unfavorable entropic ($-T\Delta S$ = +36.9 ± 22.6 kJ/mol) and favorable enthalpic (ΔH = −59.1 ± 22.6 kJ/mol) contributions (Table 4.1). The thermodynamic parameters governing these peptide–small molecule interactions can be related to the variations in their chemical structures. Since **1** and **2** or **4** are distinguished by the absence or presence of a catechol moiety for metal binding, it is reasonable to expect that they may favor dissimilar interactions with the peptide. Compound **1** contains an unsubstituted phenyl ring, which might suggest that their interactions are mainly driven by hydrophobic interaction with the peptide; these types of interactions usually translate to an increase in the entropy as measured by ITC.[96] Conversely, **4** would potentially facilitate the formation of hydrogen bonding contacts between the molecule and the peptide in solution due to the *o*-dihydroxy groups from the catechol moiety, resulting in favorable interaction indicated by the large, negative ΔH value.[96] The compound **2**, which has a catechol group in the B ring but has no functionality on the A ring, presented a similar result to **4**, suggesting that these molecules interact with Aβ similarly due to the presence of the catechol group which facilitates mainly hydrophilic contacts. Despite distinctive direct contacts predicted with the peptide for **1** compared to **2** and **4**, each of these molecules have favorable Gibbs free energy values that could be used to rationalize the ability of both of these molecules to modulate metal-free Aβ aggregation (*vide infra*).

Table 4.1. Thermodynamic values for the interaction of **1**, **2**, and **4** with $A\beta_{40}$ determined by isothermal titration calorimetry (ITC).

	1	**2**	**4**
K_A **(M^{-1})**	(6.8 ± 3.0) x 10^4	(7.9 ± 2.9) x 10^3	(3.2 ± 0.7) x 10^3
ΔG **(kJ/mol)**	−27.3 ± 1.1	−22.2 ± 0.9	−19.9 ± 0.6
ΔH **(kJ/mol)**	11.3 ± 1.2	−59.2 ± 22.6	−116.3 ± 19.6
$-T\Delta S$ **(kJ/mol)**	−38.7 ± 1.6	36.9 ± 22.6	96.4 ± 19.6

The ITC results suggest compounds **1**, **2**, and **4** bind freshly dissolved, low MW $A\beta_{40}$. The mechanism of binding, however, appears to differ with the relative balance of enthalpic and entropic contributions to binding for each compound varying depending on the presence of the catechol group. Accordingly, the binding of compounds **1** and **4** to low MW $A\beta_{40}$ was subjected to further analysis by NMR. Previously, we have shown that low MW species in freshly dissolved $A\beta_{40}$ can adopt a 3_{10} helical structure in the central hydrophobic region at moderate ionic strength and low temperature (PDB ID 2LFM).[97] Using similar conditions, we attempted to map the regions of $A\beta_{40}$ responsible for binding the aminoisoflavones.

Changes in the SOFAST-HMQC spectra of freshly dissolved $A\beta_{40}$ upon titration with **1** and **4** confirm both species were capable of binding low MW $A\beta_{40}$ (Figures 4.10 and 4.11). The chemical shift perturbations were slightly larger for compound **1** (Figures 4.11a and 4.11b) than **4** (Figures 4.11a and 4.11c), in agreement with the larger free energy change upon binding low MW $A\beta_{40}$ for compound **1** as measured by ITC. Moderate (0.02-0.15 ppm on the scaled chemical shift scale) chemical shift perturbations were detected for both compounds in two specific regions of the peptide near the N-terminus (R5-S8) and the N-terminal part of the 3_{10} helix (H13-L17) (Figure 4.11a). These two regions are close together in the $A\beta_{40}$ structure (Figure 4.11d) and appear to form a specific binding site for the compounds. A third area of chemical shift perturbation is closer to the C-terminus (M35-V40). The chemical shifts near the C-terminus may reflect either the rearrangement of the disordered C-terminus to pack against the aminoisoflavone or may be an indication of a second lower affinity binding site. The perturbation of the chemical shifts on specific residues of $A\beta_{40}$ by aminoisoflavones was notably different than what was observed with the related catechol EGCG with $A\beta_{40}$ and α-synuclein, where large nearly uniform decreases in intensity have been observed suggestive of non-specific binding[54,59,98] and indicated polyphenols do not have a single uniform mechanism.[99] To visualize the potential contacts of **1**, **2**, and **4** with $A\beta_{40}$, flexible ligand docking studies were employed with the solution NMR structure of metal-free $A\beta_{40}$ (PDB 2LFM) (Figure 4.12).[97] The docked poses of these ligands with the peptide were generally found in similar positions around

the peptide, situated nearer to the N-terminus or 3_{10}-helix, similar to the chemical shift perturbations observed by NMR and similar to previous results obtained with the structurally related catechin, EGCG.[54] Interaction near the N-terminus of $A\beta_{40}$ is desirable because the residues that bind Cu(II) and Zn(II) exist in this portion of the sequence, while interaction with the helical portion of the peptide could be beneficial to hinder the initial stages of self-association (L17-A21).[2]

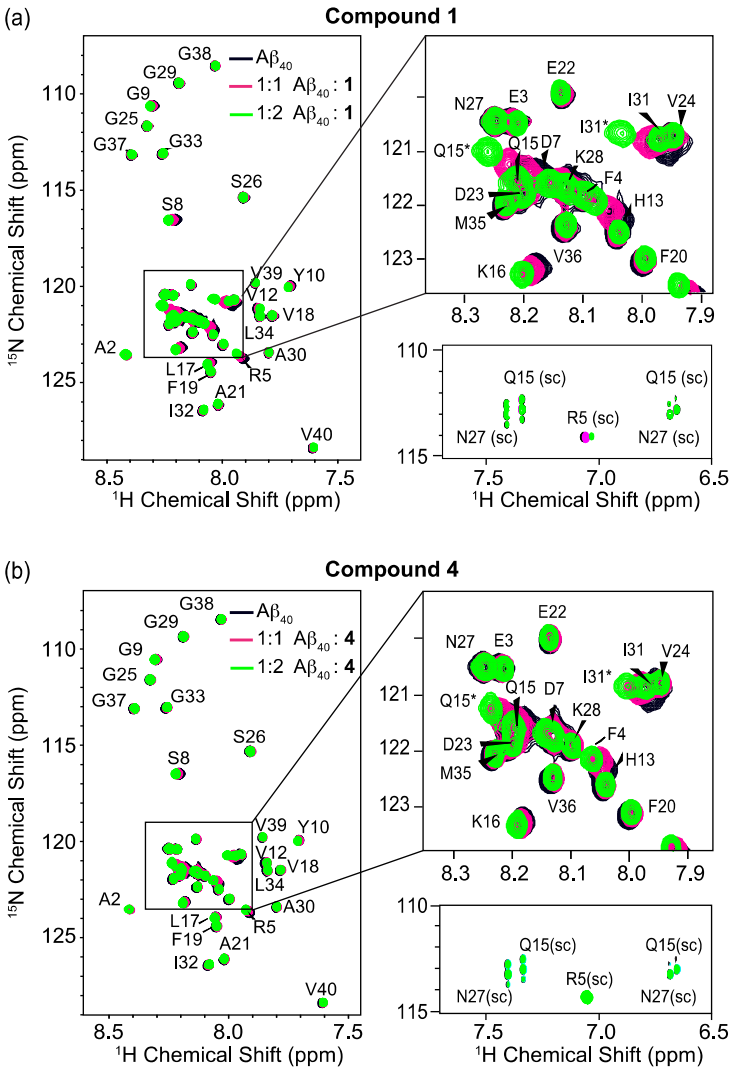

Figure 4.10. Interaction of **1** and **4** with low MW $A\beta_{40}$ at near stoichiometric ratios. SOFAST-HMQC spectra of 80 μM freshly dissolved $A\beta_{40}$ in 20 mM deuterated Tris (pH 7.4) with 50 mM NaCl and 10% D_2O and titrated with (a) **1** and (b) **4** to the indicated molar ratios at 4 °C. Chemical shift perturbations were detected primarily for the amide resonances R5-S8 and H13-L17 (see Figure 4.11).

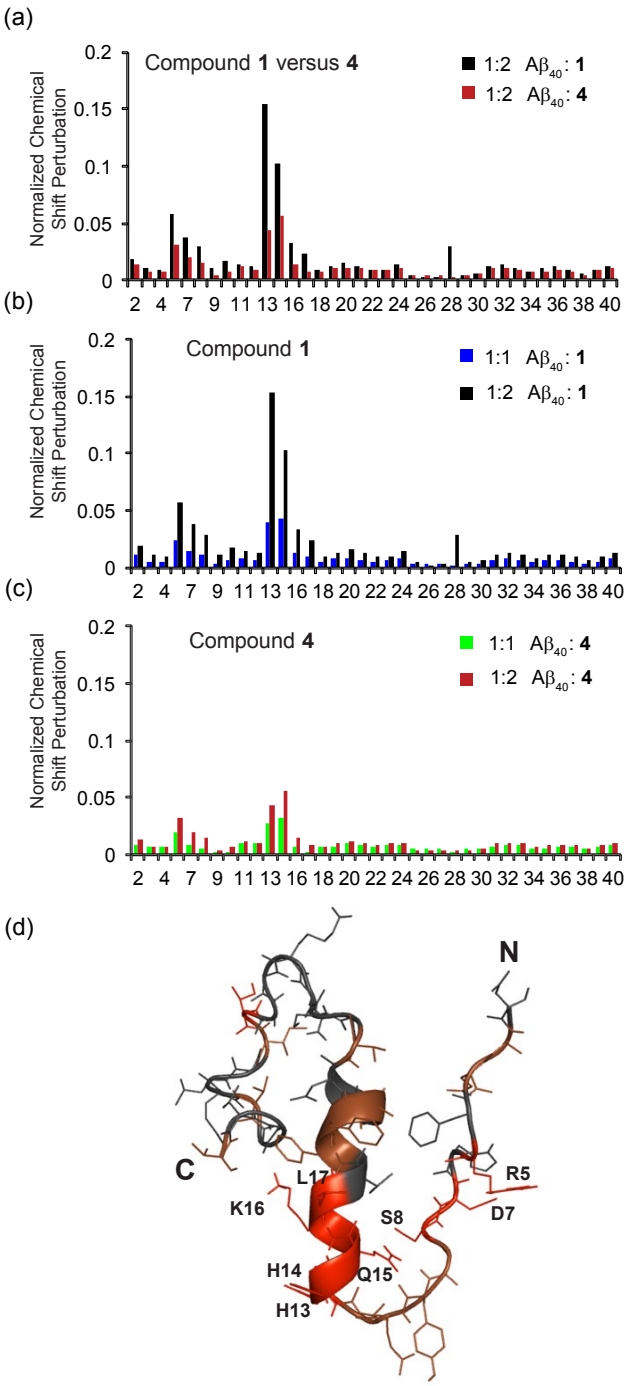

Figure 4.11. Chemical shift changes in low MW Aβ40 induced by **1** and **4**. (a) Chemical shift perturbations for Aβ40 in the presence of **1** or **4** (1:2 molar ratio). The normalized chemical shift perturbation is equivalent to $\sqrt{(\Delta^1 H)^2 + \frac{(\Delta^{15} N)^2}{\sqrt{5}}}$. Normalized chemical shift perturbations for (b) **1** and (c) **4**. (d) Residues with the largest chemical shift perturbations mapped onto the NMR structure of low MW Aβ40 (PDB 2LFM). The residues with the largest chemical shift perturbations (> 0.02 ppm) are colored red, residues with smaller chemical shift perturbations (0.01-0.02 ppm) are colored brown.

The similarity in the pattern of the chemical shift perturbations suggests **1** and **4** bind to the same site in $A\beta_{40}$ (Figure 4.11a). Although the compounds also often preferred similar binding modes in the docking studies, there were some slight deviations among the results that could support the findings from ITC. For example, there were a few instances where **4** was oriented in a more favorable position to facilitate hydrogen bonding contacts while in some poses, **1** was more aligned with the helical portion of the peptide. Compound **2** could dock in similar positions as both ligands, as expected based on its structure, with most poses being situated near the N-terminus in the area preceding the helical portion of the peptide, similar to the NMR results for compounds **1** and **2**. Although the overall view of the ligand interactions with $A\beta_{40}$ from NMR and docking are relatively consistent with the ITC results, the magnitude of the interactions cannot be completely determined from either technique.

As noted above, only moderate chemical shift perturbations were detected for specific regions of $A\beta_{40}$ at 1:1 and 1:2 protein-to-ligand molar ratios. At higher concentrations of compound **1** (1:5 $A\beta_{40}$:**1**), much larger changes in chemical shift were observed along with a strong reduction in intensity (Figure 4.13). The changes in chemical shift did not appear to match the pattern obtained at lower concentrations of **1**, although for many residues a definite assignment could not be made. Two new negative (folded) broad peaks were also apparent in the SOFAST-HMQC spectra in the side-chain region of the spectra below 7.5 ppm. The appearance of a new species at higher ligand concentrations was also supported by a strong new peak at 7.64 ppm and three weaker doublets at 6.77, 6.83, and 6.89 ppm in the ^{1}H spectrum of the ligand (Figure 4.14). The intensity changes were not accompanied by the increase in linewidth that would be expected for exchange broadening, which suggests some of the peptide was lost instead to aggregation. The dramatic changes in the SOFAST-HMQC spectra suggest either a global conformational change may have taken place, or compound **1** may have covalently attached to the peptide through Schiff base formation as has been observed before with other flavonoids.[100-102]

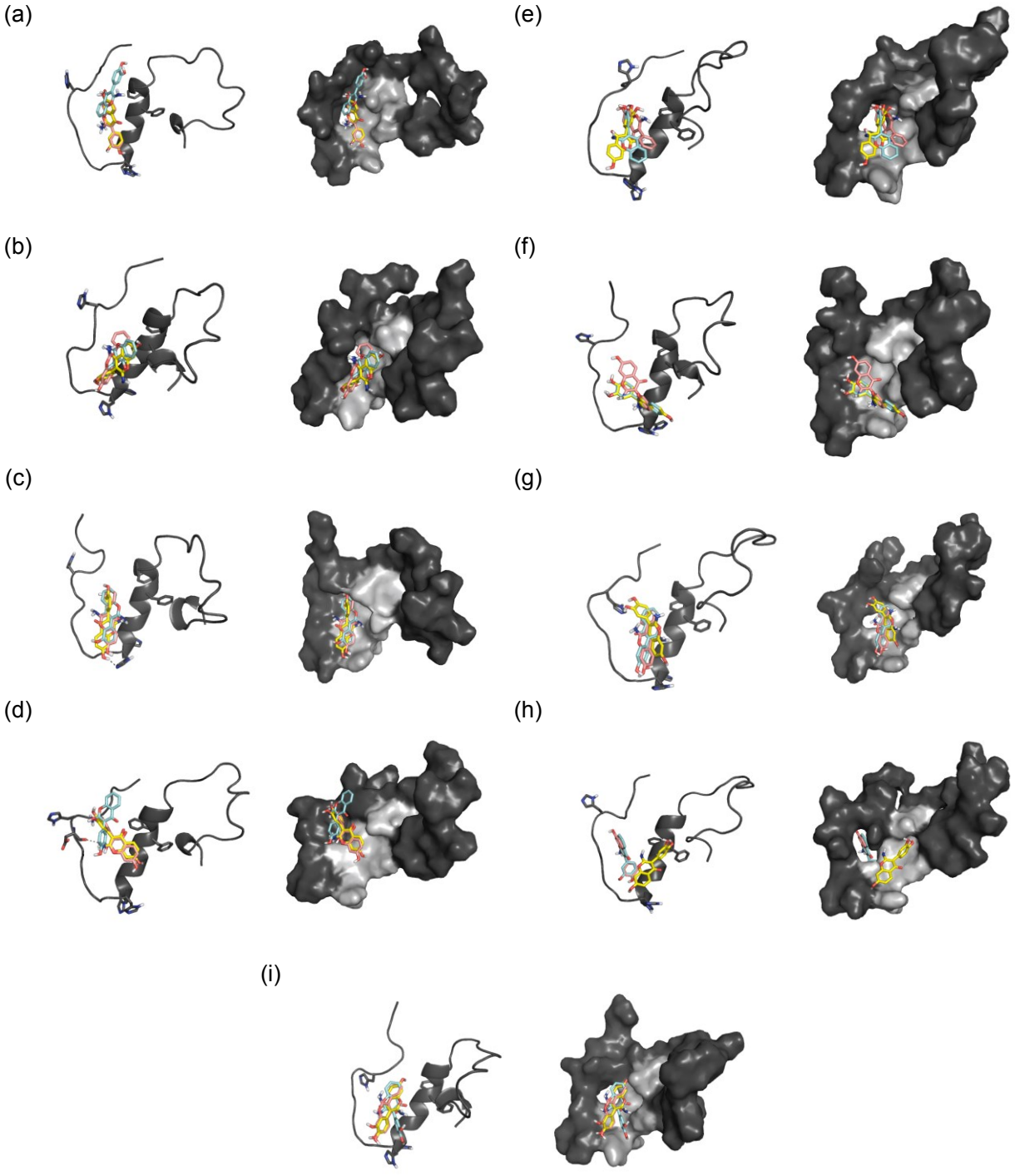
(a)
(e)
(b)
(f)
(c)
(g)
(d)
(h)
(i)

Conformation	1 (kcal/mol)	2 (kcal/mol)	4 (kcal/mol)
a	−6.4	−6.3	−6.4
b	−5.9	−5.8	−5.9
c	−6.2	−6.2	−6.3
d	−5.8	−5.9	−5.8
e	−5.8	−5.9	−6.0
f	−5.8	−6.0	−5.7
g	−5.7	−5.8	−5.7
h	−6.0	−5.9	−6.0
i	−6.2	−5.9	−6.0

Figure 4.12. Docking studies of **1**, **2**, and **4** with metal-free Aβ$_{40}$ (PDB ID 2LFM). Top: Cartoon (left) and surface (right) representations of the peptide are depicted with **1** (pink), **2** (light blue) and **4** (yellow). Bottom: Summary of predicted binding energies for the ligands docked with Aβ$_{40}$.

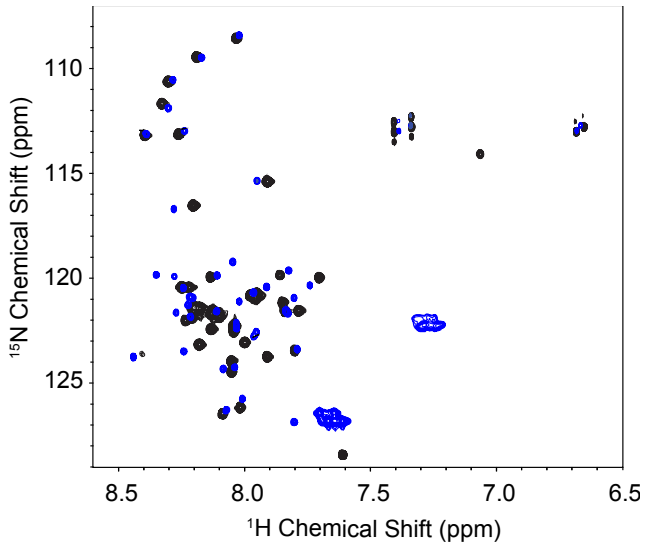

Figure 4.13. Interaction of low MW Aβ$_{40}$ with a 5 equiv of **1**. SOFAST-HMQC spectra of 80 μM freshly dissolved Aβ$_{40}$ in 20 mM deuterated Tris (pH 7.4) with 50 mM NaCl and 10% D_2O with a 5 equiv of **1** at 4 ºC. Large chemical shift changes indicate a global change in conformation has taken place, possibly due to the formation of covalent adducts.

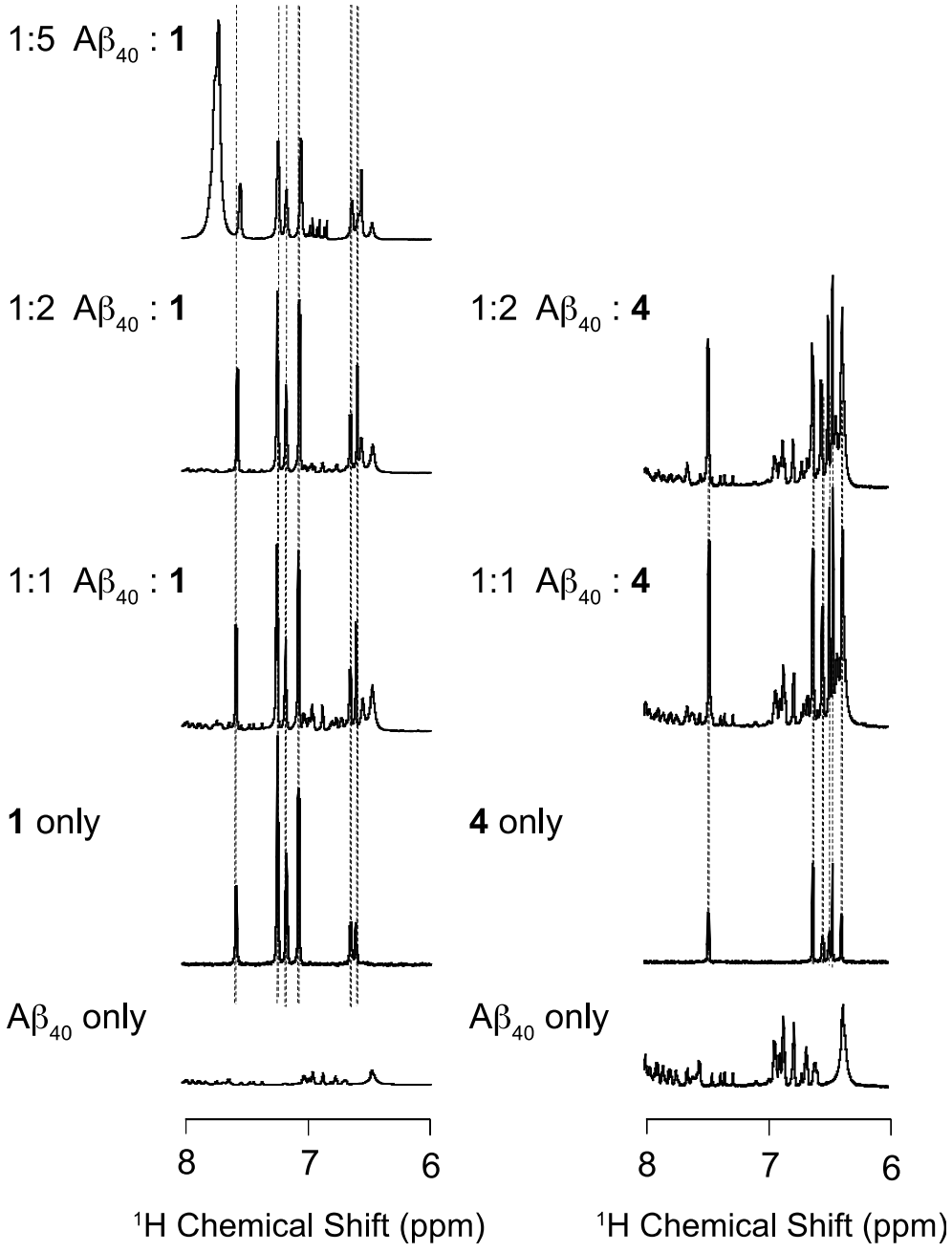

Figure 4.14. ^{1}H spectra of low MW Aβ40 titrated with **1** and **4**. A solution of freshly dissolved Aβ40 (80 μM) in 20 mM deuterated Tris (pH 7.4) with 50 mM NaCl and 10% D_2O was titrated with either **1** or **4** to the indicated molar ratios at 4 ºC New peaks at 7.64, 6.77, 6.83, and 6.89 ppm with 5 equiv of **1** indicate the presence of a new ligand species.

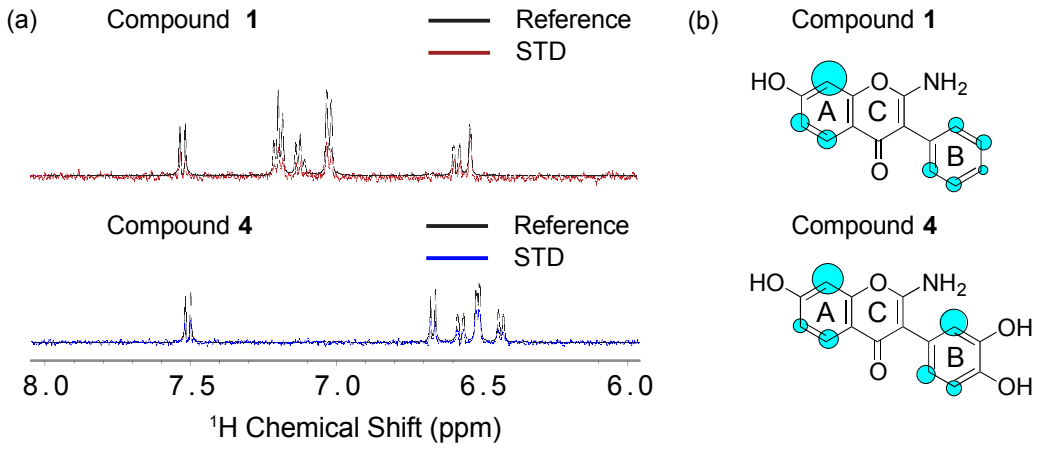

Figure 4.15. Interaction of **1** and **4** with Aβ40 fibrils by STD NMR. (a) STD NMR spectra of **1** and **4** at 10:1 ligand to peptide ratio using preassembled Aβ40 amyloid fibrils. A comparison of STD signal intensity to the STD reference reflects the relative proximity of the corresponding proton to the Aβ40 fibril. (b) Normalized STD intensities mapped onto each compound's structure. Larger blue circles indicate a more intense STD effect. Note that the hydroxyl and amine protons were not detected by this experiment.

In addition to binding to low MW Aβ40, compounds **1** and **4** may have the capability to bind to other forms of Aβ40, such as fibrils. To probe these possible interactions, we employed saturation difference (STD) NMR experiments to map the regions of the ligand, which bind to preformed fibrils of Aβ40 (Figure 4.15).[103] The normalized signal strengths (STD/STD reference) corresponding to each ligand atom are proportional to its proximity to the amyloid fibril, allowing an atomic-level map of the binding interactions from the ligand to the amyloid fibril to be made.[103] The results from the STD NMR experiments show both **1** and **4** interact fairly strongly (mM to μM dissociation constant) with the fibril to elicit a relatively strong STD signal (approximately 4.5% (compound **1**) and 5.9% (compound **4**) of the reference signal at a 3 second saturation power of 50 dB, similar in magnitude to previous results with other catechols[103]). The STD results show **1** and **4** bind similarly to the amyloid fibril (Figure 4.15b). The STD effect was distributed relatively evenly throughout both compounds, suggesting the entire molecule is packed to some degree against the fibril. In both compounds the strongest interaction is at carbon 8 on the A ring, suggesting the ketone is pointed away from the fibril in both compounds. While the STD pattern is overall similar, carbon 2' in the B ring in compound **4** has a significantly higher STD effect than

the corresponding carbon in compound **1**. The increase in this region is an indication that the presence of the catechol group causes a reorientation of compound **4** to put the B ring in closer contact with the fibril, which may explain the somewhat higher affinity of compound **4** over compound **1** for the amyloid fibril.

4.2.6. Aβ aggregation in the absence and presence of aminoisoflavones

The extent to which the aminoisoflavones could modulate Aβ aggregation in the absence and presence of Cu(II) and Zn(II) was investigated.[12,35-40,43,44,54,104,105] In the inhibition experiment (Figure 4.16), $A\beta_{40}$ or $A\beta_{42}$ (10 μM) was incubated with or without the addition of $CuCl_2$ or $ZnCl_2$ (10 μM) along with the aminoisoflavone (20 μM) for 24 h at 37 °C with constant agitation. For the disaggregation studies (Figure 4.17), $A\beta_{40}$ or $A\beta_{42}$ (10 μM) aggregates were intentionally formed upon 24 h incubation at 37 °C with constant agitation in the absence or presence of $CuCl_2$ or $ZnCl_2$ (10 μM). The aminoisoflavones were then added to the solution of Aβ aggregates for an additional 24 h. For both studies, gel electrophoresis with Western blotting was used to visualize the molecular weight (MW) distribution of the resulting Aβ species and transmission electron microscopy (TEM) was employed to detect changes to peptide morphology.

In the inhibition experiment, differences in Aβ species distribution were observed in the metal-free and Cu(II)- or Zn(II)-containing Aβ samples depending on the compound present (Figure 4.16). All of the aminoisoflavones were able to modulate metal-free $A\beta_{40}$ aggregation, as evidenced by a range of sizes visualized in the Western blot compared to the control of only $A\beta_{40}$ (Figure 4.16a, middle). In the presence of Cu(II) or Zn(II), however, the reactivity of the aminoisoflavones with Aβ was distinct from that with metal-free $A\beta_{40}$. Both Cu(II)- and Zn(II)-mediated $A\beta_{40}$ aggregation were influenced by **2**, **3**, and **4**, but not by **1**. The Aβ species generated with metal ions in the presence of **2**, **3**, and **4** were mainly below 75 kDa (Figure 4.16a, middle), which could indicate redirection of Aβ aggregation as has been previously described for flavonoids.[54,59,99,106,107] A slight difference in the Zn(II)–$A\beta_{40}$ samples was observed for **2** compared to **3** and **4**, where fewer high MW gel-permeable aggregates were detected (Figure 4.16a). This could represent a modest effect from the inclusion of the additional

substituents (*i.e.*, Cl, OH) that are present in the A ring for **3** and **4** on aggregation relative to the unsubstituted analogue, **2**. Typically, unstructured, amorphous Aβ aggregates have been shown to be products the previously reported settings.[54,59,99,106,107] Similarly, TEM images of the aggregates in the Cu(II)- and Zn(II)-treated Aβ samples treated with **4** appeared as smaller-sized, amorphous species while in the control samples for Cu(II)- and Zn(II)–$A\beta_{40}$, large Aβ aggregates were observed (Figure 4.16a, bottom). In contrast, the metal-free $A\beta_{40}$ sample in the presence of **4** mainly displayed structured aggregates similar to the control. In addition, there were minimal morphological changes to the Aβ aggregates from the samples (metal-free, Cu(II), and Zn(II)) treated with **1** compared to the controls suggesting that this compound may interact with Aβ and metal–Aβ species differently from **4**.

It is also relevant to consider the reactivity of these ligands with $A\beta_{42}$, which has been suggested to be abundant in the plaques and has been found to aggregate via different intermediates than $A\beta_{40}$.[5,7,10,108] Overall, the pattern observed for $A\beta_{42}$ is analogous to those for $A\beta_{40}$ in the inhibition experiment (Figure 4.16a and b). Metal-free $A\beta_{42}$ aggregation was influenced to a lesser degree by **1** than **2**, **3**, and **4**, which presented a modest influence on metal-free $A\beta_{42}$ aggregation. In the samples containing metal ions, **2**, **3**, and **4** clearly affected the aggregation pathway to a greater extent, generating a variety of Aβ species having different MW. The size distribution among these samples was almost indistinguishable indicating that all three of the metal binding compounds (*i.e.*, **2**, **3**, and **4**) may alter metal-induced $A\beta_{42}$ aggregation similarly (Figure 4.16b, middle). Comparison of TEM for the $A\beta_{42}$ samples treated with **1** and **4** was consistent with the gel results. Whereas compound-untreated metal-free Aβ or metal–Aβ showed relatively structured peptides, mixtures of large, amorphous aggregates were observed in samples of metal-free or metal-induced Aβ with **1** or **4**, which could represent Aβ species of various sizes in the gel samples (Figure 4.16b, bottom).

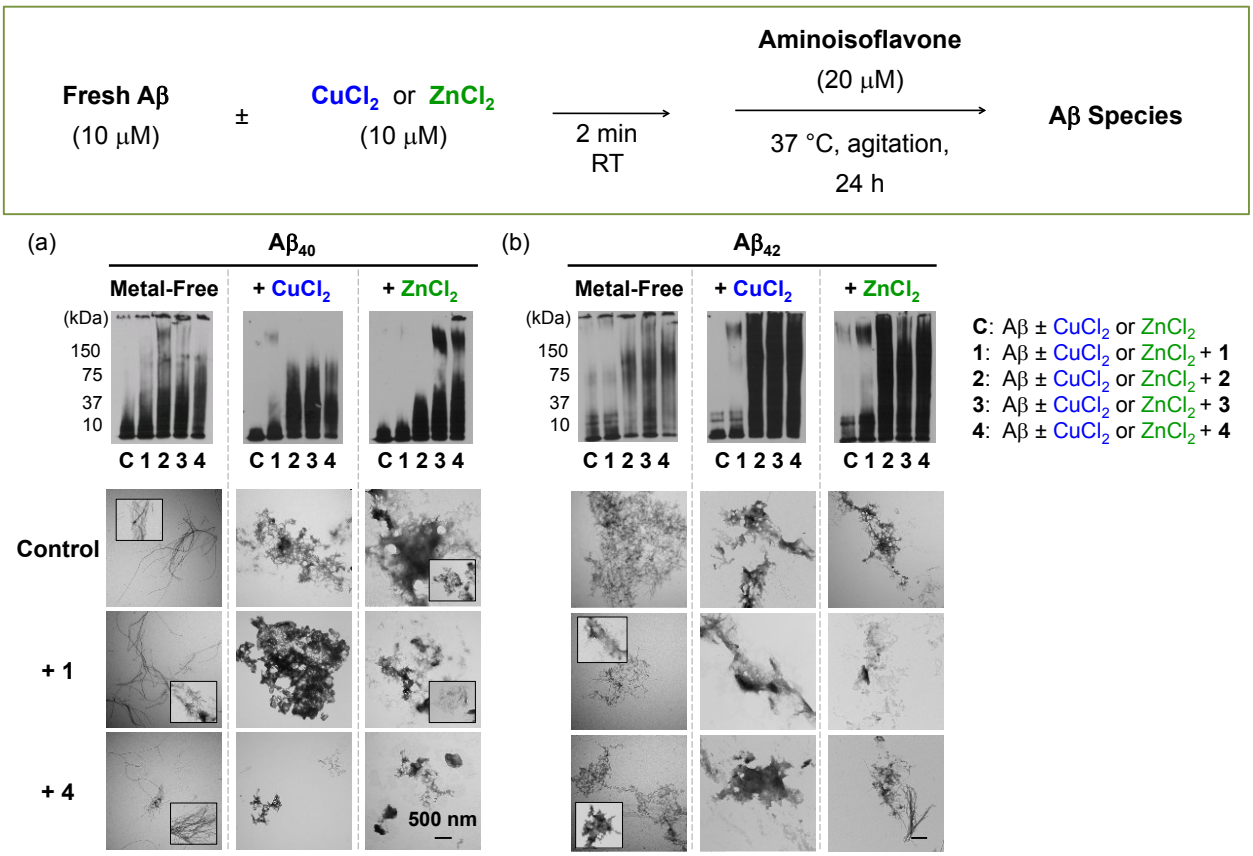

Figure 4.16. Investigation of the ability of aminoisoflavones (**1**-**4**) to modulate the formation of metal-free and metal-induced Aβ40 and Aβ42 aggregates. Top: Scheme of the inhibition experiment. Middle: Analysis of the samples including (a) Aβ40 and (b) Aβ42 by gel electrophoresis followed by Western blotting (6E10). Lanes: (C) Aβ ± $CuCl_2$ or $ZnCl_2$ (C = control), (1) C + **1**; (2) C + **2**; (3) C + **3**; (4) C + **4**. Bottom: TEM images of samples with **1** or **4** for (a) Aβ40 and (b) Aβ42. Experimental conditions: [Aβ40 or Aβ42] = 10 μM; [$CuCl_2$ or $ZnCl_2$] = 10 μM; [aminoisoflavone] = 20 μM; 1% v/v DMSO; 20 mM HEPES, pH 7.4, 150 mM NaCl; 24 h; 37 °C; agitation.

The aminoisoflavones were also evaluated with preformed metal-free and metal-associated Aβ40 or Aβ42 aggregates to determine whether they could transform structurally ordered peptide species (Figure 4.17). Similar to the inhibition results, a slight interaction between **1** or **3** but not **2** or **4** and metal-free Aβ40 aggregates was observed; however, Aβ aggregates formed in the presence of Cu(II) or Zn(II) produced a wide range of sizes when incubated with **2**, **3**, and **4** (Figure 4.17a, middle). In contrast to the inhibition experiment, a portion of gel permeable species with high MW began to enter the gel matrix for Cu(II)–Aβ samples treated with **1**. Whereas **1** was

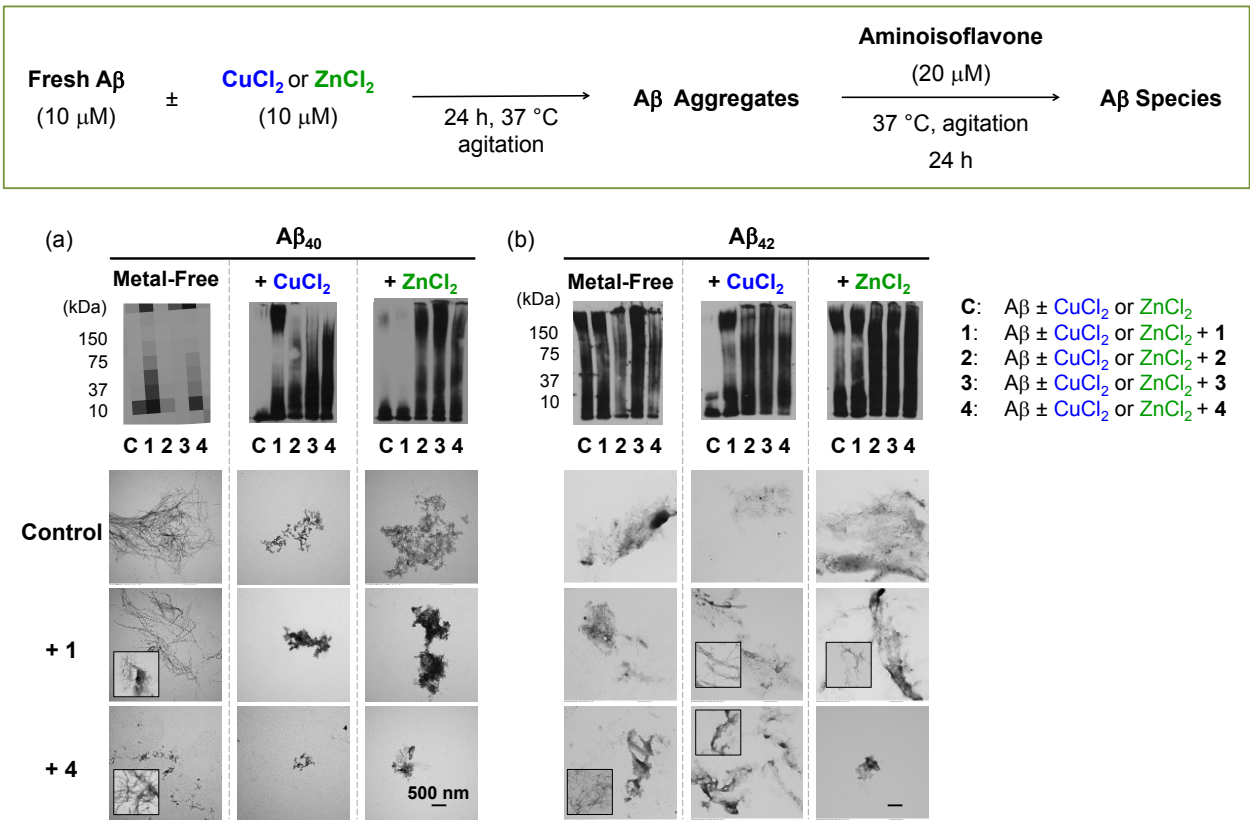

Figure 4.17. Disassembly of metal-free and metal-associated Aβ40 and Aβ42 aggregates by aminoisoflavones. Top: Scheme of the disaggregation experiment. Middle: Analysis of the samples containing (a) Aβ40 and (b) Aβ42 by gel electrophoresis followed by Western blotting (6E10). Lanes: (C) Aβ ± $CuCl_2$ or $ZnCl_2$, (1) C + **1**, (2) C + **2**, (3) C + **3**, (4) C + **4**. Bottom: TEM images of samples with **1** or **4** for (a) Aβ40 and (b) Aβ42. Experimental conditions: [Aβ40 or Aβ42] = 10 μM; [$CuCl_2$ or $ZnCl_2$] = 10 μM; [aminoisoflavone] = 20 μM; 1% v/v DMSO; 20 mM HEPES, pH 7.4, 150 mM NaCl; 24 h; 37 °C; agitation.

unable to inhibit aggregation (Figure 4.16a), this slight difference for the disaggregation results suggests this compound may interact with folded peptides, allowing it to partially promote disaggregation for preformed Cu(II)–Aβ40 species (Figure 4.17a). Different from **1**, metal chelation via the catechol moiety in **2**, **3**, and **4** likely plays a role in redirecting preformed metal–Aβ aggregates. As with the inhibition experiments using metal-associated Aβ40, there is a subtle difference in the MW distribution of the metal–Aβ disaggregation samples depending on the substituents present in **2**, **3**, or **4**. For example, Cu(II)-treated Aβ40 aggregates span a wider range of MW in the presence of **3**

or **4**, compared to **2**, which could arise from presence of the Cl or OH groups (Figure 4.11a). The TEM images from the disaggregation samples showed a mixture of large and small aggregates for metal-free Aβ_{40} in the presence of **1** and **4** (Figure 4.17a, bottom). For the samples of metal–Aβ species incubated with the compounds, their morphologies were less ordered and smaller in size compared to those of the controls. Finally, in the case of Aβ_{42}, it is challenging to discern which compounds were most efficacious against the pregenerated Aβ aggregates. In the samples of metal-free Aβ_{42} and metal–Aβ_{42}, various sizes of aggregates were detected throughout the entire gel matrix. TEM images of these samples also revealed the heterogeneity of the conformations with and without **1** or **4** (Figure 4.17b, bottom).

For comparison, the methoxylated precursors of **1**, **2**, and **4** (*i.e.*, **1a**, **2a**, and **4a**, respectively; Scheme 4.1 for structures) were studied analogously in the inhibition and disaggregation experiments (Figure 4.18). Different from the demethoxylated molecules (**1**-**4**) described above, a minimal effect on only Cu(II)–Aβ_{40} was observed upon incubation with **1a**, **2a**, and **4a** based on the patterns of MW distribution compared to those of the corresponding inhibition and disaggregation controls. In all scenarios, Zn(II)-mediated Aβ aggregation was unaffected by **1a**, **2a**, and **4a**, and overall their reactivity with metal-free and Cu(II)–Aβ samples was also reduced noticeably compared to **1**, **2**, and **4**. Thus, the catechol group for metal chelation, which has a high affinity for Cu(II) and could be capable of interacting with the peptide via hydrogen bonding based on ITC, NMR, and docking investigations, is suggested to be equally valuable for imparting proper metal/Aβ binding interactions.

Taken together, these results reveal the scope of flavonoid derivatives that can be used to modulate metal-free and metal-induced Aβ aggregation and validate the requirement for sufficient metal binding and Aβ interaction properties to suitably influence this reactivity. The inhibition results indicated aminoisoflavones may interact with metal-free and metal–Aβ species in a manner similar to other flavonoids like EGCG, which can target metal-free and metal-induced Aβ_{40} aggregation *in vitro* to different extents, although the MW distribution of Aβ achieved by the aminoisoflavones is distinct from that of EGCG.[54] The absence of a metal chelation moiety in **1** prevented

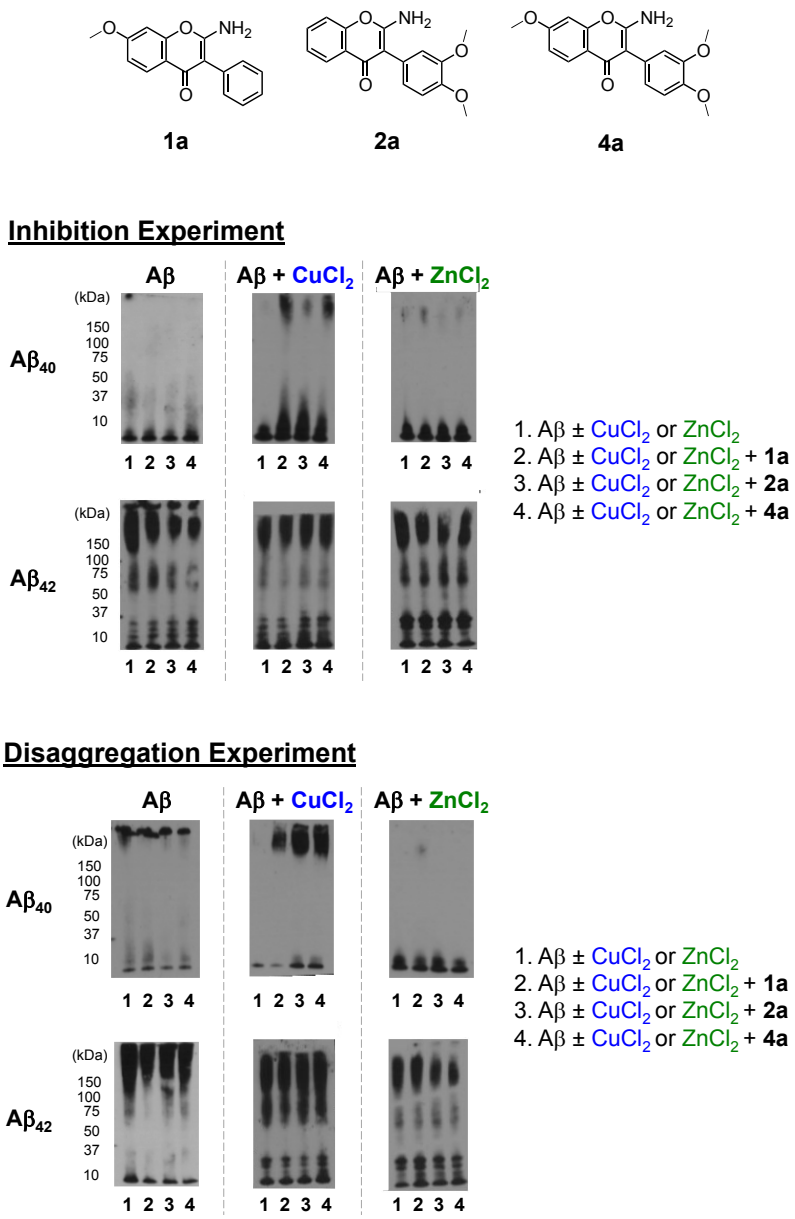

Figure 4.18. Inhibition and disaggregation experiments employing methoxylated aminoisoflavone precursors (**1a**, **2a**, and **4a**). Top: Structures of **1a** (2-amino-7-methoxy-3-phenyl-4*H*-chromen-4-one), **2a** (2-amino-3-(3,4-dimethoxyphenyl)-4*H*-chromen-4-one), and **4a** (2-amino-3-(3,4-dimethoxyphenyl)-7-methoxy-4*H*-chromen-4-one). Analysis of inhibition (middle) and disaggregation (bottom) samples with $A\beta_{40}$ and $A\beta_{42}$ by gel electrophoresis followed by Western blotting (6E10). (1) Aβ ± $CuCl_2$ or $ZnCl_2$, (2) 1 + **1a**, (3) 1 + **2a**, (4) 1 + **4a**. Experimental conditions: [$A\beta_{40}$ or $A\beta_{42}$] = 10 μM; [$CuCl_2$ or $ZnCl_2$] = 10 μM; [aminoisoflavone] = 20 μM; 1% v/v DMSO; 20 mM HEPES, pH 7.4, 150 mM NaCl; 24 h; 37 °C; agitation.

it from inhibiting metal-induced Aβ aggregation, but did allow for alteration of metal-free Aβ aggregation. For Cu(II)- and Zn(II)-treated Aβ samples, there were slight differences in the Aβ distribution between the samples containing the different metal ions, which could be the result of altered peptide conformations or metal–ligand binding modes/affinity.[5,109] In the case of disaggregation, the presence of a chelating group (*i.e.*, catechol) in **2**, **3**, and **4** was required to significantly affect the distribution of Aβ species in the presence of Cu(II) and/or Zn(II). To account for the reactivity in the inhibition and disaggregation experiments, insights from the studies of the solution speciation of Cu(II)–**4** complexes (*vide supra*) could be cited. Based on these data, which indicated a high K_d value for Cu(II), it is possible that reactivity of the aminoisoflavones with metal–Aβ species could occur as a result of Cu(II) being partially sequestered from the metal-bound peptide or obstructed from binding. Either of these possibilities might be involved in redirecting Aβ aggregation in the inhibition experiment or facilitating Aβ aggregate disassembly in the disaggregation experiment.[36,43,54] Furthermore, the differing reactivity between metal-free and metal-associated Aβ *in vitro* supports that metal–Aβ species could have a potentially relevant role *in vivo*, which can be investigated with small molecules.

4.2.7. Antioxidant properties

The antioxidant property of flavonoids has been investigated[110-112] and structural similarity of aminoisoflavones to these compounds suggests this property. To investigate free radical scavenging and ROS quenching properties for the aminoisoflavone compounds, the Trolox antioxidant equivalence capacity (TEAC) assay and horseradish peroxidase (HRP)/Amplex Red assays, respectively, were employed (Figures 4.19 and 4.20).[110] Compared to the vitamin E analogue Trolox, **3** was 2.60 ± 0.06 times more effective to quench the radical ($ABTS^{\bullet+}$) radical. **2** and **4** could also reduce the amount of the radical in solution to a similar extent as Trolox. Among the aminoisoflavones, **1** showed the lowest TEAC value suggesting its limited utility as an antioxidant. Structurally, the most likely antioxidants among these molecules contain the catechol moiety and may be able to support the resulting ligand intermediate (*e.g.*, semiquinone or quinone) upon donation of a hydrogen atom to the organic radical; the

absence of the catechol moiety in **1** may preclude its formation of a stable intermediate upon interacting with $ABTS^{\bullet+}$.[110] To account for their lower TEAC value compared to **3**, the possibility for a greater number of resonance forms of **2** and **4**, which would possibly stabilize the structures and make them less capable of hydrogen atom donation, could be cited.[110] Additionally, the Cl atom in **3** might be susceptible to radical generation that could also quench the $ABTS^{\bullet+}$.

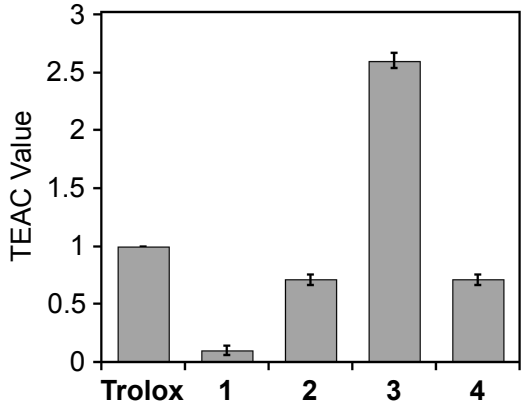

Figure 4.19. Radical scavenging ability of aminoisoflavones (**1**-**4**) determined by the Trolox equivalence antioxidant capacity (TEAC) assay. TEAC values are calculated relative to Trolox, a vitamin E analogue, after 15 min incubation and represent the mean of four independent experiments. The experimental details are described in the main text.

In AD, the generation of organic radicals as a secondary effect of Aβ aggregation or another aspect of pathology might contribute to neurotoxicity,[2,3,5,17] making the discovery of molecules to intercept such species desirable. From our studies, some of aminoisoflavones may be able to scavenge radicals leading to neuroprotection. Considering this property, their possible regulation of ROS is also of interest. Although flavonoid structures, including the aminoisoflavones, have been demonstrated as antioxidants, these properties do not necessarily correlate to control of ROS production. As redox active ligands, flavonoids can also participate in generation of ROS (*i.e.*, pro-oxidant). Furthermore, it has been suggested that Cu(II)–Aβ species may be capable of producing elevated amounts of ROS, which would lead to oxidative stress in the AD brain.[4,5,8,15-20] Using an HRP/Amplex Red assay *in vitro* to measure H_2O_2 production

(Figure 4.20), Cu(II)–Aβ in the presence of a reducing agent produced a baseline amount of H_2O_2. This amount was lowered by the addition of EDTA, a strong Cu(II) chelator. With a considerably high binding affinity for Cu(II), it might be possible for the aminoisoflavones to sequester Cu(II) in a similar manner and eliminate the redox cycling of Cu(II/I) that produces ROS *via* the Fenton reaction. According to the results, addition of each aminoisoflavone to the reaction enhanced H_2O_2 generation by *ca.* 10-30%, while EDTA lowered the amount of H_2O_2 by *ca.* 60% relative to Cu(II)–Aβ only.

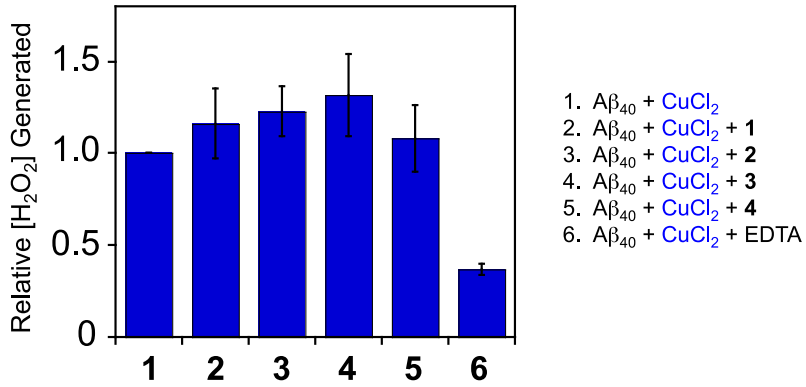

Figure 4.20. H_2O_2 production in the presence of $A\beta_{40}$, Cu(II), and ligands. Experimental conditions: [$A\beta_{40}$] = 200 nM, [$CuCl_2$] = 400 nM, [ligand] = 800 nM, [ascorbate] = 10 μM, [HRP] = 1 U/mL, [Amplex Red] = 50 μM, room temperature.

For **1**, it would be expected to be unable to mitigate H_2O_2 production due to its lack of Cu(II) chelation structure. For **2**, **3**, and **4**, Cu(II) binding to the catechol moiety has been suggested to facilitate oxidation of the ligand, which produces H_2O_2 as a byproduct in the reaction. Therefore, despite having an ability to scavenge organic free radicals that was demonstrated by the TEAC assay, these frameworks are also capable of enhancing ROS production, which might limit their utility as therapeutics for AD, which is characterized by its enhanced oxidative stress.

4.2.8. Cell viability studies

The ability of **1**-**4** to mediate toxicity induced by metal-free and metal-treated Aβ species was probed in human neuroblastoma SK-N-AS (AS) and SK-N-BE(2)-M17 (M17) cells and evaluated using the MTT assay (Figures 4.21, 4.22, and

4.23).[12,35,36,38,39,43,44,54] First, the compounds were incubated with the cells in the absence and presence of $CuCl_2$ or $ZnCl_2$ in a 1:2 metal/ligand ratio. In the AS cell line all four compounds were relatively non-toxic with *ca.* 100% cell viability after 24 h (Figure 4.21a). When the cells were treated with 0.5 equiv $CuCl_2$ or $ZnCl_2$ in addition to the ligand, the cells were relatively unaffected; they maintained viability at or near 100% following 24 h treatment. Upon incubation in AS cells for 72 h, cell viability of the aminoisoflavones in the absence of externally added metal ions was reduced by *ca.* 20% and cells treated with $CuCl_2$ or $ZnCl_2$ and the aminoisoflavones alone during this time indicated similar levels of survival (Figure 4.21b). All four compounds were relatively non-toxic in the AS with *ca.* 90-100% cells survival after 24 h (Figure 4.22). Subsequently, cell viability upon incubation of **1**-**4** with metal-free or metal-treated $A\beta_{40}$ or $A\beta_{42}$ was analyzed (Figure 4.23). The cells were treated with $A\beta_{40}$ or $A\beta_{42}$ (5 μM) and either no metal, $CuCl_2$ (5 μM), or $ZnCl_2$ (5 μM), followed by 1 or 2 equiv of the aminoisoflavone. Under this condition, the aminoisoflavones presented minimal toxicity in the absence and presence of the metal ions. With this low concentration of Aβ, *ca.* 80-90% cell survival was measured for the metal-free and Cu(II)- or Zn(II)-treated Aβ species (Figure 4.23). With 1 equiv of compound present, the aminoisoflavones had a modest influence on cell survival for $A\beta_{40}$ (Figure 4.23a). Addition of 2 equiv of compound resulted in moderate enhancement of cell viability for **2**, **3**, and **4** for all conditions, while **1** had a minimal effect on the $A\beta_{40}$-treated cells in the absence or presence of metal ions (Figure 4.23a). A similar trend was observed for cells treated with $A\beta_{42}$; 2 equiv of compound more noticeably attenuated toxicity than 1 equiv (Figure 4.23b). These cell studies support that the aminoisoflavone framework is potentially useful for applications in biological settings. In particular, the aminoisoflavones containing the catechol moiety could mediate toxicity from metal-free or metal-associated Aβ species in heterogeneous environments (*i.e.*, cells), similar to the previous reports of myricetin and EGCG (Figure 4.1 for structure).[12,54]

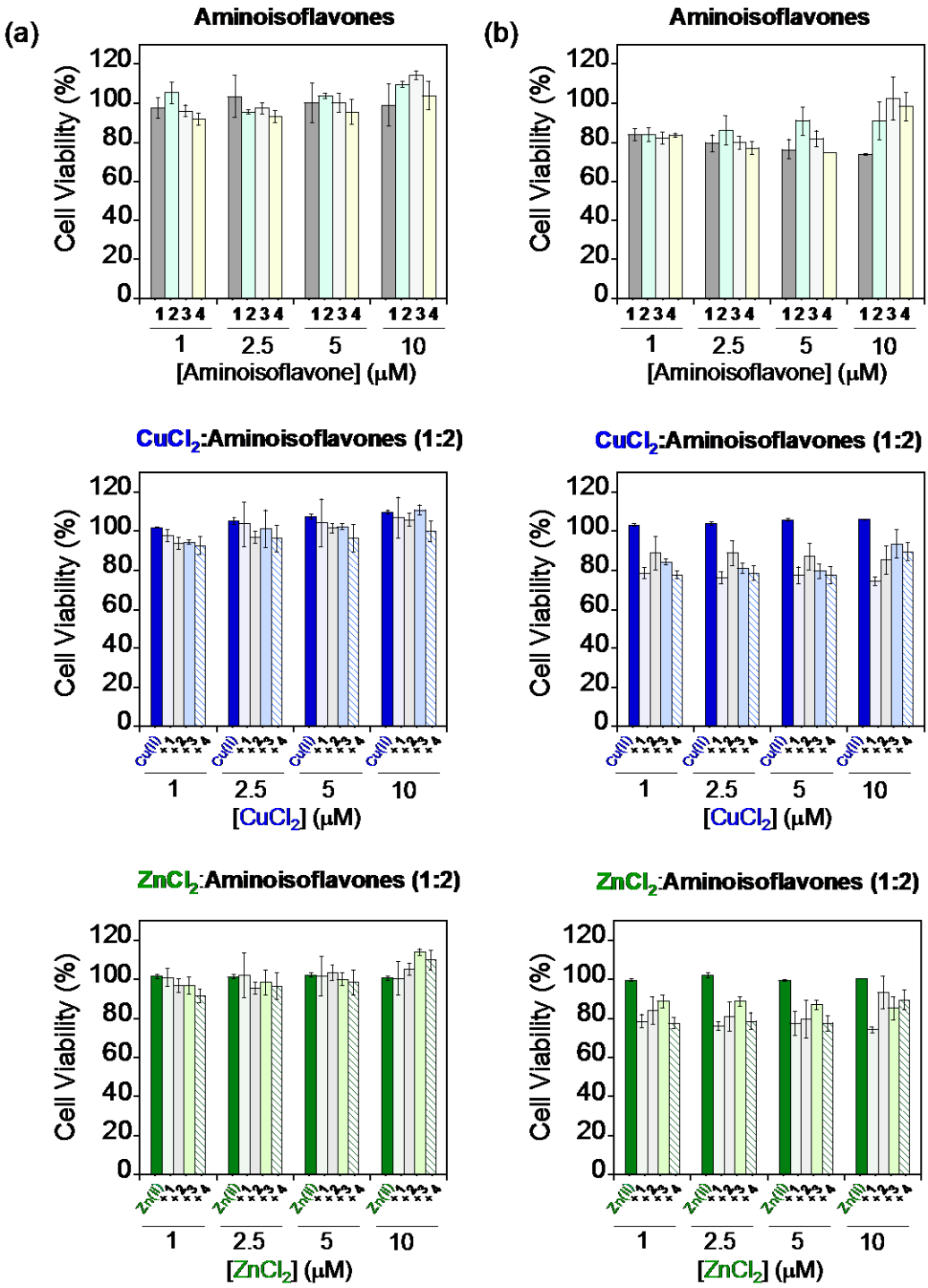

Figure 4.21. Cell viability for aminoisoflavones in the absence and presence of $CuCl_2$ or $ZnCl_2$ in human neuroblastoma SK-N-AS cells following (a) 24 h or (b) 72 h incubation. Cells were treated with various concentrations of aminoisoflavones (top), a 1:2 ratio of $CuCl_2$/aminoisoflavone (middle) or a 1:2 ratio of $ZnCl_2$/aminoisoflavone (bottom). Error bars represent the standard error for three independent experiments. Cell viability is calculated relative to cells containing an equivalent amount of DMSO.

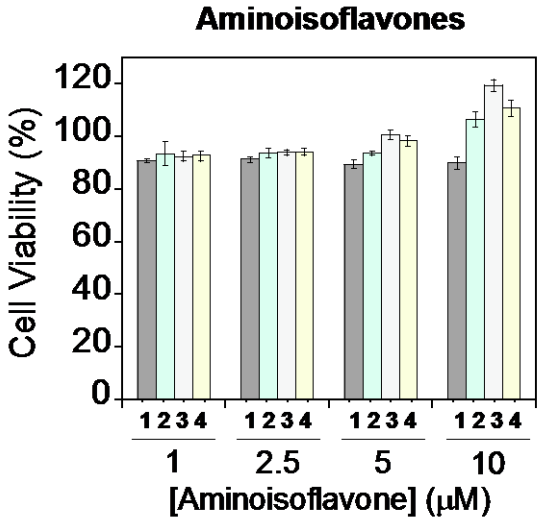
Aminoisoflavones
Cell Viability (%)
120
100
80
60
40
20
0
1 2 3 4
1 2 3 4
1 2 3 4
1 2 3 4
1
2.5
5
10
[Aminoisoflavone] (μM)

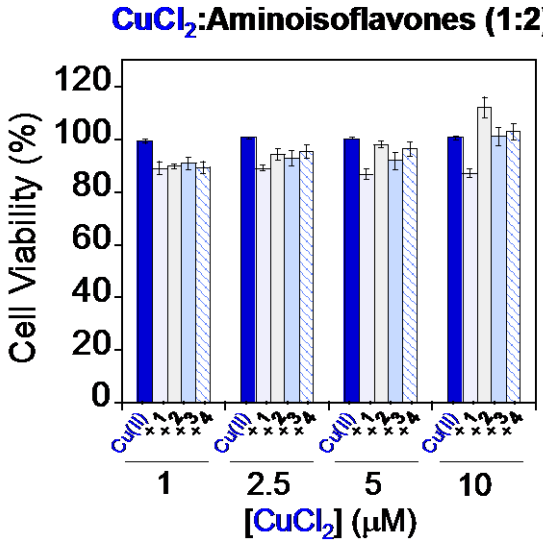
CuCl2:Aminoisoflavones (1:2)
Cell Viability (%)
120
100
80
60
40
20
0
Cu(II)
1
2
3
4
1
2.5
5
10
[CuCl2] (μM)

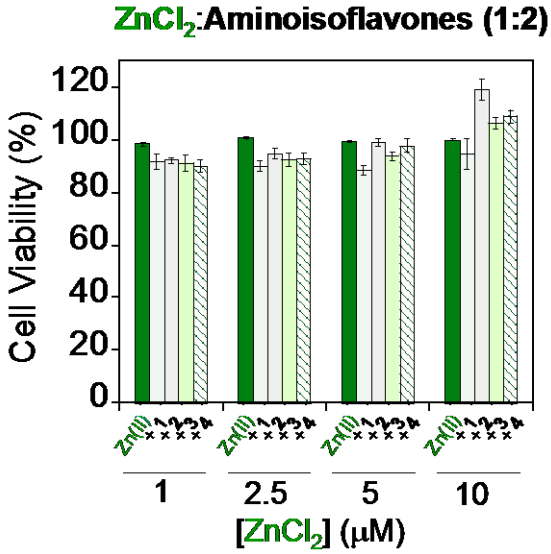
ZnCl2:Aminoisoflavones (1:2)
Cell Viability (%)
120
100
80
60
40
20
0
Zn(II)
1
2
3
4
1
2.5
5
10
[ZnCl2] (μM)

Figure 4.22. Cell viability for aminoisoflavones in the absence and presence of $CuCl_2$ or $ZnCl_2$ in human neuroblastoma SK-N-BE(2)-M17 cells following 24 h incubation. Cells were treated with various concentrations of aminoisoflavones (top), a 1:2 ratio of $CuCl_2$/aminoisoflavone (middle) or a 1:2 ratio of $ZnCl_2$/aminoisoflavone (bottom). Error bars represent the standard error for three independent experiments. Cell viability is calculated relative to cells containing an equivalent amount of DMSO.

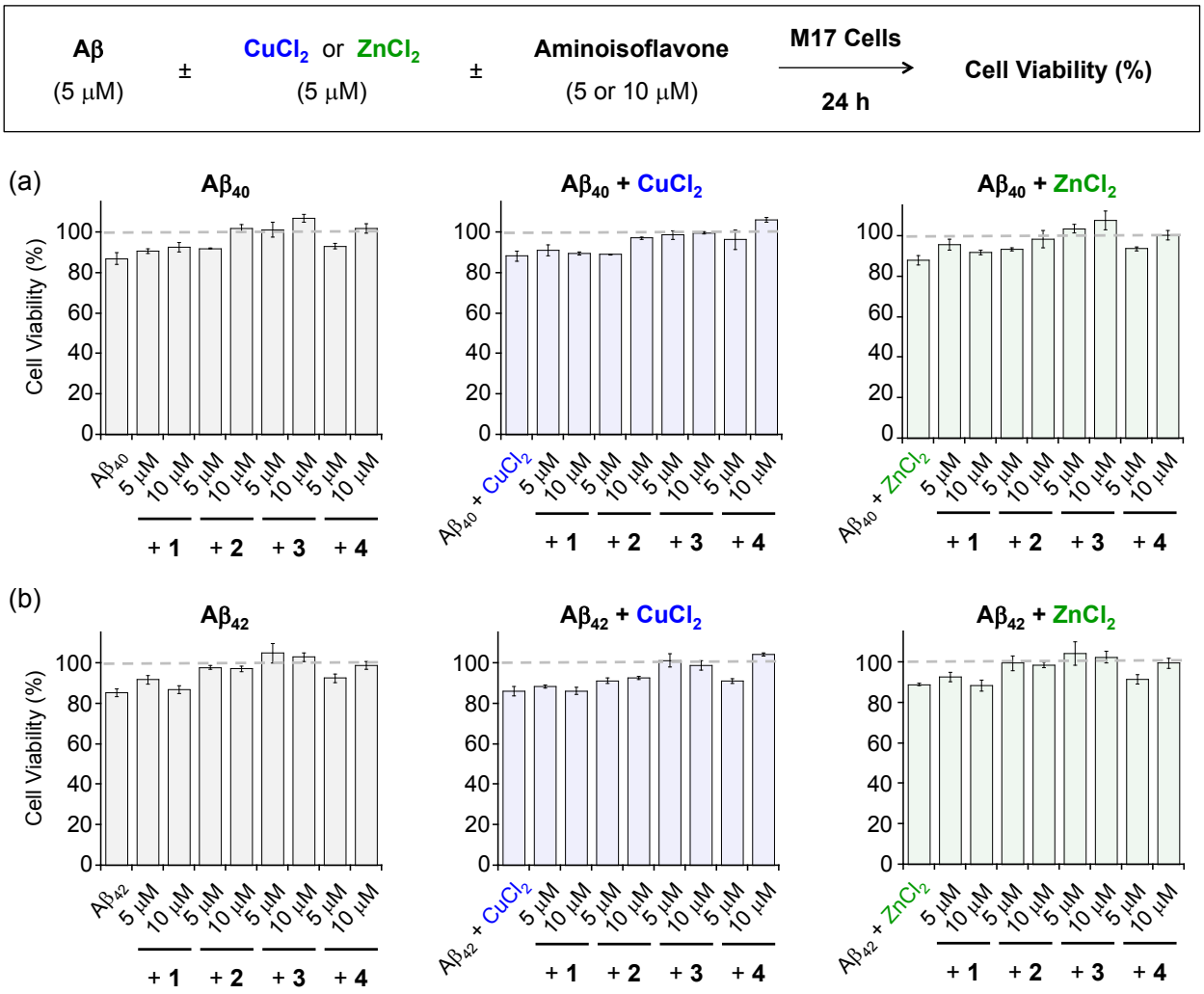

Figure 4.23. Influence of aminoisoflavones on SK-N-BE(2)-M17 (M17) cell viability in the presence of metal-free and metal-associated Aβ40 and Aβ42. M17 cells were treated with Aβ (5 μM) followed by $CuCl_2$ or $ZnCl_2$ (5 μM) and 1 or 2 equiv **1**, **2**, **3**, or **4**. Error bars represent the standard error for three independent experiments. Cell viability is calculated relative to cells containing an equivalent amount of DMSO.

4.2.9. Blood-brain barrier (BBB) permeability

Consideration of potential for brain uptake is valuable when planning to apply a compound to applications in the brain. Recommended properties for diffusion across the BBB are derived from modified parameters applied to drug-like molecule design (*i.e.*, Lipinski's rules) and calculated logBB value.[113,114] The restricted terms of Lipinski's rules dictate that molecules for brain applications would generally adhere to having a molecular weight (MW) ≤ 450 g/mol, calculated logarithm of the octanol-water partition coefficient (*c*logP) ≤ 5, number of hydrogen bond donors (HBD) ≤ 5 and hydrogen bond acceptors ≤ 10, and polar surface area (PSA) ≤ 90 Å^2.[113] The logBB calculation estimates the expected permeability based on an equation that uses the *c*logP value and PSA; values ≤ −1.00 are expected to have poor diffusion.[114] Most naturally occurring flavonoids poorly obey to these parameters and would not be expected to diffuse across the blood-brain barrier.

Among the aminoisoflavones, **1** observes all of Lipinski's rules and has a logBB value of −0.74. **2**, **3**, and **4** have additional HBD and HBA from the catechol group, which are still within the parameters; however, the PSA of these three molecules is above 90 Å^2, leading to a logBB value below −1.00. Lipinski's rules quantify parameters that tend to govern lipophilic molecules, but the solution speciation of the ligands can also suggest the likelihood of BBB permeability. Uncharged species are generally more permeable, so it would be expected that **1**, **2**, and **3** might be able to diffuse across the BBB given their neutral form dominating the solution speciation at pH 7.4 (Figure 4.2). Compound **4** is monodeprotonated and therefore should have more difficulty in entering the brain by diffusion. Using an *in vitro* parallel artificial membrane permeability assay for the blood-brain barrier (PAMPA-BBB), the likely *in vivo* activity can be predicted (Table 4.2). According the results of this assay, which employs an artificial lipid membrane to mimic the BBB, the −logP_e values ranged from 6.13–6.57. Molecules with a known ability to enter the brain generally have a −logP_e below 5.4. Therefore, despite adhering to most of Lipinski's rules, these molecules may be too polar to passively diffuse across the BBB. Thus, to apply these molecules in further studies, minor modifications to reduce the overall polar nature of these synthetic flavonoids would be helpful.

Table 4.2. BBB permeability assessed by PAMPA-BBB, Lipinski's rules, and logBB calculation.[a]

	$-\log P_e$	*n*	CNS+/− Prediction	MW	HBD	HBA	PSA (Å^2)	*c*logP	logBB
1	6.15 ± 0.08	30	CNS−	253	3	4	76.5	1.71	−0.74
2	6.37 ± 0.06	26	CNS−	269	4	5	96.7	1.03	−1.14
3	6.13 ± 0.07	25	CNS−	304	4	5	96.7	1.82	−1.02
4	6.57 ± 0.08	15	CNS−	285	5	6	117	0.45	−1.53

CNS+ $-\log P_e < \sim 5.4$ (High BBB permeation predicted)
CNS− $-\log P_e > \sim 5.7$ (Low BBB permeation predicted)
CNS+/− $5.7 > -\log P_e > 5.4$ (BBB permeation uncertain)

[a] Molecular weight (MW), hydrogen bond donors (HBD), hydrogen bond acceptors (HBA), polar surface area (PSA), calculated log of the octanol-water partition coefficient (clogP), logBB = −0.0148 x PSA + 0.152 x *c*logP +0.130, *n* = number of replicates.

4.3. Conclusion

Advancement in AD research field has been challenged by the lack of cohesive evidence to explain the origins of the disease. It is becoming more accepted that formerly competing hypotheses may be intertwined, requiring novel approaches to investigate these relationships. To target the combined metal-amyloid hypothesis of AD, efforts to make molecules with multiple functions (*i.e.*, metal chelation, Aβ interaction) have been ongoing. New frameworks for this purpose are of perpetual interest, with hopes of devising a comprehensive structure-interaction-reactivity relationship to govern design of new chemical tools and/or therapeutics. The flavonoid framework has been identified as a potential avenue for growth of this field, as many flavonoids inherently have structural components for interacting with metal ions and Aβ.[12,54] The multiple naturally occurring structural derivations within flavonoids and relative ease of synthetic manipulation have also made them an attractive class of molecules to pursue. Moving toward identification of a suitable flavonoid family that can be easily adapted to tune the interaction with Aβ and metal–Aβ species and mediate their association with

aggregation pathways, the aminoisoflavones (**1**-**4**) were designed and synthesized. The molecules, **2**, **3**, and **4** are composed of a catechol group for metal chelation, while **1** lacks this moiety. Their Cu(II) and Zn(II) binding properties were characterized, and detailed spectroscopic investigations the Cu(II)–**4** complexes were conducted showing high binding affinity for Cu(II) and the presence of a mixture of possible Cu(II) complexes in solution (*e.g.*, Cu(II)–semiquinone, Cu(II)–catecholate). Interaction of the aminoisoflavones with metal-free Aβ was investigated by ITC, NMR, and docking studies implying that these compounds may be able to interact with the peptide through multiple binding modes; however, a defined binding site was observed for the aminoisoflavones with Aβ in contrast to non-specific binding previously suggested for flavonoid derivatives. The independent abilities of these molecules to target metal ions and Aβ were translated to their ability to control $A\beta_{40}$ and $A\beta_{42}$ aggregation in the absence and presence of metal ions *in vitro*. In particular, the inclusion of the catechol group was required to achieve a balance in interaction with metal ions and/or Aβ to influence Aβ aggregate formation or disassembly for preformed Aβ aggregates when metal ions are absent or present. The catechol group also seems to offer other potentially useful biological properties, such as antioxidant behavior and improved cell viability.[63,64,72] To uncover more nuances of the structure-interaction-reactivity relationship, studies using a larger chemical library developed through further structural modification of the aminoisoflavones will be required (*e.g.*, whether removal of NH_2 group influences reactivity). In the present study, the flavonoid framework was successfully applied to a synthetic design strategy in which minimal structural components were chosen and could facilitate the ability of the compounds to target metal-free and metal-associated Aβ species and regulate their reactivity. The catechol moiety in this framework in combination with the unnatural primary amine imparts noticeable properties for interaction and reactivity with metals, Aβ, and/or metal–Aβ (*i.e.*, metal chelation, hydrophilic and hydrophobic contacts with peptide species) while additional functional groups (*e.g.*, OH, Cl) did not significantly perturb these properties. Thus, this work demonstrates that flavonoids can be manipulated into simple structures to tune chemical properties (*i.e.*, metal binding, Aβ interaction) and, subsequently, *in*

vitro reactivity of metal-free and metal–Aβ species, which offers preliminary insights on the structure-interaction-reactivity relationship for flavonoid structures with Aβ and metal–Aβ species.

4.4. Experimental

4.4.1. Materials and methods

All reagents and solvents were commercially available and used as received unless otherwise stated. The compounds 2-amino-7-hydroxy-3-phenyl-4*H*-chromen-4-one (**1**), 2-amino-3-(3,4-dihydroxyphenyl)-4*H*-chromen-4-one (**2**), 2-amino-6-chloro-3-(3,4-dihydroxyphenyl)-4*H*-chromen-4-one (**3**), and 2-amino-3-(3,4-dihydroxyphenyl)-7-hydroxy-4*H*-chromen-4-one (**4**) were synthesized from the previously reported compounds (**1a**-**4a**) (Scheme 4.1).[61,62] The ^{1}H and ^{13}C nuclear magnetic resonance (NMR) spectra of these molecules were recorded on a Varian Inova 500 spectrometer (Palo Alto, CA, USA) in DMSO-d_6. Infrared (IR) spectra were measured on a Bruker Vector 22 spectrophotometer (Billerica, MA, USA). High-resolution mass spectra were obtained on an Agilent Technologies 6520 Accurate-Mass Q-TOF LC/MS (Santa Clara, CA, USA). Crude compounds (**1**-**4**) were purified by preparative reverse-phase HPLC (Waters Delta Prep 4000 system with Waters Prep LC 40 mm Assembly column C18 (30 cm x 4 cm, 15 μm particle), Milford, MA, USA) and eluted at a flow rate of 20 mL/min with mobile phase solvent A (10% CH_3CN + 0.1% trifluoroacetic acid (TFA) in H_2O, v/v), and a linear gradient from 0 to 50% B (60%, CH_3CN + 0.1% TFA in H_2O, v/v) in 25 min. Analytical HPLC analyses were performed with a Beckman System Gold (Beckman Ultrasphere ODS column, 250 mm x 4.6 mm, 5 μm particle, Brea, CA, USA). Analytical determinations of the products were carried out by HPLC in solvents A and B programmed at flow rate of 1 mL/min with linear gradients from 0 to 100% B in 25 min.

$A\beta_{40}$ and $A\beta_{42}$ were purchased from AnaSpec (Fremont, CA, USA) ($A\beta_{42}$ = DAEFRHDSGYEVHHQKLVFFAEDVGSNKGAIIGLMVGGVVIA). An Agilent 8453 UV-Visible (UV-Vis) spectrophotometer (Santa Clara, CA, USA) was used to measure the optical spectra. Electron paramagnetic resonance (EPR) spectroscopy was conducted by a Bruker X-band (9.23 GHz) EMX spectrometer (Billerica, MA, USA) equipped with a

liquid nitrogen cryostat. Electrochemical studies were obtained by a CH1000A Electrochemical Analyzer (CH Instruments, Inc., Austin, TX, USA). Isothermal calorimetric titrations were performed using a VP isothermal titration calorimeter (MicroCal, Northampton, MA, USA). Transmission electron microscopy (TEM) images were recorded on a Philips CM-100 transmission electron microscope in the Microscopy and Imaging Laboratory at the University of Michigan (Ann Arbor, MI, USA). A Molecular Devices SpectraMax M5 microplate reader (Sunnyvale, CA, USA) was employed for the measurement of absorbance for Trolox equivalence antioxidant capacity (TEAC) and 3-(4,5-dimethylthiazol-2-yl)-2,5-diphenyltetrazolium bromide (MTT) assays.

4.4.2. General procedure for the preparation of hydroxylated 2-amino-3-aryl-4*H*-chromen-4-ones (1-4)

To a solution of the corresponding methoxylated 2-amino-3-aryl-4*H*-chromen-4-one precursor (**1a**-**4a**, 1 mmol)[62] in acetic acid (2.5 mL) and acetic anhydride (2.5 mL), 57% v/v hydroiodic acid (5 mL) was added dropwise (Scheme 4.1). The mixture was refluxed for 6 h. After solvent evaporation *in vacuo*, water (10 mL) was added to the residue; the solid obtained was filtered and washed with water (2 x 5 mL) (76-86% yield). Each compound was purified by preparative reverse-phase HPLC as described above.

2-Amino-7-hydroxy-3-phenyl-4H-chromen-4-one (**1**). Yield: 192 mg, 0.76 mmol, 76%. EtOAc:Hx = 1:1; R_f = 0.56 (TLC). ^{1}H NMR (500 MHz, DMSO-d_6)/δ (ppm): 6.84 (s, 1H, Ar), 6.95 (d, J = 8.5 Hz, 1H, Ar), 7.44 (m, 5H, Ar and NH_2), 7.54 (m, 2H, Ar), 7.94 (d, J = 8.5 Hz, 1H, Ar), 10.58 (brs, 1H, OH). ^{13}C NMR (125 MHz, DMSO-d_6)/δ (ppm): 170.6, 164.1, 162.4, 154.4, 132.1, 131.7, 129.2, 128.0, 127.0, 114.5, 113.1, 102.1, 99.2. HRMS (ESI+): Calcd for $C_{15}H_{11}NO_3$ $[M+H]^+$, 254.0817; found, 254.0863. IR (Nujol)/ν (cm^{-1}): 3465, 3319, 1628, 1603.

2-Amino-3-(3,4-dihydroxyphenyl)-4H-chromen-4-one (**2**). Yield: 221 mg, 0.82 mmol, 82%. EtOAc:Hx = 1:1; R_f = 0.51 (TLC). ^{1}H NMR (500 MHz, DMSO-d_6)/δ (ppm): 6.67 (m, 1H, Ar), 6.81 (s, 1H, Ar), 6.90 (m, 1H, Ar), 7.04 (s, 2H, NH_2), 7.48 (m, 2H, Ar), 7.73 (m, 1H, Ar), 7.94 (d, J = 8.5 Hz, 2H, Ar), 8.88 (s, 1H, OH), 8.94 (s, 1H, OH). ^{13}C NMR (125 MHz, DMSO-d_6)/δ (ppm): 173.1, 162.8, 153.0, 145.6, 114.8, 132.4, 125.7,

124.8, 124.4, 123.5, 122.4, 119.1, 116.8, 116.3, 99.7. HRMS (ESI+): Calcd for $C_{15}H_{11}NO_4$ $[M+H]^+$, 270.0766; found, 270.0765. IR (Nujol)/ν (cm^{-1}): 3453, 3165, 1642, 1601.

2-Amino-3-(3,4-dihydroxyphenyl)-6-chloro-4H-chromen-4-one (**3**). Yield: 261 mg, 0.86 mmol, 86%. EtOAc:Hx = 1:1; R_f = 0.48 (TLC). ^{1}H NMR (500 MHz, DMSO-d_6)/δ (ppm): 6.67 (s, 1H, Ar), 6.81 (s, 1H, Ar), 6.88 (m, 1H, Ar), 7.22 (s, 2H, NH_2), 7.55 (m, 1H, Ar), 7.76 (m, 1H, Ar), 7.98 (s, 1H, Ar), 8.91 (s, 1H, OH), 8.95 (s, 1H, OH). ^{13}C NMR (125 MHz, DMSO-d_6)/δ (ppm): 168.9, 164.7, 151.1, 145.9, 145.6, 132.9, 129.7, 124.4, 122.7, 122.4, 122.0, 119.3, 118.8, 116.6, 101.3. HRMS (ESI+): Calcd. for $C_{15}H_{10}ClNO_4$ $[M+H]^+$, 304.0377; found, 304.0368. IR (Nujol)/ν (cm^{-1}): 3420, 3311, 1644, 1598.

2-Amino-3-(3,4-dihydroxyphenyl)-7-hydroxy-4H-chromen-4-one (**4**). Yield: 228 mg, 0.80 mmol, 80%. EtOAc:Hx = 1:1; R_f = 0.53 (TLC). ^{1}H NMR (500 MHz, DMSO-d_6)/δ (ppm): 6.66 (m, 1H, Ar), 6.82 (m, 1H, Ar), 6.89 (m, 1H, Ar), 6.95 (m, 1H, Ar), 7.33 (s, 2H, NH_2), 7.76 (m, 1H, Ar), 7.93 (s, 1H, Ar), 8.87 (s, 1H, OH), 8.90 (s, 1H, OH), 10.67 (brs, 1H, OH). ^{13}C NMR (125 MHz, DMSO-d_6)/δ (ppm): 170.5, 164.4, 162.1, 154.2, 145.8, 145.4, 126.9, 122.6, 119.0, 116.5, 114.4, 113.2, 102.0, 99.4. HRMS (ESI+): Calcd. for $C_{15}H_{11}NO_5$ $[M+H]^+$ 286.0715; found, 286.0706. IR (Nujol)/ν (cm^{-1}): 3419, 3327, 1631, 1609.

4.4.3. Determination of solution speciation from acidity constants for aminoisoflavones and stability constants for Cu(II)–4 complexes

The acidity constants (pK_a) for **1**-**4** were determined by spectrophotometric variable-pH titrations with modifications to the previously described methods.[34,36-40,42-44,68,69] A solution (10 mM NaOH, 100 mM NaCl, pH 12) containing **1** (30 μM) was titrated with small aliquots of HCl to acquire at least 30 spectra in the range from pH 1.5-12. Solutions of **2** (20 μM), **3** (15 μM), and **4** (30 μM) in 200 mM HCl, 100 mM NaCl, pH 0.6 were titrated with small aliquots of NaOH and at least 30 spectra were acquired from pH 0.6-12.4. To measure the stability constants (logβ) for the Cu(II)–**4** complexes, **4** (30 μM) and $CuCl_2$ in a ratio of 2:1 were added to a solution (10 mM NaOH, 100 mM NaOH) at pH 8. Following overnight incubation, the solution was titrated with small aliquots of HCl in the range from pH 1.5-8. The pK_a and logβ values were calculated

using the program HypSpec (Protonic Software, UK).[115] Speciation diagrams were generated from the calculated values by the program HySS2009 (Protonic Software, UK).[116]

4.4.4. Metal binding studies

The ability of the aminoisoflavones to bind to Cu(II) or Zn(II) was investigated by UV-Vis in the absence and presence of $A\beta_{40}$.[12,35-40,43,44,54,68,104] A solution of the aminoisoflavone (20 μM, 1% v/v DMSO) in 20 mM HEPES [4-(2-hydroxyethyl)-1-piperazineethane sulfonic acid], pH 7.4, 150 mM NaCl was incubated with 0.5-5 equiv $CuCl_2$ for up to 2 h. Additionally, the interaction of **4** with $CuCl_2$ in the presence of $A\beta_{40}$ was also studied by measuring changes in the optical spectra. In the same buffered solution, Aβ (10 μM) was pre-incubated with $CuCl_2$ (5 or 10 μM) for 2 min, followed by the addition of 0.5, 1, or 2 equiv of **4**. The Cu(II)–Aβ solution was incubated with **4** at room temperature for up to 3 h. To determine Zn(II) binding properties, a solution of 100 μM aminoisoflavone in 20 mM HEPES, pH 7.4, 150 mM NaCl was incubated with $ZnCl_2$ (10 μM) for 12-24 h and monitored by UV-Vis.

4.4.5. Electron paramagnetic resonance (EPR) investigations of Cu(II)–4 complexes

Samples were prepared for solutions in 20 mM HEPES, pH 7.4, 150 mM NaCl. Compound **4** (0.5 mM, 10% v/v DMSO) was incubated with $CuSO_4$ (0.25 mM) and aliquots (350 μL) of the solution were flash-frozen in liquid nitrogen after 0, 5, 30, and 60 min. The buffer only or **4** only was prepared in the same buffered conditions and flash-frozen in liquid nitrogen (350 μL). Following partial electrochemical oxidation of **4** (250 μM, 10% v/v DMSO), a sample without or with $ZnCl_2$ (125 μM) in the same buffer was flash-frozen in liquid nitrogen. Finally, an EPR sample of $CuSO_4$ (0.25 mM) and EDTA (2.5 mM, EDTA: 2-((2-[bis(carboxymethyl)amino]-ethyl)(carboxymethyl)amino)acetic acid) was prepared in the same buffer and flash-frozen in liquid nitrogen for the EPR measurement as a Cu(II) reference. The magnetic field was calibrated to the spectrum of a frozen solution of 2,2-diphenyl-1-picrylhydrazyl (DPPH, 0.5 mM in toluene, Sigma-

Aldrich, St. Louis, MO, USA) ($g_{expected}$ = 2.00; g_{found} = 1.99). Spectra were collected at 77 K with a modulation frequency of 100 kHz, microwave power of 20 mW, and modulation amplitude of 5 G. Simulations of EPR spectra were performed using SpinCount (Professor Michael Hendrich, Carnegie Mellon University, Pittsburgh, PA, USA).

4.4.6. Electrochemistry of 4

Cyclic voltammograms of **4** (250 μM, 10% v/v DMSO) in the absence and presence of Cu(II) (125 μM) were obtained at a scan rate of 10 mV/s in buffer (20 mM HEPES, pH 7.4, 150 mM NaCl). A three-electrode system consisting of glassy carbon as the working electrode, a Pt wire as the counter electrode, and the saturated calomel electrode (SCE) as the reference electrode was employed.[117,118] For experiments in the absence of air, solutions were purged with N_2 and experiments were conducted in a glove box. In a two component cell, bulk electrolysis was conducted on a solution of **4** (250 μM, 10% v/v DMSO) by applying 200 mV to the solution for *ca.* 1000 s to partially oxidize the ligand for EPR experiments (*vide supra*). A three-electrode system was used with a carbon mesh as the working electrode along with SCE as the reference in the ligand solution; a Pt wire was used as the counter electrode in the solution of only buffer.

4.4.7. Isothermal titration calorimetry (ITC) for measurement of thermodynamic parameters for the interaction of 1, 2, or 4 with Aβ

Experiments were conducted with solutions of **1**, **2**, or **4** (200 μM, 10% v/v DMSO) and $A\beta_{40}$ (20 μM) in 20 mM HEPES buffer (pH 7.4, 150 mM NaCl).[44] All solutions were degassed for 10 min before each titration. The ligand solution (10 μL) was titrated into the $A\beta_{40}$ solution (1.43 mL) at 25 °C over 1 s with 25 repetitions at a constant interval of 200 s via a 310 rpm rotating stirrer syringe using a motor driven 250 μL syringe. In a control experiment, the identical titrant solution was injected into the same buffer used with $A\beta_{40}$ to measure the heat of dilution. A reasonable heat of binding value was measured by subtracting the heat of dilution value from the experimental results. Titration data were analyzed with the MicroCal Origin (v. 7.0)

software. The K_A (binding constant) of each ligand and ΔH (binding heat exchange) upon binding interaction between each ligand and $A\beta_{40}$ were determined from a proper fitting model. The binding curves were best fit to a sequential binding site model with one identical site. ΔG and $-T\Delta S$ were calculated via Gibb's free energy relationship ($\Delta G = \Delta H - T\Delta S$; $\Delta G = -RTln(K_A)$).

4.4.8. Docking studies of aminoisoflavones against $A\beta_{40}$ monomer

Flexible ligand docking studies using AutoDock Vina[119] using aminoisoflavones were conducted against the $A\beta_{40}$ monomer from the previously determined aqueous solution NMR structure (PDB 2LFM).[97] Representative conformations were selected for docking from those within the PDB file (1, 3, 8, 10, 12, 13, 16, 17, 20 for 2LFM). The MMFF94 energy minimization in ChemBio3D Ultra 11.0 was used to optimize the structure of aminoisoflavones for the docking studies. Individual structures of $A\beta$ and aminoisoflavones were prepared in AutoDock Tools.[120] The search space was constrained to the dimensions of the peptide. The exhaustiveness for the docking runs was set at 1024. Docked models of the aminoisoflavones were visualized with $A\beta_{40}$ using Pymol.

4.4.9. NMR sample preparation

Prior to the preparation of the $A\beta_{40}$ sample for NMR, the peptide was dissolved in ammonium hydroxide (NH_4OH, 2% v/v aq) at 1 mg/ml to remove any preformed aggregates.[121,122] Volumes equivalent to 0.1 mg (100 µL) were then aliquoted and lyophilized. The lyophilized peptide was initially dissolved in 1mM NaOH and then allowed to solubilize at 4 °C until the solution became clear (*ca.* 1 h). At this point the concentrated buffer was added to the solution and the pH was adjusted to the final value to generate freshly dissolved, low MW $A\beta_{40}$ samples. The final sample contained 20 mM deuterated Tris (pD 7.0 or a calculated pH of 7.4) with 50 mM NaCl and 10% v/v D_2O. Immediately prior to the experiment, compounds **1** and **4** were dissolved in deuterated DMSO at a concentration of 19.5 mM. The 1D ^1H NMR and 2D ^{15}N-^1H SOFAST-HMQC (SOFAST = 2D band-selective optimized flip-angle short transient; HMQC = heteronuclear multiple quantum correlation) titrations were performed directly

using the freshly dissolved, low MW Aβ40 samples. For saturation transfer difference (STD) NMR experiments on ligand binding to the amyloid fibrils, samples were prepared as above except that all of the solutions were prepared in D_2O and the sample was allowed to incubate for 48 hours at 37 ºC in a shaker (model M from IKA) at 1000 rpm to generate amyloid fibrils.

4.4.10. NMR measurements

A 900 MHz Bruker Avance NMR spectrometer equipped with a triple-resonance z-gradient cryogenic probe (SOFAST-HMQC experiments) or a 500 MHz without cryoprobe was used to collect the spectra. SOFAST-HMQC spectra of 80 μM Aβ40 in solution (20 mM Tris, pH 7.4, 50 mM NaCl) were recorded at 4 °C with 128 t_1 experiments, 16 scans, and a 100 ms recycle delay.[123] The 2D ^{15}N-^{1}H SOFAST-HMQC data were processed using TOPSPIN 2.1 (from Bruker) and Sparky.[124] Resonances were assigned based on previous assignments under similar conditions.[125] For the STD experiments, both **1** and **4** were kept at a molar ratio of 10:1 relative to the fibril (200 μM to 20 μM).[103] For the STD experiment, a 3 s train of Gaussian-shaped 50 ms pulses was employed to selectively saturate the amyloid fibril.[103] The saturation pulses were centered on −2 and 100 ppm for on and off resonance respectively. The magnitude of the STD effect for each peak was calculated by dividing the normalized signal intensity in the on resonance spectrum by its corresponding intensity in the off resonance reference spectrum.

4.4.11. Amyloid-β (Aβ) experiments

Aβ experiments were performed according to the previously published methods.[12,35-40,43,44,54,104,105] Prior to experiments, Aβ40 or Aβ42 was dissolved in ammonium hydroxide (NH_4OH, 1% v/v, aq), aliquoted, lyophilized overnight, and stored at −80 °C. For experiments described herein, a stock solution of Aβ was prepared by dissolving the peptide in 1% NH_4OH (10 μL) and diluting with ddH_2O. The concentration of Aβ in solution was determined by measuring the absorbance of the solution at 280 nm (ε = 1450 M^{-1} cm^{-1} for Aβ40 and ε = 1490 M^{-1} cm^{-1} for Aβ42). The peptide stock solution was diluted to a final concentration of 10 μM in a Chelex-treated buffered

solution containing HEPES (20 mM, pH 7.4) and NaCl (150 mM). For the inhibition studies,[12,35-40,43,44,54,104,105] an aminoisoflavone (20 μM, 1% v/v DMSO) was added to the sample of Aβ (10 μM) in the absence and presence of $CuCl_2$ or $ZnCl_2$ (10 μM) followed by incubation at 37 °C with constant agitation for 24 h. For the disaggregation studies,[12,35-40,43,44,54,104] Aβ (10 μM) with and without metal ions (10 μM) was incubated for 24 h at 37 °C with constant agitation before adding the aminoisoflavone (20 μM) to the sample. The resulting samples were incubated at 37 °C with constant agitation for 24 h.

4.4.12. Gel electrophoresis and Western blotting

Samples from the inhibition and disaggregation experiments were analyzed by gel electrophoresis and visualized by Western blot using an anti-Aβ antibody (6E10).[12,35-40,43,44,54,105] Each sample was separated on a 10-20% Tris-tricine gel (Invitrogen, Grand Island, NY, USA) and transferred onto nitrocellulose. The nitrocellulose was blocked with bovine serum albumin (BSA, 3% w/v, Sigma-Aldrich) in Tris-buffered saline (TBS) containing 0.1% Tween-20 (TBS-T) overnight. The membranes were incubated with 6E10 (1:2000, Covance, Princeton, NJ, USA) in a solution of 2% BSA (w/v in TBS-T) for 4 h at room temperature. After washing, the horseradish peroxidase-conjugated goat anti-mouse secondary antibody (1:5000, Cayman Chemical, Ann Arbor, MI, USA) in 2% BSA was added for 1 h at room temperature. The ThermoScientific SuperSignal West Pico Chemiluminescent Substrate (Rockford, IL, USA) was used to visualize the protein bands.

4.4.13. Transmission electron microscopy (TEM)

TEM samples were prepared according to the previously reported method.[12,35-39,43,44,54,104,105] Glow-discharged grids (Formar/Carbon 300-mesh, Electron Microscopy Sciences, Hatfield, PA, USA) were treated with the Aβ samples from both inhibition and disaggregation experiments (5 μL) for 2 min at room temperature. Excess sample was removed using filter paper followed by washing with ddH_2O twice. Each grid was incubated with uranyl acetate (1% w/v ddH_2O, 5 μL, 1 min) and upon removal of excess was dried for 15 min at room temperature. Images from each sample were taken by a

Philips CM-100 transmission electron microscope (80 kV, 25,000x magnification).

4.4.14. Trolox equivalence antioxidant capacity (TEAC) Assay

The TEAC assay was used to determine the antioxidant ability based on the extent of decolorization of ABTS (2,2'-azino-bis(3-ethylbenzothiazoline-6-sulfonic acid) diammonium salt) cation radical relative to that of the vitamin E analogue, Trolox.[126] The assay was performed according to the previously reported method with slight modifications.[40,43,126,127] First, $ABTS^{\bullet+}$ was generated by dissolving ABTS (19 mg, 7.0 mM) with potassium persulfate (3.3 mg, 2.5 mM) in 5 mL water and incubating for 16 h in the dark at room temperature. The resulting solution of $ABTS^{\bullet+}$ was diluted with EtOH to an absorbance of *ca.* 0.7 at 734 nm. The assay was conducted in a clear 96 well plate to which 200 μL diluted solution of $ABTS^{\bullet+}$ was added and incubated at 30 °C for 5 min in the plate reader. Each ligand was added from a stock solution prepared in DMSO (1% v/v) or in EtOH (for Trolox) and was incubated with the solution of $ABTS^{\bullet+}$ at 30 °C for different time periods (1, 3, 6, 10, 15, and 30 min). The percent inhibition was calculated according to the measured absorbance at 734 nm (% Inhibition = $100 \times (A_0 - A)/A_0$) and was plotted as a function of ligand concentration. The TEAC value of compounds for each time point was calculated as a ratio of the slope of the standard curve of the compound to that of Trolox. The measurements were carried out in triplicate.

4.4.15. Horseradish peroxidase (HRP)/Amplex Red assay for detection of H_2O_2

The production of H_2O_2 generated by Cu(II)–Aβ species in the presence of dioxygen (O_2) and a reducing agent (ascorbate) was measured using the modified horseradish peroxidase (HRP)/Amplex Red assay.[35,36,38,40,128,129] The assay was performed *in situ* and carried out in black polystyrene 96 well plates. In each well, fresh $A\beta_{40}$ (200 nM) in phosphate buffered saline (PBS, pH 7.4) was treated with $CuCl_2$ (400 nM) and was incubated for 1 h at room temperature with constant agitation. Each ligand (800 nM, 1% v/v DMSO) was introduced to the resulting solution followed by additional incubation at room temperature with constant agitation. After 1 h, the solution of ascorbate (10 μM) was added into each well. After 5 min treatment, the reaction solution

containing Amplex Red (50 μM) and HRP (1 U/mL) was treated to individual samples. After 15 min incubation, the fluorescence emission intensity was measured ($\lambda_{ex/em}$ = 530/590 nm) using a microplate reader. Catalase (10 μL of 100 U/mL) was used for the samples to confirm H_2O_2 production in the system. The total volume was 100 μL in each well.

4.4.16. Cell viability measurements

The human neuroblastoma SK-N-BE(2)-M17 (M17) cell line was purchased from the American Type Cell Collection (ATCC, Manassas, VA, USA). M17 cells were maintained in media containing [1:1 Minimum Essential Media (MEM, Invitrogen)/Ham's F12 Nutrient Mixture (Invitrogen), respectively], supplemented with 10% fetal bovine serum (FBS, Atlanta Biologicals, Atlanta, GA, USA) and 100 U/mL penicillin and 100 μg/mL streptomycin (Invitrogen). The cells were grown in a humidified atmosphere with 5% CO_2 at 37 °C. For the MTT assay, cells were seeded in a 96 well plate (20,000 cells/100 μL) according to the previously reported methods.[12,35,36,38,39,43,44,54] The cells were treated with various concentrations of aminoisoflavones (0-10 μM, 1% v/v DMSO) in the absence or presence of $CuCl_2$ or $ZnCl_2$ (1:2 metal/ligand ratio) and incubated for 24 h in the cells. After incubation, 25 μL MTT (5 mg/mL in phosphate buffered saline (PBS, Invitrogen), pH 7.4) was added to each well and the plate was incubated for 4 h at 37 °C. Formazan produced by the cells was solubilized using an acidic solution of *N*,*N*-dimethylformamide (50% v/v aq) and sodium dodecyl sulfate (SDS, 20% w/v) overnight at room temperature in the dark. The absorbance was measured at 600 nm using a microplate reader. Three independent experiments were conducted to estimate error. Cell viability was calculated relative to cells containing an equivalent amount of DMSO.

4.4.17. Parallel artificial membrane permeability assay adapted for BBB (PAMPA-BBB)

The potential BBB permeability of the AIFs was determined using the PAMPA Explorer kit (Pion, Inc., Billerica, MA, USA) with previously reported modifications. Each compound was diluted to 25 μM (1% v/v DMSO) in Prisma HT buffer (pH 7.4, Pion) and

200 μL was added to the wells of the donor plate (number of replicates = 12). The BBB-1 lipid formulation (5 μL) was painted onto the polyvinylidene fluoride (PVDF, 0.45 μm) membrane of the acceptor plate. The acceptor plate was placed on the donor plate to form a "sandwich" and brain sink buffer (BSB, 200 μL, Pion) was added to the acceptor plate wells. The "sandwich" was incubated at room temperature without stirring for 4 h. UV-Vis spectra were acquired for the solutions in reference, acceptor, and donor plates using a microplate reader. The PAMPA Explorer software (v. 3.5, Pion) was used to calculate $-\log P_e$ values. CNS± designations were assigned based on comparisons of known CNS± compounds in the literature.[36,39,130-132]

4.5. References

1. Alzheimer's Association. *Alzheimers Dement.* **2012**, *8*, 131-168.
2. DeToma, A. S.; Salamekh, S.; Ramamoorthy, A.; Lim, M. H. *Chem. Soc. Rev.* **2012**, *41*, 608-621.
3. Pithadia, A. S.; Lim, M. H. *Curr. Opin. Chem. Biol.* **2012**, *16*, 67-73.
4. Savelieff, M. G.; Lee, S.; Liu, Y.; Lim, M. H. *ACS Chem. Biol.* **2013**, *8*, 856-865.
5. Kepp, K. P. *Chem. Rev.* **2012**, *112*, 5193-5239.
6. Soto, C. *Nat. Rev. Neurosci.* **2003**, *4*, 49-60.
7. Teplow, D. B.; Lazo, N. D.; Bitan, G.; Bernstein, S.; Wyttenbach, T.; Bowers, M. T.; Baumketner, A.; Shea, J.-E.; Urbanc, B.; Cruz, L.; Borreguero, J.; Stanley, H. E. *Acc. Chem. Res.* **2006**, *39*, 635-645.
8. Rauk, A. *Chem. Soc. Rev.* **2009**, *38*, 2698-2715.
9. Hardy, J.; Selkoe, D. J. *Science* **2002**, *297*, 353-356.
10. Jakob-Roetne, R.; Jacobsen, H. *Angew. Chem. Int. Ed.* **2009**, *48*, 3030-3059.
11. Ayton, S.; Lei, P.; Bush, A. I. *Free Radical Biol. Med.* **2012**, DOI: 10.1016/j.freeradbiomed.2012.1010.1558.
12. DeToma, A. S.; Choi, J.-S.; Braymer, J. J.; Lim, M. H. *ChemBioChem* **2011**, *12*, 1198-1201.
13. Ross, C. A.; Poirier, M. A. *Nat. Med.* **2004**, *10 Suppl*, S10-17.
14. Fändrich, M. *Cell. Mol. Life Sci.* **2007**, *64*, 2066-2078.
15. Zhu, X.; Su, B.; Wang, X.; Smith, M. A.; Perry, G. *Cell. Mol. Life Sci.* **2007**, *64*, 2202-2210.
16. Faller, P.; Hureau, C. *Chem. Eur. J.* **2012**, *18*, 15910-15920.
17. Greenough, M. A.; Camakaris, J.; Bush, A. I. *Neurochem. Int.* **2012**, *62*, 540-555.
18. Eskici, G.; Axelsen, P. H. *Biochemistry* **2012**, *51*, 6289-6311.
19. Faller, P.; Hureau, C. *Dalton Trans.* **2009**, 1080-1094.
20. Faller, P. *ChemBioChem* **2009**, *10*, 2837-2845.
21. Bush, A. I. *J. Alzheimers Dis.* **2013**, *33 Suppl 1*, S277-S281.
22. Shearer, J.; Szalai, V. A. *J. Am. Chem. Soc.* **2008**, *130*, 17826-17835.
23. Shearer, J.; Callan, P. E.; Tran, T.; Szalai, V. A. *Chem. Commun.* **2010**, *46*, 9137-9139.

24. Ghosh, C.; Dey, S. G. *Inorg. Chem.* **2013**, *52*, 1318-1327.
25. Bousejra-ElGarah, F.; Bijani, C.; Coppel, Y.; Faller, P.; Hureau, C. *Inorg. Chem.* **2011**, *50*, 9024-9030.
26. Sarell, C. J.; Wilkinson, S. R.; Viles, J. H. *J. Biol. Chem.* **2010**, *285*, 41533-41540.
27. Noy, D.; Solomonov, I.; Sinkevich, O.; Arad, T.; Kjaer, K.; Sagi, I. *J. Am. Chem. Soc.* **2008**, *130*, 1376-1383.
28. Faller, P. *Free Radical Biol. Med.* **2012**, *52*, 747-748.
29. Rodríguez-Rodríguez, C.; Telpoukhovskaia, M.; Orvig, C. *Coord. Chem. Rev.* **2012**, *256* 2308-2332.
30. Braymer, J. J.; DeToma, A. S.; Choi, J.-S.; Ko, K. S.; Lim, M. H. *Int. J. Alzheimers Dis.* **2011**, *2011*, 623051.
31. Hureau, C.; Sasaki, I.; Gras, E.; Faller, P. *ChemBioChem* **2010**, *11*, 950-953.
32. Dedeoglu, A.; Cormier, K.; Payton, S.; Tseitlin, K. A.; Kremsky, J. N.; Lai, L.; Li, X.; Moir, R. D.; Tanzi, R. E.; Bush, A. I.; Kowall, N. W.; Rogers, J. T.; Huang, X. *Exp. Gerontol.* **2004**, *39*, 1641-1649.
33. Wu, W.-h.; Lei, P.; Liu, Q.; Hu, J.; Gunn, A. P.; Chen, M.-s.; Rui, W.-f.; Su, X.-y.; Xie, Z.-p.; Zhao, Y.-F.; Bush, A. I.; Li, Y.-m. *J. Biol. Chem.* **2008**, *283*, 31657-31664.
34. Rodríguez-Rodríguez, C.; Sánchez de Groot, N.; Rimola, A.; Álvarez-Larena, Á.; Lloveras, V.; Vidal-Gancedo, J.; Ventura, S.; Vendrell, J.; Sodupe, M.; González-Duarte, P. *J. Am. Chem. Soc.* **2009**, *131*, 1436-1451.
35. Hindo, S. S.; Mancino, A. M.; Braymer, J. J.; Liu, Y.; Vivekanandan, S.; Ramamoorthy, A.; Lim, M. H. *J. Am. Chem. Soc.* **2009**, *131*, 16663-16665.
36. Choi, J.-S.; Braymer, J. J.; Nanga, R. P. R.; Ramamoorthy, A.; Lim, M. H. *Proc. Natl. Acad. Sci. U. S. A.* **2010**, *107*, 21990-21995.
37. Choi, J.-S.; Braymer, J. J.; Park, S. K.; Mustafa, S.; Chae, J.; Lim, M. H. *Metallomics* **2011**, *3*, 284-291.
38. Braymer, J. J.; Choi, J.-S.; DeToma, A. S.; Wang, C.; Nam, K.; Kampf, J. W.; Ramamoorthy, A.; Lim, M. H. *Inorg. Chem.* **2011**, *50*, 10724-10734.
39. Pithadia, A. S.; Kochi, A.; Soper, M. T.; Beck, M. W.; Liu, Y.; Lee, S.; DeToma, A. S.; Ruotolo, B. T.; Lim, M. H. *Inorg. Chem.* **2012**, *51*, 12959-12967.
40. He, X.; Park, H. M.; Hyung, S. J.; DeToma, A. S.; Kim, C.; Ruotolo, B. T.; Lim, M. H. *Dalton Trans.* **2012**, *41*, 6558-6566.
41. Sharma, A. K.; Pavlova, S. T.; Kim, J.; Finkelstein, D.; Hawco, N. J.; Rath, N. P.; Mirica, L. M. *J. Am. Chem. Soc.* **2012**, *134*, 6625-6636.
42. Jones, M. R.; Service, E. L.; Thompson, J. R.; Wang, M. C.; Kimsey, I. J.; DeToma, A. S.; Ramamoorthy, A.; Lim, M. H.; Storr, T. *Metallomics* **2012**, *4*, 910-920.
43. Lee, S.; Zheng, X.; Krishnamoorthy, J.; Park, H. M.; Brender, J. R.; Savelieff, M. G.; Kim, J. H.; Kim, C.; Ramamoorthy, A.; Bowers, M. T.; Lim, M. H. **2013**, Submitted for publication.
44. Liu, Y.; Kochi, A.; Pithadia, A. S.; Lee, S.; Nam, Y.; Beck, M. W.; He, X.; Lee, D.; Lim, M. H. **2013**, Submitted for publication.
45. Ono, M.; Haratake, M.; Saji, H.; Nakayama, M. *Bioorg. Med. Chem.* **2008**, *16*, 6867-6872.

46. Ono, M.; Maya, Y.; Haratake, M.; Nakayama, M. *Bioorg. Med. Chem.* **2007**, *15*, 444-450.
47. Ono, M.; Hori, M.; Haratake, M.; Tomiyama, T.; Mori, H.; Nakayama, M. *Bioorg. Med. Chem.* **2007**, *15*, 6388-6396.
48. Ono, M.; Watanabe, R.; Kawashima, H.; Kawai, T.; Watanabe, H.; Haratake, M.; Saji, H.; Nakayama, M. *Bioorg. Med. Chem.* **2009**, *17*, 2069-2076.
49. Kung, H. F.; Lee, C. W.; Zhuang, Z. P.; Kung, M. P.; Hou, C.; Plössl, K. *J. Am. Chem. Soc.* **2001**, *123*, 12740-12741.
50. Zhang, W.; Oya, S.; Kung, M. P.; Hou, C.; Maier, D. L.; Kung, H. F. *J. Med. Chem.* **2005**, *48*, 5980-5988.
51. Kung, M.-P.; Hou, C.; Zhuang, Z.-P.; Zhang, B.; Skovronsky, D.; Trojanowski, J. Q.; Lee, V. M.-Y.; Kung, H. F. *Brain Res.* **2002**, *956*, 202-210.
52. Klunk, W. E.; Wang, Y.; Huang, G. F.; Debnath, M. L.; Holt, D. P.; Mathis, C. A. *Life Sci.* **2001**, *69*, 1471-1484.
53. Ono, M.; Watanabe, H.; Watanabe, R.; Haratake, M.; Nakayama, M.; Saji, H. *Bioorg. Med. Chem. Lett.* **2011**, *21*, 117-120.
54. Hyung, S.-J.; DeToma, A. S.; Brender, J. R.; Lee, S.; Vivekanandan, S.; Kochi, A.; Choi, J.-S.; Ramamoorthy, A.; Ruotolo, B. T.; Lim, M. H. *Proc. Natl. Acad. Sci. U. S. A.* **2013**, *110*, 3743-3748.
55. Tay, W. M.; da Silva, G. F.; Ming, L. J. *Inorg. Chem.* **2013**, *52*, 679-690.
56. Havsteen, B. H. *Pharmacol. Ther.* **2002**, *96*, 67-202.
57. Yao, L. H.; Jiang, Y. M.; Shi, J.; Tomas-Barberan, F. A.; Datta, N.; Singanusong, R.; Chen, S. S. *Plant Foods Hum. Nutr.* **2004**, *59*, 113-122.
58. Kim, J.; Lee, H. J.; Lee, K. W. *J. Neurochem.* **2010**, *112*, 1415-1430.
59. Ehrnhoefer, D. E.; Bieschke, J.; Boeddrich, A.; Herbst, M.; Masino, L.; Lurz, R.; Engemann, S.; Pastore, A.; Wanker, E. E. *Nat. Struct. Mol. Biol.* **2008**, *15*, 558-566.
60. Hirohata, M.; Ono, K.; Takasaki, J.; Takahashi, R.; Ikeda, T.; Morinaga, A.; Yamada, M. *Biochim. Biophys. Acta* **2012**, *1822*, 1316-1324.
61. Wall, R. J.; He, G.; Denison, M. S.; Congiu, C.; Onnis, V.; Fernandes, A.; Bell, D. R.; Rose, M.; Rowlands, J. C.; Balboni, G.; Mellor, I. R. *Toxicology* **2012**, *297*, 26-33.
62. Balboni, G.; Congiu, C.; Onnis, V.; Maresca, A.; Scozzafava, A.; Winum, J. Y.; Maietti, A.; Supuran, C. T. *Bioorg. Med. Chem. Lett.* **2012**, *22*, 3063-3066.
63. Middleton, E., Jr.; Kandaswami, C.; Theoharides, T. C. *Pharmacol. Rev.* **2000**, *52*, 673-751.
64. Nijveldt, R. J.; van Nood, E.; van Hoorn, D. E. C.; Boelens, P. G.; van Norren, K.; van Leeuwen, P. A. M. *Am. J. Clin. Nutr.* **2001**, *74*, 418-425.
65. Jang, B. G.; Yun, S. M.; Ahn, K.; Song, J. H.; Jo, S. A.; Kim, Y. Y.; Kim, D. K.; Park, M. H.; Han, C.; Koh, Y. H. *J. Alzheimers Dis.* **2010**, *21*, 939-945.
66. McMurry, J., *Organic Chemistry*. 6th ed.; Brooks/Cole--Thomson Learning: Belmont, CA, 2004.
67. Leuma Yona, R.; Mazères, S.; Faller, P.; Gras, E. *ChemMedChem* **2008**, *3*, 63-66.
68. Braymer, J. J.; Merrill, N. M.; Lim, M. H. *Inorg. Chim. Acta* **2011**, *380*, 261-268.

69. Storr, T.; Merkel, M.; Song-Zhao, G. X.; Scott, L. E.; Green, D. E.; Bowen, M. L.; Thompson, K. H.; Patrick, B. O.; Schugar, H. J.; Orvig, C. *J. Am. Chem. Soc.* **2007**, *129*, 7453-7463.
70. http://www.acdlabs.com.
71. Martell, A. E.; Smith, R. M., *Critical Stability Constants*. Plenum: New York, 1974-1989.
72. Schweigert, N.; Zehnder, A. J.; Eggen, R. I. *Environ. Microbiol.* **2001**, *3*, 81-91.
73. Avdeef, A.; Sofen, S. R.; Bregante, T. L.; Raymond, K. N. *J. Am. Chem. Soc.* **1978**, *100*, 5362-5370.
74. Pajouhesh, H.; Lenz, G. R. *NeuroRx* **2005**, *2*, 541-553.
75. Hider, R. C.; Liu, Z. D.; Khodr, H. H. *Methods Enzymol.* **2001**, *335*, 190-203.
76. Satterfield, M.; Brodbelt, J. S. *Anal. Chem.* **2000**, *72*, 5898-5906.
77. Sever, M. J.; Wilker, J. J. *Dalton Trans.* **2004**, 1061-1072.
78. Tyson, C. A.; Martell, A. E. *J. Am. Chem. Soc.* **1968**, *90*, 3379-3386.
79. Verma, P.; Weir, J.; Mirica, L.; Stack, T. D. *Inorg. Chem.* **2011**, *50*, 9816-9825.
80. Maity, D.; Manna, A. K.; Karthigeyan, D.; Kundu, T. K.; Pati, S. K.; Govindaraju, T. *Chem. Eur. J.* **2011**, *17*, 11152-11161.
81. Kaim, W. *Dalton Trans.* **2003**, 761-768.
82. Kundu, T.; Sarkar, B.; Mondal, T. K.; Mobin, S. M.; Urbanos, F. A.; Fiedler, J.; Jiménez-Aparicio, R.; Kaim, W.; Lahiri, G. K. *Inorg. Chem.* **2011**, *50*, 4753-4763.
83. Balla, J.; Kiss, T.; Jameson, R. F. *Inorg. Chem.* **1992**, *31*, 58-62.
84. Thompson, J. S.; Calabrese, J. C. *J. Am. Chem. Soc.* **1986**, *108*, 1903-1907.
85. Lippard, S. J.; Berg, J. M., *Principles of Bioinorganic Chemistry*. University Science Books: California, 1994.
86. Gray, H. B.; Stiefel, E. I.; Valentine, J. S.; Bertini, I., *Biological Inorganic Chemistry: Structure and Reactivity*. University Science Books: California, 2007.
87. Palmer, G., Electron Paramagnetic Resonance of Metalloproteins. In *Physical Methods in Bioinorganic Chemistry: Spectroscopy and Magnetism*, Lawrence Que, J., Ed. University Science Books: Sausalito, CA, 2000; pp 121-185.
88. Pirker, K. F.; Baratto, M. C.; Basosi, R.; Goodman, B. A. *J. Inorg. Biochem.* **2011**, *112*, 10-16.
89. Rall, J.; Wanner, M.; Albrecht, M.; Hornug, F. M.; Kaim, W. *Chem. Eur. J.* **1999**, *5*, 2802-2809.
90. Ferreira Severino, J.; Goodman, B. A.; Reichenauer, T. G.; Pirker, K. F. *Free Radical Res.* **2011**, *45*, 115-124.
91. Eaton, D. R. *Inorg. Chem.* **1964**, *3*, 1268-1271.
92. Kaim, W.; Wanner, M.; Knödler, A.; Záliš, S. *Inorg. Chim. Acta* **2002**, *337*, 163-172.
93. Harmalker, S.; Jones, S. E.; Sawyer, D. T. *Inorg. Chem.* **1983**, *22*, 2790-2794.
94. Hendrickson, D.; Pierpont, C., Valence Tautomeric Transition Metal Complexes. In *Spin Crossover in Transition Metal Compounds II*, Springer Berlin Heidelberg: 2004; Vol. 234, pp 63-95.
95. Thompson, J. S.; Calabrese, J. C. *Inorg. Chem.* **1985**, *24*, 3167-3171.
96. Wang, S. H.; Liu, F. F.; Dong, X. Y.; Sun, Y. *J. Phys. Chem. B* **2010**, *114*, 11576-11583.

97. Vivekanandan, S.; Brender, J. R.; Lee, S. Y.; Ramamoorthy, A. *Biochim. Biophys. Res. Commun.* **2011**, *411*, 312-316.
98. Sinha, S.; Du, Z.; Maiti, P.; Klarner, F. G.; Schrader, T.; Wang, C.; Bitan, G. *ACS Chem. Neurosci.* **2012**, *3*, 451-458.
99. Ladiwala, A. R.; Dordick, J. S.; Tessier, P. M. *J. Biol. Chem.* **2011**, *286*, 3209-3218.
100. Popovych, N.; Brender, J. R.; Soong, R.; Vivekanandan, S.; Hartman, K.; Basrur, V.; Macdonald, P. M.; Ramamoorthy, A. *J. Phys. Chem. B* **2012**, *116*, 3650-3658.
101. Zhu, M.; Rajamani, S.; Kaylor, J.; Han, S.; Zhou, F.; Fink, A. L. *J. Biol. Chem.* **2004**, *279*, 26846-26857.
102. Palhano, F. L.; Lee, J.; Grimster, N. P.; Kelly, J. W. *J. Am. Chem. Soc.* **2013**, *135*, 7503-7510.
103. Airoldi, C.; Sironi, E.; Dias, C.; Marcelo, F.; Martins, A.; Rauter, A. P.; Nicotra, F.; Jimenez-Barbero, J. *Chem. Asian J.* **2013**, *8*, 596-602.
104. Mancino, A. M.; Hindo, S. S.; Kochi, A.; Lim, M. H. *Inorg. Chem.* **2009**, *48*, 9596-9598.
105. Soper, M. T.; DeToma, A. S.; Hyung, S.-J.; Lim, M. H.; Ruotolo, B. T. *PhysChemChemPhys* **2013**, *15*, 8952-8961.
106. Bieschke, J.; Russ, J.; Friedrich, R. P.; Ehrnhoefer, D. E.; Wobst, H.; Neugebauer, K.; Wanker, E. E. *Proc. Natl. Acad. Sci. U. S. A.* **2010**, *107*, 7710-7715.
107. Lemkul, J. A.; Bevan, D. R. *Biochemistry* **2012**, *51*, 5990-6009.
108. Yun, S.; Urbanc, B.; Cruz, L.; Bitan, G.; Teplow, D. B.; Stanley, H. E. *Biophys. J.* **2007**, *92*, 4064-4077.
109. Abelein, A.; Bolognesi, B.; Dobson, C. M.; Gräslund, A.; Lendel, C. *Biochemistry* **2012**, *51*, 126-137.
110. Rice-Evans, C. A.; Miller, N. J.; Paganga, G. *Free Radical Biol. Med.* **1996**, *20*, 933-956.
111. Heim, K. E.; Tagliaferro, A. R.; Bobilya, D. J. *J. Nutr. Biochem.* **2002**, *13*, 572-584.
112. Bastianetto, S.; Quirion, R. *Front. Biosci.* **2004**, *9*, 3447-3452.
113. Lipinski, C. A.; Lombardo, F.; Dominy, B. W.; Feeney, P. J. *Adv. Drug Delivery Rev.* **2001**, *46*, 3-26.
114. Clark, D. E.; Pickett, S. D. *Drug Discov. Today* **2000**, *5*, 49-58.
115. Gans, P.; Sabatini, A.; Vacca, A. *Ann. Chim.* **1999**, *89*, 45-49.
116. Alderighi, L.; Gans, P.; Ienco, A.; Peters, D.; Sabatini, A.; Vacca, A. *Coord. Chem. Rev.* **1999**, *184*, 311-318.
117. Hendrickson, H. P.; Kaufman, A. D.; Lunte, C. E. *J. Pharm. Biomed. Anal.* **1994**, *12*, 325-334.
118. Hodnick, W. F.; Milosavljevic, E. B.; Nelson, J. H.; Pardini, R. S. *Biochem. Pharmacol.* **1988**, *37*, 2607-2611.
119. Trott, O.; Olson, A. J. *J. Comput. Chem.* **2010**, *31*, 455-461.
120. Morris, G. M.; Huey, R.; Lindstrom, W.; Sanner, M. F.; Belew, R. K.; Goodsell, D. S.; Olson, A. J. *J. Comput. Chem.* **2009**, *30*, 2785-2791.
121. Teplow, D. B. *Methods Enzymol.* **2006**, *413*, 20-33.

122. Suzuki, Y.; Brender, J. R.; Soper, M. T.; Krishnamoorthy, J.; Zhou, Y.; Ruotolo, B. T.; Kotov, N. A.; Ramamoorthy, A.; Marsh, E. N. *Biochemistry* **2013**, *52*, 1903-1912.
123. Schanda, P.; Forge, V.; Brutscher, B. *Proc. Natl. Acad. Sci. U. S. A.* **2007**, *104*, 11257-11262.
124. Goddard, T. D.; Kneller, D. G. **1999**, SPARKY3, University of California, San Francisco.
125. Krishnamoorthy, J.; Brender, J. R.; Vivekanandan, S.; Jahr, N.; Ramamoorthy, A. *J. Phys. Chem. B* **2012**, *116*, 13618-13623.
126. Re, R.; Pellegrini, N.; Proteggente, A.; Pannala, A.; Yang, M.; Rice-Evans, C. *Free Radical Biol. Med.* **1999**, *26*, 1231-1237.
127. Schugar, H.; Green, D. E.; Bowen, M. L.; Scott, L. E.; Storr, T.; Bohmerle, K.; Thomas, F.; Allen, D. D.; Lockman, P. R.; Merkel, M.; Thompson, K. H.; Orvig, C. *Angew. Chem. Int. Ed.* **2007**, *46*, 1716-1718.
128. Deraeve, C.; Pitie, M.; Meunier, B. *J. Inorg. Biochem.* **2006**, *100*, 2117-2126.
129. Himes, R. A.; Park, G. Y.; Siluvai, G. S.; Blackburn, N. J.; Karlin, K. D. *Angew. Chem. Int. Ed.* **2008**, *47*, 9084-9087.
130. Di, L.; Kerns, E. H.; Fan, K.; McConnell, O. J.; Carter, G. T. *Eur. J. Med. Chem.* **2003**, *38*, 223-232.
131. Avdeef, A.; Bendels, S.; Di, L.; Faller, B.; Kansy, M.; Sugano, K.; Yamauchi, Y. *J. Pharm. Sci.* **2007**, *96*, 2893-2909.
132. Pion, Inc. *BBB Protocol and Test Compounds*; Woburn (MA), 2009.

Chapter 5: Visualization of Transition Metals in Cortical and Hippocampal Brain Tissues from an Alzheimer's Disease Mouse Model

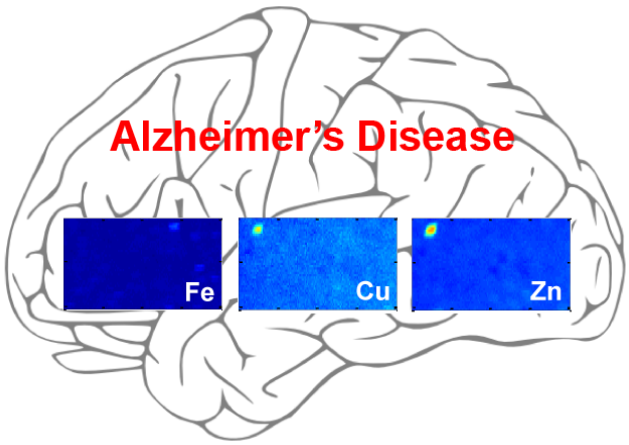

This chapter was conducted in collaboration with Professor James Penner-Hahn and Professor Henry Paulson at the University of Michigan. Tissues from Professor Paulson's laboratory were provided by Dr. Edgardo Rodríguez Lébron. Experiments were conducted at BioCAT, Sector 18 at the Advanced Photon Source at Argonne National Laboratory by Dr. Aniruddha Deb and Joseph J. Braymer. We thank Andrew Crawford with MatLab assistance.

5.1. Introduction

Alzheimer's disease (AD) is a complex form of dementia that has a staggering worldwide impact, particularly on aging populations.[1-3] A number of factors have been proposed to contribute to the onset and progression of the disease.[2-5] Among these, the accumulation of amyloid-β (Aβ) peptides has been one of the most widely studied factors. The observation of proteinaceous deposits mainly composed of aggregated Aβ peptides in the brain was early evidence viewed as supporting the contribution of Aβ peptides to AD pathology and led to the establishment of the amyloid cascade hypothesis; however, subsequent research has demonstrated the complexity not only of this hypothesis but of the disease itself.[2,4,6] Shortly after the amyloid cascade hypothesis was proposed, it was found that the Aβ aggregates and neuropil from diseased human brain tissues contained high concentrations of transition metals, such as Fe, Cu, and Zn, compared to those of age-matched healthy controls.[3,5,7-9] Thus, it was suggested that metal ion dyshomeostasis and miscompartmentalization in the brain could contribute to AD neuropathogenesis.

Investigation of the relationship between metal ion dyshomeostasis/miscompartmentalization and AD could provide a better understanding of the role of metal ions in the disease and suggest a potential avenue for therapeutic intervention. Metal chelating agents have been employed as one approach to interrogate the involvement of metals in AD pathogenesis, and some have been suggested to be potential agents for metal chelation therapy (*e.g.*, clioquinol, PBT2).[3,7,10-16] Though this indirectly supports metal involvement in AD, these metal chelators have also been unable to offer substantial insight into the molecular mechanisms by which metal ions could contribute to the initiation and progression of the disease. In part, this results from the lack of available biophysical methods to directly investigate metal ions in tissue. For example, the electronic configuration of certain metal ions (*e.g.*, Zn(II)) renders them silent to traditional spectroscopic methods which can impede detailed characterization of their chemical environment.[17] Additionally, changes in metal content and distribution ideally would be measured in a way that maintains the integrity of the sample (*i.e.*, minimal sample preparation, nominal damage to tissue during analysis) while also avoiding the introduction of trace metal

contaminants.[18-20] To circumvent these physical limitations, synchrotron-based spectroscopic techniques such as X-ray fluorescence (XRF) imaging and X-ray absorption spectroscopy (XAS) offer a convenient way to directly probe metal ions within biologically relevant tissues from diseased states, including neurodegenerative diseases.[17,19,21-28]

Previous studies have exploited X-ray-based techniques to explore various aspects of metal content in AD brain tissues.[24-29] Miller and co-workers identified regions of human AD brain tissue where Cu and Zn were co-localized, even though most of the metal content was heterogeneously distributed.[24] This work was followed by studies connecting metal content to protein density, showing that when considering protein density, only Zn was elevated in plaques from the APPswe/PS1ΔE9 transgenic mouse model of AD.[25] Recently, Feng and co-workers described the progression of metal levels in the brains of AD mice (APP/V717I) upon aging from pre-symptomatic to late stages of AD, including analysis of the oxidation states of Fe and Cu within the tissue.[28] In agreement with the previous literature, Fe, Cu, and Zn were also elevated in that AD model.[26,28] Expanding upon previous observations of metal contents in AD brain tissues, we report additional information regarding the elemental content and distribution in regions of brain tissue of late-stage (16-18 month-old) double-transgenic AD mice (APPswe/PS1ΔE9) by microbeam X-ray fluorescence (μ-XRF) microscopy.

5.2. Results and discussion

5.2.1. Metal contents and distributions in hippocampal and cortical tissues from the brains of AD and wild-type mice by μ-XRF imaging

Bioavailable metals such as Fe, Cu, and Zn are unambiguously correlated with AD, but a consensus with respect to their connection to neuropathogenesis has yet to be reached. As further indication regarding the potential role, if any, that these metals play in development of the disease, the content and distribution of these metals were measured by μ-XRF microscopy in brain tissues of APPswe/PS1ΔE9 and wild-type (WT) control mice (Figures 5.1 and 5.2). In the mouse brain tissue, several non-overlapping regions (200 x 1000 μm) of the cortex and hippocampus were selected to

scan with 5 x 5 μm beam resolution. Overall, the AD tissue presented mostly diffuse distributions of Fe, Cu, and Zn throughout the tissue; however, discrete, localized regions of the metals could also be identified in various areas.

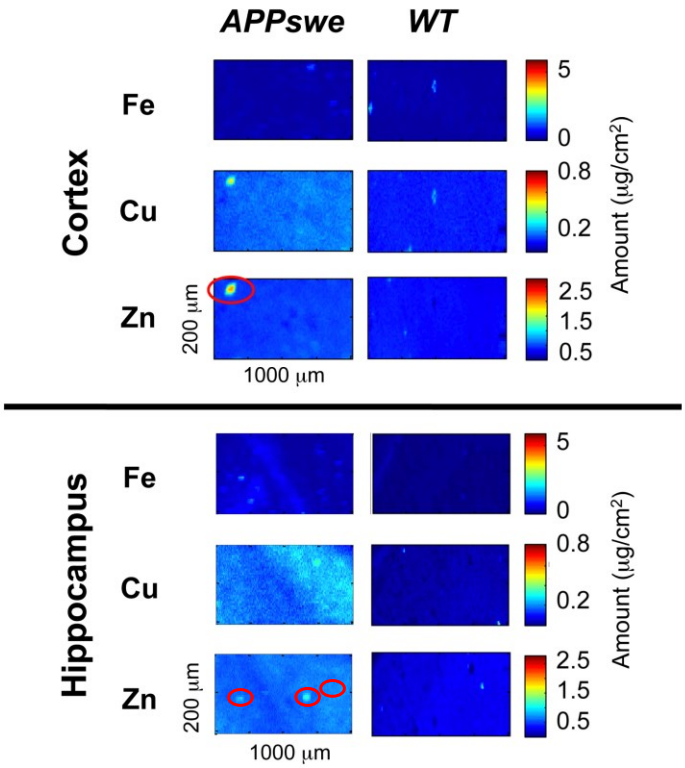

Figure 5.1. Visualization of Fe, Cu, and Zn in brain tissues of AD (APPswe/PS1ΔE9 (APPswe), left) and wild-type (WT, right) mice by microbeam X-ray fluorescence (μ-XRF) imaging. Metal distribution was measured in the cortex (top) and hippocampus (bottom) and scaled to the same color levels representing the metal content in μg/cm^2. Non-overlapping regions with dimensions of 200 μm x 1000 μm were scanned with 5 μm x 5 μm beam resolution and 5 μm step size.

Within these tissues, the average absolute metal concentrations were quantified relative to standards of known concentration (Table 5.1). Averages were taken from several independent areas for the cortex and hippocampus of APPswe/PS1ΔE9 and WT mice brain samples. In general, the metal concentrations were slightly higher in the diseased cortex than in the WT control cortex; Fe was approximately the same while Cu and Zn were approximately 1.5 times higher. The hippocampus seemed to be more

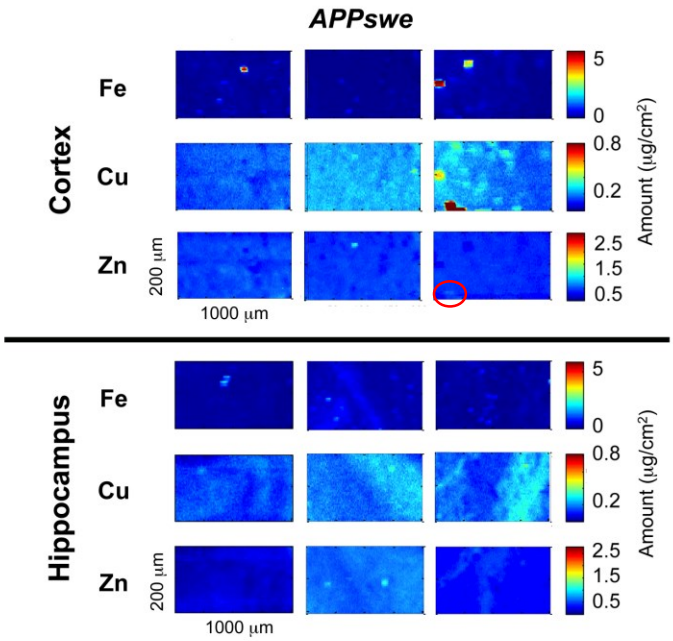

Figure 5.2. Visualization of Fe, Cu, and Zn in brain tissues APPswe mice by microbeam X-ray fluorescence (μ-XRF) imaging. Metal distribution was measured in the cortex (top) and hippocampus (bottom) and scaled to the same color levels representing the metal content in μg/cm^2.

sensitive to changes in amount of metals. In the AD mice hippocampus, Fe, Cu, and Zn amounts were found to be approximately 2, 6, and 2 times higher, respectively, than those in the hippocampus of WT mice. Comparison of the cortex and hippocampus from WT mice revealed that average metal concentrations were higher in the cortex (Table 5.1). In contrast, the amount of each metal was approximately similar in the two brain areas for the diseased mice. Along with changes in the average metal composition, there were striking differences in the distribution of metal for the WT *versus* the diseased samples. In the former, all of the metals have relatively narrow, approximately Gaussian distribution. In contrast, the distribution of metal concentrations was noticeably broader and, for Fe and Cu in the hippocampal tissue, obviously bimodal (Figure 5.3).

These observations are consistent with a redistribution of metals in the brain as the disease progresses, suggesting a disruption of typical metal homeostasis. In the previous reports, Fe and Zn content of the same AD mice (56 weeks old) were reported to be slightly greater in the cortex as compared to the hippocampus; Cu content was

approximately the same in both regions.[26] Our findings indicated higher average quantity of Fe in the hippocampus and of Cu and Zn in both brain regions in the AD model relative to those in WT mice, which may be related to the fact that the mice in this study were approximately two to four months older than those in previously reported studies with the same AD mouse model.[26]

In a different AD mouse model that expresses only an APP mutation within the Aβ sequence (APP/V717I), Feng and co-workers have reported metal distributions and quantifications for Fe, Cu, and Zn in mice aged 1, 4, 12, and 18 months.[28] Several comparisons can be made between their data set and ours, especially since the mice in the present study are similar in age to the oldest mice in the previous study. The cortical concentrations of Fe in the APPswe/PS1ΔE9 mice were within the range of concentrations measured in the APP/V717I mice, while a higher quantity of Cu and Zn was measured in the APPswe/PS1ΔE9 model.

Table 5.1. Average metal contents in cortical and hippocampal regions of APPswe/PS1ΔE9 (APPswe) and wild type (WT) mice brain tissues.

Metal	Cortex				Hippocampus			
	APPswe		*WT*		*APPswe*		*WT*	
	μg/cm^2	μM	μg/cm^2	μM	μg/cm^2	μM	μg/cm^2	μM
Fe	0.194 ± 0.024	700 ± 80	0.180 ± 0.014	640 ± 50	0.238 ± 0.043	850 ± 150	0.104 ± 0.001	372 ± 3
Cu	0.204 ± 0.015	640 ± 50	0.118 ± 0.001	373 ± 3	0.233 ± 0.013	730 ± 40	0.0388 ± 0.0009	122 ± 3
Zn	0.541 ± 0.026	1660 ± 80	0.346 ± 0.006	1059 ± 18	0.582 ± 0.085	1800 ± 300	0.302 ± 0.028	920 ± 90

In the hippocampus, Fe was moderately higher in the APPswe/PS1ΔE9 model over the APP/V717I model, but the WT control mice in the present study contained slightly less Fe than the range presented in the previous report. Zn was slightly higher in the hippocampus of APPswe/PS1ΔE9 mice than the APP/V717I mice model, while the WT controls in both experiments were more comparable. Cu concentrations were similar in the hippocampus of the WT mice for both studies, while in the APPswe/PS1ΔE9 model the amount of Cu measured in the tissue was outside the range reported for the APP/V717I model.[28]

In summary, Feng and co-workers established that in the APP/V717I transgenic mice, Fe and Cu were enriched in the cortex, and only Cu was enriched in the hippocampus. Our findings were similar for Cu, which was elevated in both the cortex and hippocampus of the APPswe/PA1ΔE9 double transgenic mice; however, we additionally observed that these AD mice also accumulated larger amounts of Fe and Zn in the hippocampus as well. Thus, despite minor differences, comparable values and sites of accumulation were obtained for the amount of Fe, Cu, and Zn in the APPswe/PS1ΔE9 mice used in our study compared with the different AD mouse model at similar ages. Taken together, these results may support that dyshomeostasis and miscompartmentalization of metal ions can possibly occur upon progression of the disease.

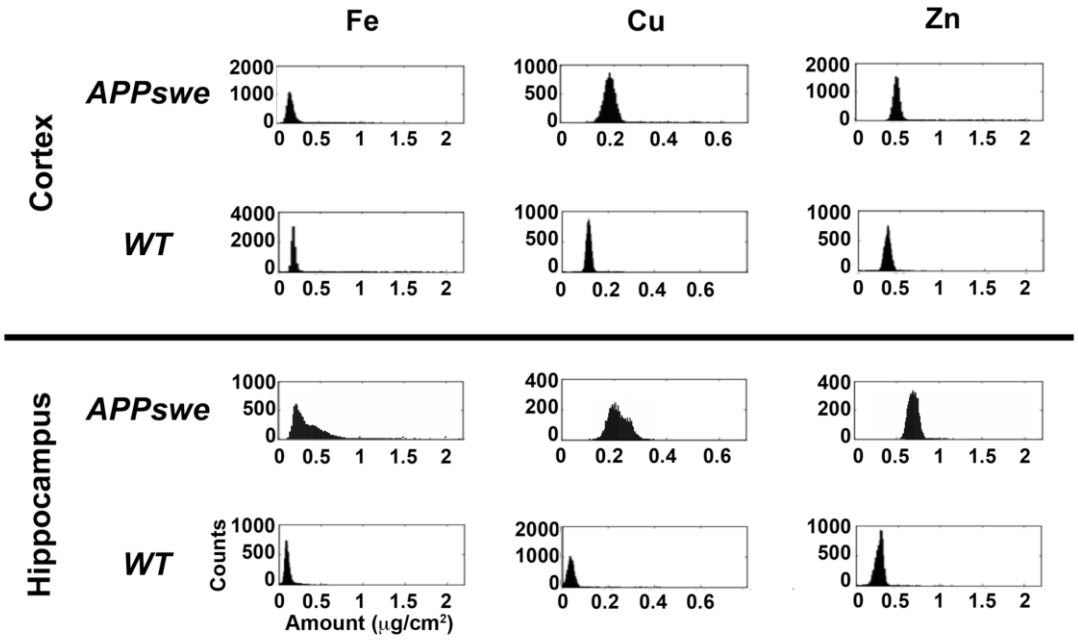

Figure 5.3. Histograms of Fe, Cu, and Zn amounts in selected brain tissue regions of AD APPswe (top) or WT (bottom) mice. The occurrence of the metal is plotted as frequency in counts versus the amount in μg/cm^2.

5.2.2. Metal correlations

In addition to defining the distribution of individual metals in the brain tissue, it would be valuable to understand their potential co-localization. To accomplish this, correlation plots illustrating the co-incidence of two metals' amounts (μg/cm^2) in each pixel were generated, with the frequency of occurrence depicted by a color gradient

(Figure 5.4). Overall, the trends in these scatterplots were variable, reflecting the heterogeneity of the tissue. One observable feature was that for the WT distributions there was, generally, a modest linear correlation between each of the metals over a narrow range. This is consistent with cells having, on average, similar metal concentrations, with the observed variation resulting primarily from changes in the amount of cells that are illuminated by the beam. In contrast, the diseased tissue appears to show more pronounced structure, suggesting that there are regions that are selectively enhanced in Cu, or Fe, or Zn.

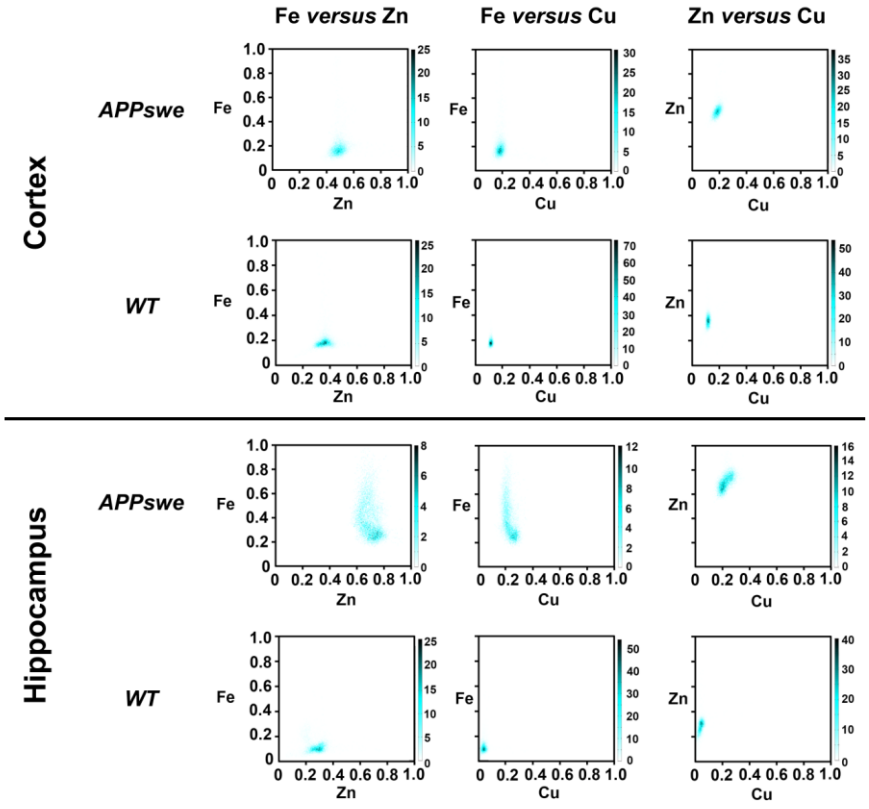

Figure 5.4. Correlation of metal contents (μg/cm^2) in regions of APPswe (top) and WT (bottom) mice brain tissue according to co-incident metal concentrations. Color gradient indicates counts of overlapping pixels within the scanned regions.

Within the AD cortex and hippocampus regions depicted in Figure 5.1, there was a slight correlation between the amounts of Cu and Zn. Since that APPswe/PS1ΔE9 mice of this age have extensive Aβ plaque deposition,[30] it is possible that the observed co-localization of Cu and Zn could occur along with these protein aggregates. Previous

work by Miller and co-workers identified Cu and Zn together in hot spots from human AD brain, as well as co-localized within plaques.[24] Thus, Cu and Zn may be able to co-localize similarly in the tissues of diseased mice. Compared to the other correlation plots and those in the WT mice, there was a less obvious connection between the localization of Fe with Cu or Zn, particularly in the cortex. Within the cortex of AD mice, increased amounts of Cu and Zn were observed compared to WT. In the hippocampus, however, both the amounts and the localization of Fe corresponding to Cu or Zn were noticeably different. This may indicate sensitivity to changes in metal ion homeostasis in the hippocampus upon AD progression compared to WT mice. Considering the small size of the scanned areas, it is difficult to be certain that there is a gross correlation between these metals in the entire cortex, hippocampus, or full brain. Overall, it is possible that Cu and Zn ion homeostasis could be mutually altered in the brains of AD, but this could be highly dependent on the specific region in the tissue.

5.3. Conclusion

In order to accelerate the development of novel therapeutic strategies to tackle AD, additional research is needed to continue exploring the complex underlying causes of the disease. Mounting experimental evidence supports the view that transition metals, such as Fe, Cu, and Zn, contribute to AD neuropathogenesis, yet uncertainty remains about the extent of their involvement. Using synchrotron XRF imaging, we investigated the distribution of Fe, Cu, and Zn in the cortex and hippocampus of an AD mouse model relative to WT control mice. In 16-18 month-old AD mice, concentrations of Fe, Cu, and Zn were increased in both cortical and hippocampal regions over the age-matched WT mice. The absolute amounts of metals in these tissues were also higher than reported previously in a relatively younger AD mouse model,[26] but only slightly higher than a different AD mouse model of the same age.[28] Therefore, along with the normal aging process, progression of AD might trigger the changes in contents and distributions of metals in the tissue. While most of the metal appeared to be uniformly distributed throughout the tissue, at least at the 5 μm resolution limit, certain regions were found to contain highly concentrated metals. Overall, these results and observations provide additional evidence to support the notion that endogenous metal

ion regulation may be disrupted in the AD diseased state. As a future direction, it will be worthwhile to obtain a better understanding of the mechanisms leading to dyshomeostasis and miscompartmentalization of metals in the brain in an effort to define their relation to AD neuropathogenesis.[29]

5.4. Experimental

5.4.1. Animal care and tissue preparation

The double-transgenic Alzheimer's disease mouse line (APPswe/PS1ΔE9) was bred and maintained at the University of Michigan animal husbandry facility. For these studies, 16-18 month-old female double-transgenic mice and age- and gender-matched littermate wild-type (WT) controls were euthanized by anesthetic overdose of a xylazine/ketamine mixture followed by cardiac perfusion with phosphate buffered saline (PBS) and a 4% paraformaldehyde solution. At this age, APPswe/PS1ΔE9 mice have a high density of Aβ deposits (*i.e.*, plaques) throughout the brain parenchyma.[30] Following dissection, brains were cryoprotected in 30% sucrose and stored frozen at −80 °C. For imaging, 50 μm thick coronal slices were prepared on a sledge microtome retrofitted with a Duraedge PTFE-coated microtome blade. Tissue sections were carefully mounted for μ-XRF imaging using Kapton tape. The University Committee on Use and Care of Animals (UCUCA) at the University of Michigan approved all mouse studies.

5.4.2. Synchrotron μ-X-ray fluorescence (μ-XRF) microscopy

Analyses of metal contents and distributions were conducted in non-overlapping regions of interest (ROI; 200 x 1000 μm) of cortical and hippocampal tissues from APPswe/PS1ΔE9 (5 or 7 ROIs, n = 3) using μ-XRF at the Biophysics Collaborative Access Team (BioCAT) beamline 18 at the Advanced Photon Source (APS) at Argonne National Laboratory (Argonne, IL, USA). The synchrotron X-ray beam was tuned to 10 keV using a Si(111) double crystal monochromator. The incident beam was focused to 5 μm x 5 μm at the sample using Kirkpatrick-Baez mirrors. Spectra were collected with a dwell time of 250 ms/pixel and 5 μm step size. Variations due to beam flux were normalized based on changes in I_0. An area of 200 x 1000 μm was scanned, and metal

concentrations were determined by comparison with the intensity from thin metal foils (Fe, 0.1 μm, Cu, 0.1 μm, and Zn, 0.08 μm) measured under identical conditions. The approximate molar concentrations were determined by accounting for the thickness of the tissue, assuming a density of 1 g/cm^3, and dividing by the atomic weight of these elements.

5.5. References

1. Alzheimer's Association. *Alzheimers Dement.* **2012**, *8*, 131-168.
2. Jakob-Roetne, R.; Jacobsen, H. *Angew. Chem. Int. Ed.* **2009**, *48*, 3030-3059.
3. DeToma, A. S.; Salamekh, S.; Ramamoorthy, A.; Lim, M. H. *Chem. Soc. Rev.* **2012**, *41*, 608-621.
4. Anand, R.; Kaushal, A.; Wani, W. Y.; Gill, K. D. *Pathobiology* **2012**, 79, 55-71.
5. A. Rauk. *Chem. Soc. Rev.* **2009**, *38*, 2698-2715.
6. Hardy, J.; Selkoe, D. J. *Science* **2002**, *297*, 353-356.
7. Scott, L. E.; Orvig, C. *Chem. Rev.* **2009**, *109*, 4885-4910.
8. Frederickson, C. J.; Koh, J.-Y.; Bush, A. I. *Nat. Rev. Neurosci.* **2005**, *6*, 449-462.
9. Lovell, M. A.; Robertson, J. D.; Teesdale, W. J.; Campbell, J. L.; Markesbery, W. R. *J. Neurol. Sci.* **1998**, *158*, 47-52.
10. Pithadia, A. S.; Lim, M. H. *Curr. Opin. Chem. Biol.* **2012**, *16*, 67-73.
11. Rodríguez-Rodríguez, C.; Telpoukhovskaia, M.; Orvig, C. *Coord. Chem. Rev.* **2012**, *256*, 2308-2332.
12. Tõugu, V.; Tiiman, A.; Palumaa, P. *Metallomics* **2011**, *3*, 250-261.
13. Perez, L. R.; Franz, K. J. *Dalton Trans.* **2010**, *39*, 2177-2187.
14. Cherny, R. A.; Atwood, C. S.; Xilinas, M. E.; Gray, D. N.; Jones, W. D.; McLean, C. A.; Barnham, K. J.; Volitakis, I.; Fraser, F. W.; Kim, Y.-S.; Huang, X. D.; Goldstein, L. E.; Moir, R. D.; Lim, J. T.; Beyreuther, K.; Zheng, H.; Tanzi, R. E.; Masters, C. L.; Bush, A. I. *Neuron* **2001**, *30*, 665-676.
15. Adlard, P. A.; Cherny, R. A.; Finkelstein, D. I.; Gautier, E.; Robb, E.; Cortes, M.; Volitakis, I.; Liu, X.; Smith, J. P.; Perez, K.; Laughton, K.; Li, Q.-X.; Charman, S. A.; Nicolazzo, J. A.; Wilkins, S.; Deleva, K.; Lynch, T.; Kok, G.; Ritchie, C. W.; Tanzi, R. E.; Cappai, R.; Masters, C. L.; Barnham, K. J.; Bush, A. I. *Neuron* **2008**, *59*, 43-55.
16. Faux, N. G.; Ritchie, C. W.; Gunn, A.; Rembach, A.; Tsatsanis, A.; Bedo, J.; Harrison, J.; Lannfelt, L.; Blennow, K.; Zetterberg, H.; Ingelsson, M.; Masters, C. L.; Tanzi, R. E.; Cummings, J. L.; Herd, C. M.; Bush A. I. *J. Alzheimers Dis.* **2010**, *20*, 509-516.
17. Penner-Hahn, J. E. *Coord. Chem. Rev.* **2005**, *249*, 161-177.
18. Ralle, M.; Lutsenko, S. *Biometals* **2009**, *22*, 197-205.
19. Fahrni, C. J. *Curr. Opin. Chem. Biol.* **2007**, *11*, 121-127.
20. Barrea, R. A.; Gore, D.; Kondrashkina, E.; Weng, T.; Heurich, R.; Vukonich, M.; Orgel, J.; Davidson, M.; Collingwood, J. F.; Mikhaylova, A.; Irving, T. C. *Proc. 8th Int. Conf. X-ray Microscopy IPAP Conf. Series 7* **2006**, 230-232.

21. Collingwood, J. F.; Mikhaylova, A.; Davidson, M. R.; Batich, C.; Streit, W. J.; Eskin, T.; Terry, J.; Barrea, R.; Underhill, R. S.; Dobson, J. *J. Phys.: Conf. Ser.* **2005**, *17*, 54-60.
22. Strange, R. W.; Feiters, M. C. *Curr. Opin. Struct. Biol.*, **2008**, *18*, 609-616.
23. Popescu, B. F. G.; Nichol, H. *CNS Neurosci. Ther.* **2011**, *17*, 256-268.
24. Miller, L. M.; Wang, Q.; Telivala, T. P.; Smith, R. J.; Lanzirotti, A.; Miklossy, J. *J. Struct. Biol.* **2006**, *155*, 30-37.
25. Leskovjan, A. C.; Lanzirotti, A.; Miller, L. M. *NeuroImage* **2009**, *47*, 1215-1220.
26. Leskovjan, A. C.; Kretlow, A.; Lanzirotti, A.; Barrea, R.; Vogt, S.; Miller, L. M. *NeuroImage* **2011**, *55*, 32-38.
27. Wang, H.-J.; Wang, M.; Wang, B.; Meng, X.-Y.; Wang, Y.; Li, M.; Feng, W.-Y.; Zhao, Y.-L.; Chai, Z.-F. *J. Anal. At. Spect.* **2010**, *25*, 328-333.
28. Wang, H.; Wang, M.; Wang, B.; Li, M.; Chen, H.; Yu, X.; Zhao, Y.; Feng, W.; Chai, Z. *Metallomics* **2012**, *4*, 289-296.
29. Wang, H.; Wang, M.; Wang, B.; Li, M.; Chen, H.; Yu, X.; Yang, K.; Chai, Z.; Zhao, Y.; Feng, W. *Metallomics* **2012**, *4*, 1113-1118.
30. Rodríguez-Lebrón, E.; Gouvion, C. M.; Moore, S. A.; Davidson; B. L.; H. L. Paulson, *Mol. Ther.* **2009**, *17*, 1563-1573.

Chapter 6: Concluding Remarks and Perspectives

In the past decade, chemists have contributed to the continued efforts to understand the role of metal–Aβ species in AD by recognizing the potential for targeting and modulating these complexes using small molecules. As a result, the literature now hosts several libraries of compounds with various frameworks and structural derivatives, which have been used to uncover some nuances of the metal-peptide interaction and its impact on aggregation and toxicity. Ongoing efforts in this area will be valuable as the onset and progression of AD are determined.

The work presented in Chapters 2-4 of this dissertation demonstrates the importance of exploring compounds' mode of action at the molecular level as a critical step toward logical advancements in new molecule design using the flavonoid family of compounds. Flavonoids have been long known to have biological properties suitable for a number of disease targets, and this work reveals explanations for their reactivity with metal-associated Aβ species by considering the balance between both metal chelation and Aβ interacting properties to modulate the *in vitro* reactivity of these complexes. From these studies, we now understand that a combination of hydrophobic and hydrophilic groups facilitates ligand-peptide contacts in addition to tuning metal binding affinity. Furthermore, evidence of a compact Aβ–flavonoid complex may rationalize an observed alternate aggregation pathway, which results in non-toxic, amorphous aggregates. In the presence of metal ions, the generation of a ternary complex consisting of Aβ, a metal ion, flavonoid, could account for a similar observation to the metal-free scenario, whereby small, amorphous aggregates are the end product of flavonoid-mediated metal-associated Aβ aggregation. With this in mind, individual aspects of each structure, such as the presence of a catechol or pyrogallol group, can be investigated and future generations of molecules can be systematically designed to optimize those properties (*i.e.*, metal binding, Aβ interaction, antioxidant properties).

In terms of ligand design, several strategies would be valuable in the near future to elaborate on the structure-interaction-reactivity relationship such as (1) altering Aβ targeting groups, (2) tuning metal binding affinities, (3) improving BBB permeability, and (4) stabilizing structures to withstand physiological conditions. The aminoisoflavone framework could serve as a template on which minor modifications could be made initially. For a comparison of structure, interaction, and reactivity, analogues of **1**-**4** should be prepared without the primary amine to determine how that chemical structure alters reactivity. It would be insightful to know whether the presence of this group serves as a targeting moiety for the peptide or if it aids in compound solubility. Clearly, between **1**-**4** and their methoxylated precursors **1a**-**4a**, the catechol group played a valuable role in mediating Aβ interaction and in metal chelation as it is known to bind well to metal ions such as Cu(II) and Fe(III). In the aminoisoflavones, compound **4**, which has this moiety, binds to Cu(II) with high affinity. Therefore, another step in modification of these compounds could include variation of the donor atoms for metal binding. To tune the binding affinity and potentially the selectivity for other cations (*e.g.*, Cu(I)), substitution of the oxygen atoms with nitrogen or sulfur could be explored. Derivatives having these various metal chelation moieties could then be useful to examine the involvement of lesser studied, biologically relevant metal ions in AD.

Another improvement to this framework would be introduction of groups to improve BBB permeability. Using both naturally occurring and synthetic compounds, simple modifications could be made to increase the likelihood of passive uptake into the brain. For example, esterification of the hydroxyl groups might be one method to facilitate BBB permeability. Alternatively, other groups have used pro-drug approaches that exploit receptors and transporters in the brain, such as GLUT-1. According to this method, sugar groups are used to mask the metal chelation site and minimize systemic metal binding. This moiety is then recognized by the transporters which then facilitate transport into the brain; cleavage of the sugar group reveals the active, metal chelating compound.[1,2] Pursuit of compounds with BBB targeting moieties or combination approaches to improve delivery of the present molecules will be an ongoing effort for these and other families of compounds. Finally, synthetic modifications that would

render compounds less susceptible to metabolism, such as the inclusion of fluorine atoms, might be worthwhile to consider.

Subsequently, with an expanded flavonoid library, more extensive *in vitro* tests could be conducted to investigate the interplay of these molecules with other proteins and biomolecules relevant to AD, as well as intracellular mechanisms that may be affected by these compounds. Flavonoids are known to have numerous biological targets, including enzymes that may be relevant in AD.[3] Screening of the newly designed flavonoid derivatives against various enzymes and proteins, in addition to evaluating their interaction and reactivity with metal-free and metal associated Aβ, would help to illuminate more details of the biological relevance of these compounds to AD. This finding would provide a comprehensive view of the structure-interaction-reactivity relationship and allow for more systematic compound development toward therapeutics or diagnostics.

In the next several years, the field will benefit from the continued compound development and chemical insights on the structure-interaction-reactivity relationships between small molecules and metal–Aβ species. Furthermore, optimization of properties that would be relevant to biological application (*e.g.*, toxicity, BBB permeability, metabolic stability) for these and other lead compounds will be required. Moving forward, the field is well poised to begin to explore ways to employ these compounds as chemical tools to probe metal–Aβ species using *in vivo* models. In the near future, fundamental knowledge on the roles of metal ions in AD should be more clearly revealed using *in vitro* models and AD animal models. Thus, the exact types of molecules could subsequently be designed more efficiently and specifically. Collaborations across disciplines, such as medicinal chemistry, biology, biophysics, and neuroscience, will enhance these efforts, since the multiple parameters that must be considered in more complex systems.

References

1. Schugar, H.; Green, D. E.; Bowen, M. L.; Scott, L. E.; Storr, T.; Bohmerle, K.; Thomas, F.; Allen, D. D.; Lockman, P. R.; Merkel, M.; Thompson, K. H.; Orvig, C. *Angew. Chem. Int. Ed.* **2007**, *46*, 1716-1718.
2. Storr, T.; Merkel, M.; Song-Zhao, G. X.; Scott, L. E.; Green, D. E.; Bowen, M. L.;

Thompson, K. H.; Patrick, B. O.; Schugar, H. J.; Orvig, C. *J. Am. Chem. So*c. **2007**, *129*, 7453-7463.
3. Nijveldt, R. J.; van Nood, E.; van Hoorn, D. E. C.; Boelens, P. G.; van Norren, K.; van Leeuwen, P. A. M. *Am. J. Clin. Nutr.* **2001**, *74*, 418-425.

Appendix A: Quantifying Potential Changes in Metal Homeostasis in Glaucoma by Synchrotron μ-X-ray Fluorescence (μ-XRF) Imaging

The work presented herein was conducted in collaboration with Professor Samuel D. Crish and Professor Cornelis van der Schyf at the Northeastern Ohio Medical Universities, as well as Professor James Penner-Hahn at the University of Michigan. Brain and retina tissue samples from mice were obtained from Professor Crish. Experiments were conducted at BioCAT, Sector 18 at the Advanced Photon Source at Argonne National Laboratory in collaboration with Dr. Aniruddha Deb and with beamline support from Dr. Raul Barrea. Kevin O'Neill assisted in processing images in MatLab.

A.1. Introduction

Glaucoma is a visual neuropathy leading to vision loss that accounts for 9–12% of blindness and affects almost 60 million people worldwide, including 3 million Americans.[1] Deterioration of retinal ganglion cell (RGC) neurons and axons, which compose the optic nerve, is cited as source of vision loss in the disease.[2] Like Alzheimer's disease (AD), glaucoma is incurable; however, it can be treated if detected early through routine eye exams.[1] There are three forms of glaucoma: primary open angle, angle closure, and normal-tension glaucoma. The most common form of glaucoma, primary open angle glaucoma, is characterized by elevated intraocular pressure (IOP) in the eye, due to improper fluid drainage. In angle closure glaucoma, IOP is elevated, but the pressure increases rapidly. Normal-tension glaucoma is rare and is characterized by damage to the optic nerve without an increase in IOP. Glaucoma can be diagnosed at any age and in some cases there may be no outward symptoms.[1] Risk increases with age, family history, diabetes, or extreme nearsightedness.[1] Elevated IOP is the only modifiable symptom of the disease, but lowering the IOP does not always guarantee that vision loss will be stopped.[3,4]

Although the exact cause of glaucoma is unknown, it was long-believed to affect only the retina and other areas of the eye. Its consideration as a neurodegenerative disease (*i.e.*, involving the brain) has occurred recently, however, redefining the way

researchers address the problem.[2] It has been demonstrated that areas of the brain may provide early signs of neurodegeneration in conjunction with the onset of glaucoma. In particular, degeneration of the optic nerve could be an early sign of disease progression. Crish *et al.* recently presented evidence to support this hypothesis.[2] Using a glaucoma mouse model, early injury to axons in the optic nerve was found to damage transport of a fluorescent dye between the retina and brain.[2] Furthermore, their results showed the sectorial nature of glaucoma; progression of the disease is independent in each eye and pathological features can occur in various, discrete sections of the retina.[2] Interestingly, they suggested that impaired transport was an early sign of glaucoma that preceded the damage to the retina.[2] These studies demonstrated the involvement of the entire visual system in glaucoma and justified its classification as a form of neurodegeneration.

Along with this paradigm shift, it has been recognized that other external factors could contribute to the complexity of glaucoma. For example, glaucoma incidence correlates with AD, suggesting their respective neuropathogenesis may be similar. According to several reports, the abnormally folded protein (*i.e.*, amyloid-β (Aβ)) of AD have been found in the eye.[4,5] Interestingly, Ito *et al.* suggested that $A\beta_{42}$ expression in the retina increased as glaucoma progressed in the monkeys.[3] Furthermore, evidence of retinal degeneration has been observed in AD mice models, along with deposition of Aβ in the retina.[4] It has also been observed that soluble oligomeric forms of Aβ, which are currently implicated in AD as a potentially toxic species,[6] can induce apoptosis of RGCs in glaucoma.[4,5]

In AD and other neurodegenerative diseases, including glaucoma, oxidative stress is pervasive, leading some researchers to suggest a disruption of metal ion homeostasis in affected tissues could be a contributing factor.[6-10] With some similar features in glaucoma (*e.g.*, oxidative stress), it is possible that metal ions in the retina, optic nerve, and/or brain could be disrupted as well; however, there have been only a few attempts to address this question. A recent report implied that Cu and Zn could be involved in pseudoexfoliation syndrome (PEX), which is prevalent in Turkish populations and can lead to a glaucoma.[11] Most research on metals in glaucoma to date, however, has been focused on Fe homeostasis.[12,13] Because of the tendency of unbound Fe to

produce reactive oxygen species (ROS; *e.g.*, H_2O_2), accumulation of Fe has been linked to retinal degradation and some Fe overload diseases have accompanying vision loss.[13] For example, deficiency of ceruloplasmin, a ferroxidase, can lead to the accumulation of Fe in the retina and subsequent retinal damage.[13] Farkas *et al.* mapped genetic changes in monkeys with glaucoma to uncover changes in transferrin, ceruloplasmin, and ferritin expression. In mild glaucoma, there was no change to transferrin expression in mild cases of glaucoma but increased in moderate-to-severe cases.[12] Ceruloplasmin was 1.3-fold higher than the control for mild glaucoma while monkeys with severe glaucoma had a six-fold increase in gene expression. Finally, ferritin presented a 2.2-fold increase in both mild and severe cases compared to the control.[12] As a result, the authors suggested that Fe, and potentially Cu, could be involved in neurodegeneration. Thus, changes in the expression of transferrin, ceruloplasmin, and ferritin could be neuroprotective, where upregulation of these proteins is intended mitigate the consequences of abnormal transition metal ion homeostasis.

To expand on these previous works, it would be valuable to directly determine if changes to the metal distribution (*i.e.*, quantity, localization) occur. A variety of approaches have been utilized to probe this question in neurodegenerative diseases.[14] Among them, X-ray techniques have been employed to investigate the distribution, localization, and quantification of transition metals in AD brain tissue. Synchrotron μ-X-ray fluorescence (μ-XRF) provides a quantifiable, metal-specific approach to identify discrete accumulations of metals in tissue.[14] Its requirements for sample preparation are minimal and it is relatively non-destructive, making it an ideal method to interrogate metal homeostasis in biological tissues. With the mounting evidence suggesting the involvement of metals in AD and other neurodegenerative diseases,[6-10] it would be interesting to consider their possible role in glaucoma as well. To the best of our knowledge, there have been no reports of μ-XRF applied to tissue derived from a glaucoma mouse model to determine metal ion concentration or distribution in the retina or brain.

In the present study, a mouse model of glaucoma, DBA2/J, which is known to display age-related IOP elevation, was used to measure changes in metal ion homeostasis in the retina (RGC layers) and in the superior colliculus (SC) region of the

brain, compared to a non-disease control mouse model C57BL/6. Young mice (2-5 months), which do not show glaucoma pathology, were compared with older mice (10-12 months) that have signs of the disease (*i.e.*, retinal degradation). Two sets of μ-XRF data were collected independently for preliminary investigations of the metal content changes in regions of the retina and brain of glaucoma-affected mice. The outcomes of these preliminary experiments will be discussed herein.

A.2. Results and discussion

A.2.1. Imaging of metals and quantification of Fe, Cu, and Zn in the retina and superior colliculus

To date, there have been few reports on the metal contents and their potential changes in glaucoma-affected tissues.[11-13] Using μ-XRF, initial attempts have been made to visualize the distribution of metals, particularly Fe, Cu, and Zn, in the retinorecipient layer of the retina, which is affected by glaucoma, and in the SC of the brain. Furthermore, the amounts of these metals were quantified by comparison with known standards.

In the first data set, multiple, non-overlapping sections of retina tissue were scanned. Representative images are shown in Figure A.1. The images show both discrete and diffuse concentrations of metal within the particular region. In both the control and diseased mice, Fe was found in mainly localized areas. Cu and Zn were more dispersed with overall higher amounts in the diseased mice over the controls. The quantification of all tissues from these regions suggested, however, that overall there were no changes to the amounts of metals present in the retina depending on age or strain (Figure A.2). In the retina, the amount of Zn was highest among all samples, while Fe and Cu levels remained relatively constant. In the brain tissues, the overall concentrations of Cu and Zn were much lower than that of the retina; the amount of Fe was approximately the same as the retina. There was a slight overall decrease in Fe in the young and old diseased mice brain tissue, which might indicate a potential change with glaucoma progression compared to healthy aging. It is worthwhile to point out that the data presented here typically contained a blank area along with regions of the brain

tissue that are not affected in glaucoma due to the dimensions of the scan area. Therefore, in order to draw conclusions for these data, quantification of metals in the brain tissues should be refined to more specifically characterize the SC, which is limited to the top 300 μm of the brain slice.

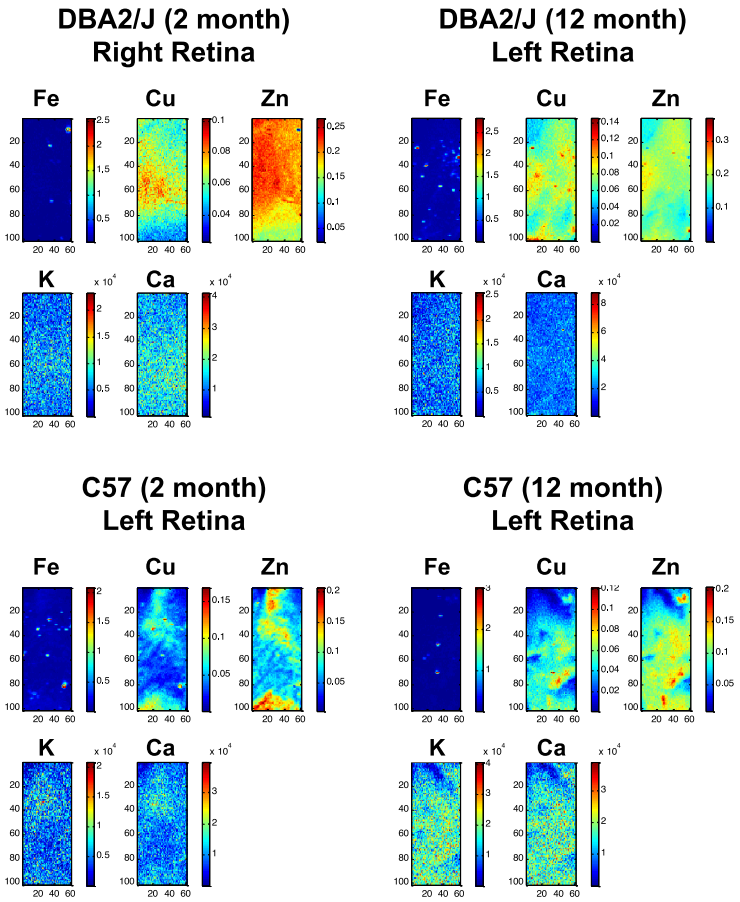

Figure A.1. Images depicting the concentration of Fe, Cu, Zn, K, and Ca in retinal tissues from first sample set (10 μm x 10 μm beam size). Concentrations are in μg/cm^2 for Fe, Cu, and Zn and in total counts for K and Ca.

In the first set of samples, the beam size was small and representative regions of the tissue were scanned. To probe whether we could obtain useful information with less sensitivity, the second set of data was collected using a larger beam. Fewer samples were measured, but the larger beam size afforded the opportunity to investigate a single large area of the retina; regions of the brain tissue remained small to focus on the SC (Figure A.3). From these results, the overall amounts of metal were found to be

significantly higher than in the first sample set, possibly as a result of the larger scan area (Figure A.4). Comparison of the retina results suggests that Fe and Cu may be decreased in old mice compared to younger mice and in the control mice *versus* the diseased mice at a young age. Young and old diseased mice had similar amounts of Fe and Cu, potentially indicating a deficit that is not recovered upon progression of the disease.

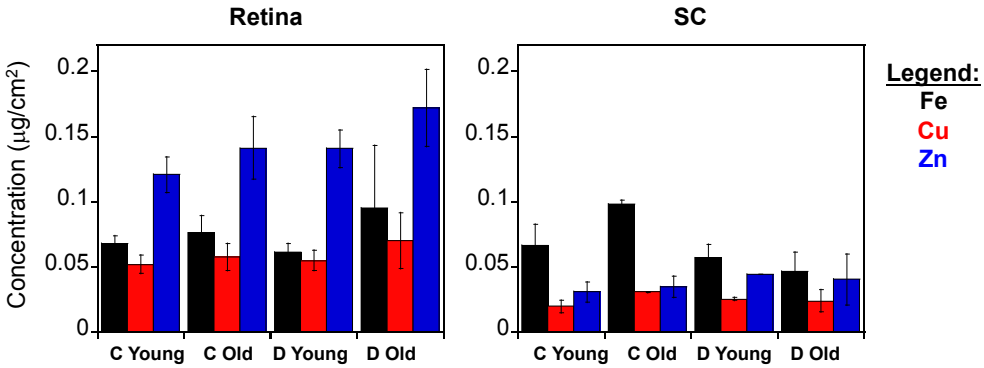

	Retina (μg/cm²)			SC (μg/cm²)		
	Fe	Cu	Zn	Fe	Cu	Zn
C57 (Normal), Young	0.068 ± 0.006	0.052 ± 0.007	0.121 ± 0.014	0.067 ± 0.017	0.020 ± 0.005	0.031 ± 0.008
C57 (Normal), Old	0.076 ± 0.013	0.058 ± 0.011	0.141 ± 0.024	0.098 ± 0.003	0.031 ± 0.001	0.035 ± 0.008
DBA2/J (Disease), Young	0.061 ± 0.007	0.055 ± 0.008	0.141 ± 0.015	0.057 ± 0.010	0.025 ± 0.001	0.044 ± 0.002
DBA2/J (Disease), Old	0.096 ± 0.048	0.070 ± 0.021	0.172 ± 0.030	0.046 ± 0.015	0.024 ± 0.008	0.040 ± 0.020

Figure A.2. Quantification of Fe, Cu, and Zn content in retinal and brain (SC) tissue from first sample set. Error bars represent the mean of several independent sections measured across multiple retinas from *n* = 2 mice per group, which are considered to be independent samples.

There have been several challenges to data collection and analysis that should be considered for future success in this project. First, one challenge arises from the nature of the tissue samples. The retina tissues can be non-uniform in thickness since they are obtained through dissection, whereas the brain tissues are sliced to an even thickness by a microtome. Transmission of the X-ray beam through areas of different thickness could misrepresent the actual metal contents. The retina is *ca.* 300 μm thick and can vary by 20-50 μm locally. Furthermore, the top three layers of the retinal cells (*ca.* 20-30 μm) contain the cells of interest in this disease. Therefore, transmission of the beam through the tissue could reflect metal contents in areas that are not of interest.

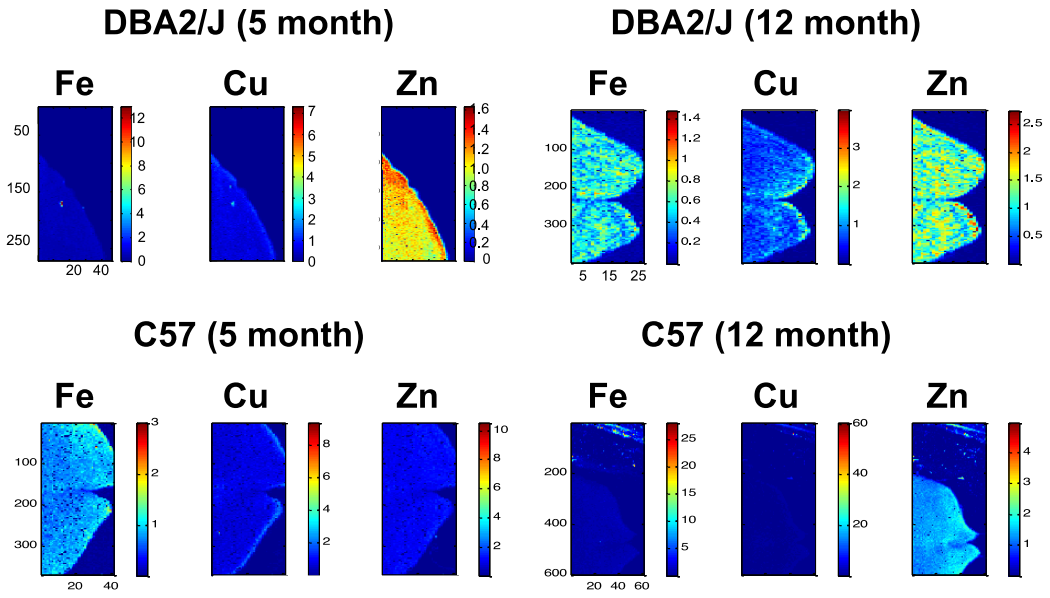

Figure A.3. Images depicting the concentration of Fe, Cu, and Zn in brain tissues from second sample set (20 μm x 20 μm beam size). Concentrations are in μg/cm^2 for Fe, Cu, and Zn.

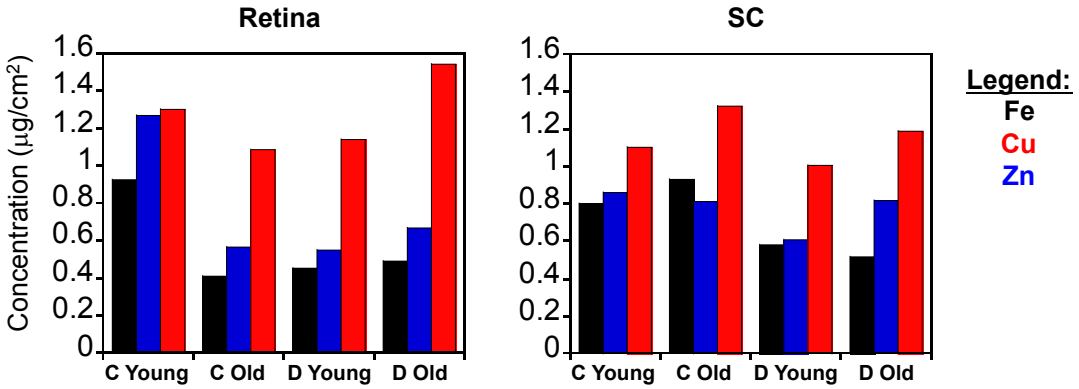

	Retina (μg/cm^2)			SC (μg/cm^2)		
	Fe	Cu	Zn	Fe	Cu	Zn
C57 (Normal), Young	0.926	1.266	1.298	0.799	0.861	1.098
C57 (Normal), Old	0.409	0.563	1.084	0.930	0.813	1.323
DBA2/J (Disease), Young	0.453	0.546	1.139	0.579	0.607	1.004
DBA2/J (Disease), Old	0.487	0.664	1.544	0.516	0.817	1.187

Figure A.4. Quantification of Fe, Cu, and Zn content in retinal and brain (SC) tissue from second sample set. Sample size was insufficient to calculate mean or error.

A.3. Conclusion and Future Directions

Although there have been many efforts to investigate the role of metal ion dyshomeostasis in neurodegenerative diseases such as AD, relatively few efforts have been made to explore if metals have a connection to the progression of glaucoma. The present study was conducted to determine the amounts and localization of metals in retina and brain tissues from healthy and diseased mice. Based on the data presented herein, metal contents may be affected based on age and disease state. Some of the preliminary results suggest that Fe may be constant or slightly higher in the diseased mice retinas compared to the young diseased mice, as was previously suggested,[13] while Cu and Zn are relatively unchanged. For the brain tissue, more detailed data analysis would be beneficial to refine the conclusion. Based on these preliminary findings, further efforts to comprehensively characterize metal ion homeostasis in glaucoma with larger sample sizes will be worthwhile as the outcomes from such studies could shed light on a new target areas for glaucoma research.

It appears that glaucoma could originate from multiple factors. As protein aggregation and metal dyshomeostasis are hallmarks of AD and other neurodegenerative diseases like AD, it is possible that these are found and may be interconnected in glaucoma as well. As next steps in this project following the determination of metal concentrations, relating those observations to specific proteins might be of interest. Broadly, it will be interesting to see if correlations between glaucoma and other diseases can be made more conclusively. There have been suggestions that glaucoma and AD may be linked, for example. Thus, it will be valuable to elucidate the pathological connection, if any, between glaucoma and AD, perhaps using metal ions and/or Aβ as a mediating player, as efforts continue to find ways to halt progression of both diseases and eventually offer a cure.

A.4. Experimental

A.4.1. Animal care and tissue preparation

The DBA2/J glaucoma mice and C57BL/6 control mice were purchased from Jackson Laboratories and maintained at the Northeast Ohio Medical University

(NEOMED) animal husbandry facility. For these studies, young (2 or 5 month) and old (10 or 12 month) DBA2/J mice were compared with age-matched controls. The older glaucoma mice used in the study have been shown to express glaucoma pathology while the young mice do not display neurodegeneration. There were at least 2 animals for each age and strain; each eye is an independent sample. The mice were deeply anesthetized followed by cardiac perfusion with 0.9% w/v NaCl and a 4% paraformaldehyde solution. The eyes were removed and stored in 0.9% w/v NaCl. Brains were also removed and stored in either 0.9% w/v NaCl or 20% w/v sucrose. Retinas were removed from the eyes by microdissection and placed within the open region of the sample holder. For imaging, 50 μm thick brain slices were prepared. The samples were prepared by affixing double sided tape to the XRF sample holder. Tissue sections (retina and brain) were carefully mounted between two sheets of Ultralene film (SPEX Sample Prep, Metuchen, NJ, USA). The Institutional Animal Care and Use Committee at NEOMED approved all mouse studies.

A.4.2. Synchrotron μ-X-ray fluorescence (μ-XRF) microscopy

Analyses of metal contents and distributions were conducted in non-overlapping regions of interest (ROI) of various sizes within the RGC layers in the retina and the SC region of the brain using μ-XRF at the Biophysics Collaborative Access Team (BioCAT) beamline 18 at the Advanced Photon Source (APS) at Argonne National Laboratory (Argonne, IL, USA). The synchrotron X-ray beam was tuned to 10 keV using a Si(111) double crystal monochromator. In the retinal tissue, several non-overlapping of 600 μm x 1000 μm (for 10 x 10 μm beam) or a single large regions of interest (ROI) (for 20 x 20 μm beam) were scanned. In the brain tissue, the SC is restricted to the upper 300 μm of the tissue that remains upon removal of the cortex; an ROI sufficiently large to encompass this area was scanned. The incident beam was focused to 10 μm x 10 μm or 20 μm x 20 μm at the sample using Kirkpatrick-Baez mirrors. Spectra were collected with a dwell time of 250 ms/pixel and 10 or 20 μm step size. Variations due to beam flux were normalized based on changes in I_0. Metal concentrations were determined by comparison with the intensity from thin metal foils (Fe, 0.1 μm, Cu, 0.1 μm, and Zn, 0.08

μm) measured under identical conditions. The approximate molar concentration was determined by accounting for the thickness of the tissue, assuming a density of 1 g/cm^3 and dividing by the atomic weight of these elements.

Data were processed in MatLab using a program adapted by Dr. Aniruddha Deb. To circumvent some of these data processing challenges described above, another MatLab program written in the Penner-Hahn group could be applied to selectively analyze specific ROIs from within a larger area. This program would be particularly useful for eliminating aberrant background contributions and focus only on areas of the scan that contained tissue. Additionally, this program could be used to generate images and quantify the metal in a specific set of pixels. It has been applied to some of the data that was obtained in the second set to evaluate the metal contents in the SC as compared to the rest of the brain tissue slice. Given the limitations mentioned above, the quantified data resulting from use of the program would be more useful on future data sets after confirming the conditions, which produce the most reproducible results.

A.5. References

1. http://www.glaucoma.org.
2. Crish, S. D.; Sappington, R. M.; Inman, D. M.; Horner, P. J.; Calkins, D. J. *Proc. Natl. Acad. Sci. U. S. A.* **2010**, *107*, 5196-5201.
3. Ito, Y.; Shimazawa, M.; Tsuruma, K.; Mayama, C.; Ishii, K.; Onoe, H.; Aihara, M.; Araie, M.; Hara, H. *Mol. Vis.* **2012**, *18*, 2647-2657.
4. Chiu, K.; Chan, T. F.; Wu, A.; Leung, I. Y.; So, K.-F.; Chang, R. C.-C. *Age* **2012**, *34*, 633-649.
5. Yin, H.; Chen, L.; Chen, X.; Liu, X. *Med. Hypotheses* **2008**, *71*, 77-80.
6. Savelieff, M. G.; Lee, S.; Liu, Y.; Lim, M. H. *ACS Chem. Biol.* **2013**.
7. DeToma, A. S.; Salamekh, S.; Ramamoorthy, A.; Lim, M. H. *Chem. Soc. Rev.* **2012**, *41*, 608-621.
8. Pithadia, A. S.; Lim, M. H. *Curr Opin Chem Biol* **2012**, *16*, 67-73.
9. Kepp, K. P. *Chem. Rev.* **2012**, *112*, 5193-5239.
10. Faller, P. *Free Radical Biol. Med.* **2012**, *52*, 747-748.
11. Ceylan, O. M.; Can Demirdöğen, B.; Mumcuoğlu, T.; Aykut, O. *Biol. Trace Elem. Res.* **2013** *153*, 28-34.
12. Farkas, R. H.; Chowers, I.; Hackam, A. S.; Kageyama, M.; Nickells, R. W.; Otteson, D. C.; Duh, E. J.; Wang, C.; Valenta, D. F.; Gunatilaka, T. L.; Pease, M. E.; Quigley, H. A.; Zack, D. J. *Invest. Ophthalmol. Vis. Sci.* **2004**, *45*, 1410-1417.
13. He, X.; Hahn, P.; Iacovelli, J.; Wong, R.; King, C.; Bhisitkul, R.; Massaro-Giordano, M.; Dunaief, J. L. *Prog. Retin. Eye Res.* **2007**, *26*, 649-673.
14. Bourassa, M. W.; Miller, L. M. *Metallomics* **2012**, *4*, 721-738.